HEAT TRANSFER AND FLUID FLOW CHARACTERISTICS OF SUPERCRITICAL CARBON DIOXIDE FLOW

A Dissertation
Presented to
The Academic Faculty

by

Sandeep R Pidaparti

In Partial Fulfillment
of the Requirements for the Degree
Doctor of Philosophy in Mechanical Engineering

Georgia Institute of Technology
August 2019

HEAT TRANSFER AND FLUID FLOW CHARACTERISTICS OF SUPERCRITICAL CARBON DIOXIDE FLOW

Approved by:

Dr. Devesh Ranjan, Advisor
George W. Woodruff School of Mechanical Engineering
Georgia Institute of Technology

Dr. Srinivas Garimella
George W. Woodruff School of Mechanical Engineering
Georgia Institute of Technology

Dr. Mostafa Ghiaasiaan
George W. Woodruff School of Mechanical Engineering
Georgia Institute of Technology

Dr. Wenting Sun
George W. Woodruff School of Mechanical Engineering
Georgia Institute of Technology

Dr. Peter Loutzenhiser
George W. Woodruff School of Mechanical Engineering
Georgia Institute of Technology

Dr. Anton Moisseytsev
Nuclear Science and Engineering
Argonne National Laboratory

Dr. Asegun Henry
Department of Mechanical Engineering
Massachusetts Institute of Technology

Date Approved: July 11, 2019

To my beloved family

ACKNOWLEDGEMENTS

This dissertation would not be possible without involvement of several people. I would like to take this opportunity to thank all the people who helped me directly or indirectly to complete this work.

First of all, I would like to thank my advisor, Dr. Devesh Ranjan for his kind support and guidance during my time at STAM Lab. He has been an excellent mentor and the discussions I had with him over years were always enriching and enhanced my critical thinking. Throughout my graduate education, I made several mistakes and am grateful for the patience and faith Dr. Ranjan had in me. I cannot thank him enough for supporting my decision to accept full-time position at National Energy Technology Laboratory (NETL), Pittsburgh and finish this dissertation as a part-time student.

I am also grateful to the other committee members: Dr. Srinivas Garimella, Dr. Mostafa Ghiaasiaan, Dr. Asegun Henry, Dr. Wenting Sun, Dr. Peter Loutzenhiser and Dr. Anton Moisseytsev for taking time out of their busy schedules to review and provide valuable inputs to improve this dissertation. I would like to extend special thanks to Dr. Anton Moisseytsev and Dr. James J. Sienicki for mentoring me during the two summers I interned at Argonne National Laboratory. A portion of this dissertation is inspired by their work at ANL. I would also like to express gratitude to Dr. Mark Anderson and his graduate students at the University of Wisconsin-Madison for their advice during the course of this project and also for providing some of the resources needed for this work.

I am also grateful to all my lab mates and friends during my graduate studies at Texas A&M University: Dr. Sarat Kuchibhatla, Dr. Bhanesh Akula, Dr. Jacob McFarland, Bryce Matsuo, Eric Umrigar and Tom Finn. I would like to specially thank all the people who worked on the supercritical CO_2 projects at Georgia Tech – Taegyu Kang, Chang Hyeon Lim, Won Sup Song, Jacob Cloward, Alon Katz, Dr. Dorrin Jarrahbashi and Dr. Svyatoslav Yorish. They all helped me during the setup phase and to run some of the experiments. Also, I would like to thank my other fellow lab mates and friends at Georgia Tech: David Reilly, Stephen Johnston, John Carter, Dr. Mohammad Mohaghar, Mark Mikhaeil, Prasoon Suchandra, Dr. Gokul Pathikonda, Sam Petter, Jessica Imgrund, Miad Karimi and Steven Roth for all the fun times we had together. These little moments left me with several good memories that I will cherish throughout my life.

I am also grateful to my close friends: Dr. Sarat Kuchibhatla, Dr. Sujan Reddy Gudigopuram, Dr. Krishna Reddy Gujjula and Dr. Sireesh Dadi. The time we spent together were some of the best moments of my life.

Above all, I would like to thank my parents, Subba Reddy Pidaparti and Sridevi Pidaparti and my sister, Divya Pidaparti for their patience and the moral support. The sacrifices they made and the selfless love they showered upon me made me the person I am today. Last but not the least, I will forever be grateful to my wife, Rishi Ninnetha Attunuru who I married during the PhD program. I cannot thank her enough for all the sacrifices she made while I finish my PhD program.

TABLE OF CONTENTS

LIST OF TABLES

LIST OF FIGURES

LIST OF SYMBOLS AND ABBREVIATIONS

A	area [m^2]
A_c	flow cross-sectional area [m^2]
A_s	heat transfer area [m^2]
A_{c_b}	Jackson's bulk flow acceleration parameter [-]
Bo	Jackson's buoyancy parameter [-]
Bu	Kim's buoyancy parameter [-]
C_p	specific heat [J kg^{-1} K^{-1}]
$\overline{C_p}$	integrated specific heat [J kg^{-1} K^{-1}] ($i_w - i_b / T_w - T_b$)
D	diameter [mm]
D_h	hydraulic diameter [mm]
D_i	inner diameter [m]
D_o	outer diameter [m]
E_o	specific work of thermal expansion/contraction [-]
f	fanning friction factor [-]
g	acceleration due to gravity [m s^{-2}]
G	mass flux [kg m^{-2} s^{-1}]
Gr	Grashof number [-]
h	enthalpy [J kg^{-1}]
htc	local heat transfer coefficient [W m^{-2} K^{-1}]
$\overline{htc}$	average heat transfer coefficient [W m^{-2} K^{-1}]
i	enthalpy [J kg^{-1}]
I	current [Amps]

ID	inner diameter [mm]
j	Colburn j-factor [-]
k	thermal conductivity [W m^{-1} K^{-1}]
L	length [m]
$\dot{m}$	mass flow rate [kg s^{-1}]
Nu	local Nusselt number [-]
$\overline{Nu}$	average Nusselt number [-]
OD	outer diameter [mm]
P	pressure [kPa]
Pr	Prandtl number [-]
P_R	normalized pressure (P/P_c) [-]
$\dot{q}$	volumetric heat generation [W m^{-3}]
Q	heat duty [W]
$Q"$	heat flux [W m^{-2}]
Res	thermal resistance [K-m W^{-1}]
R	radius [m] or electrical resistance [Ω]
Ri	Richardson number [-]
Re	Reynolds number [-]
s	entropy [J kg^{-1} K^{-1}]
T	Temperature [°C]
$\bar{T}$	average temperature [°C]
t_{wall}	wall thickness [mm]
t_w	plate thickness [mm]
UA	overall conductance [W K^{-1}]

u velocity [m s^{-1}]

V volume [m^3] or voltage [Volts]

$\dot{V}$ volumetric flow rate [m^3 s^{-1}]

WP wetted perimeter [m]

$\dot{W}$ power [W]

x distance along the length [m] or split fraction between compressors

y distance from the wall [m]

Y^+ non-dimensional distance from the wall [-]

z wall thermocouple distance from heat transfer surface

Greek Symbols

α heat transfer coefficient [W m^{-2} K^{-1}]

β volumetric thermal expansion coefficient [K^{-1}]

∞ ambient

ΔP pressure drop [kPa]

ΔT temperature difference, $|T_w - T_b|$ [°C]

$\Delta\tau$ change in shear stress [N m^{-2}]

ε thermal emissivity [-] or isentropic efficiency [%]

μ dynamic viscosity [kg m^{-1} s^{-1}]

ρ density [kg m^{-3}] or electrical resistivity [Ω-m]

τ shear stress [N m^{-2}]

η fin efficiency/cycle efficiency/plant efficiency

σ Stephan-Boltzmann constant [W m^{-2} K^{-4}]

Φ porosity [-]

θ_b	zigzag channel bend angle

Subscripts

316ss	316 stainless steel
av	average
b	bulk
c	critical or cold
$calc$	calculated
DHT	deteriorated heat transfer
exp	experimental
GL	gas-like
h	hot
in	inlet
$loss$	heat loss
max	maximum
min	minimum
out	outlet
PS	power supply
pc	pseudocritical
w	wall
wi	inner wall
$water, in$	water inlet to cooling block
wo	outer wall
$water, out$	water outlet from cooling block

$w, meas$	measured wall temperature
$w, calc$	calculated wall temperature

Abbreviations

AFR	advanced fast reactor
ANL	Argonne National Laboratory
CB	cooling block
CW	cooling water
CFD	computational fluid dynamics
CMM	coordinate measuring machine
DAQ	data acquisition
EDM	electrical discharge machining
EIA	Energy Information Administration
HPLC	high pressure liquid chromatography
HTR	high temperature recuperator
LTR	low temperature recuperator
LMTD	log-mean temperature difference [°C]
MAE	mean average error [%]
NPH	number of pressure heads
NTU	number of transfer units
PDC	Plant Dynamics Code
PHX	primary heat exchanger
PID	proportional-integral-derivative
PC	pre-cooler
PCHE	printed circuit heat exchanger

RCBC	recompression Brayton cycle
RMSE	root mean square error [%]
RTD	resistance temperature detector
sCO_2	supercritical carbon dioxide

SUMMARY

The goal of this dissertation is to enhance the fundamental understanding of heat transfer phenomenon of supercritical (sCO_2) especially near the critical point and to investigate the thermal-hydraulic characteristics of printed circuit heat exchangers used in supercritical CO_2 power cycles. To achieve these goals an experimental test facility was constructed to investigate the heat transfer and pressure drop characteristics of sCO_2 flow inside circular tubes and prototypic printed circuit heat exchangers.

To achieve the first goal of this dissertation, the test facility was used to investigate the effect of variable fluid properties on the sCO_2 flow inside heated circular tubes. Two circular tube test sections with inner diameters of 10.9 and 7.9 mm were selected for investigation. Wall temperatures and heat transfer coefficients were measured for a wide range of operating conditions by varying the fluid inlet temperature, mass flux, heat flux and system pressure. Three different test section orientations – horizontal, upward and downward flows were tested to investigate the effect of buoyancy on the heat transfer. For the conditions tested, striking differences were noted in the measured wall temperatures and the heat transfer coefficients for three different test section orientations. Several existing heat transfer correlations from the literature were evaluated against the experimental data to propose the best possible existing correlations and to guide the model development effort. Separate set of correlations are proposed for the horizontal, upward and downward flow test data. For the horizontal flows, the proposed correlation was able to predict the test data with mean absolute error (MAE) of ±14.2%. The proposed

correlations for the upward and downward flows were able to predict the experimental data with MAE of ±12.4% and ±16.3% respectively.

To achieve the second goal of this dissertation, the thermal-hydraulic characteristics of two discontinuous fin printed circuit heat exchangers (PCHEs) with offset rectangular and offset NACA0020 airfoil fin patterns were evaluated experimentally. The pressure drops and the heat transfer coefficients for both the PCHEs were measured over a wide range of conditions with Reynolds numbers in the range of 2,700–38,000 and Prandtl numbers in the range of 0.8–25. Based on the experimental data, friction factor and Nusselt number correlations were developed for both the PCHE test sections. The proposed friction factor correlations were able to calculate the frictional pressure drops for the offset rectangular fin and the offset NACA0020 airfoil fin PCHEs with MAE of ±11%. The proposed Nusselt number correlations were able to calculate the experimental Nusselt numbers for the offset rectangular fin and the offset NACA0020 airfoil fin PCHEs with MAE of ±9.1% and ±5.2% respectively. A computational fluid dynamics (CFD) study was conducted in FLUENT to predict the thermal-hydraulic behavior of the discontinuous fin PCHEs. The CFD models underpredicted the pressure drop for both the PCHEs by 30-40%. For conditions far away from the critical point, the CFD models captured the heat transfer data satisfactorily. However, in the vicinity of the pseudocritical temperatures, up to ~30% deviation was noted between the experimental data and the CFD models.

Final goal of this dissertation is to study the impact of the tested discontinuous fin printed circuit heat exchangers (PCHEs) on the performance and the capital cost of supercritical CO_2 Brayton cycle as investigated. A simulation model was developed for supercritical CO_2 Brayton cycle and optimal flow regimes for several PCHEs were

identified. The offset rectangular fin PCHE offered highest cycle efficiency and lowest capital cost (on $/KWe basis) followed by S-shaped fin, zigzag channel and the offset NACA0020 airfoil fin PCHEs.

CHAPTER 1. INTRODUCTION

As we are into the 21st century, the demand for affordable power continues to increase rapidly due to the ever-growing population of the earth and the rapid shift from industrialization to an economy based on information technology. Power production at the utility scales is dominated by conversion of thermal energy to electricity using thermodynamic cycles such as Brayton or Rankine cycles. Heat sources for these cycles include traditional fossil fuels (coal, natural gas, and petroleum), nuclear fission, solar, geothermal or industrial waste heat. According to U.S. EIA, 2016 [1], traditional fossil fuels represent ~66% of the total US electricity generation followed by nuclear fission (~20%) whereas other heat sources represent only a small fraction of the total electricity produced. To reduce the emission of greenhouse gases and meet future energy demands, power generation from fossil fuels needs to become more efficient and stringent in carbon emissions and at the same time the production of electricity using other heat sources such as nuclear and solar must become more cost effective. As we know from Carnot's theorem, the thermodynamic efficiency of a heat engine increases as the temperature difference between the hot and cold reservoirs increase. Therefore, there is a motivation to achieve higher temperatures of heat addition. At the same time, there is a need for development of new technologies that are cleaner and more efficient in power generation while being compact and cost effective. Thermodynamic cycles which use working fluids in a supercritical state are gaining popularity as they have the potential to meet all the above-mentioned requirements. Water, Helium and Carbon dioxide are identified as the potential candidates for the next generation power cycles based on supercritical fluids [2, 3].

1.1 Overview of supercritical fluids

On a temperature-pressure (T-P) phase diagram, critical point is the highest temperature and pressure at which a vapor and a liquid can coexist in equilibrium. When a substance is at or above its critical temperature (T_c) and pressure (P_c), vapor and liquid phases of the substance merge into a single phase known as "supercritical fluid". Mathematically, the critical point is defined as [4],

$$\left(\frac{\partial P}{\partial v}\right)_{T_c} = \left(\frac{\partial^2 P}{\partial v^2}\right)_{T_c} = 0 \tag{1.1}$$

Critical properties of candidate working fluids for the power cycles are shown in Table 1-1.

Table 1-1: Comparison of critical properties for potential candidate supercritical fluids for the power cycles

Fluid	P_c [MPa]	T_c [°C]	ρ_c [kg/m^3]
Water	22.060	373.95	300.8
Helium	0.227	-267.95	56.3
Carbon Dioxide	7.38	31.04	468.2

Out of these candidate working fluids, supercritical CO_2 is chemically and thermally stable, abundantly available, non-toxic, non-flammable and low-cost, making it an attractive working fluid. CO_2 also has a moderate critical pressure and near ambient critical temperature making dry cooling feasible [5].

During boiling/condensation of a fluid at a constant pressure below the critical pressure ($P < P_c$), the fluid transitions from saturated liquid to saturated vapor or vice versa. During the transition, fluid achieves a two-phase state where the liquid and vapor

phases co-exist. The two-phase region is characterized by isothermal heat absorption/rejection as shown on a T-h diagram in Figure 1-1.

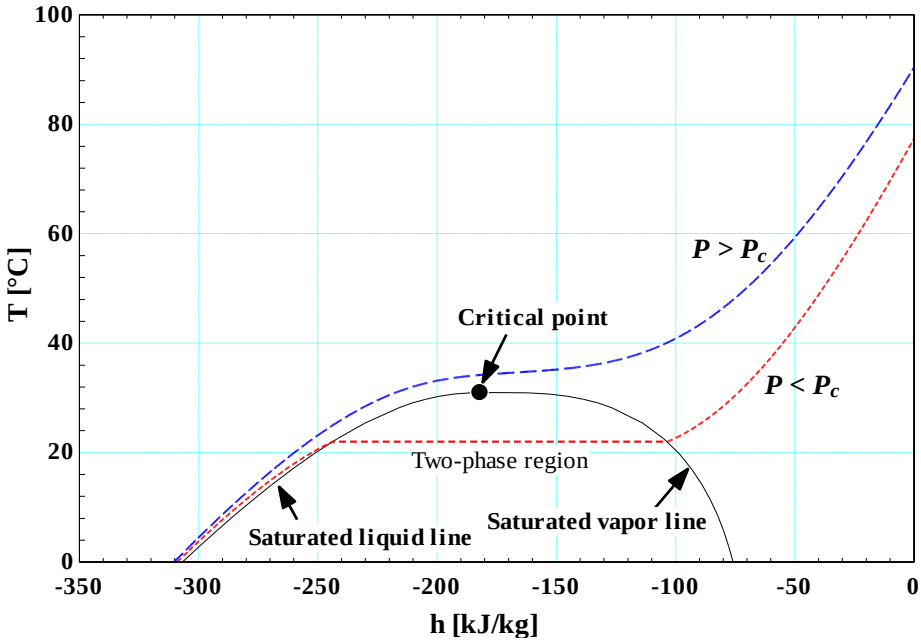

Figure 1-1: Temperature-enthalpy (T-h) diagram of CO_2 along with isobars for pressure above and below the critical pressure

However, when a fluid is heated/cooled at a constant pressure above the critical pressure ($P > P_c$), the fluid doesn't exhibit two distinct phases and the process doesn't follow isothermal path as depicted in Figure 1-1. Although there are no discontinuities above the critical pressure, it is believed that the transition along an isobar occurs between liquid-like and gas-like cluster of molecules [6].

Supercritical fluids exhibit interesting property variations which are favorable but at the same time present challenges for using them as working fluids in power cycles. Supercritical fluids exhibit peaks in the isobaric specific heat (C_p) for pressures above the fluid's critical pressure as presented in Figure 1-2. The temperature at which the isobaric

specific heat peaks is known as the pseudocritical temperature (T_{pc}). Another interesting point to note is that the peak in the specific heat decreases with increasing pressure and the variation of specific heat is not as drastic as near the critical pressure.

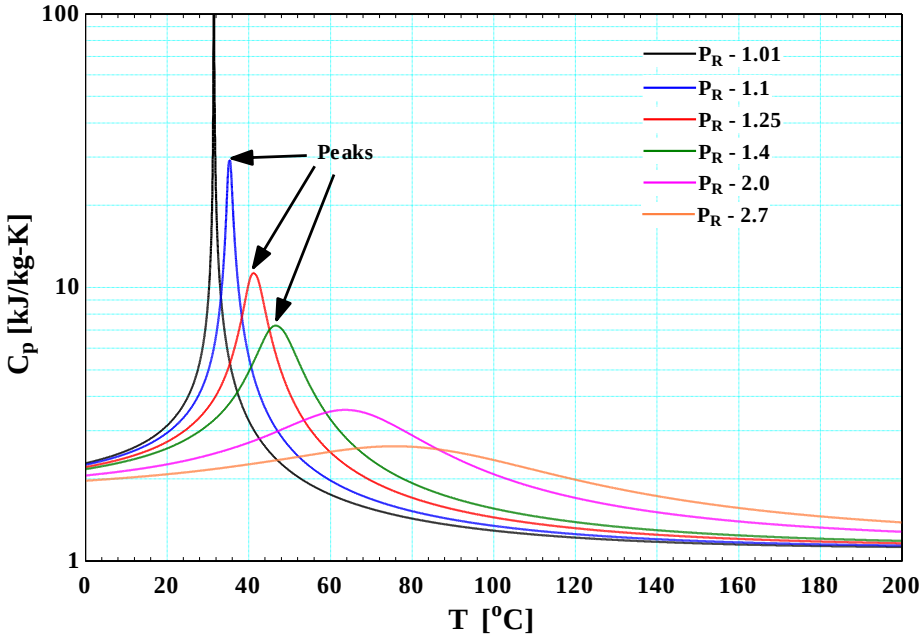

Figure 1-2: Specific heat of CO_2 plotted as a function of temperature for several isobars ($P_R = P/P_c$) above the critical pressure

Liao and Zhao [7] developed following approximate relationship for the pseudocritical temperature as a function of pressure for CO_2. The pseudocritical points calculated using the relationship of Liao and Zhao are plotted on a temperature-enthalpy (T-h) diagram in Figure 1-3.

$$T_{pc} = -122.6 + 6.124P - 0.1657P^2 + 0.01773P^{2.5} - 0.0005608P^3 \qquad (1.2)$$

where T_{pc} is in °C and P is in bar.

Near the pseudocritical temperature other thermophysical properties such as density, thermal conductivity, viscosity etc. exhibit steep property variations as well. For

example, Figure 1-4 shows variation of CO_2 density as a function of temperature for several isobars. For the sake of convenience, the terms critical and pseudocritical will be used interchangeably throughout the thesis.

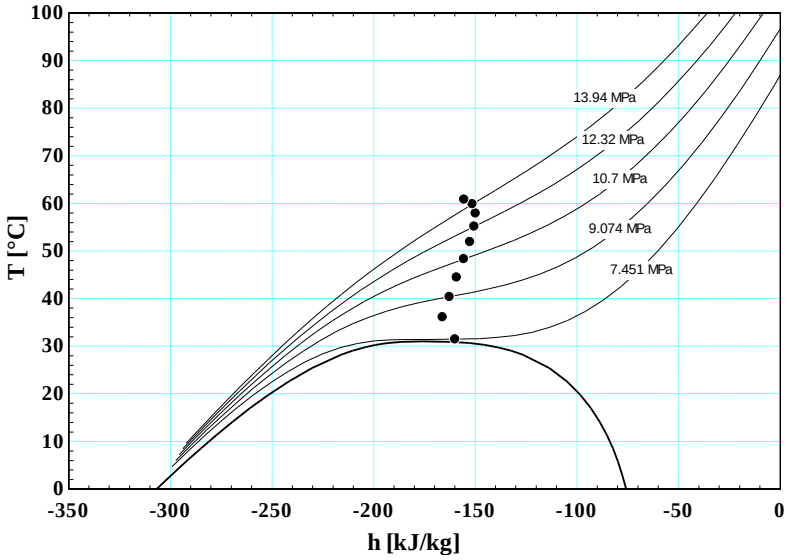

Figure 1-3: Temperature-enthalpy diagram showing locations of pseudocritical points using correlation of Liao and Zhao

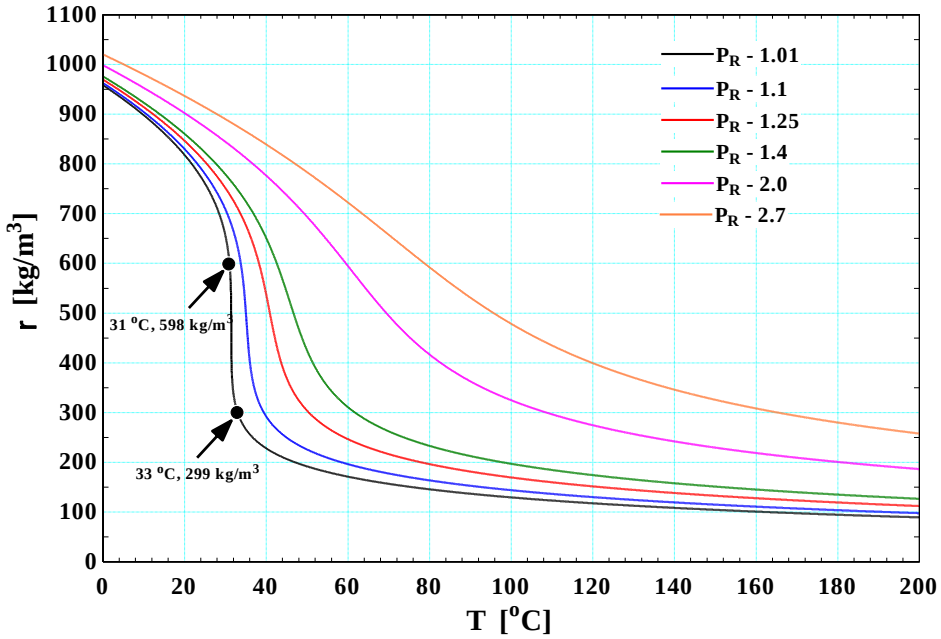

Figure 1-4: Density of CO_2 plotted as a function of temperature for several isobars ($P_R = P/P_c$) above the critical pressure

Near the critical pressure, P/P_c = 1.01, it is very interesting to note that the density changes by a factor of ~2 within a span of ~2 °C near the pseudocritical temperature. It is also worthwhile to note that as the pressure increases the variation of density across the pseudocritical temperature tend to flatten out and become less sensitive to the temperature. Similar trends can be observed for other properties such as viscosity and thermal conductivity shown in Figure 1-5 and Figure 1-6 respectively.

These rapid variation in thermophysical properties present significant challenges in terms of design and operation of components such as heat exchangers and compressors close to the critical point. For example, both heat transfer augmentation and deterioration can occur under supercritical conditions due to several competing factors that will be explained in more detail in CHAPTER 2.

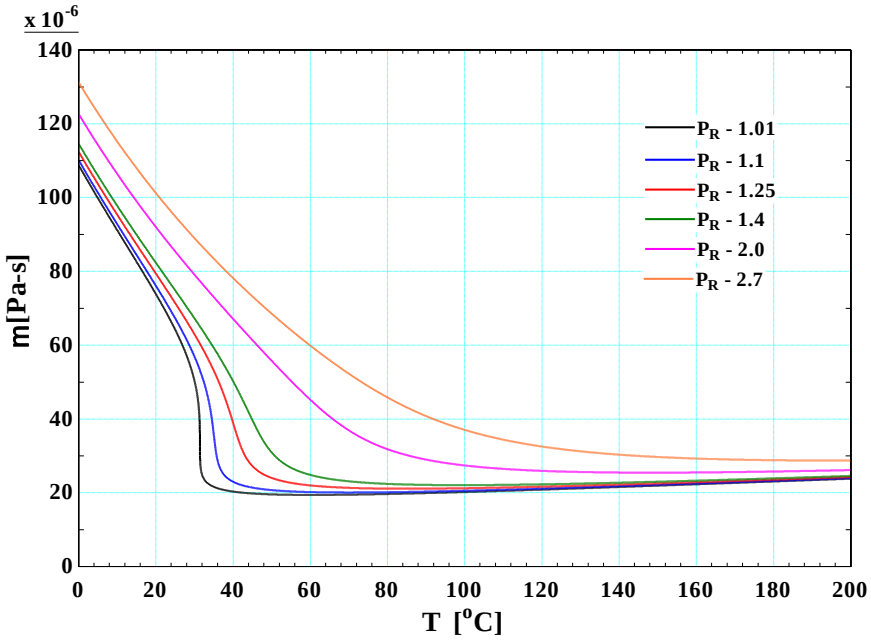

Figure 1-5: Dynamic viscosity of CO_2 plotted as a function of temperature for several isobars ($P_R = P/P_c$) above the critical pressure

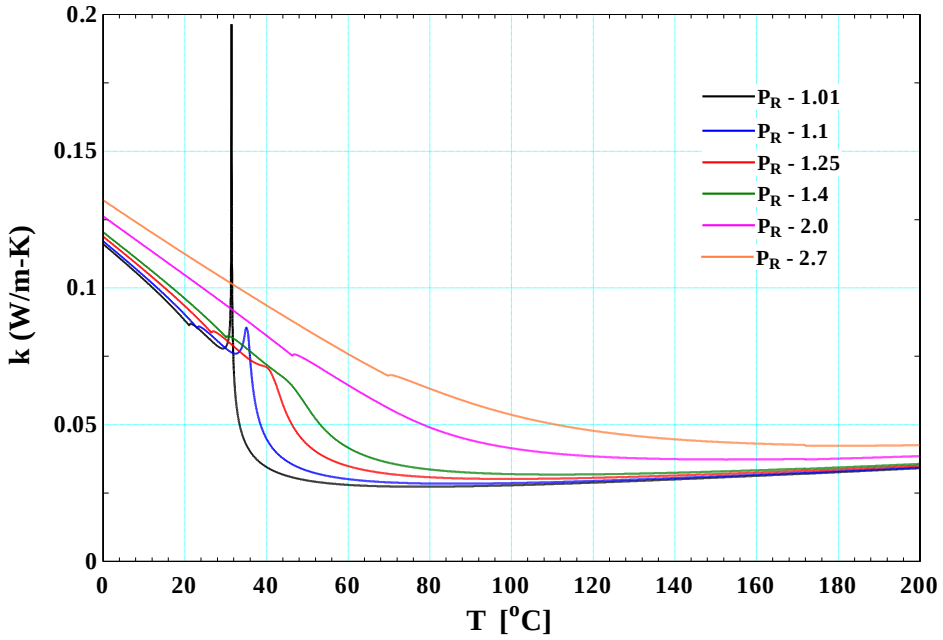

Figure 1-6: Thermal conductivity of CO_2 plotted as a function of temperature for several isobars ($P_R = P/P_c$) above the critical pressure

1.2 Supercritical Carbon Dioxide Brayton cycles

Typical closed-loop Brayton cycles utilize working fluid in the gas phase. The inherent disadvantage of these cycles is that a low density fluid (e.g., Air, Helium etc.) needs to be compressed and the compression process becomes very energy intensive consuming a significant portion of the power generated by the turbine. In order to improve the efficiency of closed-loop Brayton cycles, the heat from turbine exhaust is recuperated by pre-heating the compressor outlet stream as shown in Figure 1-7.

In case of supercritical CO_2 (sCO_2) Brayton cycle, the compressor is operated close to the critical/pseudocritical point where the density of fluid is high, thereby significantly reducing the amount of energy required for compression. The idea of using sCO_2 as the working fluid for Brayton cycles has been around for a while. Some of the earliest detailed investigations of sCO_2 Brayton cycles were carried out by Angelino [8, 9] and Feher [10].

Angelino and Feher analyses showed that the full potential of the low compression power in sCO_2 Brayton cycles can only be realized by dealing with the "pinch-point" problem in the recuperator. Pinch point is the location in the recuperator (or any heat exchanger in general) where the temperature difference between hot and cold streams is minimum. Generally, pinch points occur at either end of the recuperator. However, when the specific heat capacities of both the fluid streams differ significantly as shown in Figure 1-8 for the sCO_2 recuperator, pinch points can occur within the recuperator. This phenomenon will drastically reduce the effectiveness of the recuperator and the overall cycle efficiency. To circumvent the recuperator pinch point issue associated with the sCO_2 Brayton cycle, Angelino [8] considered four different cycle configurations for the sCO_2 Brayton cycle. Of these four, re-compression cycle is found to be the most promising configuration. The schematic of the re-compression sCO_2 Brayton cycle (RCBC) proposed by Angelino is shown in Figure 1-9.

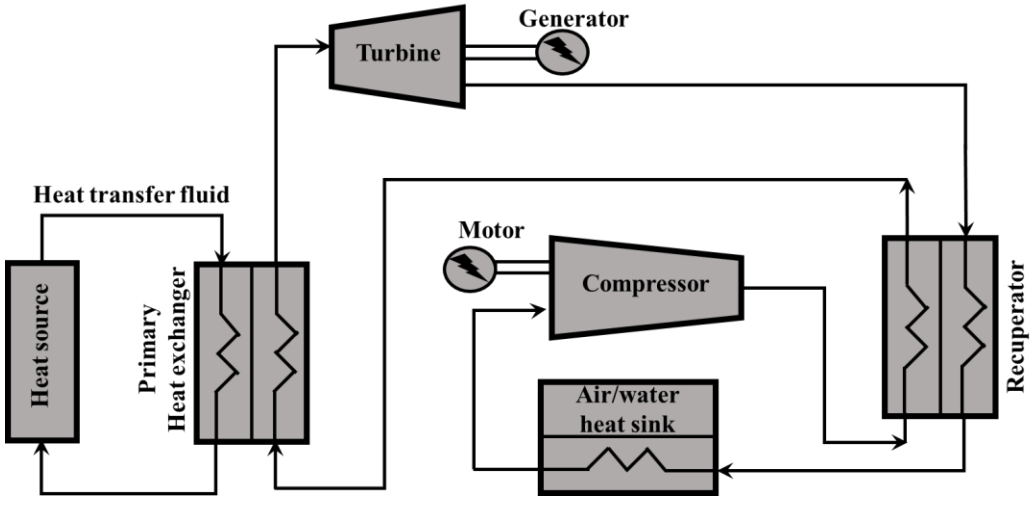

Figure 1-7: Schematic of a typical closed-loop Brayton cycle with a single stage of recuperation and without any intercooling or reheating stages

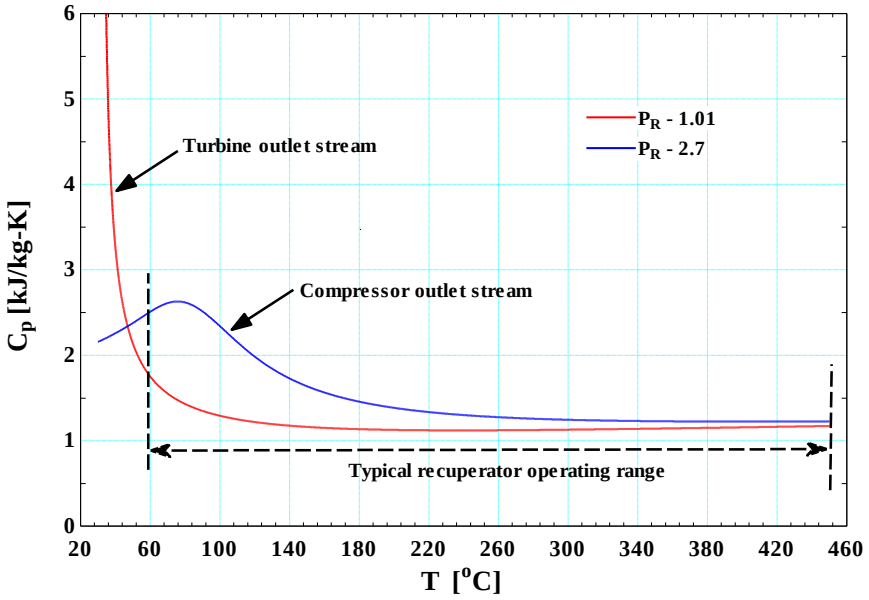

Figure 1-8: Comparison of specific heat capacity of fluid streams in the sCO_2 recuperator of closed-loop Brayton cycle

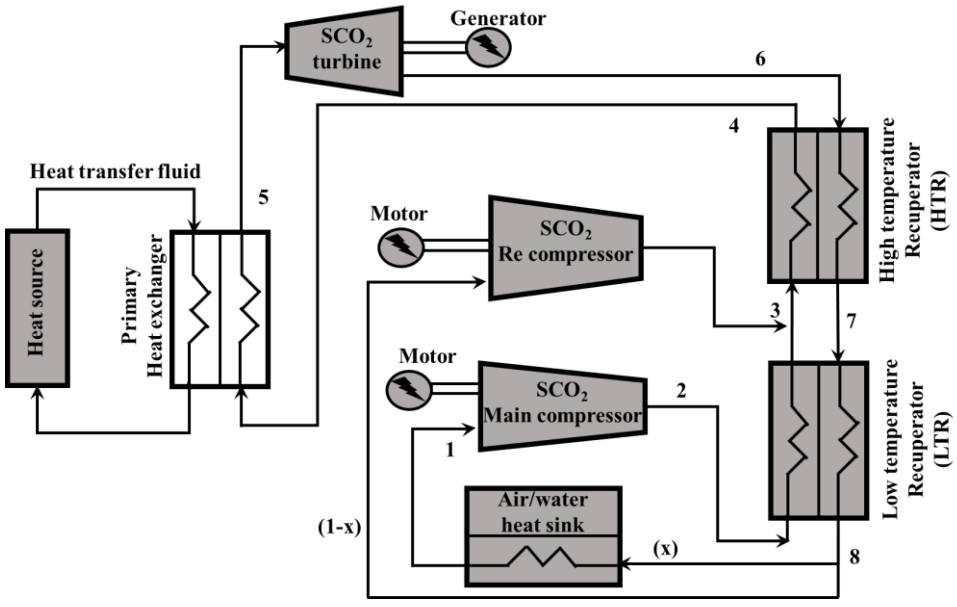

Figure 1-9: Schematic of re-compression sCO_2 Brayton cycle (RCBC) proposed by Angelino (1969) to overcome the pinch-point issue in the recuperator

Comparing a typical closed-loop Brayton cycle with a single recuperator from Figure 1-7 and the re-compression sCO_2 Brayton cycle from Figure 1-9; the key difference is that the recuperation process is split into two stages along with an addition of a re-

compressor in parallel to the main compressor. Prior to the heat sink, the fluid stream is split into two parallel streams. Mainstream, (x) gets cooled to near pseudocritical temperature in the heat sink and gets compressed in the main compressor while taking advantage of the high fluid density. The parallel stream, (1-x) bypasses the heat sink and the hotter fluid gets compressed in the re-compressor. This allows for better balance of the heat capacities, $C = \dot{m}C_p$ of hot and cold streams in the low temperature recuperator (LTR), thereby increasing the recuperation effectiveness and the cycle efficiency. However, additional components needed to achieve split compression and recuperation increases the complexity and capital cost of the cycle. Also, sCO_2 compressed in the re-compressor is at a lower density (due to higher temperature), thereby increasing the power consumption for the compression process. Due to these tradeoffs, selection of appropriate split fraction, x is the key to achieve maximum cycle efficiency.

Dostal *et al.* [3] compared cycle efficiencies of the sCO_2 re-compression Brayton cycle, superheated/supercritical steam Rankine cycle and Helium Brayton cycle. Owing to the significantly lower critical temperature and critical pressure, Helium-based power cycles required a significantly higher turbine inlet temperature (> 800^{o}C), multiple intercooling and reheat stages to attain the same net efficiencies as sCO_2 and steam-based cycles [3]. These high turbine inlet temperatures present material challenges and require development of advanced materials. Dostal also noted that at turbine inlet temperatures above ~550^{o}C, the sCO_2 RCBC offered a higher net efficiency than superheated and supercritical steam Rankine cycles with a significantly simpler and compact plant footprint. Figure 1-10 shows typical operating state points of sCO_2 RCBC from Dostal's study on a temperature-entropy (T-s) and temperature-enthalpy (T-h) diagram.

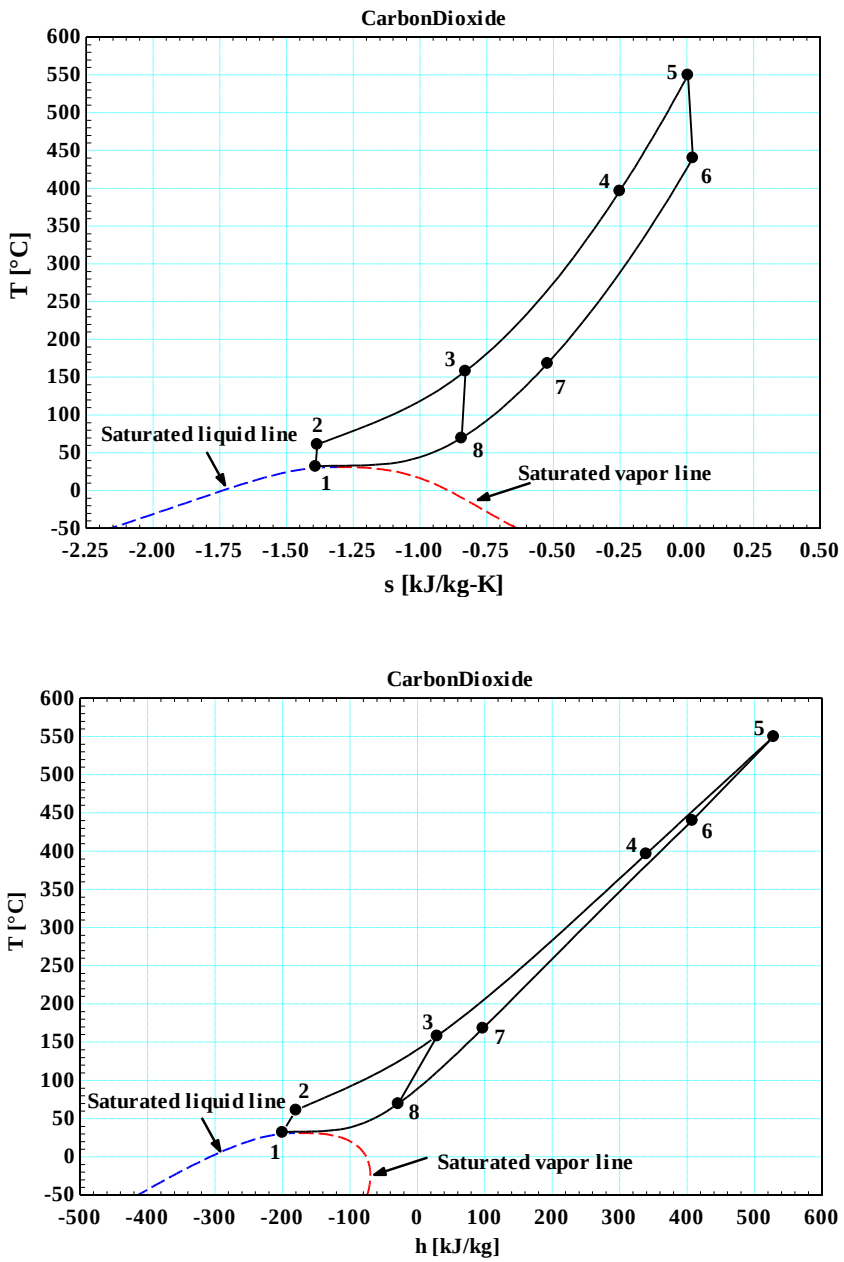

Figure 1-10: Temperature-entropy diagram (top) and temperature-enthalpy diagram (bottom) of Carbon dioxide showing typical state points of RCBC from Dostal *et al.* (2002). Refer to Figure 1-9 for the locations of state points on RCBC

It is important to understand that there is a big difference between supercritical steam and supercritical CO_2 cycles. The nomenclature used for these cycles is rather ambiguous in the literature. In the case of supercritical CO_2 power cycles, the entire cycle operates above the critical pressure as can be seen in Figure 1-10. However, in the case of

supercritical steam cycle only the high-pressure side of the cycle operates above the critical pressure. In the literature, equivalent CO_2 based cycles are referred to as either "transcritical" or "condensing" CO_2 cycles [8, 11]. Transcritical CO_2 cycles are particularly more attractive for the medium temperature heat sources than supercritical CO_2 cycles. However, as noted by Angelino [8], the requirement for low temperature cooling source to attain high efficiencies represent geographical limitation for application of transcritical/condensing CO_2 cycles.

One important point to note from Figure 1-10 is the non-linear path (e.g., entropy, enthalpy versus temperature) inside components operating close to the critical point. Therefore, design of the components (for e.g., heat exchangers) based on the end state points is no longer accurate and detailed discretization procedure is needed to account for the real-gas behavior of CO_2 near the critical point. The discretization procedure will be explained in more detail in CHAPTER 6.

Although supercritical fluid power cycles are attractive, significant advancements are needed to move from theoretical or lab-scale studies to commercial-scale adoption. One of the challenges for sCO_2 Brayton cycles is that they require a significant amount of internal heat recuperation (approximately ~2x the heat input to the cycle), thus requiring numerous, large heat exchangers to achieve high cycle efficiencies. Consequently, the total capital cost of the sCO_2 Brayton cycle is strongly coupled to the capital cost of the heat exchangers. An effective way to handle the high operating pressures, temperatures and to reduce the capital cost is to use compact heat exchangers such as diffusion-bonded heat exchangers. Compact diffusion-bonded heat exchangers, commercially known as printed circuit heat exchangers (PCHEs) are the leading potential heat exchanger candidates for

the sCO_2 Brayton cycles. PCHEs are fabricated using two innovative technologies of photo-chemical etching and diffusion bonding. Desired flow channels/patterns are photo-chemically etched on to flat metal plates. The etched plates are then stacked, and diffusion-bonded to form a monolithic core to which the flow distribution headers are welded or in some cases, the headers are integrated into the etched plates. One of the advantages of PCHEs is that they allow for etching of a wide range of surface geometries thus altering the thermal-hydraulic performance of the PCHE core quite easily to meet the design requirements. Therefore, it is important to explore various surface geometries to identify optimum heat exchanger designs for the sCO_2 Brayton cycles.

1.3 Scope of current research

Based on the research needs described in the introductory sections, following research goals were established and will be addressed in this dissertation.

1) Enhance the fundamental understanding of heat transfer phenomenon of sCO_2, especially near the critical point. Provide supplemental experimental data and contribute to the existing heat transfer databank for sCO_2 from literature.
2) Investigate flow geometries for printed circuit heat exchangers and develop correlations that can be used to design heat exchangers for the sCO_2 Brayton cycles.
3) Study the impact of investigated printed circuit heat exchangers on the sCO_2 Brayton cycle performance and capital cost.

1.4 Organization of the thesis

The last three sections outlined the challenges associated with the development of supercritical CO_2 power cycles and served as the basis for outlining the goals of the thesis. CHAPTER 2 will provide the necessary background information and reviews the pertinent studies from literature. CHAPTER 3 describes the details of the experimental facility constructed and the test sections investigated in this study. CHAPTER 4 is dedicated for the data processing, discussion of heat transfer results for flow through heated circular tubes. CHAPTER 5 discusses the thermal-hydraulic experimental data of the prototypic printed circuit heat exchangers. Experimental data is supplemented with comparison to computational fluid dynamics (CFD) solutions. CHAPTER 6 studies the impact of tested prototypic printed circuit heat exchangers on the performance and cost of the sCO_2 Brayton cycle coupled to sodium cooled nuclear reactor. CHAPTER 7 offers concluding remarks and recommendations for the future work in this area.

CHAPTER 2. BACKGROUND

One of the challenges encountered during development of the supercritical fluids based thermodynamic cycles is lack of complete knowledge of the heat transfer phenomenon, especially near the critical point. Heat transfer mechanisms in supercritical fluids are quite different from ideal fluids due to the rapidly varying thermodynamic and transport properties near the critical point. As a result, the heat and momentum transport processes are strongly coupled. Heat transfer (or heat flux, $Q"$) is proportional to the temperature difference, $\Delta T = |T_w - T_b|$ and the proportionality constant is the heat transfer coefficient, α.

$$Q" = \alpha . \Delta T \tag{2.1}$$

Heat transfer to supercritical fluids can be categorized as either normal, enhanced or deteriorated heat transfer depending on the flow conditions such as heat flux, mass flux, temperatures, flow orientation, flow geometry [12]. There are hundreds of papers in literature dedicated for experimental, numerical and analytical analysis of heat transfer to supercritical carbon dioxide flowing inside different flow geometries. Majority of these publications studied flow through heated or cooled vertical circular tubes due to their simplicity and wide range of applications. There are relatively fewer studies focused on the thermal-hydraulic characteristics of printed circuit heat exchangers. This chapter provides the necessary background information and an in-depth review of relevant studies from the literature.

2.1 Supercritical heat transfer studies in heated circular tubes

There has been a significant amount of progress made in understanding the fundamental heat transfer phenomenon for supercritical CO_2 flow inside heated circular tubes and several review papers have been published in the literature. The reviews of Bishop *et al.* (1964) [13], Hall *et al.* (1968) [14], Petukhov *et al.* (1968) [15], Hendricks *et al.* (1970) [16], Duffey and Pioro (2005) [17] are amongst some of the earliest works in this area. Owing to its moderate critical pressure and temperature, most of these early studies used supercritical CO_2 as a surrogate fluid to understand the heat transfer characteristics of supercritical water. Table 2-1 summarizes selected experimental studies from the literature in chronological order. For each reference, the tube dimensions, the flow conditions, and the flow orientation are also reported.

Table 2-1: Selected experimental supercritical CO_2 heat transfer studies in heated circular tubes

Reference	ID (mm)	L (mm)	P (MPa)	T_b/T_{in} (°C)	$Q"$ (kW/m^2)	G (kg/m^{2}s)	Flow Orientation
Bringer and Smith (1957) [18]	4.572	610	8.27	T_{in}= 21–49	31–315	100–1300	Vertical
Krasnoshchekov *et al.* (1964) [19]	4.08	208	7.8–9.8	T_b= 20–110	≤ 2600	350	Vertical
Shiralkar and Griffith (1969, 1970) [20], [21]	3.175, 6.35	1524	7.6–7.9	T_{in}= 10–32	50–455	670– 3400	Vertical
Bourke *et al.* (1970) [22]	22.8	4560	7.4–10.4	T_b= 15–70	8–350	311–1702	Vertical
Tanaka *et al.* (1971) [23]	6	1000	7.84	T_b= 0–170	488–640	1180–2360	Vertical
Fewester (1976) [24]	5.08	1524	7.58	T_{in}= 16–28	10–455	276–3350	Vertical
Fewester (1976) [24]	7.88	2364	7.58	T_{in}= 10–34	10–300	180–2050	Vertical
Fewester (1976) [24]	18.97	2450	7.58	T_{in}= 5–35	0.7–57	100–570	Vertical
Adebiyi and Hall (1976) [25]	22.14	2440	7.6	T_{in}= 10–33	5–27	104–392	Horizontal
Kurganov *et al.* (1992, 1993) [26], [27]	22.7	5220	9	T_b= 20–100	40–460	800–2100	Vertical
Liao and Zhao (2002) [28]	0.7, 1.4, 2.16	110	7.4–12	T_b= 20–110	-	-	Vertical, Horizontal
Jiang *et al.* (2004) [29]	0.948	55	9.5	T_{in}= 32–51	31–108	580–1650	Vertical

J.K. Kim *et al.* (2007) [30]	7.8	1200	8	T_{in}= 15–32	3–180	209–1230	Vertical
Jiang *et al.* (2008) [31]	0.27	90	8.6	T_{in}= 25–30	90–550	-	Vertical
Bae and Kim (2009) [32]	4.4, 9	2100, 2650	7.7–8.9	T_{in}= 5–27	≤ 150	400–1200	Vertical
Bae *et al.* (2010) [33]	6.32	2650	7.7–8.2	T_{in}= 5–37	30–170	285–1200	Vertical
Li *et al.* (2010) [34]	2	290	7.8–9.5	T_{in}= 25–40	6–52	150 – 890	Vertical
Kim *et al.* (2011) [35]	4.5	900	7.4–10.3	T_b= 29–115	38–234	208 – 874	Vertical
Gupta *et al.* (2012) [36]	8	2208	7.5–8.8	T_b= 20–136	9–617	706 – 3169	Vertical
Zahlan *et al.* (2015) [37]	8, 22	1940, 2000	7.4–8.7	T_{in}= 7–14	5–436	197–2027	Vertical
Tanimizu and Sadr (2016) [38]	8.7	1140	7.5–9.0	T_{in}= 24–28	16–64	185–286	Horizontal

2.1.1 Forced convective normal heat transfer in supercritical fluids

Figure 2-1 presents an example of forced convective normal heat transfer to supercritical CO_2 flowing inside heated vertical tube from Fewester (1976) [24].

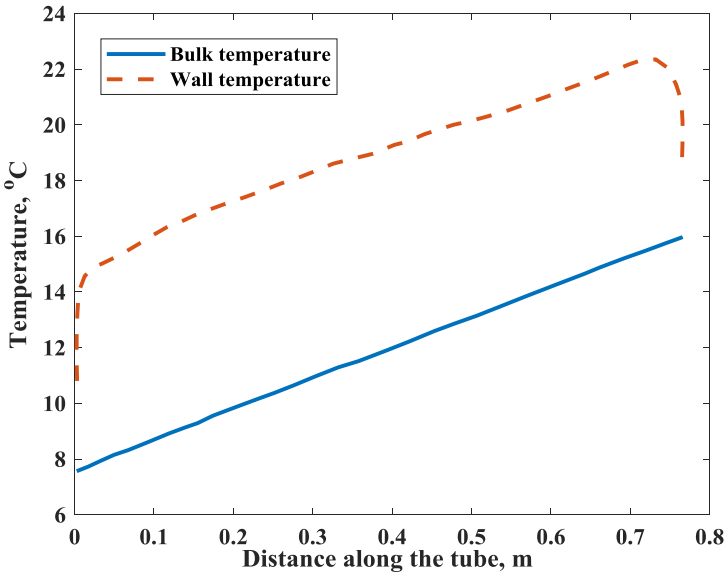

Figure 2-1: Variation of bulk fluid and wall temperature along the tube length. Data of Fewester (1976); CO_2, P = 7.58 MPa, Q'' = 9.9 kW/m^2, G = 286 kg/m^{2}s, upward flow, ID = 5.08 mm

In this example, the bulk and the wall temperatures increase linearly along the tube length and the temperature difference, ΔT is nearly constant along the heated surface. Consequently, the heat transfer coefficient, α is nearly constant as one would expect in constant property flows. Normal heat transfer behavior in supercritical fluids is typically achieved when the bulk and wall temperatures are sufficiently far away from the pseudocritical temperature ($T_w, T_b << T_{pc}$ or $T_w, T_b >> T_{pc}$).

Depending on the flow conditions and orientation, heat transfer enhancement or deterioration can occur in supercritical fluids during which the heat transfer coefficient, α is either higher or lower than reference normal heat transfer conditions.

2.1.2 Forced convective heat transfer enhancement in supercritical fluids

For relatively high mass flux, G compared to the heat flux, $Q"$ and provided that the $\Delta T = |T_w - T_b|$ is small, the heat transfer is significantly enhanced near the pseudocritical temperature. Figure 2-2 presents an example of heat transfer enhancement from Liao and Zhao (2002) [28]. The enhancement in heat transfer near the pseudocritical temperature marked as dashed vertical lines (34.6 °C for P = 8 MPa, 45 °C for P = 10 MPa) is clearly evident. The primary reason for the enhancement in heat transfer is increase of specific heat and reduction of viscosity near the wall region [14]. As the bulk temperature passes through T_{pc}, the thermophysical properties and heat transfer resemble that of a gas. The magnitude of enhancement in heat transfer near the pseudocritical temperature decreases with increase in pressure. The magnitude of enhancement in heat transfer also increases with mass flux and decrease with increase in heat flux [39].

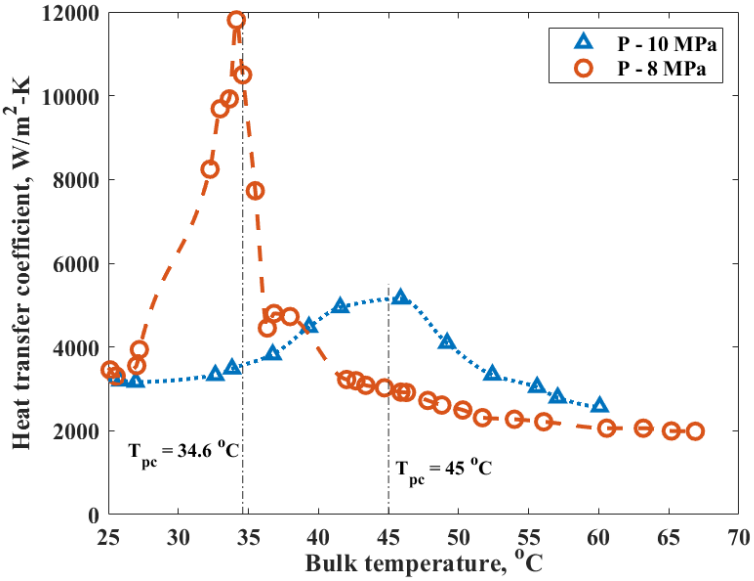

Figure 2-2: Variation of heat transfer coefficient versus bulk temperature. Data of Liao and Zhao (2002); CO_2, G = 541 kg/m^{2}s, horizontal flow, ID = 1.4 mm

2.1.3 Heat transfer deterioration in supercritical fluids

Heat transfer deterioration can occur at high heat flux, $Q"$ relatively to the mass flux, G. Shiralkar and Griffith (1969, 1970) [20], [21] undertook a detailed experimental program to investigate heat transfer deterioration in supercritical fluids. Figure 2-3 presents an example of variation of wall temperature versus bulk enthalpy from Shiralkar and Griffith (1969) [20] for supercritical CO_2 flow in uniformly heated circular tube with upward flow orientation. For the highest value of mass flux (G = 2712 kg/m^{2}s), the wall temperature profile is nearly constant or increases slightly as the bulk fluid temperature increases; similar in characteristics to Figure 2-1. However, the wall temperature profile exhibits a peak (sometimes referred to as "hot spot" in literature) as the mass flux is decreased and the magnitude of peak is higher for lower mass fluxes. Shiralkar and Griffith also noted that the as the fluid inlet temperature is varied, the peak in the wall temperature

moved to a different location along the tube. Similar results were also obtained for a tube with smaller diameter (D = 3.125 mm) [21].

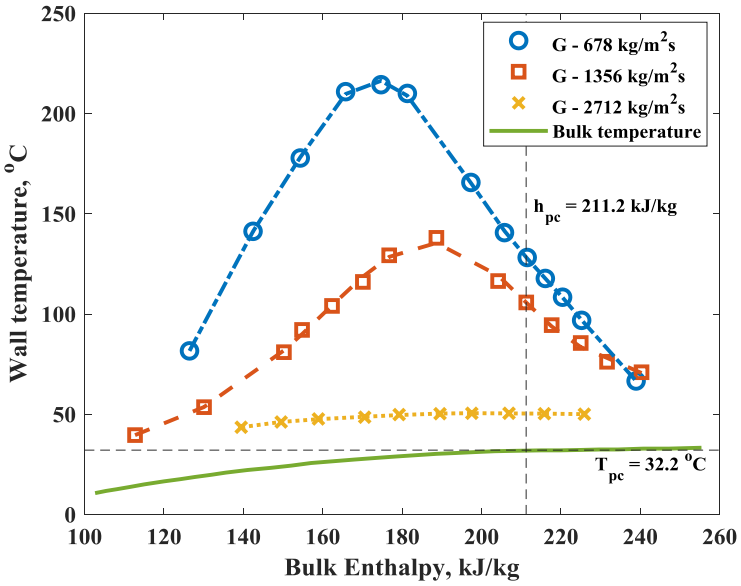

Figure 2-3: Variation of wall temperature as a function of bulk enthalpy at various mass fluxes for CO_2 flow in a heated tube. Data of Shiralkar and Griffith (1969); P = 7.58 MPa, Q'' = 157.7 kW/m^2, upward flow, ID = 6.35 mm

This heat transfer deterioration is not just confined to upward flow but also occurs in the case of downward flow as shown in Figure 2-4. This is a clear indication of heat transfer deterioration resulting from rapid variation of thermophysical properties near the critical point. The nature of heat transfer deterioration in Figure 2-3 and Figure 2-4 is fundamentally different from the heat transfer deterioration due to buoyancy. Figure 2-5 compares the wall temperature profiles for upward and downward flows under identical conditions from Fewester (1976) [24]. In this case, the wall temperature peaks appear in the upward flow but not in the downward flow indicating strong influence of buoyancy forces. The wall temperatures for the downward flow are consistently lower than the

upward flow. Heat transfer deterioration induced by buoyancy forces tend to have sharp localized peaks in the wall temperature compared to the broad peaks from Figure 2-3.

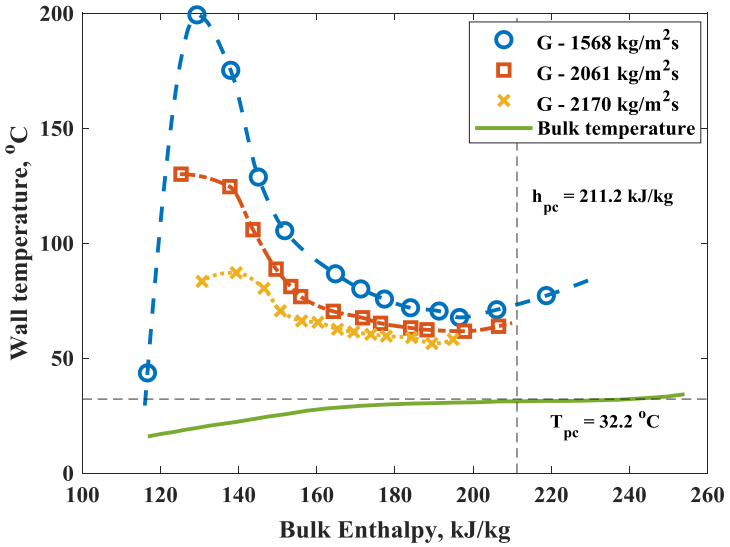

Figure 2-4: Variation of wall temperature as a function of bulk enthalpy at various mass fluxes for CO_2 flow in a heated tube. Data of Shiralkar and Griffith (1969); P = 7.58 MPa, Q'' = 211.3 kW/m^2, downward flow, ID = 6.35 mm

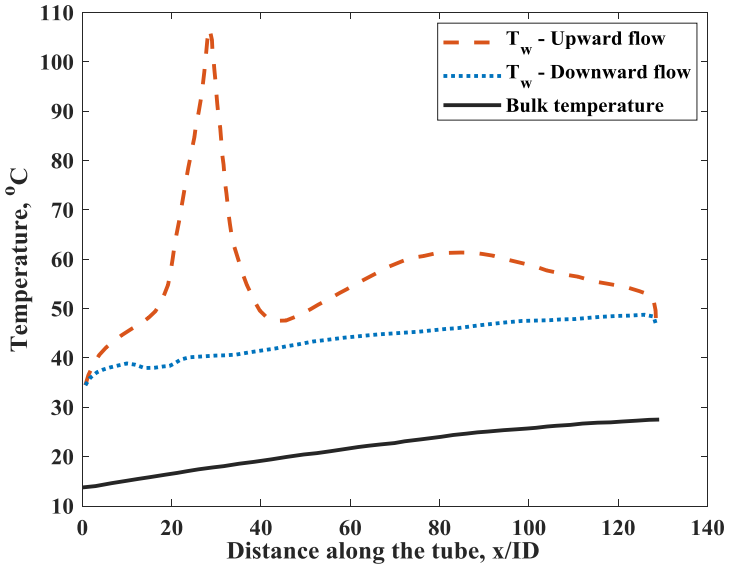

Figure 2-5: Variation of bulk and wall temperature along the tube length. Data of Fewester (1976); CO_2, P = 7.58 MPa, T_{in}= 14 °C, Q'' = 56.7 kW/m^2, G = 566 kg/m^{2}s, ID = 18.97 mm

Adebiyi and Hall (1975) [25] experiments showed that the influence of buoyancy is not just confined to vertical flows but is also present in the horizontal flows. In the case of horizontal flow, circumferential variation in the wall temperature exists and the large wall temperature gradient between the top and the bottom sides of the tube is evident from Figure 2-6. Early researchers have often linked the heat transfer enhancement and deterioration behaviour in supercritical fluids to subcritical nucleate boiling and film boiling phenomenon respectively; see Goldmann (1961) [40] for example. However, the popularity of this concept diminished rather quickly since it didn't produce desirable results for strong buoyancy influenced flows. For example, in the film boiling phenomenon once the dry out occurs it dominates the whole downstream region as well. Therefore, the rapid heat transfer improvement downstream of the local wall temperature peak in Figure 2-5 cannot be explained on the basis on film boiling theory.

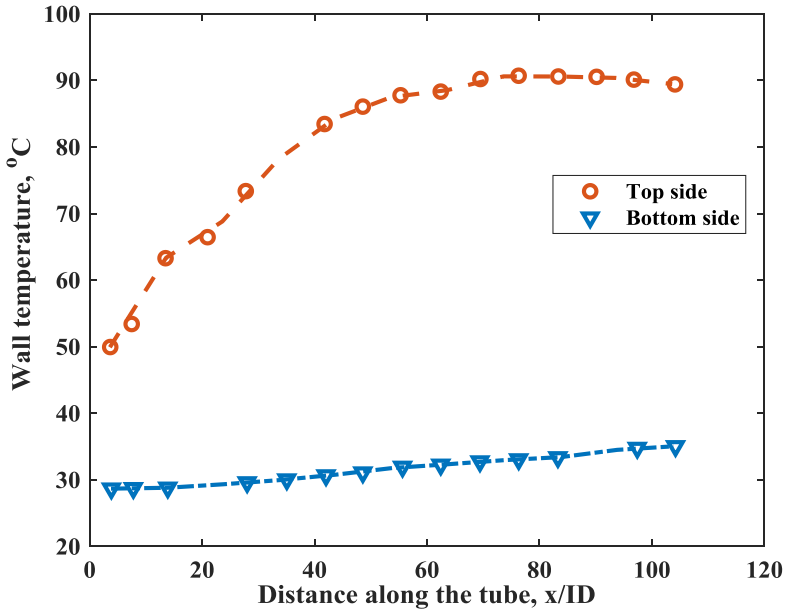

Figure 2-6: Variation of wall temperature along the tube length. Data of Adebiyi and Hall (1975); CO_2, P = 7.614 MPa, T_{in} = 10.7 °C, Q'' = 30.2 kW/m^2, G = 107 kg/m^{2}s, horizontal flow, ID = 22.14 mm

2.1.4 Buoyancy influence on supercritical heat transfer

As described in the previous section, buoyancy forces have a strong influence on the supercritical fluid heat transfer in both vertical and horizontal flows (see Figure 2-5 and Figure 2-6). For vertical upward flows, if the buoyancy force increase to a certain value severe localized heat transfer deterioration occurs. As the buoyancy force increases further there is a rapid recovery in heat transfer following the deterioration. Hall and Jackson (1969) [41] proposed that the heat transfer deterioration and immediate recovery are primarily a result of redistribution of shear stress in the flow due to the influence of buoyancy force. The buoyancy force arises due to large density gradient across the pseudocritical temperature. When $T_b < T_{pc} < T_w$, the density of fluid in the near wall region is significantly lower than the bulk region resulting in buoyancy force which act upon the flow field to alter the shear stress distribution. Jackson (2013) [6] assumed a two-layer model and showed that a very thin layer (Order of microns) of low-density fluid in the near wall region is sufficient to reduce the shear stress in the core to zero. When this happens, it greatly reduces the diffusivity of heat into the core region leading to localized heat transfer deterioration. This phenomenon is often described as "flow laminarization" in the literature [41]. The representative velocity and shear stress profiles during the flow laminarization and onset of deterioration are shown in Figure 2-7 (top). With further increase in thickness of low-density fluid layer near the wall, the buoyancy force increases to a point where negative shear stress develops in the core region forming a "M-shaped" velocity profile. The negative shear stress increases turbulent production and restores the heat transfer. The representative velocity and shear stress profiles during the recovery phase are shown in Figure 2-7 (bottom).

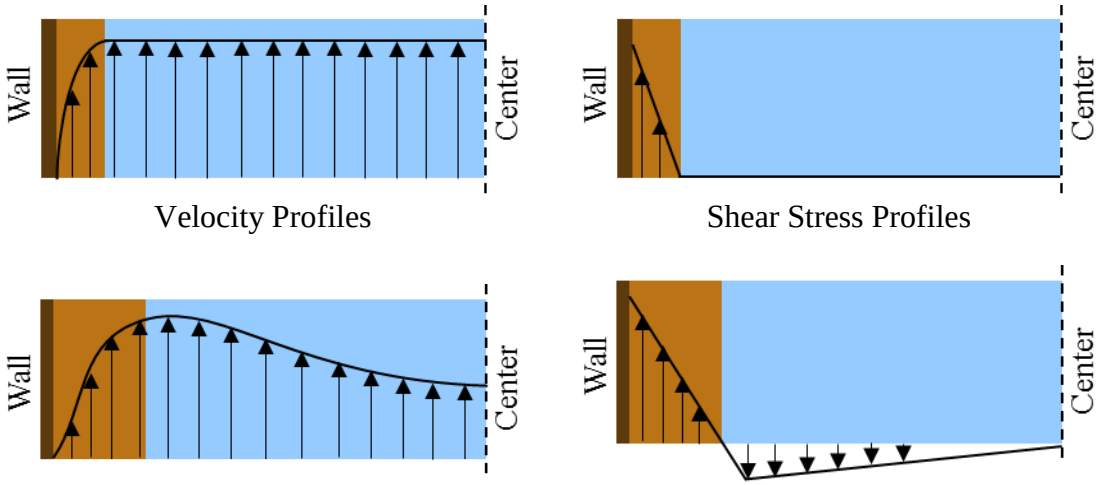

Figure 2-7: Representation of velocity profiles (Left) and shear stress profiles (Right) during onset of deterioration (Top) and recovery of heat transfer (Bottom)

The theory described above was later validated by the experiments of Bourke and Pulling (1971) [42], Kurganov *et al.* (1986) [43], and Licht *et al.* (2008) [44]. The former two used pitot tubes and micro thermocouples to show the reduction of local flow shear stress during deterioration. Licht *et al.* (2008) [44] utilized laser Doppler velocimetry (LDV) diagnostics to examine the local turbulent characteristics in supercritical water and showed presence of "M-shaped" velocity profile downstream of the deterioration. For vertical downward flows, the turbulent shear stress is always enhanced by the buoyancy forces under similar conditions resulting in enhanced heat transfer.

Very few studies in the literature focused on investigating buoyancy effects in horizontal tubes. In the case of horizontal flow, when $T_b < T_{pc} < T_w$, the density of fluid near the wall region is significantly lower than the density of fluid in the bulk region and the buoyancy effects become prominent. This density gradient causes the low-density fluid to rise from the bottom side of the tube, thereby enhancing the heat transfer on the bottom side; whereas the top side is covered by a layer of fluid with low thermal conductivity

reducing the heat transfer on the top side. This phenomenon results in a significant circumferential variation in the wall temperature (See Figure 2-6) which was observed in the experimental studies of Bazargan *et al.* (2005) [45] and Adebiyi and Hall (1976) [25] using supercritical water and CO_2 as the working fluids respectively. The circumferential variation in the wall temperature is often more pronounced at low mass flux, G and high heat flux, $Q"$ conditions.

2.1.5 Thermal bulk flow acceleration influence on supercritical heat transfer

The bulk flow acceleration influences the heat transfer due to the variation of density in the axial direction of flow. This was first observed by Shiralkar and Griffith (1969) [20] in their experiments where the heat transfer deterioration occurred regardless of the flow direction indicating that buoyancy was not the dominant factor (See Figure 2-3 and Figure 2-4). This deterioration phenomenon appears when the bulk temperature, T_b passes through the pseudocritical temperature for flows inside heated tubes with relatively small diameters, high heat fluxes and mass fluxes. As the fluid gets heated, its bulk temperature and enthalpy increases, and the bulk density falls. In order to maintain a constant mass flow rate at all locations the bulk fluid velocity increases as the density falls, as a result fluid accelerates in the direction of the flow. Therefore, the bulk flow acceleration is stronger if the density gradient is stronger in the direction of the flow. According to Jackson (2013) [6], this flow acceleration creates an extra pressure gradient which is generally larger than required to accelerate the flow. This increased pressure gradient acts up on the flow field to alter the shear stress distribution and can lead to heat transfer deterioration [6]. For the heat transfer deterioration caused by thermal bulk flow acceleration, the shear stress gradient in the near wall region and production of turbulence

is lower than that of normal flows under identical conditions. Zahlan (2015) [37] explained that this scenario can be viewed as a flow with lower mass flow rate having thicker viscous sub-layer with less turbulence production and energy transport.

2.1.6 Criteria for the Onset of heat transfer deterioration

Most of the researchers in the past have attempted to correlate the minimum heat flux, Q''_{DHT} in kW/m^2 at which heat transfer deterioration occurs with mass flux, G in kg/m^{2}s. Table 2-2 shows some of these heat transfer deterioration criteria from the literature. Out of these criteria, the correlation of Cheng *et al.* (2009) [46] includes a pressure effect in the form of specific heat, $C_{p,pc}$ and volumetric thermal expansion coefficient, β_{pc}.

Some researchers proposed correlations which contain the effect of tube diameter in addition to the effect of mass flux and pressure. For example, Schatte *et al.* (2016) [47] proposed following correlation for the onset of heat transfer deterioration.

$$Q''_{DHT} = mF_D F_P G^n \tag{2.2}$$

Where, m = 1.942 x 10^{-6}, n = 0.795, $F_D = (30 - D)^{0.339}$ and $F_P = \left(\frac{C_{p,pc}}{\beta_{pc}}\right)^{2.065}$

Kline *et al.* (2018) [48] conducted experiments using three different tube diameters and modified the criteria proposed by Bae *et al.* (2010) [33] from Table 2-2 to include effect of the tube diameter on the onset of heat transfer deterioration.

$$Q''_{DHT} = 2e - 4\, F_D G^2 \tag{2.3}$$

where $F_D = 0.7 + \frac{0.3}{1+e^{4\left(\frac{D}{D_{ref}}-2.35\right)}}$ and D_{ref} = 8 mm

Table 2-2: Heat transfer deterioration for supercritical fluids criteria correlating heat flux and mass flux

Reference	Fluid	Criterion
Vikhrev *et al.* (1967) [49]	Water	$Q^{"}_{DHT}/G \geq 0.4$
Yamagata *et al.* (1972) [50]	Water	$Q^{"}_{DHT}/G^{1.2} \geq 0.2$
Styrikovich *et al.* (1967) [51]	Water	$Q^{"}_{DHT}/G \geq 0.58$
Cheng *et al.* (2009) [46]	Water	$Q^{"}_{DHT}/G \geq 1.354 \times 10^{-3} \left(\frac{C_{p,pc}}{\beta_{pc}}\right)$
Bae *et al.* (2010) [33]	CO_2	$Q^{"}_{DHT}/G^2 \geq$ 2e-4
Mokry *et al.* (2011) [52]	Water	$Q^{"}_{DHT} \geq 0.745G - 58.97$

Criteria described above might be satisfactory to predict the onset of heat transfer deterioration, however, it is not possible to quantify the effect and location of deterioration. Moreover, such simple approach lacks accuracy and the complex problem cannot be uniquely described by only two parameters ($Q^{"}_{DHT}$, G) when bulk and wall temperatures span pseudocritical temperature [6]. A more sophisticated criteria developed by Hall and Jackson (1969) [41], Jackson (2013) [6] and Kim *et al.* (2010) [53] have a better physical basis and can better account for the heat transfer deterioration due to buoyancy and thermal bulk flow acceleration effects.

Criteria for onset of buoyancy induced deterioration: Hall and Jackson (1969) [41] developed an empirical model to account for reduction in flow shear stress due to the influence of buoyancy. When the bulk and the wall temperature span the pseudocritical temperature a two-region model was used to account for sharp variation in density. The reduction in the shear stress due to buoyancy force was expressed as,

$$\frac{\Delta\tau_{\delta_B}}{\tau_w} = 1.33 \times 10^{-4} \frac{\overline{Gr_b}}{Re_b^{2.7}} \left(\frac{\mu_w}{\mu_b}\right) \left(\frac{\rho_b}{\rho_w}\right)^{0.5} \tag{2.4}$$

Using a fractional shear stress $\left(\frac{\Delta\tau_{\delta_B}}{\tau_w}\right)$ value of 0.1 to impart a 5% impairment in heat transfer and neglecting the property ratio terms, $\left(\frac{\mu_w}{\mu_b}\right) \left(\frac{\rho_b}{\rho_w}\right)^{0.5}$, the following simplified criterion was derived by Hall and Jackson (1969) [14].

$$Bo = \frac{\overline{Gr_b}}{Re_b^{2.7}} < 10^{-5} \tag{2.5}$$

where $\overline{Gr_b} = \frac{(\rho_b - \bar{\rho})D^3 g}{\rho_b \nu_b^2}$, $\bar{\rho} = \frac{\int_{T_b}^{T_w} \rho dT}{T_w - T_b}$ and $Re_b = \frac{GD}{\mu_b}$

Following similar procedure, for conditions where the bulk and wall temperatures don't exceed the pseudocritical temperature, the following criterion was derived by Hall and Jackson [41].

$$\frac{\overline{Gr_b}}{Re_b^{2.7} Pr_b^{0.5}} < 10^{-5} \tag{2.6}$$

More recently, Jackson (2013) [6] proposed a buoyancy criterion which accounts for variation of properties across the boundary layer.

$$C_B Bo_b F_{VP_1} F_{VP_3} F_{VP_4} < 0.04 \tag{2.7}$$

where $Bo_b = \frac{Gr_b}{Re_b^{2.625} Pr_b^{0.4}}$, $F_{VP_1} = \left(\frac{\mu_{av}}{\mu_b}\right) \left(\frac{\rho_{av}}{\rho}\right)^{-0.5}$, $F_{VP_3} = \left(\frac{Pr_{av}}{Pr_b}\right)^{-0.4}$, $F_{VP_4} = \left(\frac{\rho_b - \rho_{av}}{\rho_b - \rho_w}\right)$. The coefficient C_B is calculated to be ~4600 by assigning dimensionless buffer layer thickness value of 30. The average property values in Equation (2.7), μ_{av}, ρ_{av}, Pr_{av} are

evaluated by integrating the properties across the boundary layer assuming a linear temperature from T_b to T_w.

Starting from the Navier-Stokes equation, Kim *et al.* (2010) [53] derived an expression for the shear stress distribution in supercritical fluids.

$$\tau_w - \tau = \rho_b u_b \frac{du_b}{dx} y + (\rho_b - \rho_r) g y + \frac{\tau_w}{y} R \tag{2.8}$$

where τ_w is the wall shear stress, ρ_r is a reference density and R is the radius of the tube. Equation (2.8) shows that the shear stress distribution in the flow can be altered by either buoyancy term (2nd term on RHS) or bulk flow acceleration term (1st on RHS). Kim *et al.* (2010) derived the following Buoyancy parameter from Equation (2.8) by making assumptions regarding the boundary-layer thickness.

$$Bu = \frac{Gr_q}{Re_b^{3.425} Pr_b^{0.8}} \left(\frac{\mu_w}{\mu_b}\right) \left(\frac{\rho_b}{\rho_w}\right)^{0.5} \tag{2.9}$$

The main difference between the buoyancy parameters in Equation (2.7) and (2.9) is that Kim *et al.* (2010) [53] used a Grashof number based on heat flux, $Gr_q = \frac{g \beta_b q" D^4}{k_b \nu_b^2}$.

For horizontal flows, Adebiyi and Hall (1976) [25] proposed the following criterion to neglect the buoyancy effects,

$$Bo_j = \frac{Gr_b}{Re_b^2} \left(\frac{\rho_b}{\rho_w}\right) \left(\frac{x}{D}\right)^2 < 10 \tag{2.10}$$

Petukhov *et al.* (1974) [54] studied horizontal flows and derived two Grashof parameters, Gr_{th} and Gr_q to study the influence of buoyancy on heat transfer. These parameters are defined as follows,

$$Gr_{th} = 3 \times 10^{-5} Re_b^{2.75} \overline{Pr}^{0.5} \left[1 + 2.4 Re_b^{-\frac{1}{8}} \left(\overline{Pr}^{\frac{2}{3}} - 1\right)\right] \quad (2.11)$$

where $\overline{Pr} = \frac{i_w - i_b}{T_w - T_b}\left(\frac{\mu_b}{k_b}\right)$

$$Gr_q = \frac{g\bar{\beta} q" D^4}{k_b \nu_b^2} \quad (2.12)$$

where $\bar{\beta} = \frac{1}{\rho_{film}}\left(\frac{\rho_b - \rho_w}{T_w - T_b}\right)$

Petukhov *et al.* (1974) stated that the flow is completely dominated by forced convection for $Gr_q < Gr_{th}$.

Criteria described in Equations (2.5)–(2.12) can be used to determine the onset of buoyancy-induced heat transfer deterioration and screening of the experimental data. One way to quantify buoyancy influenced heat transfer is by comparing experimental Nusselt numbers to well-established correlations for forced turbulent convection (free of buoyancy and bulk flow acceleration effects). In this method, the normalized Nusselt number (Nu/Nu_o) is plotted against the non-dimensional buoyancy parameters; see Figure 2-8 for example. Figure 2-8 shows the variation of Nu/Nu_o for upward and downward flows as a function of Buoyancy parameter from Equation (2.7) [6]. For upward flow, when the buoyancy parameter is small ($C_B Bo_b F_{VP_1} F_{VP_3} F_{VP_4}$ < 0.04) the normalized Nusselt number is close to unity indicating that the flow is dominated by forced convection. As the buoyancy parameter increases, the normalized Nusselt number falls systematically and reaches a minimum value around a certain value of the buoyancy parameter (0.385 in the case of Figure 2-8). Upon further increase in the buoyancy parameter, the heat transfer recovers as the flow becomes dominated by natural convection and the normalized Nusselt

number becomes greater than unity. For downward flow, there is a systematic enhancement in heat transfer as the buoyancy parameter increases.

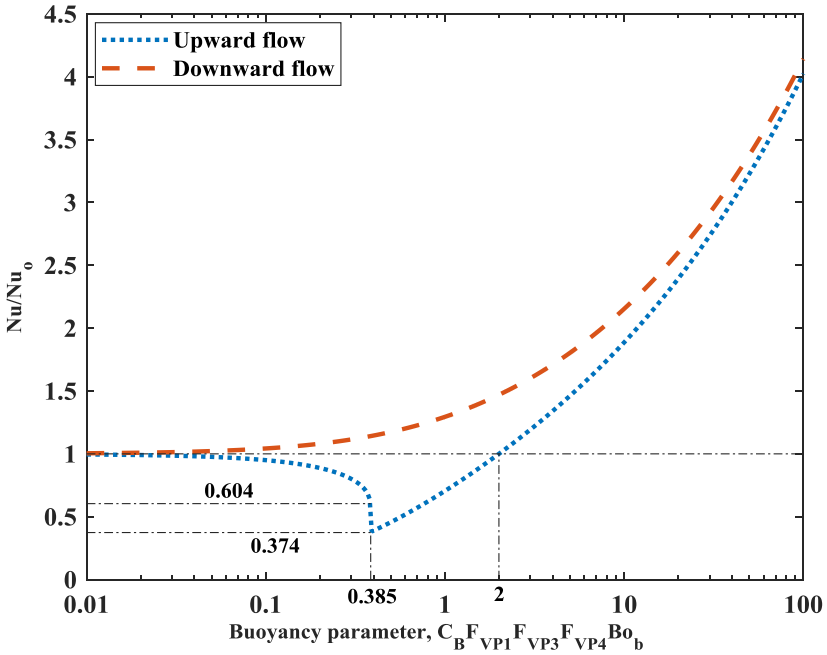

Figure 2-8: Effect of Buoyancy parameter proposed by Jackson (2013) on the supercritical heat transfer in upward and downward flows under heating conditions

Criteria for onset of bulk flow acceleration induced deterioration: As mentioned earlier, thermal bulk flow acceleration influences the heat transfer due to the variation of density in the axial direction of flow. Influence of the bulk flow acceleration on heat transfer can be quantified by plotting the normalized Nusselt number (Nu/Nu_o) against the relevant non-dimensional acceleration parameters from the literature. Several researchers have attempted to derive semi-empirical acceleration parameters following similar procedures described in the previous section. Jackson (2013) [6] proposed the following criteria to neglect the influence of bulk flow acceleration,

$$A_{c_b} = \frac{\beta_b q" D}{k_b Re_b^{1.625} Pr_b} < 4 \times 10^{-6} \quad (2.13)$$

Kim *et al.* (2010) [53] derived the following bulk flow acceleration parameter from Equation (2.8) by making assumptions regarding the boundary-layer thickness.

$$A_c = \frac{\beta_b q"}{G C_{p,b} Re_b^{0.625}} \left(\frac{\mu_w}{\mu_b}\right) \left(\frac{\rho_b}{\rho_w}\right)^{0.5} \quad (2.14)$$

2.1.7 Existing empirical heat transfer correlations

Single-phase heat transfer correlations: Most popular heat transfer correlation for single-phase fluids at subcritical pressures is that of Dittus and Boelter (1930) [55],

$$Nu_b = 0.023\, Re_b^{0.8} Pr_b^n \quad (2.15)$$

where n = 0.3 for the fluid being cooled and 0.4 for the fluid being heated. The correlation of Sieder and Tate (1936) [56] is of the same form as Equation (2.15) but includes viscosity ratio term to account for difference between fluid viscosity in the bulk flow and at the wall. Another more widely accepted single-phase heat transfer correlation is that of Gnielinski (1976) [57],

$$Nu_b = \frac{\left(\frac{f}{8}\right)(Re_b - 1000) Pr}{1 + 12.7\left(\frac{f}{8}\right)^{0.5}\left(Pr^{\frac{2}{3}} - 1\right)} \quad (2.16)$$

where $f = (0.79 \ln(\mathrm{Re_b}) - 1.64)^{-2}$

Supercritical heat transfer correlations: Most of the existing heat transfer correlations for fluids at supercritical pressures are of Dittus and Boelter correlation form along with additional correction factors to account for property variations near the critical point. Pioro *et al.* (2004) [12] conducted a survey of the empirical heat transfer correlations for supercritical fluids. One of the earliest heat transfer correlation for supercritical fluids was developed by Bringer and Smith (1957) [18] based on the experiments conducted for CO_2 flow in heated horizontal tube. The correlation is of form,

$$Nu_x = C\ Re_x^{0.77} Pr_w^{0.55} \tag{2.17}$$

where C = 0.0375 for CO_2 and 0.0266 for water. In the above equation, Nusselt number and Reynolds number are evaluated at a reference temperature, T_x. T_x is defined as T_b if $E = \frac{T_{pc}-T_b}{T_w-T_b} < 0$, as T_{pc} if $0 \leq E \leq 1$ and as T_w if $E > 1$. This approach produced satisfactory results for pressures significantly higher than the critical pressure (e.g., $P/P_c > 1.2$). For pressures close to the critical point (e.g., $P/P_c < 1.1$), it is difficult to calculate a reference temperature which is applicable for a wide range of flow conditions.

Shitsman (1959) [58] proposed the following correlation based on the data for supercritical water, oxygen and carbon dioxide,

$$Nu_b = 0.023\ Re_b^{0.8} Pr_{min}^{0.8} \tag{2.18}$$

where Pr_{min} is minimum of Pr_b and Pr_w.

Bishop *et al.* (1964) [13] conducted experiments with supercritical water flowing in heated vertical tubes and proposed the following correlation for best fit to the data:

$$Nu_x = 0.0069 Re_x^{0.9} \overline{Pr}_x^{0.66} \left(\frac{\rho_w}{\rho_b}\right)_x^{0.43} \left(1 + \frac{2.4D}{x}\right) \tag{2.19}$$

where x is the axial location along the tube. The above correlation predicted Bishop *et al.* (1964) [13] experimental data within ±15%.

Swenson *et al.* (1965) [59] recommended the following correlation based on measured local heat transfer coefficients for supercritical water flow inside smooth tubes. The correlation predicted their experimental data within ±15%.

$$Nu_w = 0.00459 Re_w^{0.923} \overline{Pr}_w^{0.613} \left(\frac{\rho_w}{\rho_b}\right)^{0.231} \tag{2.20}$$

where $\overline{Pr}_w = \frac{i_w - i_b}{T_w - T_b} \frac{\mu_w}{k_w}$

Yamagata *et al.* (1972) [50] recommended the following correlation to predict their experimental data of forced convective heat transfer to supercritical water:

$$Nu_b = 0.0135 Re_b^{0.85} Pr_b^{0.8} F_c \tag{2.21}$$

where F_c = 1 for $E = \frac{T_{Pc} - T_b}{T_w - T_b} > 1$, $F_c = 0.67 Pr_{pc}^{-0.05} \left(\frac{\overline{C_p}}{C_{pb}}\right)^{n1}$ for $0 \le E \le 1$, $F_c = \left(\frac{\overline{C_p}}{C_{pb}}\right)^{n2}$ for $E < 0$; $n1 = -0.77\left(1 + \frac{1}{Pr_{pc}}\right) + 1.49$ and $n_2 = 1.44\left(1 + \frac{1}{Pr_{pc}}\right) - 0.53$

Krasnoshchekov and Protopopov (1959) [60] proposed the following correlation using forced convective heat transfer data for supercritical carbon dioxide and water:

$$Nu_b = Nu_o \left(\frac{\mu_b}{\mu_w}\right)^{0.11} \left(\frac{k_b}{k_w}\right)^{-0.33} \left(\frac{\overline{C_p}}{C_{pb}}\right)^{0.35} \tag{2.22}$$

where $Nu_o = \frac{\left(\frac{f}{8}\right) Re_b \overline{Pr}}{12.7\left(\frac{f}{8}\right)^{0.5}\left(\overline{Pr}^{\frac{2}{3}}-1\right)+1.07}$ and $f = (1.82 \log_{10} Re_b - 1.64)^{-2}$

Krasnoshchekov *et al.* (1966) [61] included additional data and modified their original correlation from Equation (2.22) to the following form:

$$Nu_b = Nu_o \left(\frac{\rho_w}{\rho_b}\right)^{0.3} \left(\frac{\overline{C_p}}{C_{pb}}\right)^{n} \tag{2.23}$$

where exponent n = 0.4 for $T_w/T_{pc} \leq 1$ or $T_b/T_{pc} \geq 1.2$; $n = n_1 = 0.22 + 0.18\left(T_w/T_{pc}\right)$ for $1 \leq T_w/T_{pc} \leq 2.5$; $n = n_1 + (5n_1 - 2)\left(1 - T_b/T_{pc}\right)$ for $1 \leq T_b/T_{pc} \leq 1.2$

Jackson and Fewester (1975) [62] modified the original correlation of Krasnoshchekov *et al.* (1966) from Equation (2.23) to replace the Nu_o with the Dittus-Boelter correlation form. Finally, the following correlation was obtained:

$$Nu_b = 0.0183 Re_b^{0.82} \overline{Pr}^{0.5} \left(\frac{\rho_w}{\rho_b}\right)^{0.3} \tag{2.24}$$

Equation (2.24) is similar in nature to the correlation of Bishop *et al.* (1964) from Equation (2.19) and hence, both the correlations are expected to follow each other closely.

Jackson (2002) [63] modified the original correlation of Krasnoshchekov *et al.* (1967) from Equation (2.23) and proposed the following correlation to predict forced convective heat transfer in supercritical CO_2 and water:

$$Nu_b = 0.0183\, Re_b^{0.82} Pr_b^{0.5} \left(\frac{\rho_w}{\rho_b}\right)^{0.3} \left(\frac{\overline{C_p}}{C_{p,b}}\right)^n \tag{2.25}$$

Exponent n is evaluated as described below:

$$n = 0.4 \qquad T_b < T_w \leq T_{pc} \; and \; 1.2T_{pc} \leq T_b < T_w$$

$$n = 0.4 + 0.2\left(\frac{T_w}{T_{pc}} - 1\right) \qquad T_b \leq T_w < T_{pc}$$

$$n = 0.4 + 0.2\left(\frac{T_w}{T_{pc}} - 1\right)\left(1 - 5\left[\frac{T_b}{T_{pc}} - 1\right]\right) \qquad T_b < T_w \; and \; T_{pc} < T_b \leq 1.2T_{pc}$$

Liao and Zhao (2002) [28] proposed separate set of correlations for horizontal, upward and downward flows to account for the buoyancy effects:

$$Nu_b = 0.124 Re_b^{0.8} Pr_b^{0.4} \left(\frac{Gr_b}{Re_b^2}\right)^{0.203} \left(\frac{\rho_w}{\rho_b}\right)^{0.842} \left(\frac{\overline{C_p}}{C_{p,b}}\right)^{0.384} \quad \text{for Horizontal flow} \tag{2.26}$$

$$Nu_b = 0.354 Re_b^{0.8} Pr_b^{0.4} \left(\frac{Gr_m}{Re_b^{2.7}}\right)^{0.157} \left(\frac{\rho_w}{\rho_b}\right)^{1.297} \left(\frac{\overline{C_p}}{C_{p,b}}\right)^{0.296} \quad \text{for Upward flow} \tag{2.27}$$

$$Nu_b = 0.643 Re_b^{0.8} Pr_b^{0.4} \left(\frac{Gr_m}{Re_b^{2.7}}\right)^{0.186} \left(\frac{\rho_w}{\rho_b}\right)^{2.154} \left(\frac{\overline{C_p}}{C_{p,b}}\right)^{0.751} \quad \text{for Downward flow} \tag{2.28}$$

where $Gr_m = \frac{\rho_b(\rho_b - \rho_m) g D^3}{\mu_b^2}$ and $\rho_m = \frac{1}{T_w - T_b}\int_{T_b}^{T_w} \rho(T) dT$

Bae *et al.* (2010) [33] developed separate heat transfer correlations for normal and deteriorated heat transfer for vertical flows depending on the value of buoyancy parameter, $Bu = \overline{Gr_b}/Re_b^{2.7}$.

For normal heat transfer:

$$\frac{Nu_b}{Nu_o} = (1 + 3 \times 10^5 Bu)^{0.35} \text{ for } Bu < 2\times10^{-6} \quad (2.29)$$

$$\frac{Nu_b}{Nu_o} = 0.48Bu^{-0.07} \text{ for } Bu > 2\times10^{-6}$$

For deteriorated heat transfer:

$$\frac{Nu_b}{Nu_o} = 1 \text{ for } Bu < 2\times10^{-7} \quad (2.30)$$

$$\frac{Nu_b}{Nu_o} = 0.043Bu^{-0.2} \text{ for } 2\times10^{-7} < Bu < 6\times10^{-6}$$

$$\frac{Nu_b}{Nu_o} = 1120Bu^{0.64} \text{ for } 6\times10^{-6} < Bu < 1.5\times10^{-5}$$

$$\frac{Nu_b}{Nu_o} = 3.6 \times 10^{-8}Bu^{-1.53} \text{ for } 1.5\times10^{-5} < Bu < 4\times10^{-5}$$

$$\frac{Nu_b}{Nu_o} = 200Bu^{0.68} \text{ for } 4\times10^{-5} < Bu < 2\times10^{-4}$$

where Nu_o is the forced convective heat transfer correlation from Equation (2.25).

Kim and Kim (2011) [35] developed a heat transfer correlation for vertical flows including the flow acceleration parameter, $q^+ = q_w"\beta_b/GC_{p,b}$:

$$Nu_b = 2.0514\, Re_b^{0.928} Pr_b^{0.742} \left(\frac{\rho_w}{\rho_b}\right)^{1.305} \left(\frac{\mu_w}{\mu_b}\right)^{-0.669} \left(\frac{\overline{C_p}}{C_{p,b}}\right)^{0.888} (q^+)^{0.792} \quad (2.31)$$

2.2 Supercritical heat transfer studies in cooled circular tubes

When compared to the studies on flow inside heated circular tubes described in Section 2.1, relatively fewer number of studies focused on supercritical CO_2 heat transfer in cooled circular tubes. Table 2-3 provides a summary of the selected experimental studies from the literature in chronological order. For each reference, the tube dimensions, the flow conditions, and the flow orientation are reported.

Table 2-3: Selected experimental supercritical CO_2 heat transfer studies in cooled circular tubes

Reference	ID (mm)	L (mm)	P (MPa)	T_b/T_{in} (°C)	$Q"$ (kW/m^2)	G (kg/m^{2}s)	Flow Orientation
Pettersen *et al.* (2000) [64]	0.79	540	8.1–10.1	T_b=10–80	10–20	600–1200	Horizontal
Pitla *et al.* (2001) [65]	4.72	12900	8.1–13.5	T_b=20–130	40–70	1100–2220	Horizontal
Liao and Zhao (2002) [7]	0.5, 0.7, 1.1, 1.4, 1.55, 2.16	110	7.4–12	T_b= 20–110	10–200	-	Horizontal
Yoon *et al.* (2003) [66]	7.73	4000	7.5–8.8	T_{in}=50–80	-	225–450	Horizontal
Dang and Hihara (2004) [67]	1, 2, 4, 6	500	8–10	T_b= 20–70	6–33	200–1200	Horizontal
Kuang *et al.* (2004) [68]	0.79	635	8–10	T_b= 15–55	-	300–1200	Horizontal
Huai *et al.* (2005) [69]	1.31	500	7.4–8.5	T_{in}=22–53	0.8–9	110–420	Horizontal
Son and Park (2006) [70]	7.75	6000	7.5–10	T_{in}=90–100	-	200–400	Horizontal
Jiang *et al.* (2009) [71]	2	150	7.8–9.8	T_{in}=55–70	-	-	Vertical
Bruch *et al.* (2009) [72]	6	750	7.4–12	T_{in}=15–70	-	50–590	Vertical
Oh and Son (2010) [73]	4.55, 7.75	4000, 6000	7.5–10	T_{in}=90–100	-	200–600	Horizontal
Ma *et al.* (2016) [74]	12	1500	8–10	T_b= 20–70	-	490–830	Vertical

Pettersen *et al.* (2000) [64] measured the heat transfer coefficients for supercritical CO_2 flow in aluminum multiport extruded test section containing 25 round parallel tubes with inner diameter of 0.79 mm and length of 0.54 m. They used Wilson plot method [76] for data reduction and to determine the heat transfer coefficient of CO_2 side. In the Wilson

plot method, the heat transfer coefficient of coolant (water in this case) is assumed to follow Dittus-Boelter type correlation ($Nu = cRe^{m}Pr^{0.4}$) and the coefficients c, m are calculated from the calibration tests. The Wilson plot methods introduces additional uncertainty in determination of the CO_2 side heat transfer coefficient but eliminates the need to measure the wall temperature of mini channels. The calculated heat transfer coefficients were found to be in good agreement with the Gnielinski correlation [57].

Wilson plot method was also adopted by Kuang *et al.* (2004) [68] for data reduction, who investigated the heat transfer and pressure drop characteristics of sCO_2 flow through microchannel heat exchanger containing 10 parallel tubes with inner diameter of 0.79 mm. The heat transfer coefficients they measured are similar to those of Pettersen *et al.* (2000) [64] with some differences near the pseudocritical temperature. They proposed the following correlation which was able to predict their experimental data within ±20%:

$$Nu_b = 0.00158\, Re_b^{1.05} Pr_b^{0.648} \left(\frac{\rho_w}{\rho_b}\right)^{0.367} \left(\frac{\overline{C_p}}{C_{p,b}}\right)^{0.4} \tag{2.32}$$

Pitla *et al.* (2001) [65] measured the heat transfer coefficients of sCO_2 flow in a tube-in-tube counterflow heat exchanger. The sCO_2-side heat transfer coefficient was determined by calculating the water-side heat transfer coefficient using published correlations from literature for annular flow.

Yoon *et al.* (2003) [66] and Son and Park (2006) [70] studied heat transfer and pressure drop characteristics of sCO_2 flow in a series of tube-in-tube counter flow heat exchangers. They calculated the heat transfer coefficient by measuring the tube wall temperature using thermocouples. This eliminates the need to make assumptions regarding

the heat transfer coefficient of water side unlike previous studies. Yoon *et al.* (2003) [66] found that the existing correlations under-predicted the heat transfer coefficient near the pseudocritical temperature and proposed the following correlation:

$$Nu_w = 1.38 Nu_w' \left(\frac{\rho_w}{\rho_b}\right)^{0.57} \left(\frac{\overline{C_p}}{C_{p,w}}\right)^{0.86} \tag{2.33}$$

where $Nu_w{}'$ is the Nusselt number evaluated at wall temperature using the Gnielinski correlation [57]. Son and Park (2006) [70] developed following correlation of Dittus-Boelter form which predicted their experimental data with mean deviation of ±17.6%:

$$Nu_b = Re_b^{0.55} Pr_b^{0.23} \left(\frac{C_{p,b}}{C_{p,w}}\right)^{0.15} \text{ for } \frac{T_b}{T_{pc}} > 1$$

$$Nu_b = Re_b^{0.35} Pr_b^{1.9} \left(\frac{\rho_b}{\rho_w}\right)^{-1.6} \left(\frac{C_{p,b}}{C_{p,w}}\right)^{-3.4} \text{ for } \frac{T_b}{T_{pc}} \leq 1 \tag{2.34}$$

Later, Oh and Son (2010) [73] proposed following correlation based on large experimental data which includes the data of Son and Park (2006) and additional data for tube with smaller diameter (ID=4.55 mm):

$$Nu_b = a' Re_b^{b'} Pr_b^{c'} \left(\frac{\rho_b}{\rho_w}\right)^{d'} \left(\frac{C_{p,b}}{C_{p,w}}\right)^{e'} \tag{2.35}$$

where a'=0.023, b'=0.7, c'=2.5, d'=0, e'=-3.5 for $T_b/T_{pc} > 1$ and a'=0.023, b'=0.6, c'=3.2, d'=3.7, e'=-4.6 for $T_b/T_{pc} \leq 1$

Dang and Hihara (2004) [67] investigated heat transfer and pressure drop characteristics of CO_2 flow inside cooled tubes with four different diameters. They used

average temperature between CO_2 and wall to calculate the heat transfer coefficient. The average temperature difference was defined as the arithmetic average of the log-mean temperature difference (LMTD) and the mean temperature difference. They found out that the heat transfer coefficients are slightly higher in the larger tubes when $T_b \geq T_{pc}$.

Huai *et al.* (2005) [69] studied the heat transfer and fluid flow characteristics of sCO_2 flow in a multi-port extruded aluminum test section containing 10 circular channels with diameter of 1.31 mm and length of 0.5 m. Heat transfer coefficients were calculated using measured heat flux via heat flux sensors and wall temperature. They proposed following correlation based on their experimental data which predicted the data within ±30%:

$$Nu_b = 0.022186\, Re_b^{0.8} Pr_b^{0.3} \left(\frac{\rho_b}{\rho_w}\right)^{-1.4652} \left(\frac{\overline{C_p}}{C_{p,w}}\right)^{0.0832} \tag{2.36}$$

2.2.1 Buoyancy influence on supercritical heat transfer under cooling conditions

Fewer studies in the literature focused on investigating the influence of buoyancy on supercritical heat transfer under cooling conditions. Liao and Zhao (2002) [7] investigated heat transfer characteristics of sCO_2 flow inside horizontal cooled tubes with six different diameters to understand the effect of tube diameter on the heat transfer. They concluded that the heat transfer coefficient increased with tube diameter and attributed it to the influence of buoyancy effect. The influence of buoyancy force on heat transfer was tested using the buoyancy criterion proposed by Jackson for horizontal flows [14],

$$Ri = \frac{Gr_b}{Re_b^2} < 10^{-3} \tag{2.37}$$

Liao and Zhao (2002) [7] proposed the following correlation based on their experimental data. The correlation is similar to that of Jackson from Equation (2.25), expect that additional buoyancy term was included to account for the influence of buoyancy.

$$Nu_w = 0.128\, Re_w^{0.8} Pr_w^{0.3} \left(\frac{Gr_b}{Re_b^2}\right)^{0.205} \left(\frac{\rho_b}{\rho_w}\right)^{0.437} \left(\frac{\overline{C_p}}{C_{p,w}}\right)^{0.411} \tag{2.38}$$

Jiang *et al.* (2009) [71] investigated convective heat transfer of sCO_2 in cooled vertical tube with diameter of 2 mm. Local heat transfer coefficients were calculated using measured wall temperatures and local heat flux determined using numerical simulations. They noted that the wall temperature and heat transfer coefficients for upward flow are significantly different compared to downward flow under certain conditions. They attributed this to the influence of buoyancy. As described in Section 2.1.4, during heating conditions, heat transfer deterioration occur for upward flow whereas heat transfer is enhanced for downward flows. However, under cooling conditions the heat transfer deterioration occur for the downward flow whereas enhancement is observed for the upward flow. Figure 2-9 presents an example of heat transfer differences between upward and downward flows from Jiang *et al.* (2009) [71]. Similar heat transfer differences between upward and downward flows were also observed by Bruch *et al.* (2009) [72] who investigated mixed convection characteristics of CO_2 in a cooled vertical tube with a diameter of 6 mm. They identified the buoyancy influence on heat transfer by plotting normalized Nusselt number (Nu/Nu_o) against buoyancy parameter of Hall and Jackson [41]. Based on the trends observed following correlations were proposed for upward and downward flows.

Upward flow:

$$\frac{Nu}{Nu_o} = \left(1.542 + 3243\left(\frac{\overline{Gr_b}}{Re_b^{2.7}}\right)^{0.91}\right)^{1/3} \tag{2.39}$$

Downward flow:

$$\frac{Nu}{Nu_o} = 1 - 75\left(\frac{\overline{Gr_b}}{Re_b^{2.7}}\right)^{0.46} \quad \text{for} \quad \frac{\overline{Gr_b}}{Re_b^{2.7}} < 4.2 \text{ x } 10^{-5} \tag{2.40}$$

$$\frac{Nu}{Nu_o} = 13.5\left(\frac{\overline{Gr_b}}{Re_b^{2.7}}\right)^{0.4} \quad \text{for} \quad \frac{\overline{Gr_b}}{Re_b^{2.7}} > 4.2 \text{ x } 10^{-5}$$

where Nu_o is the forced convective heat transfer correlation from Equation (2.24). Ma *et al.* (2016) [74] also identified the influence of buoyancy on heat transfer in their experimental studies using the buoyancy parameter of Hall and Jackson for vertical flows [41].

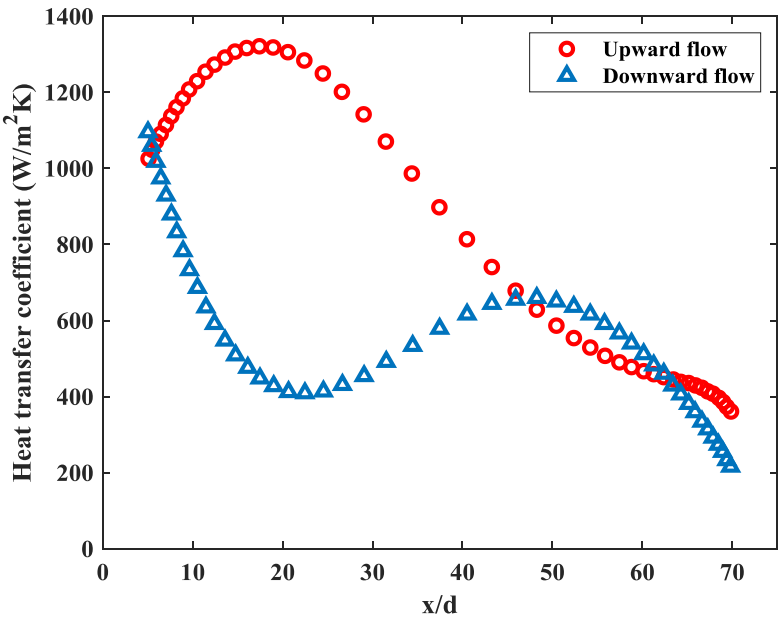

Figure 2-9: Variation of local heat transfer coefficient along the tube length during in tube cooling of CO_2 for upward and downward flow. Data of Jiang *et al.* (2009)

2.3 Compact heat exchangers

As mentioned in the introduction section, sCO_2 Brayton cycles requires a significant amount of internal heat recuperation, thus requiring numerous, large heat exchangers to achieve high cycle efficiency. An effective way to handle the high operating pressures, temperatures, and to reduce the capital cost is to use compact heat exchangers. Heat exchangers are arbitrarily considered compact if it has a heat transfer area to volume ratio, β greater than 700 m^2/m^3 [76]. Other parameters which can be used to characterize compact heat exchangers are hydraulic diameter, d_h (< 4 mm) and porosity, ϕ.

$$\beta = \frac{A_s}{V} = \frac{4\phi}{d_h} \tag{2.41}$$

$$d_h = \frac{4\,V_{fluid}}{A_s} \tag{2.42}$$

$$\phi = \frac{V_{fluid}}{V} = 1 - \frac{V_{solid}}{V} \tag{2.43}$$

There are several different types of compact heat exchangers that can be selected depending on the process requirements, cost constraints etc. An extensive review of different types of compact heat exchangers and their applications was conducted by Li *et al.* (2011) [77] and Hesselgreaves (2016) [76]. Commonly used compact heat exchangers are plate heat exchanger (PHEs), plate-fin heat exchangers (PFHEs), chemically-machined plate heat exchangers commercially known as the printed circuit heat exchangers (PCHEs) and the Marbond heat exchangers, more generally known as the chemically-blanked plate heat exchangers (CBHEs). Table 2-4 presents a summary of the flow surface characteristics, maximum pressure and temperature ratings for most commonly used compact heat exchangers.

Table 2-4: Characteristics, maximum pressure and temperature ratings of commonly used compact heat exchangers. From Li *et al.* (2011) and Hesselgreaves (2016)

Compact heat exchanger type	β (m^2/m^3)	d_h (mm)	P_{max} (MPa)	T_{max} (°C)
Plate heat exchanger (Gasketed)	120 – 660	2–10	3.5	250
Plate-fin heat exchanger (Brazed)	1000 – 1500	1 – 2	12	800
Plate-fin heat exchanger (Diffusion-bonded)	700 – 800	1 – 2	62	800
Printed circuit heat exchanger (Diffusion-bonded)	> 2500	0.5 – 3	50–100	900
Marbond heat exchanger (Diffusion-bonded)	Up to 10,000	0.33 – 1	40	900

2.3.1 Comparison of thermal-hydraulic performance of compact heat exchangers

The performance characteristics of different compact heat exchangers can be compared using the fanning friction factor, f and the Colburn j-factor, j. Both f and j are dependent on the Reynolds number and the flow geometry. For example, proportionality index b in Equation (2.44) is dependent on whether the flow is laminar or turbulent. Likewise, Colburn j-factor is proportional to Nusselt number which is again dependent on the flow regime.

$$f = \Delta P \frac{d_h}{L} \frac{\rho}{G^2/2} \propto Re^b \tag{2.44}$$

$$j = \frac{Nu}{RePr^{1/3}} \tag{2.45}$$

Figure 2-10 is an example of variation of the ratio, f/j as a function of flow Reynolds number for several types of PCHEs and plate-fin surface geometries from Southall *et al.* (2008) [78]. Being Heatric proprietary data, numerical scale was not published for the vertical axis. However, the plot is still useful to understand the qualitative

trends of f/j. Compact heat exchangers with lower ratios of f/j or higher ratios of flow area goodness factor, j/f are generally desirable. Figure 2-10 also shows that the optimum heat exchanger design will depend on the desired flow regime. For example, comparing the plain etched and low zigzag etched surface geometries; plain etched surface has lower f/j for Re > 5000 but for 1000 < Re < 5000, low zigzag etched surface performs better. Therefore, it is quite important to understand the optimum flow regime for each heat exchanger.

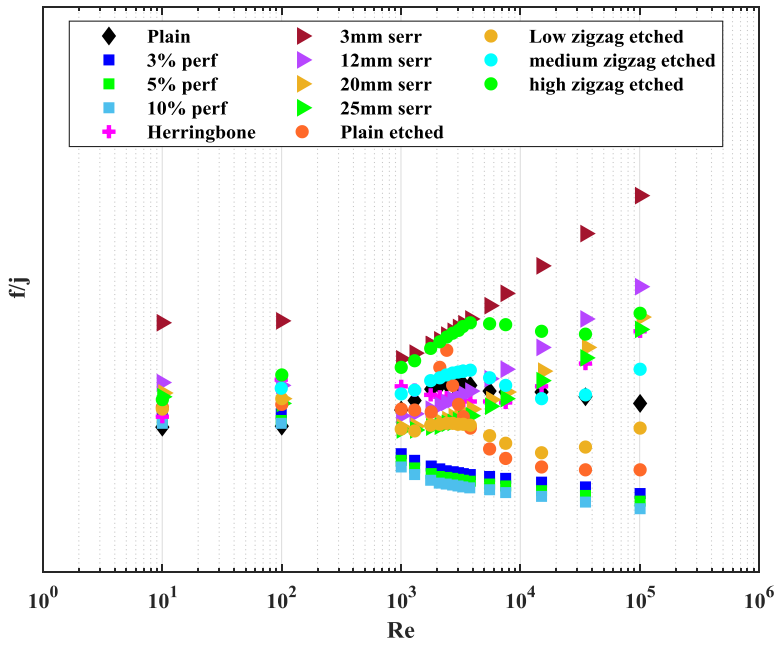

Figure 2-10: Plot of ratio of the fanning friction factor, f and the Colburn j-factor, j of some compact heat exchangers. Data from Southall *et al.* (2008)

An alternative method to compare the performance of different types of regenerators is proposed by Ruhlich and Quack (1998) [79]. In this method, the number of pressure heads (NPH) and the number of transfer units (NTU) are used as the parameters for comparison. The ratio, $\frac{NPH}{NTU} = \frac{1}{4}\frac{f}{j}Pr^{2/3}$ allows for direct comparison of various heat

transfer surfaces and flow regimes as shown in Figure 2-11 [79]. Lower value of $\frac{NPH}{NTU}$ is generally desirable and according to Figure 2-11, single plate performs the best followed by parallel plates.

$$NPH = \frac{2\,\Delta P \rho}{G^2} = f\,\frac{L}{D} \tag{2.46}$$

$$NTU = \frac{Nu}{RePr}\,\frac{4L}{D} \tag{2.47}$$

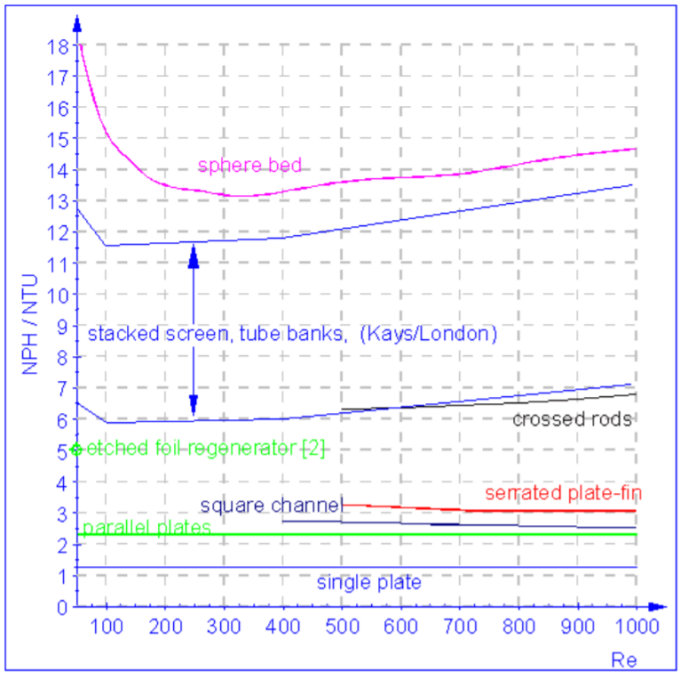

Figure 2-11: Plot of *NPH/NTU* vs. Reynolds number for different heat transfer surfaces, Pr=0.7. From Ruhlich and Quack (1998)

2.4 Review of studies on printed circuit heat exchangers

Printed circuit heat exchangers (PCHEs) are the leading potential heat exchanger candidates for the sCO_2 Brayton cycles [3]. PCHEs are fabricated using two innovative technologies of photo-chemical etching and diffusion bonding. Desired flow/heat transfer

surfaces are photo-chemically etched on to flat metal plates. The etched plates are then stacked, and diffusion-bonded to form a monolithic core to which the flow distribution headers are welded or in some cases, the headers are integrated into the etched plates. Although PCHEs have been around for a while, mainly in the Oil & Gas industry, their use in the power generation industry gained popularity only about a decade ago. Since then a decent number of experimental and computational studies have been published in open literature focusing on the thermal-hydraulic performance of PCHEs mainly using Carbon dioxide, air, water, or Helium as the working fluid. One of the advantages of PCHEs is that they allow for etching of a wide range of surface geometries thus altering the thermal-hydraulic performance of the PCHE core quite easily to meet the design requirements.

In terms of the surface geometries, PCHEs can be categorized as either continuous or discontinuous fin types. Most widely investigated continuous flow channel types include straight and zigzag channels and that of discontinuous flow channels include S-shaped, and airfoil fins. Figure 2-12 shows channel configuration and associated nomenclature for the continuous straight and zigzag channels.

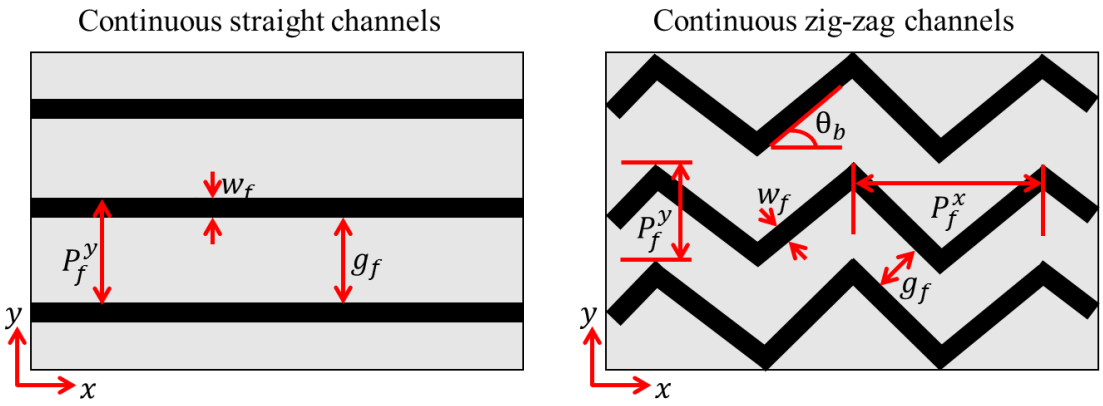

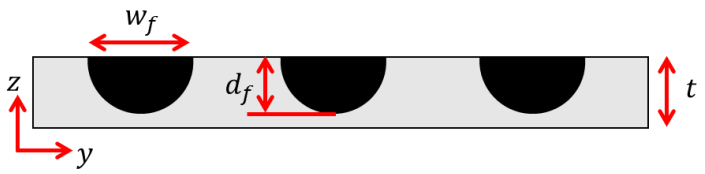

Figure 2-12: Schematic of fluid channel configuration & nomenclature for continuous straight and zigzag channels

Notable experimental studies on PCHEs with straight channels are of Kruizenga (2010) [80], Mylavarapu (2011) [81], Seo *et al.* (2015) [82], Chen *et al.* (2016) [83] and Chu *et al.* (2017) [84]. Table 2-5 provides details of the PCHEs used for these experimental studies.

Table 2-5: Details of the PCHEs with continuous straight channels tested in literature. Refer to Figure 2-12 for nomenclature of the geometrical parameters listed in the table

Reference	**Kruizenga (2010)** [80]	**Mylavarapu (2011)** [81] **& Chen *et al.* (2016)** [83]	**Seo *et al.* (2015)** [82]	**Chu *et al.* (2017)** [84]
	Hot side	Hot/Cold side	Hot/Cold side	Hot/Cold side
Core Dimensions (mm)	-	-	40 x 16 x 141	100 x 150
Core Dry Mass (kg)	-	-	-	-
Material of Construction	SS 316L	Alloy 617	SS 304	SS 304
Fluid	CO_2	He/He	Water/Water	CO_2/Water
Channel Pattern	Straight	Straight	Straight	Straight
Number of Plates	1	10/10	3/4 and 5/6	28/28
Plate Thickness, t (mm)	6.3	1.63/1.63	-	2.2/2.2
Number of Channels per Plate	9	12/12	22/22	32/32
Channel length, L (mm)	500	305/272	137/137	150
Vertical Pitch, P_f^y (mm)	2.51	2.5/2.5	1.4/1.4	4/4
Channel width, w_f (mm)	1.9	2/2	0.8/0.8	2.8/2.8
Channel depth, d_f (mm)	0.85	1/1	0.6/0.6	1.4/1.4
Hydraulic diameter, d_h (mm)	1.16/1.16	1.22/1.22	0.66/0.66	1.71/1.71
Heat transfer area, A_s (m^2)	-	-	0.026/0.034	-
Free flow area, A_c (m^2)	-	1.88e-4/1.88e-4	31.7e-6/42.2e-6	-

Mylavarapu (2011) [82] tested two custom fabricated Alloy 617 PCHEs with semicircular straight channels. Experimental data suggested that in the case of semicircular channel flow, the transition to turbulence occurred at Re of ~1700; earlier than Re of ~2300 for circular channel flow. This expedited transition was attributed to the rough inlet at the entrance to the PCHE. Chen *et al.* (2016) [84] conducted tests using the same test facility and the test sections of Mylavarapu (2011) [82]. Based on the test data, they proposed following Nusselt number correlation that can be used to predict the dynamic respose of PCHE in their tests:

$$Nu = 0.01352\ Re^{0.80058} \quad \text{for } 1200 \leq Re \leq 1850$$
$$Nu = 3.6361\ \times 10^{-4}\ Re^{1.2804} \text{ for } 1850 \leq Re \leq 2900 \tag{2.48}$$

Seo *et al.* (2015) [82] investigated heat transfer and pressure drop characteristics of two straight channel PCHEs and proposed following empirical correlations for friction factor and Colburn j-factor:

$$f = 1.3383\ Re^{-0.5003} \quad \text{for } 100 \leq Re \leq 850 \tag{2.49}$$
$$j = 0.706\ Re^{-0.8208} \text{ for } 100 \leq Re \leq 850 \tag{2.50}$$

Chu *et al.* (2017) [84] studied heat transfer characteristics of a straight channel PCHE for conditions near the pseudocritical temperature where thermophysical property variations are significant. Accounting for the property variations and influence of buoyancy, they proposed the following Nusselt number correlation:

$$\frac{Nu}{Nu_o} = 0.58 - 53\left(\frac{Gr}{Re^{2.7}}\right)^{0.36} \quad \text{for } 30000 \leq Re \leq 60000 \;\&\; T_w \approx T_{pc} \qquad (2.51)$$

$$\frac{Nu}{Nu_o} = 0.36 - 22\left(\frac{Gr}{Re^{2.7}}\right)^{0.42} \quad \text{for } 30000 \leq Re \leq 70000 \;\&\; T_w > T_{pc} \qquad (2.52)$$

where Nu_o is the forced convective heat transfer correlation proposed by Jackson and Fewester [62] listed in Equation (2.24).

Table 2-6: Details of the PCHEs with continuous zigzag channels tested in literature. Refer to Figure 2-12 for nomenclature of the geometrical parameters

Reference	**Nikitin *et al.* (2006)** [85]	**Ngo *et al.* (2007)** [86]	**Kim *et al.* (2009)** [87]	**Moisseytsev *et al.* (2010)** [88]	**Chen *et al.* (2016)** [89]	**Baik *et al.* (2017)** [90]
	Hot/Cold side	Hot/Cold side	Hot/Cold side	Hot/Cold side	Hot/Cold side	Hot/Cold side
Core Dimensions (mm)	71 x 76 x 896	29 x 76 x 745.2	150 x 144 x 896	120 x 200 x 1200	50.8 x 126 x 339.1	84 x 99.2 x 200
Core Dry Mass (kg)	40	-	146	200	-	-
Material of Construction	SS 316L	SS 316L	Alloy 800H	SS 316	Alloy 617	SS 316L
Fluid	CO_2/CO_2	CO_2/CO_2	He/He	CO_2/CO_2	He/He	CO_2/Water
Channel Pattern	Zigzag	Zigzag	Zigzag	Zigzag	Zigzag	Zigzag
Number of Plates	12/6	8/4	40/40	-	8/8	28/28
Plate Thickness, t (mm)	1.63/1.63	1.5/1.5		-	1.6/1.6	1.5/1.5
Number of Channels per Plate	12/11	12/11	32/32	-	11/11	32/32
Vertical Pitch, P_f^y (mm)	2.97/3.25	3.42/3.42		-	2.5/2.5	-
Horizontal Pitch, P_f^x (mm)	9/7.24	7.56/7.56		-	24.6/24.6	9/9
Channel width, w_f (mm)	1.9/1.8	0.8/0.8	1.51/1.51	1.5/1.5	2/2	1.8/1.8
Channel depth, d_f (mm)	-	0.94/0.94	-	0.75/0.75	1/1	0.75/0.75
Channel bend angle, θ_b (deg)	32.5/40	52/52	15/15	38/45	15/15	32.5/32.5
Hydraulic diameter, d_h (mm)	1.15/1.15	1.09/1.09	0.92/0.92	0.91/0.91	1.22/1.22	1.16/1.16
Heat transfer area, A_s (m^2)	0.697/0.356	0.465/0.235	3.8/3.8	-	-	-
Free flow area, A_c (m^2)	2e-4 /0.92e-4	11.82e-5 /5.42e-5	11.55e-4 /11.55e-4	-	-	-

Commercial PCHEs typically use zigzag channels to enhance the heat transfer compared to straight channels. Notable experimental studies for the zigzag channel PCHEs are of Nikitin *et al.* (2006) [85], Ngo *et al.* (2007) [86], Moisseytsev *et al.* (2010) [88], Kim *et al.* [87, 91, 92], Kruizenga (2010) [80], Carlson (2012) [93], Chen *et al.* (2016) [89], Baik *et al.* (2017) [90].

Nikitin *et al.* (2006) [94, 85] experimentally investigated the heat transfer and pressure drop characteristics of a 3 kW_{th} zigzag channel PCHE in a sCO_2 test facility. Empirical correlations were developed for the local heat transfer coefficients and effective friction factor as a function of Re in the range of 2,800–12,100:

$$h_{hot} = 2.52\, Re^{0.681} \quad \text{for } 2800 \le Re \le 5800 \tag{2.53}$$

$$h_{cold} = 5.49\, Re^{0.625} \quad \text{for } 6200 \le Re \le 12100 \tag{2.54}$$

$$f_{hot} = 0.04495 - 1.402 \times 10^{-6} Re \quad \text{for } 2800 \le Re \le 5800 \tag{2.55}$$

$$f_{cold} = 0.09318 - 1.545 \times 10^{-6} Re \quad \text{for } 6200 \le Re \le 12100 \tag{2.56}$$

Moisseytsev *et al.* (2010) [88] tested a 17.5 kW_{th} 316L stainless steel Heatric PCHE with zigzag channels. Using the published sample friction factor and Colburn j-factors for Heatric PCHEs [78], Moisseytsev *et al.* (2010) proposed fanning friction factor and Colburn j-factor correlations for straight and zigzag channels with different channel angles. These correlations are valid for laminar, transition and turbulent flow regimes. The fanning friction factor for the continuous straight channels is calculated as follows:

$$f_o = \frac{16}{Re} \quad \text{for } Re < 1700 \tag{2.57}$$

$$f_o = \frac{0.0791}{Re^{0.25}} \text{ for } Re > 2300$$

With a linear function for the transition region, $1700 \leq Re \leq 2300$. Increase in the friction factor for continuous zigzag channel relative to the straight channel is calculated as,

$$\begin{gathered} \frac{f}{f_o} = 1 + a_f(Re + 50) \quad \text{for } Re < 1300 \\ \frac{f}{f_o} = k\, Re^c \quad \text{for } Re > 2300 \end{gathered} \tag{2.58}$$

where the coefficients a_f, k, c are defined as follows:

$$a_f = 4.5 \times 10^{-3} \tan \theta_b$$
$$k = 1 + a_f . \frac{1800}{1300^c}$$
$$c = \frac{\ln \frac{1+223283.a_f^2}{1+a_f.1800}}{\ln\left(\frac{1000}{13}\right)}$$

The comparison of the friction factor correlations from Equation (2.57) and Equation (2.58) with the unscaled data from Heatric [78] is shown in Figure 2-13. Overall, a good agreement was found except for some discrepancies in the high Reynolds number regime [88]. The Colburn j-factor for the continuous straight and zigzag channels is calculated as follows:

For turbulent region:

$$j = a_{j,turb}(0.1341)Re^{-0.3319} \text{ for } Re \geq 2300 \tag{2.59}$$

where $a_{j,turb} = 0.6 + 0.5 \tan \theta_b$

For laminar region:

$$j_{o,lam} = \frac{4.1}{Re} \quad \text{for} \quad Re < 2300$$
$$\frac{j_{lam}}{j_{o,lam}} = 1 + a_{j,lam}(Re + 50) \quad \text{for } Re < 2300 \tag{2.60}$$

where $a_{j,lam} = \frac{3.9361.a_{j,turb} - 1}{1800}$

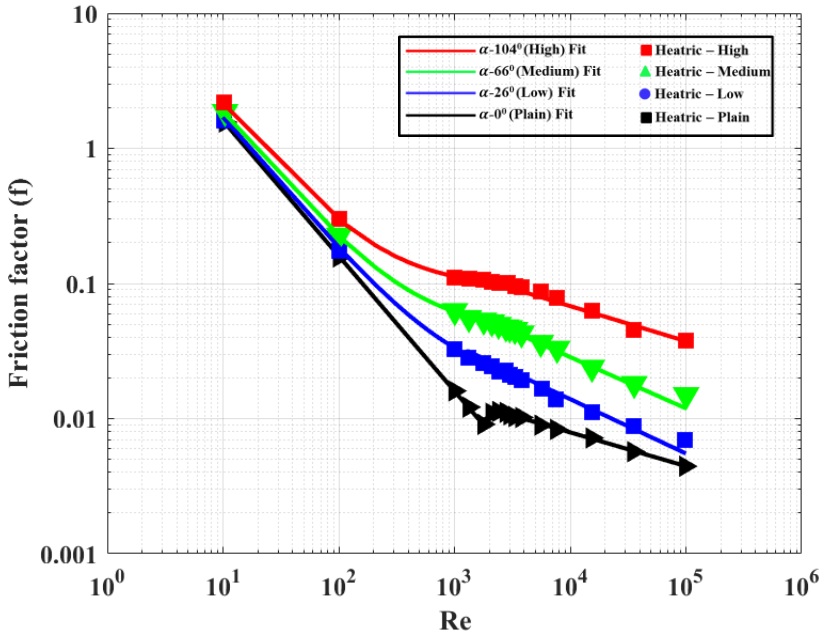

Figure 2-13: Comparison of unscaled Heatric friction factor data with the friction factor correlations proposed by Moisseytsev *et al.* (2010)

The comparison of the Colburn j-factor correlations from Equation (2.59) and Equation (2.60) with the unscaled data from Heatric [78] is shown in Figure 2-14. For the straight channel, special treatment was needed in the transition region to match the data [88].

$$j_{o,tran} = 352\, Re^{-1.4562} \quad \text{for } 1700 < Re < 2300 \tag{2.61}$$

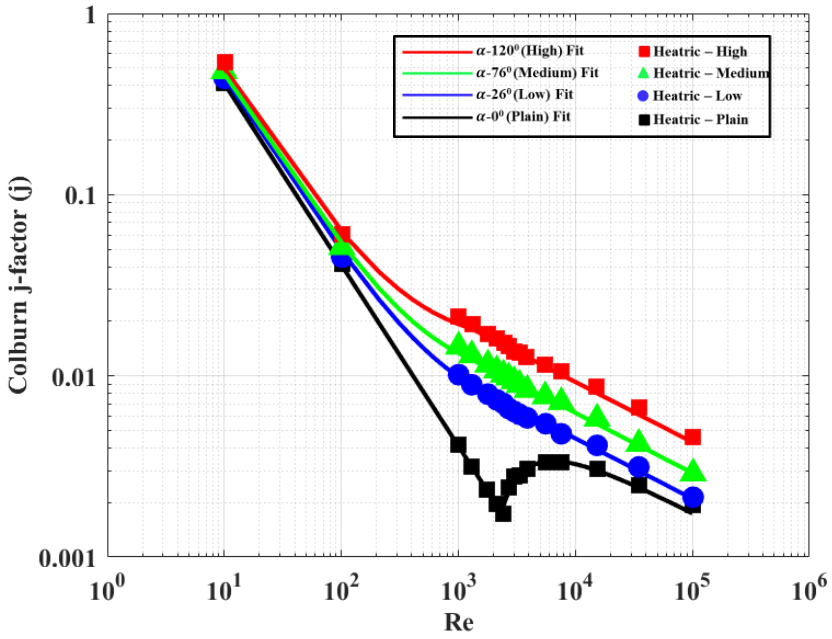

Figure 2-14: Comparison of unscaled Heatric Colburn j-factor data with the j-factor correlations proposed by Moisseytsev *et al.* (2010)

Kim *et al.* (2013) conducted a series of tests on Alloy 800H Heatric PCHE with semicircular straight channels for He-to-He [87], He-to-water [91], and He & CO_2 mixture-to-water [92] heat exchange. They proposed the following friction factor and Nusselt number correlations which are valid for 0 < Re < 3000.

$$f.Re = 15.78 + 0.0557\, Re^{0.82} \quad \text{for } 0 < Re < 3000 \tag{2.62}$$

$$Nu = 4.089 + 0.00497\, Re^{0.95} Pr^{0.55} \text{ for } 0 < Re < 3000,\ 0.66 < Pr < 13.41 \tag{2.63}$$

Kruizenga (2010) [80] and Carlson (2012) [93] investigated heat transfer and pressure drop characteristics of two zigzag channel PCHEs. However, no empirical correlations were published. Chen *et al.* (2016) [89] compared their experimental data to

the empirical correlation proposed by Kim *et al.* (2012) [92] and found that heat transfer performance is underpredicted. They attributed this to geometrical differences in the flow channels. Following friction factor and Nusselt number correlations were proposed:

$$\begin{aligned} f &= \frac{17.639}{Re^{0.8861}} \quad \text{for } 1400 \leq Re \leq 2200 \\ &= 0.019044 \quad \text{for } 2200 < Re \leq 3558 \end{aligned} \tag{2.64}$$

$$\begin{aligned} Nu &= 0.05516\, Re^{0.69195} \text{ for } 1400 \leq Re \leq 2200 \\ &= 0.09221\, Re^{0.62507} \text{ for } 2200 \leq Re \leq 3558 \end{aligned} \tag{2.65}$$

The idea of using discontinuous fins for PCHEs was originally promoted by Tsuzuki *et al.* (2007) [95]. Discontinuous fins are gaining popularity as an alternative to the continuous channel type PCHEs since they are anticipated to offer lower pressure drop with higher heat transfer surface area. The number of experimental studies on the discontinuous fin PCHEs are quite limited in literature. Most commonly investigated discontinuous flow channels include S-shaped and airfoil fins. Figure 2-15 shows channel configuration and associated nomenclature for the discontinuous S-shaped and airfoil fins.

Tsuzuki *et al.* (2007) [95] conducted CFD study for S-shaped, similar to that of a sine curve, and concluded that the discontinuous S-shaped fins offered significantly lower pressure drop compared to the zigzag channels. The discontinuous S-shaped fins offered a more uniform velocity profile and eliminated the swirl flows, eddies, and recirculation zones experienced in the zigzag channels. Figure 2-16 shows thermal-hydraulic characteristics of several surface geometries under identical operating conditions [95]. For a fin angle, θ_b of 52^o they concluded that pressure drop for the S-shaped fins is reduced to 1/5th of the continuous zigzag channel while maintaining nearly same thermal performance.

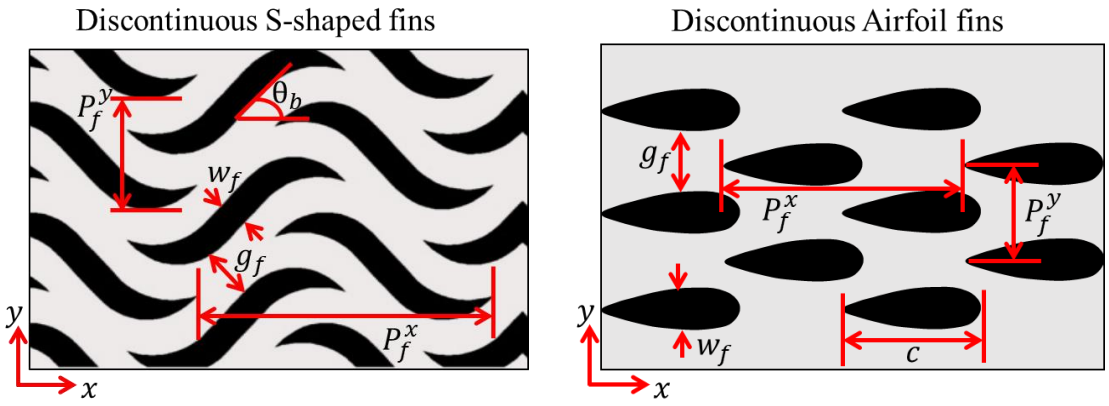

Figure 2-15: Schematic of fluid channel configuration & nomenclature for discontinuous S-shaped fin and continuous zigzag channels

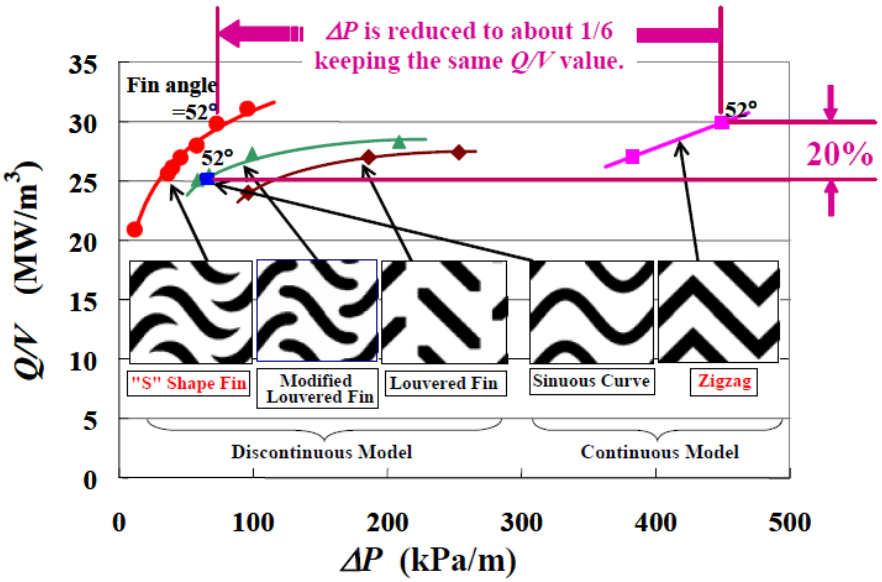

Figure 2-16: Heat transfer and pressure drop characteristics of different PCHE surface geometries. From Ngo *et al.* (2006)

Ngo *et al.* [96] fabricated a PCHE with discontinuous S-shaped fins and tested it for CO_2-to-water heat exchange service. Nikitin *et al.* [94] experimentally evaluated the thermal-hydraulic performance of a PCHE with S-shaped fins and a conventional PCHE with zigzag channels. The geometrical parameters of the S-shaped fins and zigzag channel PCHEs are the kept the same. The details of the zigzag channel PCHE can be found in

Table 2-6. It was noted that the pressure drops offered by the PCHE with S-shaped fins is 4-5 times lower than that of the PCHE with zigzag channels while the Nusselt number is 24-34% lower, depending on the Reynolds number.

Based on their experimental data, Ngo *et al.* [86] proposed the following Nusselt number and friction factor empirical correlations for both the S-shaped fins and zigzag channel PCHEs.

S-shaped fin:

$$f = 0.4545\, Re^{-0.34} \quad \text{for } 3500 \leq Re \leq 23{,}000 \tag{2.66}$$

$$Nu = 0.174\, Re^{0.593} Pr^{0.43} \text{ for } 3500 < Re < 23{,}000;\ 0.75 < Pr < 2.2 \tag{2.67}$$

Zigzag channel:

$$f = 0.1924\, Re^{-0.091} \quad \text{for } 3500 \leq Re \leq 22{,}000 \tag{2.68}$$

$$Nu = 0.1696\, Re^{0.629} Pr^{0.317} \text{ for } 1400 \leq Re \leq 2200;\ 0.75 < Pr < 2.2 \tag{2.69}$$

The idea of utilizing airfoil fins for PCHEs is motivated by the CFD study conducted by Kim *et al.* [97]. In this study, the NACA0020 airfoil fin yielded the same heat transfer performance as the zigzag channel but at a significantly lower pressure drop (~1/20) due to the suppression of separated flows. Although not as dramatic as shown by the CFD study, Carlson [93] experiments indicated that the airfoil fin geometries offer significantly lower pressure drop compared to the zigzag channels. However, most of these experiments were conducted near the pseudo-critical point (T_b/T_{pc} < 1.2), where the heat transfer is significantly influenced by thermophysical property variations as noted by

Pidaparti *et al.* [39] amongst others. Wang *et al.* [98] tested a PCHE with airfoil fins for molten salt heat transfer applications. The PCHE with airfoil fins offered better heat transfer performance for Re in the range of 500–1600 when compared to the published empirical correlations for straight and zigzag channels. Xu *et al.* [99] compared the thermal-hydraulic performance of different discontinuous fins using numerical simulations. The performance of airfoil and rectangular fins were found to be nearly idential at Re < 20,000 but as the Re is increased airfoil fin performed better compared to the rectangular fin. However, no experimental data is available for the rectangular fin PCHEs in literature to validate these CFD studies.

In the present study, the thermal-hydraulic performance of discontinuous rectangular fin and NACA0020 airfoil fin PCHE geometries will be evaluated experimentally. The impact of using discontinuous fin PCHEs on the performance and capital cost of sCO_2 Brayton cycles will be evaluated as well.

CHAPTER 3. TEST FACILITY

An experimental test facility was constructed to investigate the thermal-hydraulic characteristics of supercritical CO_2 (sCO_2) flow through several geometries. During the first phase of this work, the test facility was used to study the influence of buoyancy on heat transfer behavior of sCO_2 flow through heated horizontal and vertical circular tubes. During the second phase, the test facility was modified slightly to investigate the heat transfer and pressure drop characteristics of sCO_2 flow through printed circuit heat exchangers. This chapter provides details of the test facility and the test sections.

3.1 Overview of the test facility

The schematic of the test facility is shown in Figure 3-1. The loop consists of a high-pressure liquid chromatography (HPLC) pump, circulation gear pump, Coriolis mass flow meter, preheater, accumulator, test section and a coiled tube-in-tube cooler.

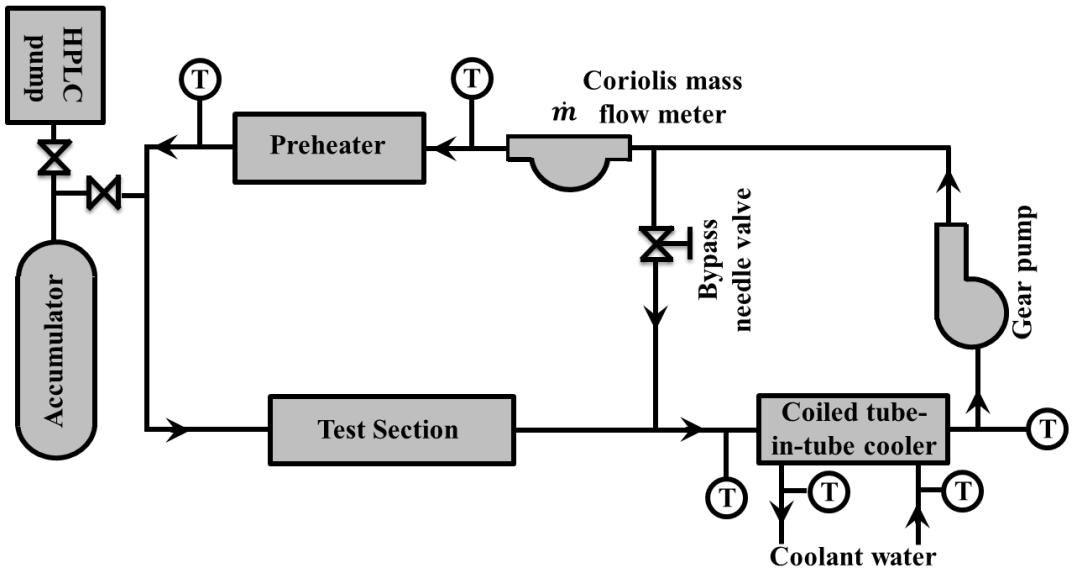

Figure 3-1: Schematic of the experimental test facility

CO_2 from a cylinder is fed to SFC-24, positive-displacement, constant-pressure HPLC pump (Scientific Systems, Inc., Woburn, MA) to fill the test facility to the desired pressure and maintain the system pressure during experiments. It can pressurize the test facility up to 69 MPa (~10,000 psi) and is equipped with a pressure sensor that can measure the system pressure with an accuracy of ±2% of full scale.

An accumulator of volume ~0.5 m^3 is connected to the test facility to increase the system volume and damp the transients in the system. The circulation pump is a magnetically driven gear pump, Micropump (Vancouver, WA). The maximum operating pressure of the pump is 10.35 MPa and can generate flow rates ranging from 0.1 to 1.6 m^3/h, a differential pressure of 0.86 MPa. Circulating pump is coupled to a Baldor variable frequency drive (St. Louis, MO) and this in conjunction with the bypass needle valve is used to precisely control the CO_2 mass flow rate to the test section.

A Micro Motion Coriolis flow meter and transmitter (Emerson, Boulder, CO) are used to measure the mass flow rate in the test loop. The flow meter is capable of measuring flow rates up to 0.27 kg/s with an accuracy of ±0.1% at full scale. Measurements from the flow meter also serve as a feedback control for the circulating pump variable frequency drive.

Temperatures in the loop excluding the test section are controlled using a high-pressure preheater and coiled tube-in-tube cooler. Preheater is a custom fabricated heater used to raise the temperature of CO_2 to the desired test section inlet temperature. In the preheater, CO_2 flows in an annular tube parallel to a 5.5 kW Tempco cartridge heater (Wood Dale, IL). The space between the cartridge heater and the annular tube is filled with

a highly conductive thermal paste to prevent formation of hot spots. Power to the cartridge heater is regulated by a solid-state control relay (SCR). Using PID scheme to control the SCR, the inlet temperature can typically be controlled within ±0.1 °C of the desired set point. Upon exiting the test section, the CO_2 enters a high-pressure coiled tube-in-tube heat exchanger where chilled water runs through the outside tube. This removes excess heat from the CO_2, facilitating the gear pump to operate under liquid-like densities. Inlet and outlet temperatures for all the major components are measured using Omega Engineering K-type thermocouples. A NI DAQ system is used to interface all the instrumentation and controls to the LabVIEW program.

3.2 Circular tube test sections

Two circular tube test sections with different diameters were used to investigate the fundamental heat transfer characteristics for sCO_2 flow under heating conditions.

Figure 3-2 shows a schematic of the test section with larger diameter along with the instrumentation details. This test section is constructed out of 316 stainless steel, has an outer diameter (OD) of 12.7 mm (0.5”), a wall thickness (t_{wall}) of ~0.89 mm (0.035”) and is approximately 1 m long.

Figure 3-3 shows schematic of the test section with smaller diameter along with the instrumentation details. This test section is constructed out of 316 stainless steel, has an outer diameter (OD) of ~9.52 mm (0.375”), a wall thickness (t_{wall}) of ~0.81 mm (0.032”) and is approximately 1 m long.

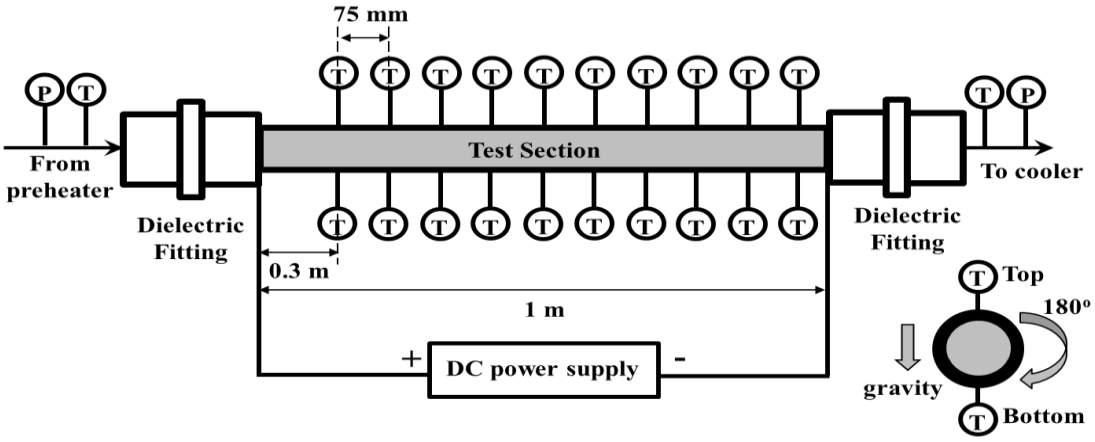

Figure 3-2: Schematic of the larger circular tube test section showing instrumentation, OD=12.7 mm, ID=10.9 mm

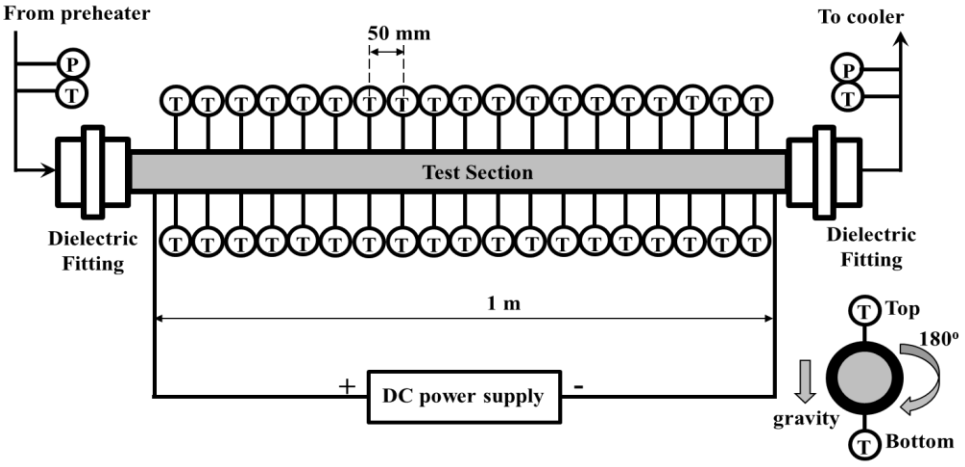

Figure 3-3: Schematic of the smaller circular tube test section showing instrumentation, OD=9.52 mm, ID=7.9 mm

Constant heat flux boundary condition is provided to the test sections through resistive heating using 5 kW Magna-Power electronics direct current (DC) power supply (Magna-Power electronics, Flemington, NJ). To handle the high direct current, Gauge 000 wires and custom fabricated 6.35 mm (0.25") thick copper bar stock were used to make connections between the power supply and the test sections. Heat flux to the test sections is varied by adjusting the voltage across the copper terminals clamped at either ends of the test section. The accuracy of voltage reading is ±0.01% of full scale, while that of current

is ±0.04% of full scale. The test section is electrically and thermally isolated from rest of the test facility by using Swagelok dielectric fittings (Swagelok, Solon, OH) at both ends of the test sections.

The inlet and outlet temperatures to/from the test sections are measured by Omega 3 wire platinum resistance temperature detectors (RTDs) having a maximum uncertainty of ±0.25 °C. These RTDs are calibrated against boiling water and an ice bath to quantify the systematic error. The pressure at the inlet and outlet sections are monitored by Omega gauge pressure transducers with an accuracy of ±0.25% of the measured value.

For the test section with larger diameter, outer wall temperatures are measured by twenty Omega E-type stick-on thermocouples. Out of these twenty thermocouples, ten thermocouples are mounted on the top side and ten on the bottom side (180˚ apart) at axial locations that are 75 mm apart from each other; Refer to Figure 3-2 for details. The first thermocouple is mounted 300 mm from the inlet side to allow for the flow to be hydrodynamically fully developed.

For the test section with smaller diameter, outer wall temperatures are measured by thirty-eight Omega E-type stick-on thermocouples. Out of these thirty-eight thermocouples, nineteen thermocouples are mounted on the top side and nineteen on the bottom side (180˚ apart) at axial locations that are 50 mm apart from each other; Refer to Figure 3-3 for details.

The Omega E-type stick-on thermocouples have a manufacturer-specified uncertainty of ±1.0 °C or 0.4% of the measurement, whichever is greater. Drift in the wall

thermocouple measurements are corrected by performing *in situ* calibration of thermocouples under zero heat flux conditions as described in APPENDIX A.

The primary goal of these experiments is to study the influence of buoyancy on the heat transfer. Therefore, it was required to reconfigure the orientation of test sections to vertical upward, vertical downward and horizontal configurations as needed. Figure 3-4 shows a picture of the test facility with smaller circular tube test section installed in the vertical upward orientation. Depending on the orientation, separate sets of tubes are used to connect the test sections to rest of the test facility. Prior to conducting tests with supercritical carbon dioxide, the facility was validated with the well-known heat transfer correlations using water as the working fluid. Details of the test facility validation can be found in APPENDIX B.

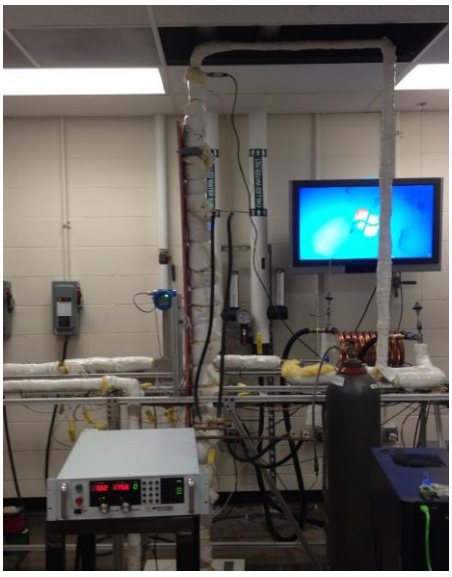

Figure 3-4: Picture of the test facility showing the circular tube test section installed in vertical upward orientation

3.3 Printed circuit heat exchanger test sections

Thermal-hydraulic characteristics of sCO_2 flow through two printed circuit heat exchanger (PCHE) test sections were investigated under cooling conditions. The schematic shown in Figure 3-5 is a representation of the PCHE test section, fluid paths, and the instrumentation. The test section comprises of the PCHE test plate, the mating plate, and the cooling blocks [80, 93].

The PCHE test plate is a 316L stainless steel plate with the desired flow pattern chemically etched (Microphoto Inc.) on it and the total length of the etched pattern is 500 mm. On each end of the plate, entrance and exit manifolds are machined into the plate to distribute and collect the flow entering and leaving the test section.

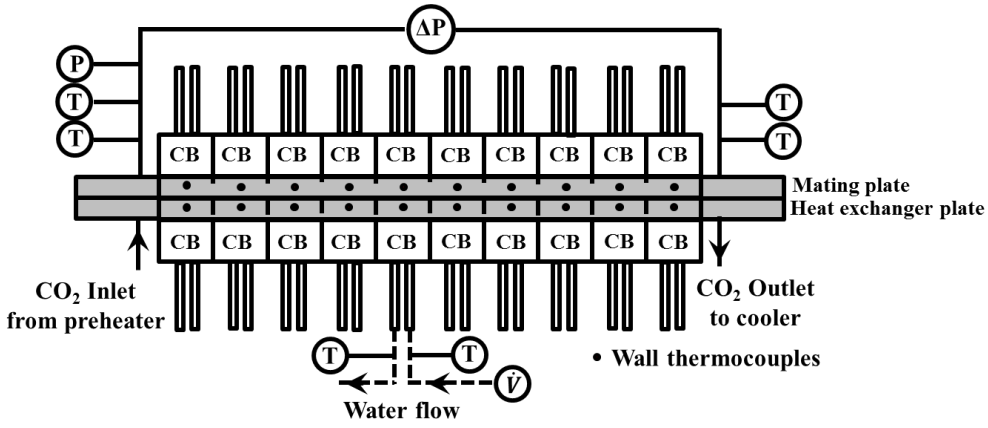

Figure 3-5: Schematic of the PCHE test section showing fluid flow paths and the instrumentation details; CB refers to cooling block

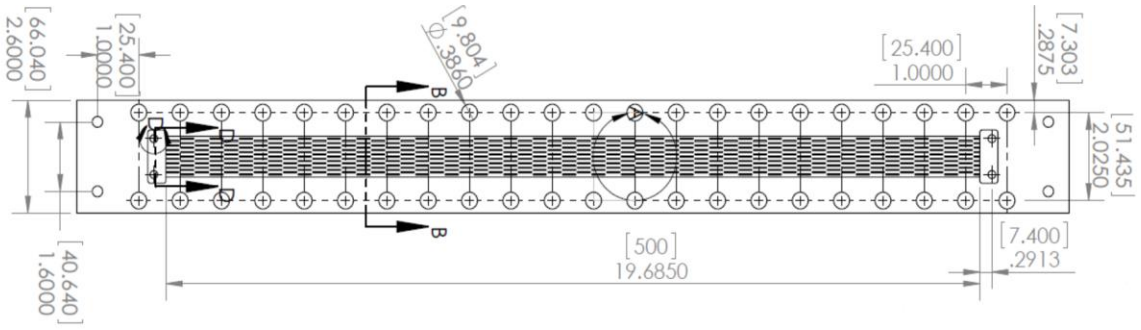

Figure 3-6: Drawing of the offset rectangular fin PCHE test plate showing inlet and outlet manifolds, bolt holes, and other relevant dimensions in inches [mm]

Two PCHE test plates were designed and fabricated; one with rectangular fins and the other one with NACA0020 airfoil fins. Detailed drawing of the offset rectangular fin PCHE test plate is presented in Figure 3-6. Figure 3-7 shows a section of the rectangular and NACA0020 airfoil PCHE test plates along with their corresponding unit cell geometry. A predetermined section of the test plates was scanned under a laser scanner with a scan resolution of 0.0127 mm to measure the geometrical parameters of the unit cell in Figure 3-7. This yielded a point could data of the test plate surfaces which could also be used as an input for the computational fluid dynamics (CFD) simulations and validation. Table 3-1 and Table 3-2 present the designed and measured geometrical parameters of the rectangular and NACA0020 airfoil PCHE test plates respectively. The differences between the designed and the actual measured surface geometries are due to the chemical etching defects such as overhang, islanding and dishing. Moreover, the chemical etching process creates characteristic rounded corners depending on the etch depth, width and the manufacturing conditions. Details of the manufacturing conditions and defects from the chemical etching process are thoroughly explained by Allen [100] and Black *et al.* [101].

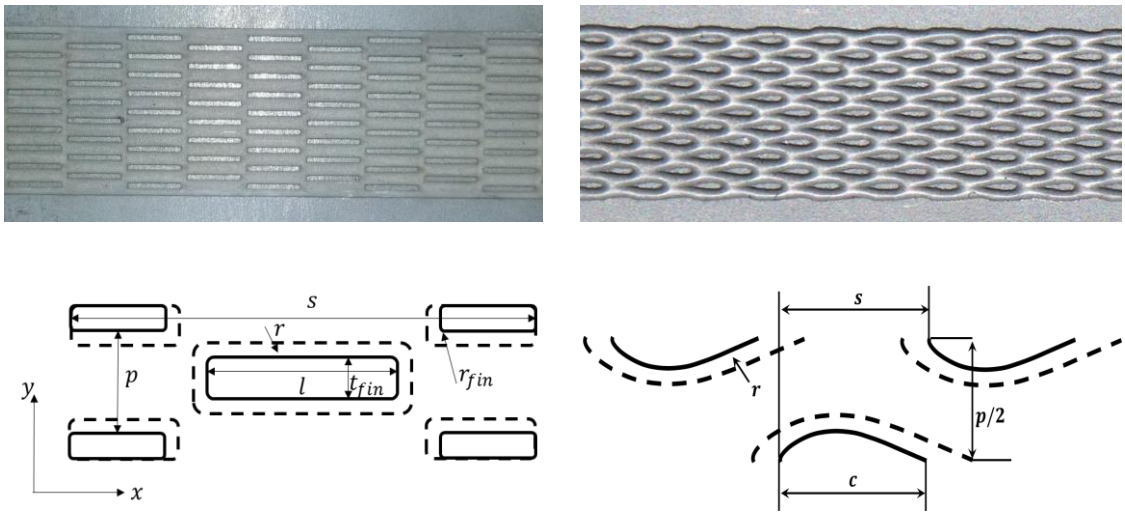

Figure 3-7: Images of a section of the rectangular fin (top left) and NACA0020 airfoil fin (top right) PCHE test plates. Unit cell representation of the rectangular fin (bottom left) and NACA0020 airfoil fin (bottom right) surface pattern. Dashed lines represent the curvature of the fins

Table 3-1: Designed and measured geometrical parameters of the rectangular fin test plate; Refer to Figure 3-7 for the nomenclature

Geometrical parameter	Designed	Measured
Fin thickness, t_{fin} (mm)	0.65	0.65
Fillet radius, r (mm)	0	0.47
Fillet radius, r_{fin} (mm)	0	0.18
Fin depth, h (mm)	0.65	0.65
Lateral pitch, p (mm)	1.95	1.95
Fin length, l (mm)	9.025	7.69
Axial pitch, s (mm)	18.05	17.68
Plate thickness, t (mm)	6.3	
Number of unit cells along length (N_x)	28	
Number of unit cells per row (N_y)	9	
Hydraulic diameter, D_h (mm)	0.9502	0.9973
Unit cell heat transfer area, A_s (mm^2)	82.01	91.133
Flow cross-sectional area, A_c (mm^2)	11.43	11.567
Measured Relative roughness	-	7.4e-3

Table 3-2: Designed and measured geometrical parameters of the NACA0020 airfoil fin test plate; Refer to Figure 3-7 for the nomenclature

Geometrical parameter	Designed	Measured
Chord width, *c* (mm)	4	3.566
Thickness/Chord length	0.2	0.202
Fillet radius, *r* (mm)	0	0.795
Fin depth, *h* (mm)	0.95	0.685
Axial pitch, *s* (mm)	3.5	3.466
Lateral pitch, *p* (mm)	3.6	3.657
Plate thickness, *t* (mm)	6.3	
Number of unit cells along length (N_x)	144	
Number of unit cells per row (N_y)	6	
Hydraulic diameter, D_h (mm)	1.205	1.112
Unit cell heat transfer area, A_s (mm^2)	30.18	24.94
Flow cross-sectional area, A_c (mm^2)	15.96	12.07
Measured Relative roughness	-	7.259e-3

The mating plate is a 316L stainless steel plate with an O-ring groove machined into the surface. The mating plate contains three holes at each end, two for temperature measurement and one for pressure measurement; refer to Figure 3-8. The PCHE test plate is bolted to the mating plate and both the surfaces are sealed using custom fabricated O-ring from 1/16" Viton fluoroelastomer cord stock that is cut to length and glued together.

The inlet and outlet temperatures to/from the test section are measured using four Omega platinum RTDs (two at each end) with an uncertainty of ±0.15 °C. The inlet pressure is measured using Meriam gage pressure transmitter (Meriam ZM1500-GI3000) with an accuracy of ±0.025% of full scale (0-3000 psig). The pressure drop across the PCHE test sections is measured using Meriam differential pressure transmitter (Meriam ZM1500-DN0415) with an accuracy of ±0.025% of full scale (0-15 psi).

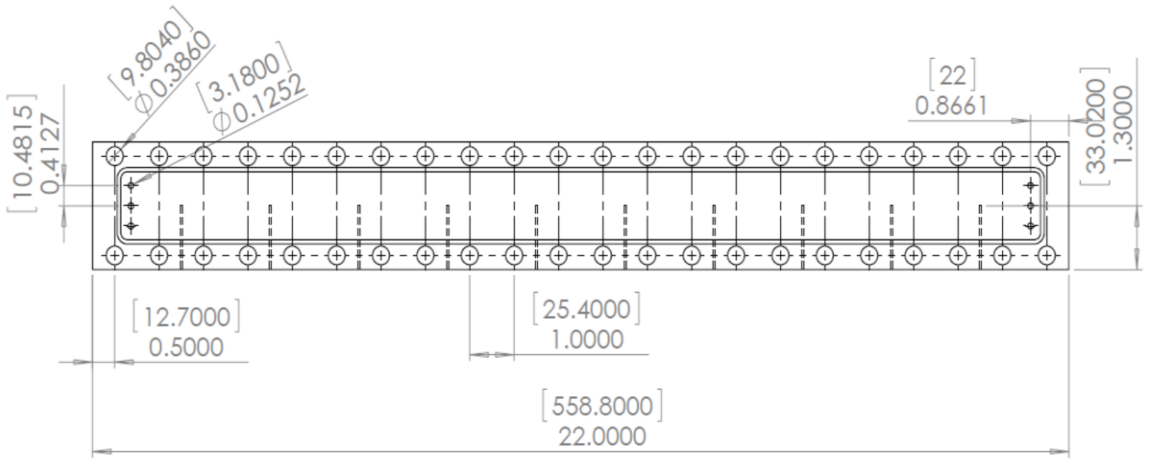

Figure 3-8: Drawing of the mating plate showing O-ring groove, bolt holes, holes for temperature and pressure measurements. The dimensions are in inches [mm]

Ten 1/16" K-type thermocouples are embedded into the side wall of the PCHE test plates and the mating plate to measure the local wall temperature. The thermocouple holes were initially machined using electrical discharge machining (EDM) process due to the large hole length to diameter ratio (L/D~33). However, the EDM process resulted in low precision for the thermocouple hole locations. Later, the thermocouple holes were machined using conventional drilling process. The drilling process was accomplished through a series of drilling operations with different diameter drill bits to meet the large L/D requirements. The location of the thermocouple holes relative to the surface is measured using coordinate measuring machine (CMM) with an accuracy of ±0.002" as shown in Figure 3-9. Thermocouple holes are filled with the conductive paste to ensure a good thermal contact and that no air gaps are present.

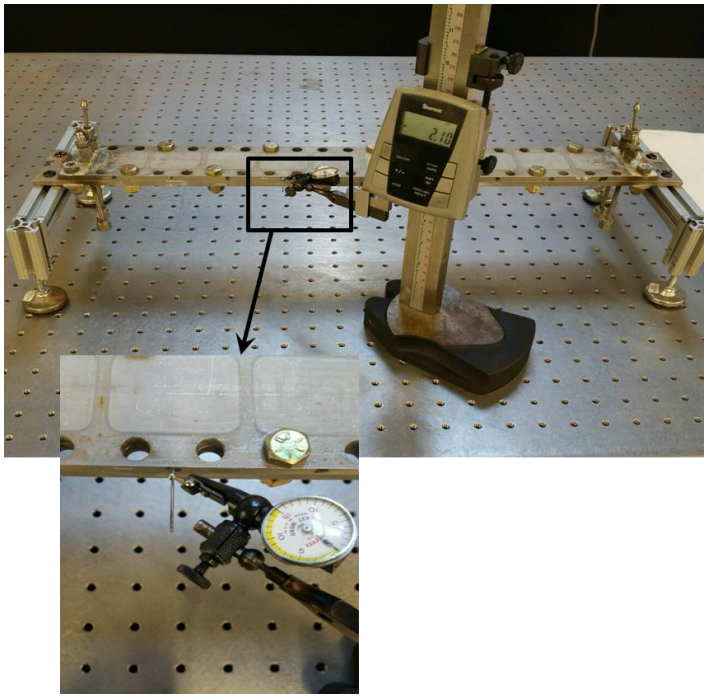

Figure 3-9: Image showing measurement of the thermocouple hole location using the coordinate measuring machine (CMM)

Attached to the top of the mating plate and the bottom of the PCHE test plate are a set of ten individual 316 stainless steel cooling blocks that are used to measure the local heat removal rate. Figure 3-10 shows the cooling block details along the flow path of water (marked as red arrows). The volumetric flow rate of water flowing to each cooling block is measured using turbine type flowmeters. Two K-type thermocouples are located at the inlet and outlet of each cooling block to measure the temperature of water entering and leaving the cooling block; refer to Figure 3-5 for the instrumentation details.

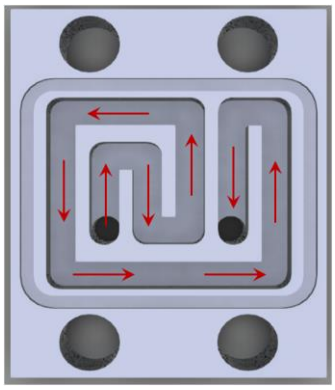

Figure 3-10: Model of the cooling block used to remove heat from the PCHE test section. The water flow path is marked as red arrows

All the water flowmeters are connected in series and the cooling water is flown through and collected into a 2000 ml graduated cylinder with an uncertainty of ±20 ml. The frequency output from the flowmeters and the time taken to fill up the cylinder were recorded. Following this procedure, a calibration curve between the frequency and flow rate were generated for each flowmeter with an overall uncertainty of ±1.5% in measurement of volumetric flow rates. To reduce the uncertainty of water temperature difference measurements, water outlet thermocouples are calibrated against the inlet thermocouples *in-situ* by flowing water through each cooling block at temperature ranging from 10-35 °C. The maximum estimated uncertainty in the measurement of water temperature difference is ±0.15 °C. Figure 3-12 shows a picture of the modified test facility with the offset rectangular fin PCHE test section installed and fully insulated.

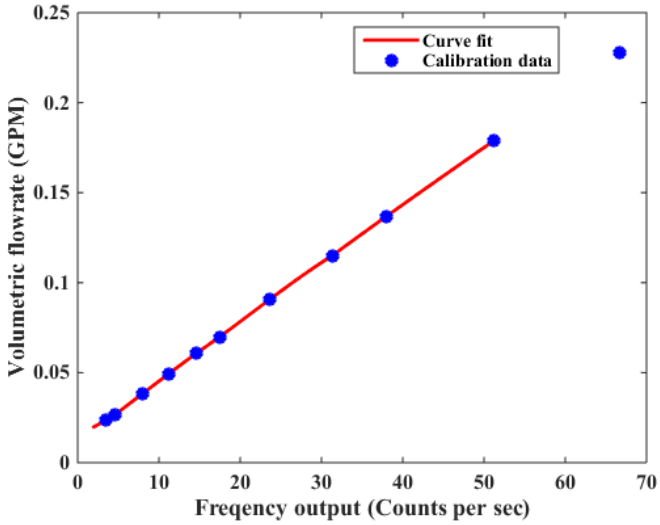

Figure 3-11: Calibration curve for one of the water flowmeters

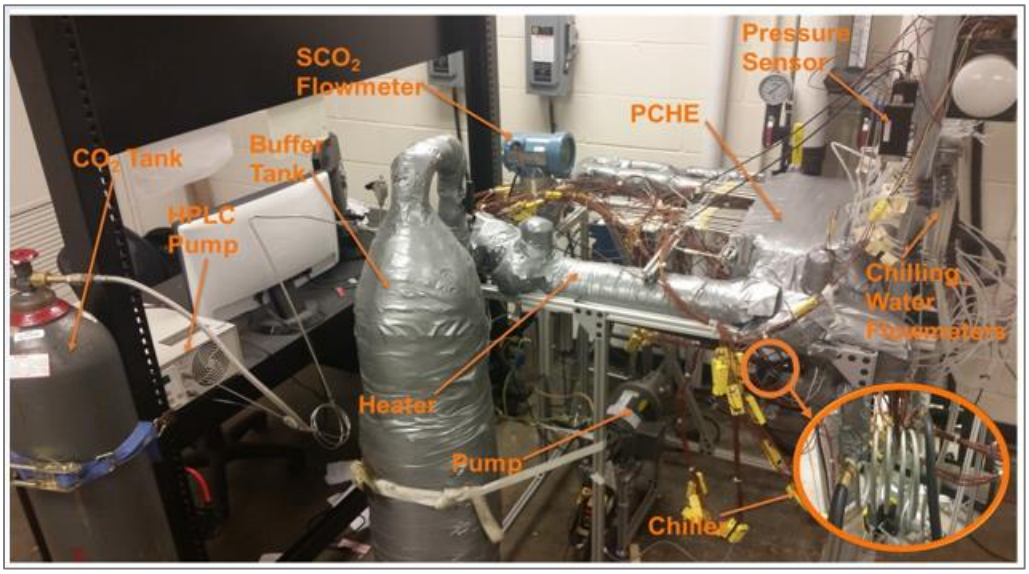

Figure 3-12: A picture of the modified experimental test loop with offset rectangular fin PCHE test section installed

CHAPTER 4. HEATED CIRCULAR TUBES DATA ANALYSIS AND RESULTS

This chapter is dedicated for data analysis, discussion of the results for flow through heated circular tubes. A series of integral experiments were conducted by changing the fluid inlet temperature, mass flow rate, heat flux and operating pressure. The fluid inlet temperature to the test sections was varied from 20 to 60 °C to cover the whole range of bulk fluid temperatures spanning the pseudocritical temperature. The mass flux was varied in the range of 100–1000 kg/m^{2}s and the heat flux was varied in the range of 10–100 kW/m^2. Three different test section orientations - horizontal, upward and downward flow were tested to investigate the effects of buoyancy. During the experiments, all the independent parameters such as test section inlet temperature, mass flow rate, pressure and heat flux were controlled and monitored. For each operating condition, the system was assumed to have achieved a steady state once the experimental parameters were constant (within the accuracy of associated instrumentation) for at least ten minutes. Once the system achieved steady state, the data was recorded for 500 seconds at the rate of 1 Hz and average of the data points was used for the data processing.

4.1 Data Reduction Procedure

4.1.1 Local heat flux

Local heat flux to the test section, $Q_i^{"}$ is calculated by discretizing the test section into multiple sub-sections as shown in Figure 4-1.

$$Q_i^{"} = \frac{Q_{PS,i} - Q_{loss,i}}{\pi D_i \Delta x_i} \tag{4.1}$$

where $Q_{PS,i}$ is the local resistive heating, $Q_{loss,i}$ is the heat loss to the ambient and D_i is the inner diameter of the test section.

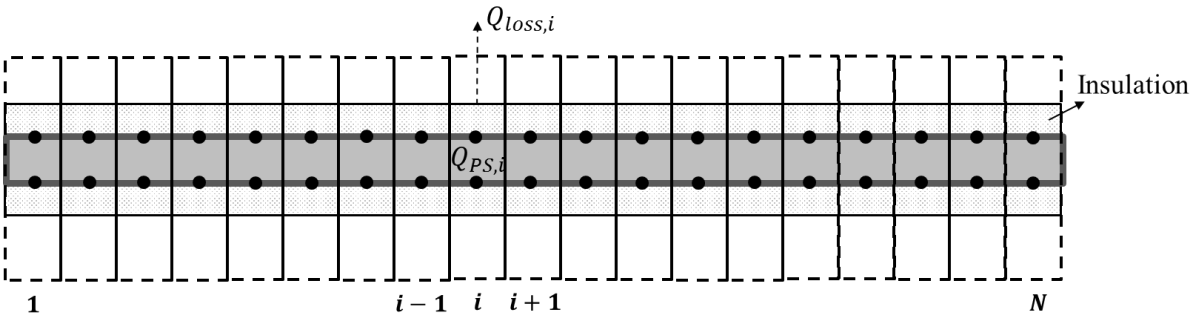

Figure 4-1: Discretization of the test section to determine local heat flux

The local resistive heating for each sub-section varies depending on the electrical resistivity, ρ. The electrical resistivity of 316 stainless steel is calculated from the local measured wall temperature using a linear curve fit to data from literature [102].

$$\rho(10^{-8}\Omega.m) = 0.0673\,T + 57.76 \tag{4.2}$$

The electrical resistance, R_i is calculated from the electrical resistivity, ρ_i and the tube dimensions as follows,

$$R_i = \frac{\rho_i \Delta x_i}{A} \tag{4.3}$$

where A is the cross-sectional area of the tube wall and Δx_i is the length of each sub-section.

The local resistive heating for each sub-section is calculated from the measured power by the DC power supply and the electrical resistance network as follows:

$$Q_{PS,i} = V_{PS} I_{Ps} \frac{R_i}{\sum_i^N R_i} \tag{4.4}$$

where V_{PS} is the voltage applied across the section by DC power supply, I_{PS} is the current flow through the test section and R_i is the local electrical resistance from Equation (4.3). For similar studies in literature, electrical resistivity (ρ) and hence, heat flux is assumed to be constant across the test section. This is only true if the test section is short or variation of the wall temperature along the tube length is small. In the present study, the variation of electrical resistivity with temperature is taken into account according to Equation (4.2). Figure 4-2 compares the heat transfer coefficients calculated assuming constant heat flux with the values calculated according to the data procedure reduction procedure described above (labelled as corrected heat flux) for one of the experimental cases. Depending on the measured wall temperatures, a deviation of up to ±10% was noted between the two methods.

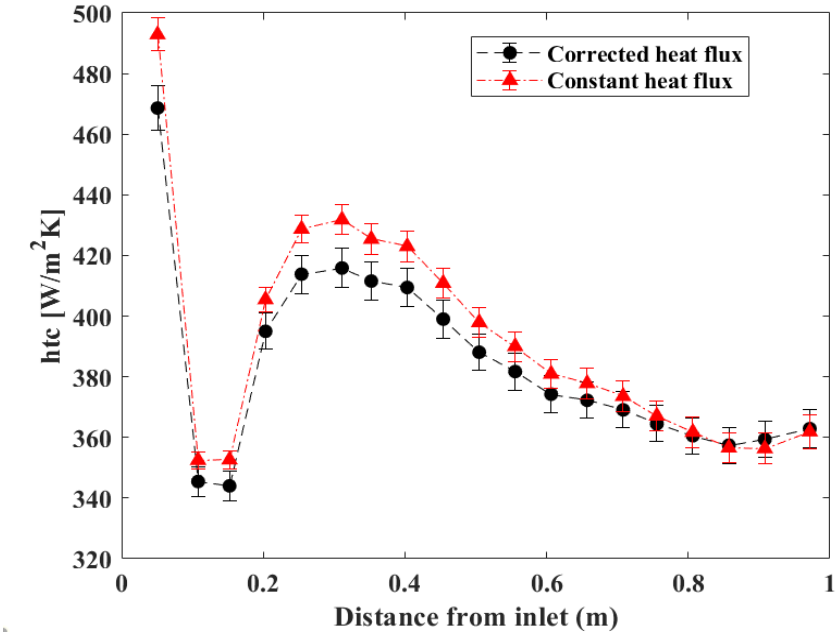

Figure 4-2: An example showing comparison of the heat transfer coefficients calculated using constant heat flux assumption and the current methodology.

4.1.2 Test section heat loss

Heat loss from the test sections to the ambient is estimated using the heat transfer resistance network shown in Figure 4-3. The ambient heat loss based on the resistance network can be expressed as,

$$Q_{loss,i} = \frac{T_{wo,i} - T_{s,i}}{R_1} = \frac{T_{s,i} - T_\infty}{R_2 + R_3} \tag{4.5}$$

The test section is wrapped with ~ 2" thick fibreglass insulation ($k_{insulation}$~0.04 W/m-K) and the conductive resistance, R_1 of the insulation is calculated as follows:

$$R_1 = \frac{\ln\left(\frac{D_{insulation}}{D_o}\right)}{2\pi k_{insulation} \Delta x_i} \tag{4.6}$$

where D_o and $D_{insulation}$ is the outer diameter of the test section and insulation respectively.

Heat transfer from the insulation to the ambient occurs through the natural convection resistance, R_2 and radiation resistance, R_3.

$$R_2 = \frac{1}{h_{air}\, \pi D_{insulation} \Delta x_i} \tag{4.7}$$

$$R_3 = \frac{1}{h_{rad}\, \pi D_{insulation} \Delta x_i} \tag{4.8}$$

The natural convection heat transfer coefficient, h_{air} is calculated using the correlation of Churchill and Chu (1975) [103].

$$h_{air} = \left(0.6 + 0.387 \frac{Ra^{\frac{1}{6}}}{\left(1+\left(\frac{0.559}{Pr_{air}}\right)^{\frac{9}{16}}\right)^{\frac{8}{27}}} \right)^2 . \frac{k_{air}}{D_{insulation}} \quad (4.9)$$

where Ra is the Rayleigh number and is defined as follows:

$$Ra = \frac{g\beta_{air}(T_s - T_\infty)D_{insulation}^3 \rho_{air}^2 Pr_{air}}{\mu_{air}^2} \quad (4.10)$$

where g is the acceleration due to gravity, β_{air} is the coefficient of thermal expansion of air. The air properties such as ρ, Pr, μ are evaluated at the average of the insulation surface temperature and the ambient temperature, $T_{air} = (T_{s,i} + T_\infty)/2$.

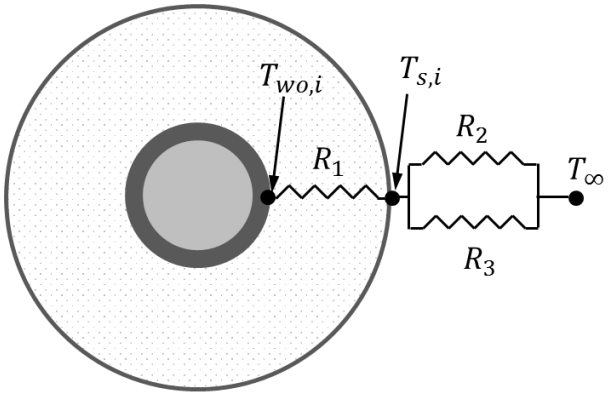

R_1 = Insulation resistance
R_2 = Natural convection resistance
R_3 = Radiation resistance

Figure 4-3: Resistance network for the test section heat loss analysis

The radiative heat transfer coefficient, h_{rad} is evaluated as follows:

$$h_{rad} = \sigma\varepsilon(T_s^2 + T_\infty^2)(T_s + T_\infty) \quad (4.11)$$

In Equation (4.11), the emissivity of Fiberglass insulation is assumed as 0.85. A conservative error of 50% is used for the heat loss for uncertainty analysis.

4.1.3 Wall temperature

Local inner wall temperatures ($T_{wi,i}$) are calculated from the measured outer wall temperatures ($T_{wo,i}$) by using a one-dimensional, steady-state conduction equation.

$$T_{wi,i} = T_{wo,i} + \frac{\dot{q}_i}{4k_{ss316}}\left[\left(\frac{D_o}{2}\right)^2 - \left(\frac{D_i}{2}\right)^2\right] - \frac{\dot{q}_i}{2k_{ss316}}\left(\frac{D_o}{2}\right)^2 \ln\left(\frac{D_o}{D_i}\right) \tag{4.12}$$

where $\dot{q}_\iota$ is the local volumetric heat generation (W/m^3) expressed as,

$$\dot{q}_\iota = \frac{Q_{PS,i}}{\left[\frac{\pi}{4}(D_o^2 - D_i^2)\Delta x_i\right]} \tag{4.13}$$

4.1.4 Bulk fluid temperature

The local bulk fluid enthalpy at the exit of each sub-section in Figure 4-1 was obtained by performing energy balance on the differential control volume.

$$i_{i+1} = i_i + \frac{Q_{PS,i} - Q_{loss,i}}{\dot{m}_{CO_2}} \tag{4.14}$$

The local average bulk fluid temperature, $T_{b,i}$ and other state-dependent thermophysical properties are determined based on average enthalpy and pressure for each subsection. All the fluid properties are calculated using the NIST REFPROP v9.1 [104].

4.1.5 Heat transfer coefficient and Nusselt number

The local heat flux, inner wall temperature and the bulk fluid temperature are used to calculate the local heat transfer coefficient and the Nusselt number as described below:

$$htc_i = \frac{Q_i^{"}}{(T_{wi,i} - T_{b,i})} \tag{4.15}$$

$$Nu_{b,i} = htc_i . \frac{D_i}{k_{b,i}} \tag{4.16}$$

4.2 Uncertainty Analysis

Uncertainty in the local heat transfer coefficient and the Nusselt number is estimated through the error propagation method of Kline and McClintock [105]. The method is described below in the generalized form:

$$R = R(X_1, X_2, \dots, X_N) \tag{4.17}$$

$$\sigma_R = \left[\sum_{i=1}^{N} \left(\frac{\partial R}{\partial X_1}\sigma_{X_1}\right)^2\right]^{0.5} \tag{4.18}$$

Uncertainty in the calculated local heat flux is calculated from Equation (4.19).

$$\frac{\sigma_{Q"}}{Q"} = \left[\left(\frac{\sigma_{V_{PS}}}{V_{PS}}\right)^2 + \left(\frac{\sigma_{I_{PS}}}{I_{PS}}\right)^2\right]^{0.5} \tag{4.19}$$

Uncertainty in the calculated inner wall temperature is expressed as follows:

$$\sigma_{T_{wi}} = \left[\sigma_{T_{wo}}^2 + \left(\frac{T_{wi} - T_{wo}}{\dot{q}}\sigma_{\dot{q}}\right)^2 + \left(\frac{T_{wi} - T_{wo}}{k_{ss316}}\sigma_{k_{ss316}}\right)^2\right]^{0.5} \tag{4.20}$$

$$\frac{\sigma_{\dot{q}}}{\dot{q}} = \left[\left(\frac{\sigma_{V_{PS}}}{V_{PS}}\right)^2 + \left(\frac{\sigma_{I_{PS}}}{I_{PS}}\right)^2\right]^{0.5} \tag{4.21}$$

Uncertainty in the local fluid enthalpy and bulk fluid temperature are calculated from Equation (4.22) and (4.23) respectively.

$$\sigma_{i_{i+1}}^2 = \sigma_{i_i}^2 + \left(\frac{i_{i+1} - i_i}{Q_{PS,i} - Q_{loss,i}}\sigma_{Q_{PS,i}}\right)^2 + \left(\frac{i_{i+1} - i_i}{Q_{PS,i} - Q_{loss,i}}\sigma_{Q_{loss},i}\right)^2 + \left(\frac{i_{i+1} - i_i}{\dot{m}_{CO_2}}\sigma_{\dot{m}_{CO_2}}\right)^2 \tag{4.22}$$

$$\sigma_{i_b} = 0.5(\sigma_{i+1}^2 + \sigma_i^2)^{0.5}$$

$$\sigma_{T_b} = \left[\left(\frac{\partial T_b}{\partial i_b}\right)^2 \sigma_{i_b}^2 + \left(\frac{\partial T_b}{\partial P_b}\right)^2 \sigma_{P_b}^2\right]^{0.5} \tag{4.23}$$

Uncertainty in the inlet fluid enthalpy is calculated as follows:

$$\sigma_{i_{in}} = \left[\left(\frac{\partial i_{in}}{\partial P_{in}}\sigma_{P_{in}}\right)^2 + \left(\frac{\partial i_{in}}{\partial T_{in}}\sigma_{T_{in}}\right)^2\right]^{0.5} \tag{4.24}$$

$$\frac{\partial i_{in}}{\partial T_{in}} = \frac{i(T_{in}+\sigma_{T_{in}},P_{in}) - i(T_{in}-\sigma_{T_{in}},P_{in})}{2\sigma_{T_{in}}}$$

$$\frac{\partial i_{in}}{\partial P_{in}} = \frac{i(T_{in},P_{in}+\sigma_{P_{in}}) - i(T_{in},P_{in}+\sigma_{P_{in}})}{2\sigma_{P_{in}}}$$

The pressure drop across the test section is not measured during the experiments. Therefore, the pressure drops and consequently the bulk fluid pressures are estimated by making assumptions. The friction factor correlation of Kirillov *et al.* (1990) [106] is used to calculate the frictional pressure drop. The correlation of Kirillov *et al.* (1990) is valid for normal, enhanced and deteriorated flow regimes. A conservative error of 50% is assumed for the calculated pressure drop, ΔP.

$$P_b = P_{in} - \Delta P \tag{4.25}$$

$$\Delta P = \Delta P_f + \Delta P_{acc} + \Delta P_{gravity}$$

$$\Delta P_f = f.\left(\frac{x}{D_i}\right)\left(\frac{G^2}{2\rho_b}\right); f = \left(\frac{1}{(1.82\log_{10} Re_b - 1.64)^2}\right)\left(\frac{\rho_w}{\rho_b}\right)^{0.4}$$

$$\Delta P_{acc} = G^2\left(\frac{1}{\rho_b} - \frac{1}{\rho_{in}}\right)$$

$$\Delta P_{gravity} = \pm g\left(\frac{\rho_{in}+\rho_b}{2}\right) x.sin\theta$$

Where, θ is the test section angle with respect to horizontal. In the above equation, $+$ sign indicates upward flow and $-$ sign indicates downward flow.

Uncertainty in the bulk fluid pressure is then estimated as,

$$\sigma_{P_b} = \left[\sigma_{P_{in}}^2 + \sigma_{\Delta P}^2\right]^{0.5} \tag{4.26}$$

Finally, uncertainty in the measurement of heat transfer coefficient and the Nusselt number can be expressed as follows:

$$\frac{\sigma_{htc}}{htc} = \left[\left(\frac{\sigma_{Q"}}{Q"}\right)^2 + \left(\frac{\sigma_{T_{wi}}}{T_{wi}-T_b}\right)^2 + \left(\frac{\sigma_{T_b}}{T_{wi}-T_b}\right)^2\right]^{0.5} \tag{4.27}$$

$$\frac{\sigma_{Nu}}{Nu} = \left[\left(\frac{\sigma_{htc}}{htc}\right)^2 + \left(\frac{\sigma_{k_b}}{k_b}\right)^2\right]^{0.5} \tag{4.28}$$

4.3 Results and Discussion

This section explains the effect of different experimental parameters on the measured wall temperatures and the heat transfer coefficients by presenting the results for select experimental cases. Table 4-1 shows the average heat transfer coefficient uncertainties for both the circular tube test sections; Refer to Figure 3-2 and Figure 3-3 for details of the test sections. An example of the data reduction and the uncertainty calculations for the smaller circular tube test section is presented in APPENDIX C. Higher average uncertainties for the smaller diameter test section can be attributed to the higher heat transfer coefficients in the smaller diameter test section. Higher heat transfer coefficients result in smaller difference between the wall temperature (T_w) and the bulk fluid temperature (T_b) increasing the uncertainty in measurement of $T_w - T_b$. The

maximum heat transfer coefficient uncertainties occurred in the vicinity of pseudocritical temperature (T_{pc}), especially for low heat flux and high mass flux conditions resulting in smaller $T_w - T_b$.

Table 4-1: Average heat transfer coefficient uncertainties for both the circular tube test sections

Test Section	Flow configuration	Number of data points	Average htc uncertainty (%)
Larger circular tube (ID = 10.9 mm)	Upward	650	±4.6%
	Downward	770	±6.5%
	Horizontal	640	±4.6%
Smaller test section (ID = 7.9 mm)	Upward	836	±6.0%
	Downward	798	±8.5%
	Horizontal	1178	±8.2%

4.3.1 Effect of operating pressure

The effect of pressure on heat transfer was investigated by comparing the test results for downward flow in the larger circular tube test section (ID = 10.9 mm) at three different pressures, 7.5, 8.1 and 10.2 MPa, for a mass flux of 195 kg/m^{2}s and a heat flux of 13.5 kW/m^2. The heat transfer coefficients are plotted as a function of the bulk fluid temperature in Figure 4-4.

For all the pressures, the heat transfer coefficients exhibited a peak value in the vicinity of pseudocritical temperature, marked as dashed vertical lines in Figure 4-4. The pseudocritical temperatures for the three pressures under consideration are also listed in

Table 4-2. For example, at P/P_c = 1.015, the measured heat transfer coefficient at T_b = 23.5 °C is 2072.4±199 W/m^2-K whereas the heat transfer coefficient increases to 4435±893.7 W/m^2-K at T_b = 31.35 °C (~2.1x increase compared to the value at T_b = 23.5 °C). The peak value of heat transfer coefficient decreased with increase in pressure. From Figure 4-4, the peak value of heat transfer coefficient at P/P_c = 1.015 is 4435±893.7 W/m^2-K whereas the peak value decreases to 2065.3±199.2 W/m^2-K at P/P_c = 1.38 (~2.15x decrease compared to the value at P/P_c = 1.015). As described in CHAPTER 2, this dependence of heat transfer coefficient on the pressure and temperature can be attributed to the variation of isobaric specific heat and Prandtl number; see Figure 1-2 for example. These results were also observed to be true for upward and downward flow configuration, provided that the mass flux is sufficiently high relative to the heat flux, and the buoyancy effects and thermal-bulk flow acceleration effects are negligible.

Table 4-2: Pseudocritical temperatures for different pressures under consideration

Pressure (MPa)	Normalized pressure (P/P_c)	Pseudocritical temperature (°C)
7.5	1.015	31.75
8.1	1.096	35.2
10.2	1.38	45.96

As described in CHAPTER 2, under certain conditions buoyancy and thermal bulk-flow acceleration can have a strong influence on the heat transfer. To understand the effect of pressure on heat transfer deterioration the three experimental cases listed in Table 4-3 were selected. The variation of measured wall temperatures and heat transfer coefficients along the test section length are plotted in Figure 4-5 for these three cases. A peak in the measured wall temperature and strong heat transfer deterioration is observed for all three pressures.

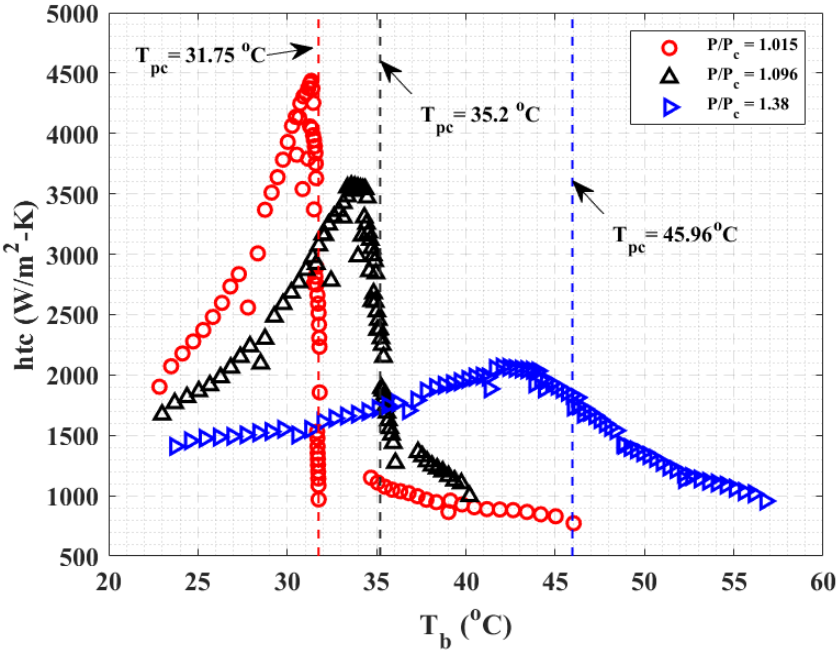

Figure 4-4: Effect of operating pressure on the heat transfer coefficients in the downward flow configuration; ID=10.9 mm, Q" = 13.5 kW/m^2, G = 195 kg/m^{2}s

The heat transfer deterioration is stronger for higher pressures in this particular case. For example, at P/P_c = 1.015, the peak in wall temperature occurred at x≈0.38 m and the measured heat transfer coefficient at this location is 917.7±23.8 W/m^2-K; whereas the measured heat transfer coefficient at the location of deterioration is 875.9±21.8 W/m^2-K for P/P_c = 1.096 (at x≈0.38 m) and 749.5±16.5 W/m^2-K for P/P_c = 1.38 (at x≈0.46 m).

Table 4-3: Experimental parameters for the selected cases to describe the effect of operating pressure on heat transfer deterioration

Case ID	P/P_c	T_{in} (°C)	ID (mm)	Q" (kW/m^2)	G (kg/m^2)	Flow orientation
Case 1	1.015	20	10.9	24	320	Upward
Case 2	1.096	20				
Case 3	1.38	25				

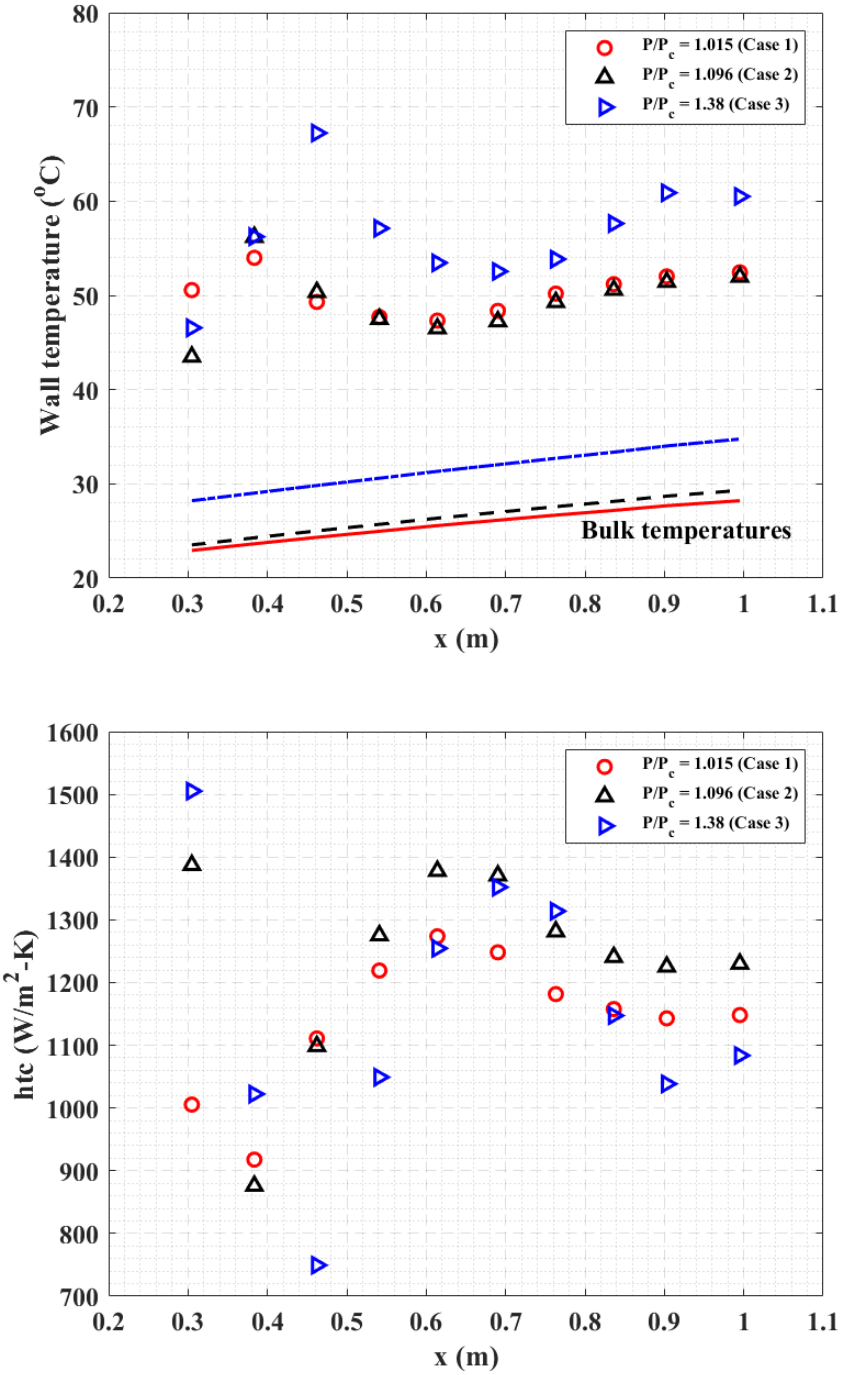

Figure 4-5: Effect of pressure on the measured wall temperatures (top) and the heat transfer coefficients (bottom) for the upward flow configuration. Experimental conditions for the three cases are listed in Table 4-3

To study the influence of buoyancy and thermal bulk-flow acceleration on the heat transfer the buoyancy parameter, Bo of Hall and Jackson (1969) from Equation (2.5) and

thermal-bulk flow acceleration parameter, A_{c_b} of Jackson (2013) from Equation (2.13) were selected. The variation of these two parameters along the test section length is presented in Figure 4-6 for the three experimental cases from Table 4-3. The Buoyancy parameter, Bo is greater than the recommended threshold value of 10^{-5} for all the cases indicating strong influence of buoyancy on the heat transfer. Interestingly, though the values of Bo are higher for the lower-pressure case (P/P_c = 1.015), the heat transfer deterioration is stronger for the higher-pressure case (P/P_c = 1.38). Therefore, higher Bo values don't necessarily result in lower heat transfer coefficients. In fact, for sufficiently high values of Bo the heat transfer is dominated by natural convection and the heat transfer coefficients can be greater than the corresponding forced convective heat transfer coefficients under identical conditions.

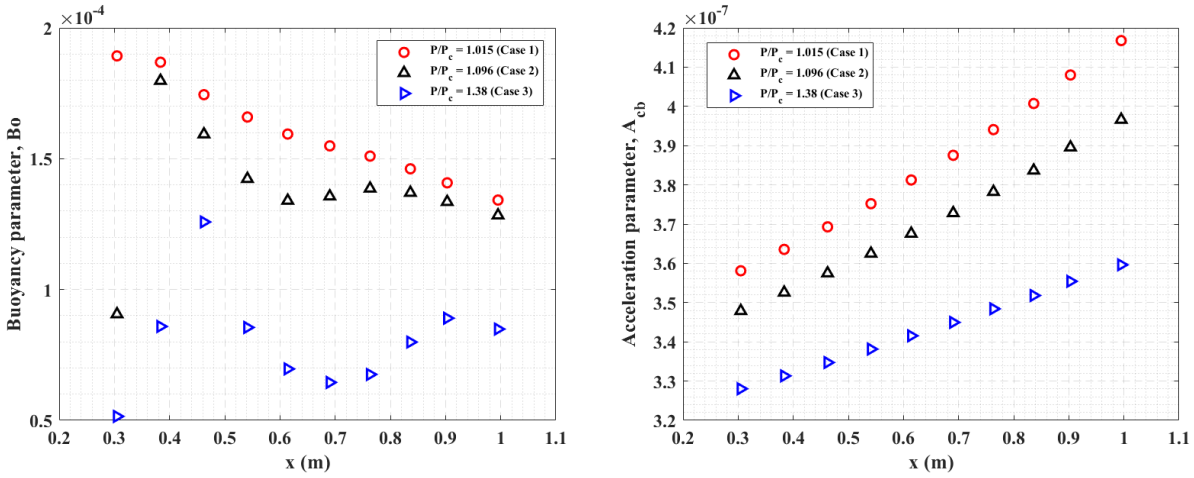

Figure 4-6: Effect of pressure on the Buoyancy parameter, Bo (left) and the thermal bulk-flow acceleration parameter, A_{c_b} (right) for the upward flow configuration. Experimental conditions for the three cases are listed in Table 4-3

The thermal-bulk flow acceleration parameter, A_{c_b} is lower than the recommended threshold value of $4\text{x}10^{-6}$ for all three pressures. This indicates that the thermal-bulk flow

acceleration doesn't have a significant influence on the heat transfer for the experimental conditions listed in Table 4-3.

4.3.2 Effect of flow orientation

The effect of flow orientation on heat transfer was investigated by comparing the test results for upward, downward and horizontal flows in the smaller circular tube test section (ID = 7.9 mm) at a pressure of 7.5 MPa and inlet temperature of 20 °C, for a mass flux of 320 kg/m^{2}s, a heat flux of 13.5 kW/m^2. The variation of the measured wall temperatures and the heat transfer coefficients along the length of the test section is presented in Figure 4-7. In the case of upward flow, localized peak in the wall temperature and heat transfer deterioration followed by recovery in heat transfer was observed due to the influence of buoyancy force as described in Section 2.1.4. In the case of downward flow, the wall temperatures are significantly lower, and the heat transfer coefficients are significantly higher than the corresponding values for upward flow. Unlike the upward flow, the wall temperature profile for the downward flow do not exhibit any localized peaks. In the case of horizontal flow, the wall temperatures on the top side of the tube are higher than the bottom side of the tube, indicating presence of a circumferential variation in the wall temperature. This is consistent with prior observations from literature; Refer to Section 2.1.4 for more details. The circumferential variation in the wall temperature was found to be more pronounced at low mass flux, high heat flux conditions and will be described in the subsequent sections. The circumferential and axial variation in the wall temperature will result in circumferential and axial conductive heat transfer. The axial and circumferential conductive heat transfer components are computed using a rough order of magnitude analysis, as described in APPENDIX D. For the representative case from

APPENDIX C, the total circumferential and axial conductive heat transfer is ~2.3% of the total resistive heat input from DC power supply. For all the cases, the total circumferential and axial conductive heat transfer contributed to <5% of the total resistive heat input.

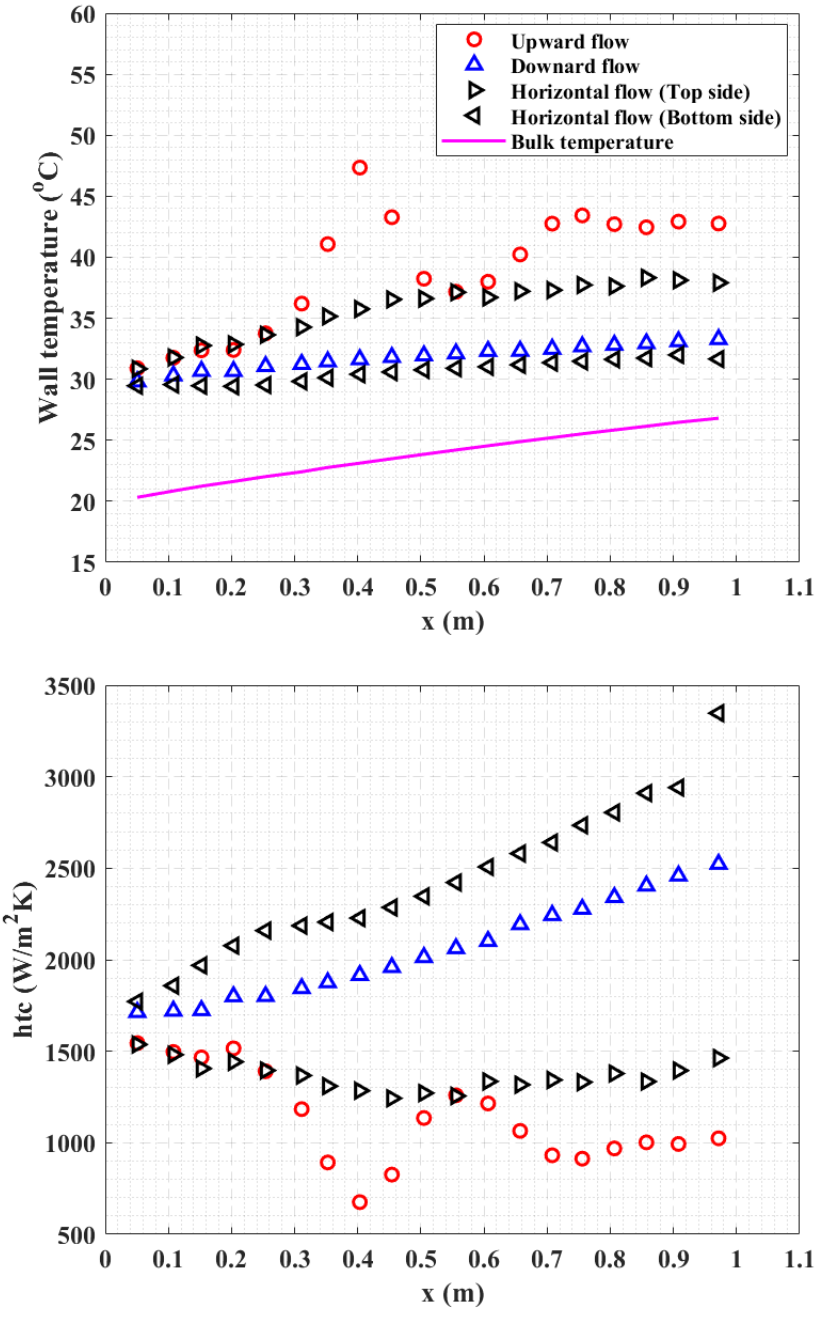

Figure 4-7: Effect of flow orientation on the measured wall temperatures and the heat transfer coefficients for flow in the smaller diameter tube (ID = 7.9 mm); P = 7.5 MPa, T_{in} = 20 °C, Q" = 13.5 kW/m^2, G = 320 kg/m^{2}s

Based on the above discussion, the flow orientation has a significant influence on the heat transfer. For example, at the location of peak in wall temperature for upward flow (x≈0.4 m) the measured heat transfer coefficient is 675.8±21.5 W/m^2-K. At the same location the measured heat transfer coefficient for downward flow is 1915.3±164.9 W/m^2-K and for horizontal flow it is 1284.7±103.8 W/m^2-K (based on the top side wall temperature), 2227.7±310.5 W/m^2-K (based on the bottom side wall temperature). The circumferential average heat transfer coefficient for the horizontal flow is calculated based on the average of the top and the bottom side wall temperatures. The circumferential average heat transfer coefficient for the horizontal flow at x≈0.4 m is 1629.6±119.7 W/m^2-K for this case.

4.3.3 Effect of heat flux

The effect of heat flux on heat transfer was investigated by comparing the test results for cases shown in Table 4-4. For the upward flow orientation, the variation of the measured wall temperature profiles and the heat transfer coefficient along the length of the test section is presented in Figure 4-8. The peak in wall temperature moved towards the test section inlet as the heat flux is increased. For example, at Q'' = 13.5 kW/m^2, the peak in wall temperature occurred at x≈0.4 m; whereas the peak moved to x≈0.1 m for Q'' = 40 kW/m^2. For the highest value of heat flux (Q'' = 62.5 kW/m^2), the sharp localized wall temperature peak occurred at the inlet and at x≈0.55 m, the wall temperature profile changes slope as the fluid temperature exceeds the pseudocritical temperature. It is interesting to note that at certain locations along the test section, heat transfer deterioration is stronger for lower heat fluxes. For example, at x≈0.4 m, the heat transfer coefficient for

Q" = 13.5 kW/m^2 is 675.8±21.5 W/m^2-K but the value increases to 769.6±12 W/m^2-K for Q" = 40 kW/m^2 and to 1274.8±20.3 W/m^2-K for Q" = 62.5 kW/m^2.

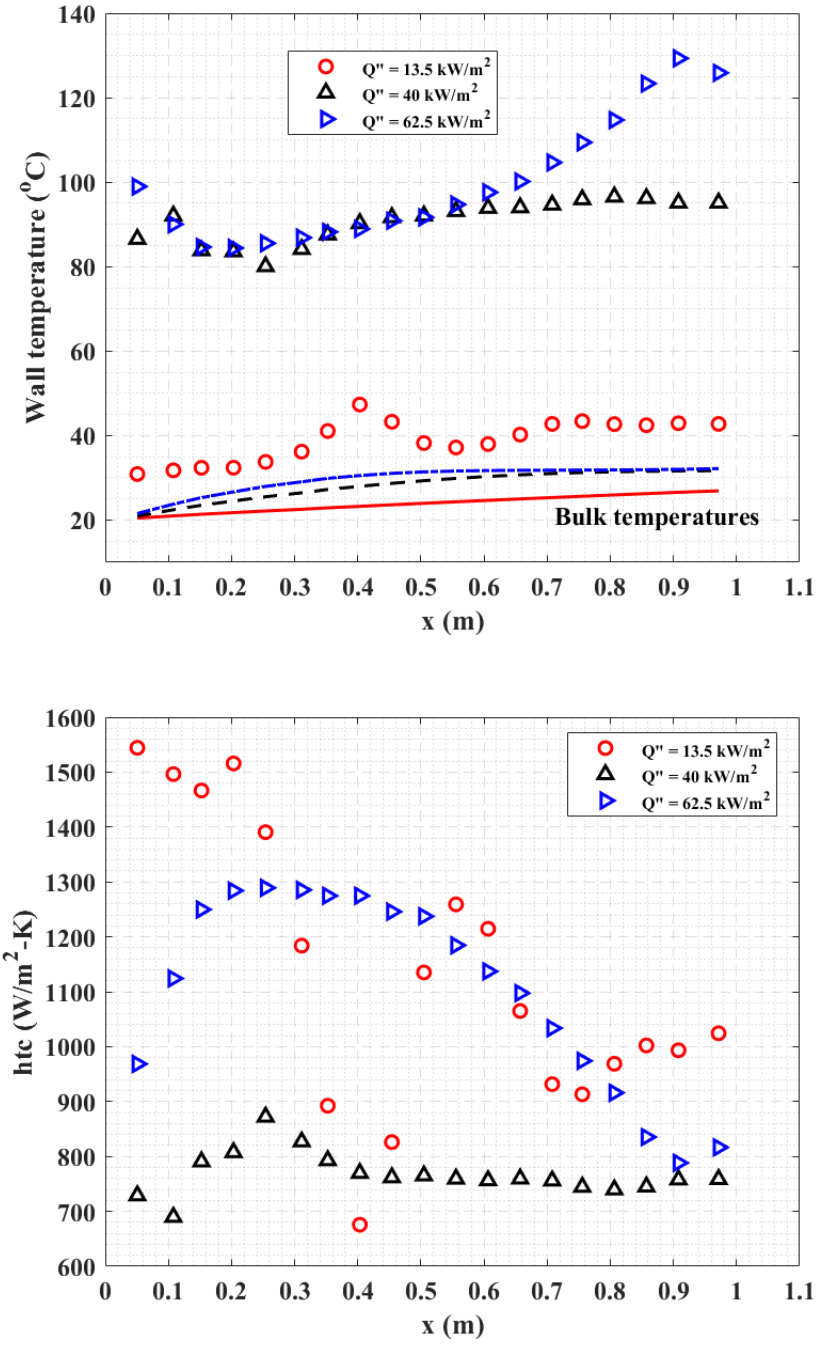

Figure 4-8: Effect of heat flux on the measured wall temperatures (top) and the heat transfer coefficients (bottom) for the upward flow configuration. Experimental conditions are listed in Table 4-4

Table 4-4: Experimental parameters for the selected cases to describe the effect of heat flux

ID (mm)	P (MPa)	T_{in} (°C)	Q" (kW/m^2)	G (kg/m^2)	Flow orientation
7.9	7.5	20	13.5	320	Upward, Horizontal
			40.0		
			62.5		

The variation of the buoyancy parameter, Bo and the thermal bulk-flow acceleration parameter, A_{c_b} along the test section length is presented in Figure 4-9 for the data points corresponding to Figure 4-8. The Bo values are greater than the recommended threshold value of 10^{-5} for all the data points. For some data points, higher values of Bo lead to lower heat transfer coefficients; see data at x≈0.4 m for example. However, at some locations trend in Bo don't correspond to the trend in heat transfer coefficients indicating influence of other properties variations.

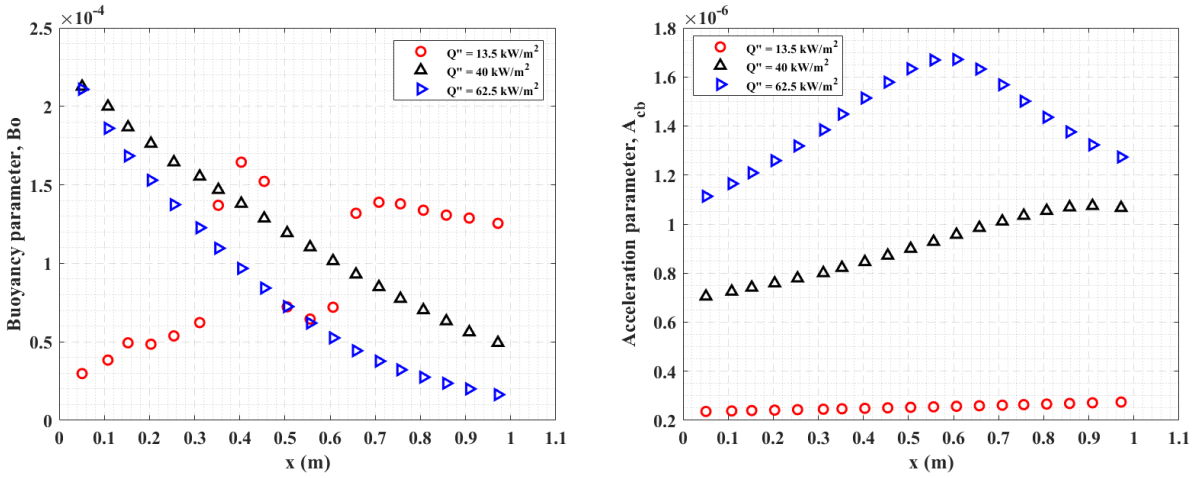

Figure 4-9: Effect of heat flux on the Buoyancy parameter, Bo (left) and the thermal bulk-flow acceleration parameter, A_{c_b} (right) for the upward flow configuration. Experimental conditions are listed in Table 4-4

The value of A_{c_b} is less than the recommended threshold value of $4x10^{-6}$ for all the data points. For the highest value of heat flux ($Q"$ = 62.5 kW/m^2), A_{c_b} reached a maximum value of ~$1.7x10^{-6}$ where the fluid temperature just exceeds the pseudocritical temperature.

Figure 4-10 presents variation of downward flow heat transfer coefficients versus the bulk fluid temperatures for different levels of heat flux. The peak value of heat transfer coefficient in the vicinity of pseudocritical temperature decreased with increase in heat flux. For example, at $Q"$ = 13.5 kW/m^2 the peak measured value of the heat transfer coefficient is 4628±944 W/m^2-K for T_b = 31.32 °C; the peak value decreased to 2084.5±68.1 W/m^2-K for $Q"$ = 40 kW/m^2 and to 1563±28.2 W/m^2-K for $Q"$ = 62.5 kW/m^2. As the heat flux increases, the region of maximum specific heat moves away from the boundary layer making it is easier to overcome the region of highest specific heat. In other words, the integrated value of specific heat, $\overline{C_{p,b}} = \frac{i_w - i_b}{T_w - T_b}$ decrease near the pseudocritical region, causing a reduction in enhancement of the heat transfer. For temperatures farther away from the pseudocritical temperature (e.g., T_b > 50 °C), the heat transfer coefficients tend to become independent of the heat flux which is typical of an ideal-gas behavior.

The variation of the measured local average wall temperatures, temperature difference between the top and the bottom sides (ΔT_w) and the circumferential averaged heat transfer coefficients along the test section length for horizontal flow are plotted in Figure 4-11; Refer to Table 4-4 for the experimental conditions for these cases.

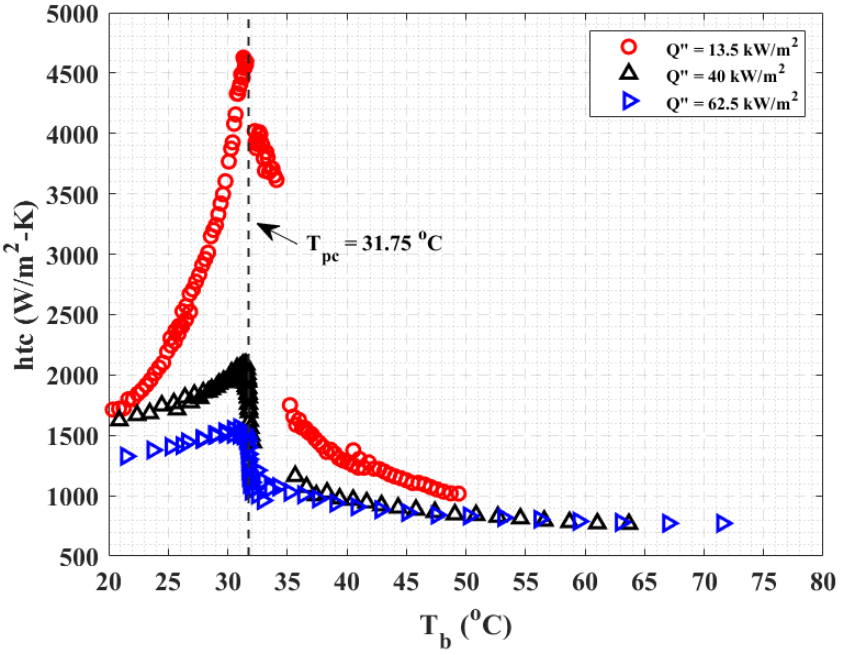

Figure 4-10: Effect of heat flux on the heat transfer coefficients in the downward flow configuration; ID = 7.9 mm, G = 320 kg/m^{2}s, P = 7.5 MPa

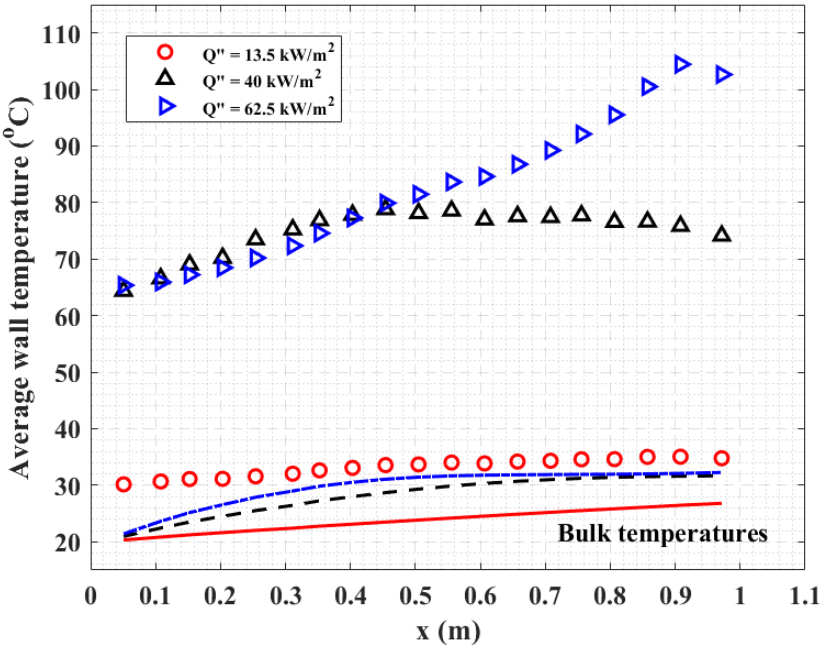

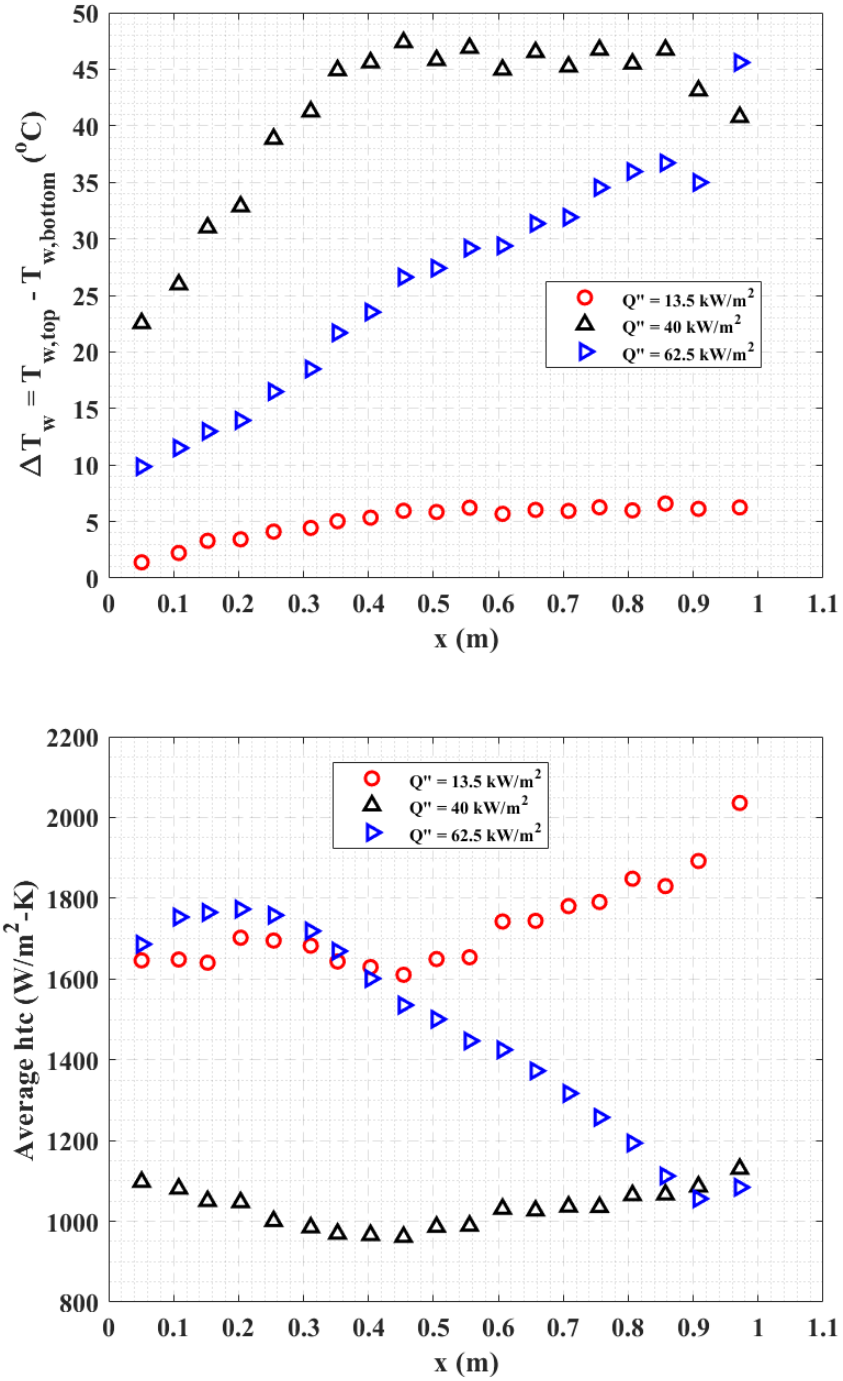

Figure 4-11: Effect of heat flux on the measured local average wall temperatures (top), ΔT_w (middle) and the local average heat transfer coefficients (bottom) for the horizontal flow configuration. Experimental conditions are listed in Table 4-4

The local average wall temperature and ΔT_w generally increased with the heat flux and correspondingly the average heat transfer coefficient decreases with increase in heat

flux. However, depending on the bulk fluid temperature, heat transfer coefficients can be higher for higher heat fluxes. For example, in Figure 4-11, for $Q"$ = 40 kW/m^2 the average heat transfer coefficient at x≈0.45 m is 961.3±16.9 W/m^2-K, T_b = 28.7 °C and ΔT_w = 47.4 °C. At the same location (x≈0.45 m), the average heat transfer coefficient increased to 1535.3±27.2 W/m^2-K for $Q"$ = 62.5 kW/m^2, T_b = 31.1 °C and ΔT_w = 26.6 °C. However, towards the outlet of the test section where the bulk temperature reaches the pseudocritical temperature for both the heat fluxes ($Q"$ = 40 and 62.5 kW/m^2), the average heat transfer coefficients and ΔT_w tend to approach each other. For the highest heat flux ($Q"$ = 62.5 kW/m^2) the bulk fluid temperature approaches the pseudocritical temperature much earlier and the average wall temperature increased continuously along the tube length unlike the wall temperature profile for $Q"$ = 40 kW/m^2; where a near constant average wall temperature was recorded for a section of the tube. This is also the case for lowest value of heat flux ($Q"$ = 13.5 kW/m^2) even though the bulk fluid temperature is less than the pseudocritical temperature at all locations. Therefore, it can be concluded that if $T_b < T_{pc}$ at all locations along the tube, the average wall temperature and ΔT_w attain a constant value along a section of the tube. This situation appears to be similar to pre-critical and post-critical heat flux scenarios at subcritical pressures.

4.3.4 Effect of mass flux

The effect of mass flux on heat transfer was investigated by comparing the test results for cases shown in Table 4-5. For the upward flow orientation, the variation of the measured wall temperature profiles and the heat transfer coefficients along the length of the test section is presented in Figure 4-12.

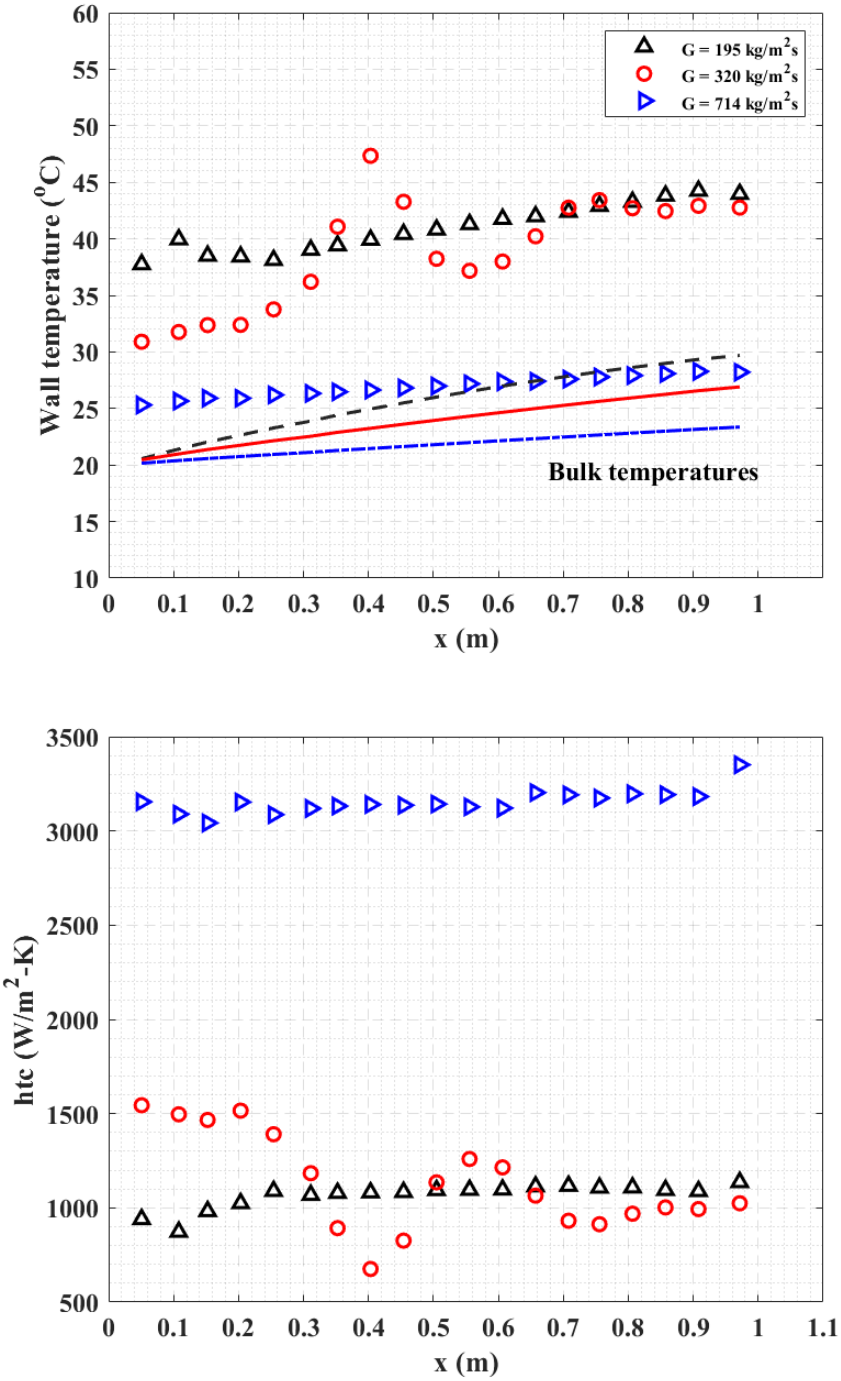

Figure 4-12: Effect of mass flux on the measured wall temperatures (top) and the heat transfer coefficients (bottom) for the upward flow configuration. Experimental conditions are listed in Table 4-5

It appears that the peak in wall temperature tend to move towards the test section outlet as the mass flux increases. For example, at G = 320 kg/m^{2}s, the peak in wall

temperature occurred at x≈0.4 m; whereas the peak moved to x≈0.1 m for G = 195 kg/m^{2}s. For the highest value of mass flux (G = 714 kg/m^{2}s), there is no evidence of localized wall temperature peak and the heat transfer coefficient is nearly constant along the tube. It is interesting to note that at certain locations along the test section, heat transfer deterioration is stronger for higher mass fluxes. For example, at x≈0.4 m, the heat transfer coefficient for G = 320 kg/m^{2}s is 675.8±21.5 W/m^2-K (Re≈37,180 and Pr≈2.78) but the value increases to 1081.6±53.3 for G = 195 kg/m^{2}s (Re≈23,735 and Pr≈3).

Table 4-5: Experimental parameters for the selected cases to describe the effect of mass flux

ID (mm)	P (MPa)	T_{in} (°C)	Q'' (kW/m^2)	G (kg/m^2)	Flow orientation
7.9	7.5	20	13.5	195	Upward, Downward, Horizontal
				320	
				714	

The variation of the buoyancy parameter, Bo and the thermal bulk-flow acceleration parameter, A_{c_b} along the test section length is presented in Figure 4-13 for the data points corresponding to Figure 4-12. The values of Bo are higher than the recommended threshold value of 10^{-5} for mass fluxes of 195 and 320 kg/m^{2}s indicating strong influence of buoyancy for these cases. Again, higher values of Bo don't necessarily result in higher heat transfer coefficients. The values of A_{c_b} are significantly lower than the recommended threshold value of 4×10^{-6} for all the data points.

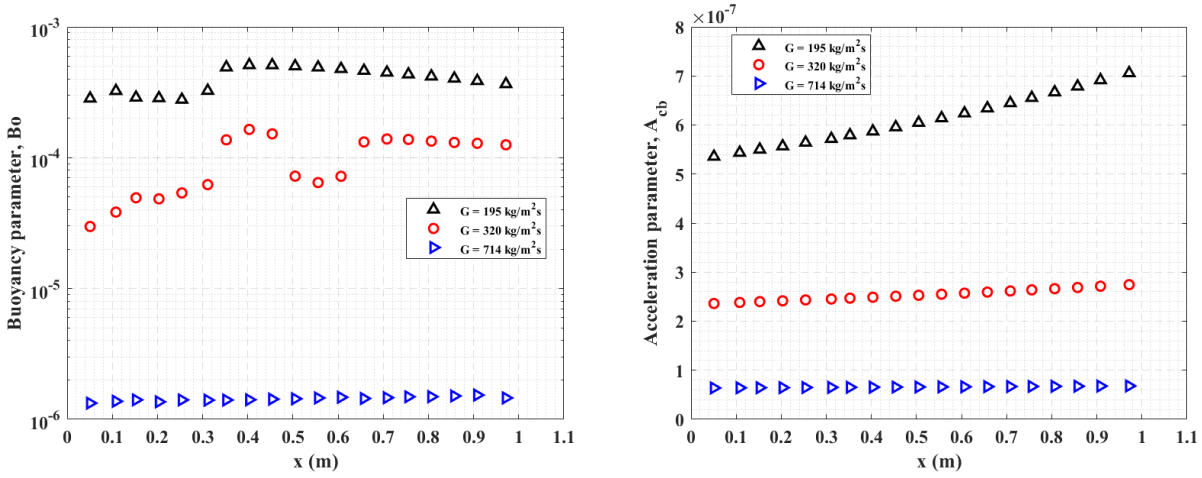

Figure 4-13: Effect of mass flux on the Buoyancy parameter, Bo (left) and the thermal bulk-flow acceleration parameter, A_{c_b} (right) for the upward flow configuration. Experimental conditions are listed in Table 4-5

Figure 4-14 presents variation of downward flow heat transfer coefficients versus the bulk fluid temperatures for different levels of mass flux. The peak value of heat transfer coefficient in the vicinity of pseudocritical temperature decreases with the mass flux due to reduction in the flow Reynolds number. For example, at G = 714 kg/m^{2}s the peak measured value of heat transfer coefficient is 5926±523.7 W/m^2-K for T_b = 31.54 °C; the peak value decreased to 2087.4±68.2 W/m^2-K for G = 320 kg/m^{2}s and to 1906.7±58.3 W/m^2-K for G = 195 kg/m^{2}s. As the mass flux decreases, the integrated value of specific heat, $\overline{C_{p,b}}$ also decreases in the pseudocritical region, causing a reduction in enhancement of the heat transfer. For temperatures farther away from the pseudocritical temperature (e.g., T_b > 50 °C) the heat transfer coefficients tend to become nearly independent of the bulk temperature, T_b which is again typical of an ideal-gas behavior.

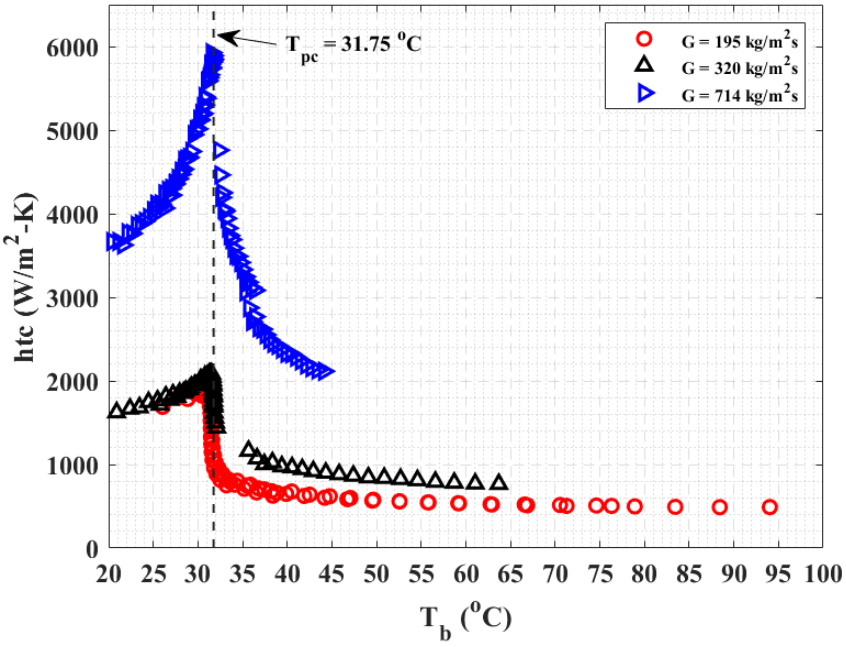

Figure 4-14: Effect of mass flux on the heat transfer coefficient in the downward flow configuration; ID = 7.9 mm, Q" = 40 kW/m^2, P = 7.5 MPa

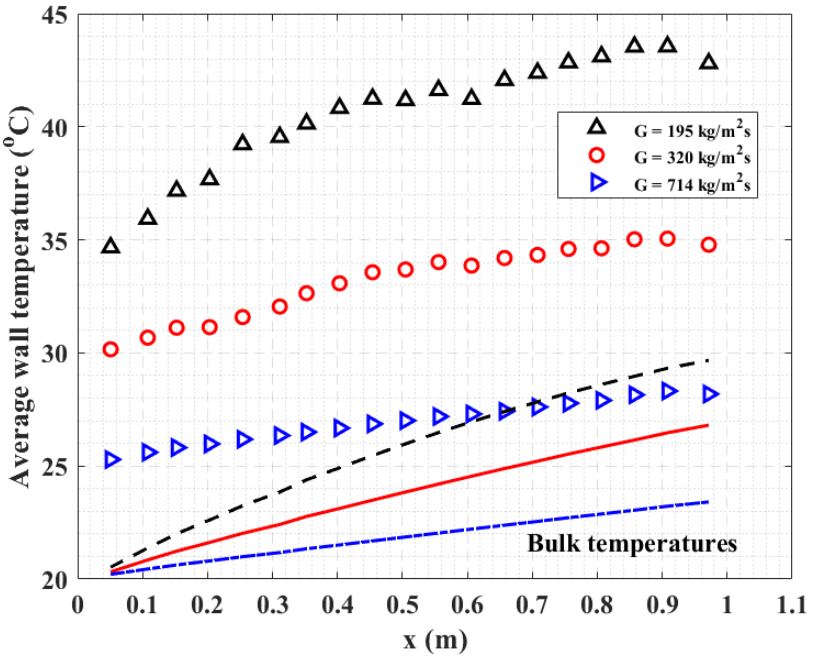

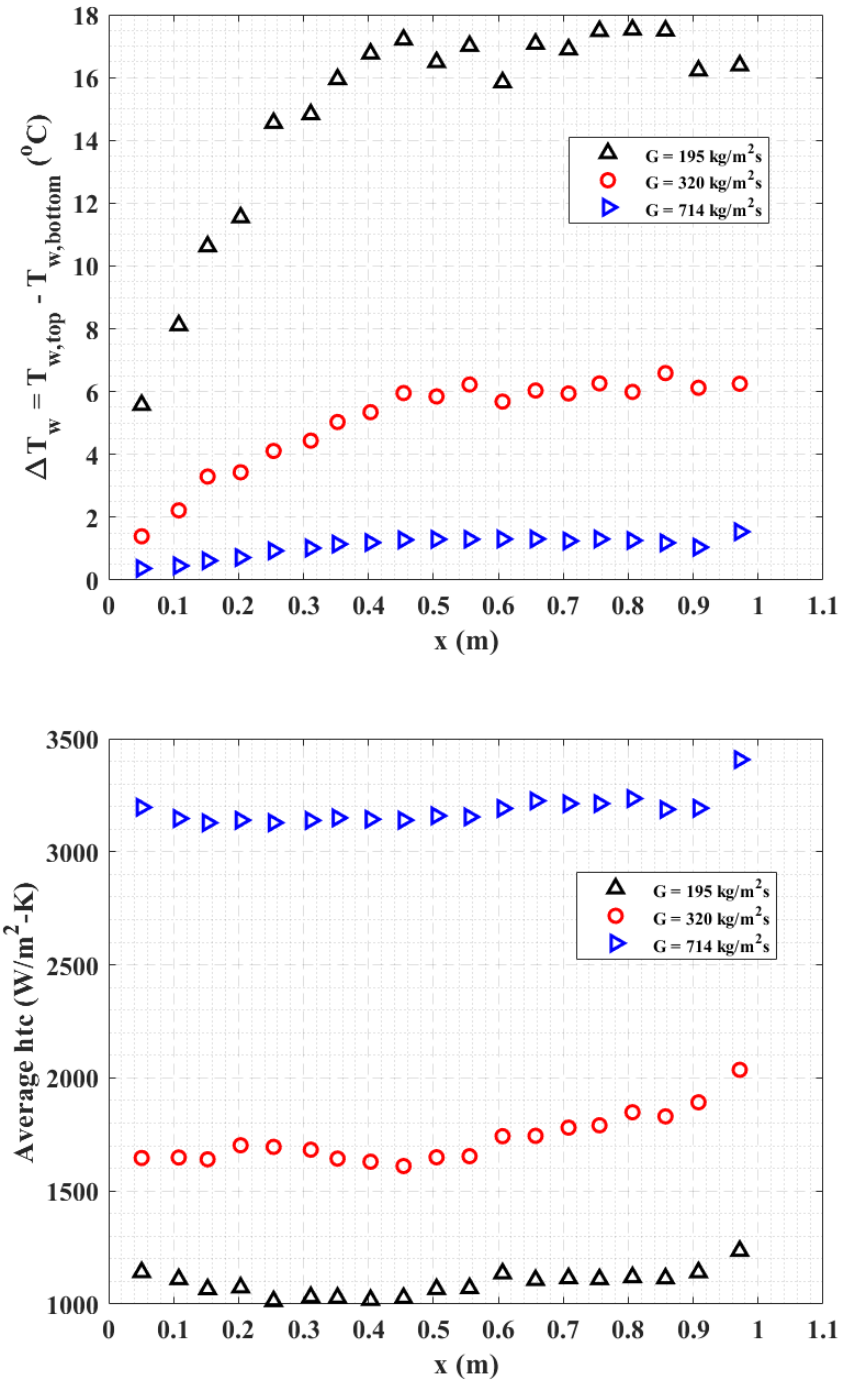

Figure 4-15: Effect of mass flux on the measured wall temperatures (top), ΔT_w (middle) and the heat transfer coefficients (bottom) for the horizontal flow configuration. Experimental conditions are listed in Table 4-5

The variation of the measured local average wall temperatures, temperature difference between the top and the bottom sides (ΔT_w) and the circumferential averaged heat transfer coefficients along the test section length for the horizontal flow are plotted in Figure 4-15; Refer to Table 4-5 for the experimental conditions for these cases.

The average wall temperature, ΔT_w increased with decrease in mass flux and correspondingly the average heat transfer coefficient decreases with the mass flux. For the highest value of mass flux (G = 714 kg/m^{2}s), ΔT_w is less than 2 °C at all locations along the tube and therefore, the effect of buoyancy on heat transfer can be considered to be negligible. As the mass flux decreases, the ΔT_w increased and the buoyancy effects become more prominent.

4.3.5 Effect of inlet temperature

The effect of inlet temperature on heat transfer was investigated by comparing the test results for cases shown in Table 4-6. For the upward flow orientation, variation of the measured wall temperature profiles and the heat transfer coefficients along the length of the test section is presented in Figure 4-16.

It appears that the peak in wall temperature tend to move towards the test section inlet as the fluid inlet temperature increases. For example, at T_{in} = 20 °C, the peak in wall temperature occurred at x≈0.4 m; whereas the peak moved to x≈0.25 m for T_{in} = 25 °C. For the fluid inlet temperature greater than the pseudocritical temperature (T_{in} = 35 °C), there is no evidence of a localized wall temperature peak. The variation of the buoyancy parameter, Bo and the thermal bulk-flow acceleration parameter, A_{c_b} along the test section length is presented in Figure 4-17 for the data points corresponding to Figure 4-16. For T_{in}

= 35 °C, the Bo values are less than the threshold value of 10^{-5} at all locations, hence the influence of buoyancy on heat transfer is negligible. However, for T_{in} = 20 °C and 25 °C the Bo values are higher than the threshold value of 10^{-5} and the buoyancy effects are strong as evident from the measured wall temperature and the heat transfer coefficient profiles. The values of A_{c_b} are less than the threshold value of $4x10^{-6}$ for all the cases.

Table 4-6: Experimental parameters for the selected cases to describe the effect of fluid inlet temperature

ID (mm)	P (MPa)	T_{in} (°C)	Q" (kW/m^2)	G (kg/m^2)	Flow orientation
7.9	7.5	20	13.5	320	Upward, Horizontal
		25			
		35			

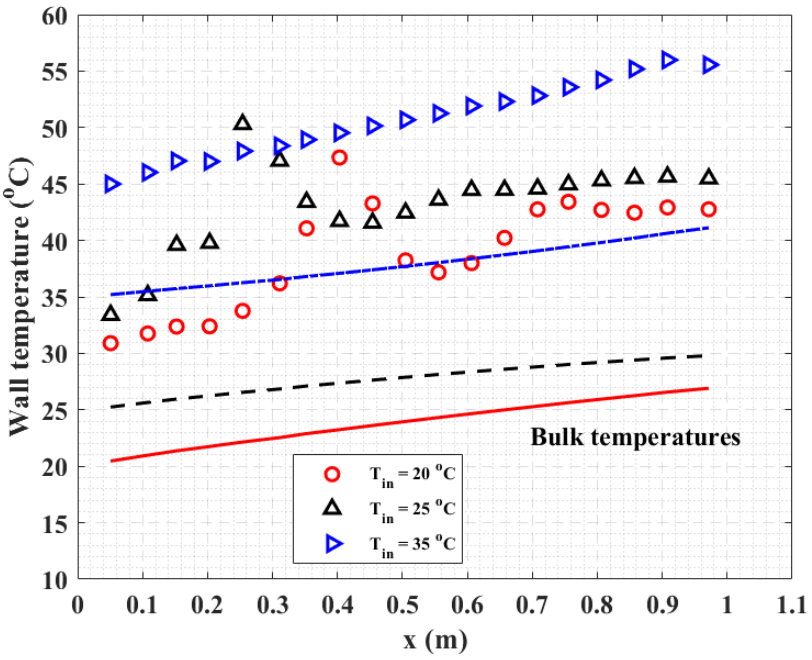

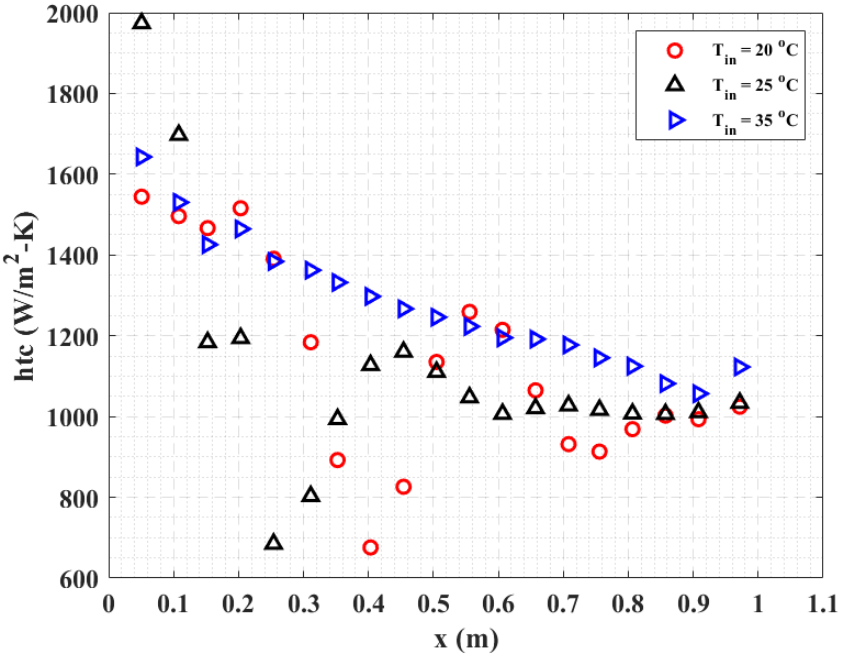

Figure 4-16: Effect of the fluid inlet temperature on the measured wall temperatures and the heat transfer coefficients for the upward flow configuration. Experimental conditions are listed in Table 4-6

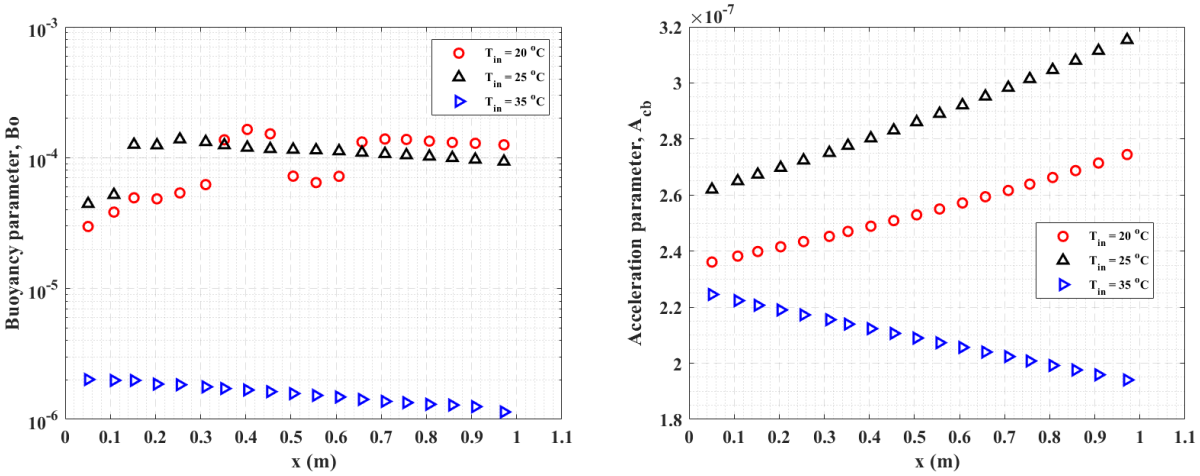

Figure 4-17: Effect of fluid inlet temperature on the Buoyancy parameter, Bo (left) and thermal bulk-flow acceleration parameter, A_{c_b} (right) for upward flow configuration. Experimental conditions are listed in Table 4-6

The variation of the measured local average wall temperatures, the temperature difference between the top and the bottom sides (ΔT_w) and the heat transfer coefficients

along the test section length for the horizontal flow are plotted in Figure 4-18; Refer to Table 4-6 for the experimental conditions for these cases.

The average wall temperature increased with increase in the fluid temperature. For the fluid inlet temperature greater than the pseudocritical temperature (T_{in} = 35 °C), ΔT_w is less than ~4 °C at all locations along the tube and therefore, the effect of buoyancy on heat transfer is small. However, for the fluid temperatures less than the pseudocritical temperature (T_{in} = 20 °C and 25 °C), the ΔT_w increased and the buoyancy effects become more prominent. The values of ΔT_w and average heat transfer coefficients are higher for T_{in} = 25 °C than for T_{in} = 20 °C even though the buoyancy effects are more prominent for T_{in} = 25 °C (see ΔT_w profiles).

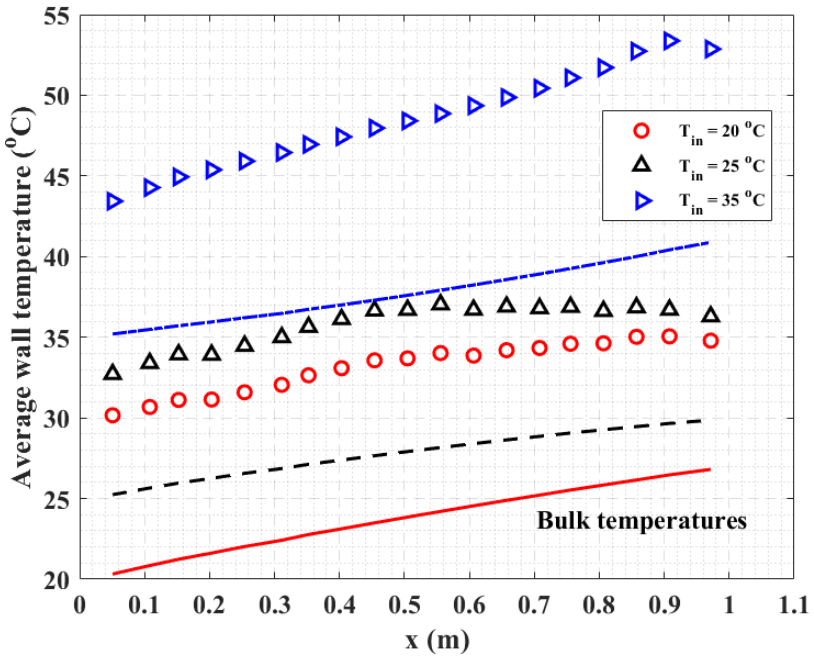

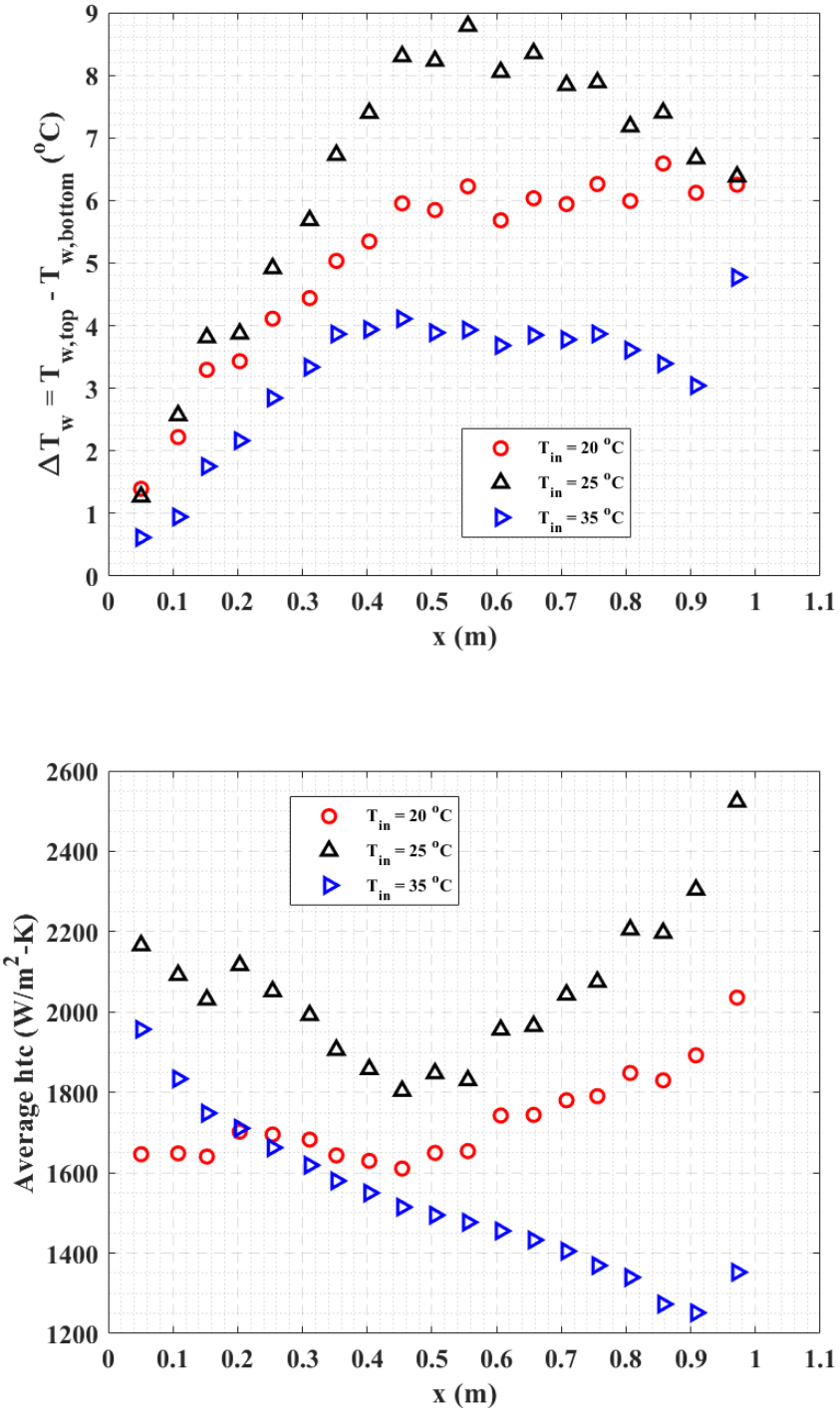

Figure 4-18: Effect of the fluid inlet temperature on the measured wall temperatures (top), ΔT_w (middle) and the heat transfer coefficients (bottom) for the horizontal flow configuration. Experimental conditions are listed in Table 4-6

4.4 Comparison with Existing Correlations

Based on discussion of the sample results in the previous sections it is clear that several parameters (such as heat flux, mass flux, fluid temperature, flow orientation, tube diameter) influence the supercritical CO_2 heat transfer coefficients. In this section the existing heat transfer correlations described in Section 2.1.7 were evaluated against the experimental data to propose the best possible existing correlations and to guide the model development effort. To evaluate the performance of each correlation following statistical parameters were selected:

$$MAE = \frac{1}{N}\sum_{i=1}^{N}\left|\frac{Nu_{exp,i}-Nu_{correlation,i}}{Nu_{exp,i}}\right| \tag{4.29}$$

$$RMSE = \frac{1}{N}\left(\sum_{i=1}^{N}\left(\frac{Nu_{exp,i}-Nu_{correlation,i}}{Nu_{exp,i}}\right)^2\right)^{0.5} \tag{4.30}$$

where MAE is the mean absolute error, RMSE is the root mean square error, Nu_{exp} is the experimental Nusselt number, $Nu_{correlation}$ is the Nusselt number determined using existing correlations and N is the total number of the experimental data points.

Table 4-7 presents the statistics from comparison of the existing correlations with the experimental data for the upward flow in the larger circular tube test section (ID = 10.9 mm). Out of the evaluated correlations, Kim and Kim (2011) correlation from Equation (2.35) performed the best followed by the correlations of Swenson (1965) and Jackson and Fewester (1975). Kim and Kim (2011) correlation predicted the experimental data with MAE of ±8.6% and RMSE of ±11.2%. Out of the 650 experimental data points, 83.7% and 96.3% of the data points were predicted with error less than ±15% and ±25% respectively.

The predictions using the Kim and Kim (2011) correlation are plotted against the experimental Nusselt numbers for the upward flow in the larger circular test section in Figure 4-19. It should be noted that most of these correlations are developed for upward flows and using specific set of conditions. So, they are certainly not applicable to all the test conditions investigated in this study.

Table 4-7: Statistics from comparison of the existing correlations with the experimental data for the upward flow in the larger circular tube test section (ID = 10.9 mm); Total number of experimental data points are 650

Correlation	Equation	MAE (%)	RMSE (%)	Percentage of data points with Error < ±15%	Percentage of data points with Error < ±25%
Dittus-Boelter (1930)	(2.15)	136.5%	274.8%	18.5%	33.5%
Gnielinski (1976)	(2.16)	86.7%	142.3%	5.2%	10.6%
Shitsman (1959)	(2.18)	41.4%	63.3%	30.9%	48.3%
Bishop (1964)	(2.19)	26.5%	34.9%	40.3%	53.5%
Swenson (1965)	(2.20)	16.4%	21.1%	57.7%	84.7%
Yamagata *et al.* (1972)	(2.21)	49.5%	61.5%	15.2%	30.9%
Krasnoshchekov and Protopopov (1959)	(2.22)	34.1%	43.7%	25.5%	49.1%
Krasnoshchekov *et al.* (1966)	(2.23)	30.9%	37.0%	18.0%	48.1%
Jackson and Fewester (1975)	(2.24)	25.1%	36.1%	48.6%	65.4%
Jackson (2002)	(2.25)	36.3%	57.2%	42.0%	55.4%
Liao and Zhao (2002)	(2.27)	95.1%	115.5%	2.8%	6.8%

Bae *et al.* (2010)	(2.29)	53.8%	72.5%	14.0%	27.5%
Kim and Kim (2011)	(2.31)	8.6%	11.2%	83.7%	96.3%

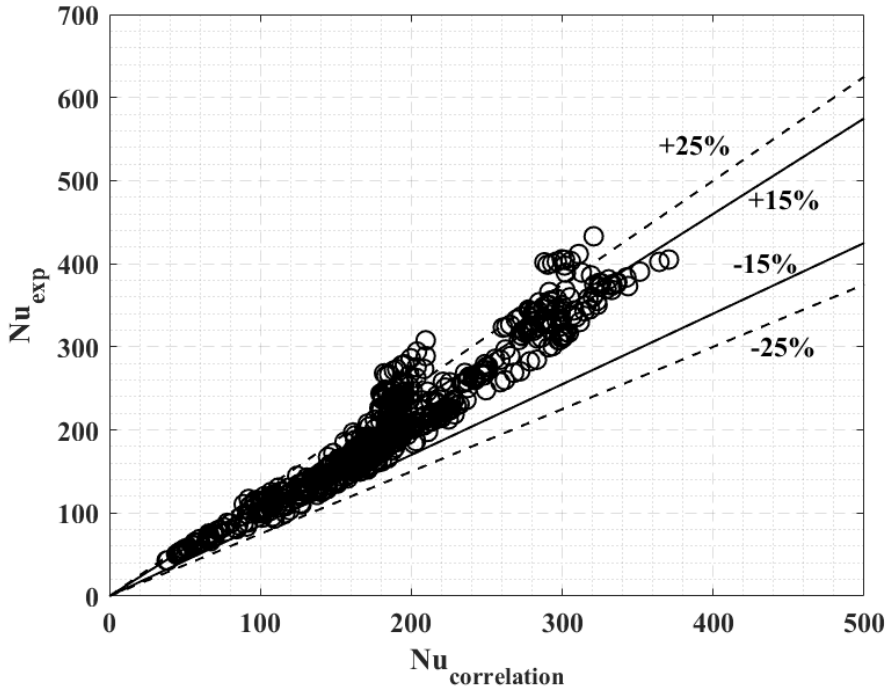

Figure 4-19: Comparison of the experimental data with Kim and Kim (2011) correlation for the upward flow in the larger circular tube test section (ID = 10.9 mm); Total number of experimental data points are 650

Table 4-8 presents the statistics from comparison of the existing correlations with the experimental data for the upward flow in the smaller circular tube test section (ID = 7.9 mm). Out of the evaluated correlations, Kim and Kim (2011) correlation from Equation (2.35) performed the best followed by the correlations of Swenson (1965) and Jackson and Fewester (1975). Kim and Kim (2011) correlation was able to predict the experimental data with MAE of ±17.9% and RMSE of ±23.9%. Out of the 836 experimental data points, 55.3% and 78.3% of the data points were predicted with error less than ±15% and ±25% respectively. The predictions using the Kim and Kim (2011) correlation are plotted against

the experimental Nusselt numbers for the upward flow in the smaller circular test section in Figure 4-20.

Table 4-8: Statistics from comparison of the existing correlations with the experimental data for the upward flow in the smaller circular tube test section (ID = 7.9 mm); Total number of experimental data points are 836

Correlation	Equation	MAE (%)	RMSE (%)	Percentage of data points with Error < ±15%	Percentage of data points with Error < ±25%
Dittus-Boelter (1930)	(2.15)	239.9%	472.1%	14.7%	18.2%
Gnielinski (1976)	(2.16)	121.2%	236.8%	4.9%	9.2%
Shitsman (1959)	(2.18)	63.7%	93.7%	16.3%	31.2%
Bishop (1964)	(2.19)	39.3%	48.9%	11.9%	37.7%
Swenson (1965)	(2.20)	21.2%	33.1%	53.3%	73.9%
Yamagata *et al.* (1972)	(2.21)	67.7%	78.8%	1.9%	5.6%
Krasnoshchekov and Protopopov (1959)	(2.22)	43.7%	64.9%	29.2%	47.5%
Krasnoshchekov *et al.* (1966)	(2.23)	38.9%	54.3%	30.6%	48.9%
Jackson and Fewester (1975)	(2.24)	38.6%	50.0%	22.9%	42.0%
Jackson (2002)	(2.25)	54.0%	77.0%	19.4%	37.2%
Liao and Zhao (2002)	(2.27)	70.2%	95.7%	16.3%	29.7%
Bae *et al.* (2010)	(2.29)	86.9%	107.4%	3.6%	7.9%
Kim and Kim (2011)	(2.31)	17.9%	23.9%	55.3%	78.3%

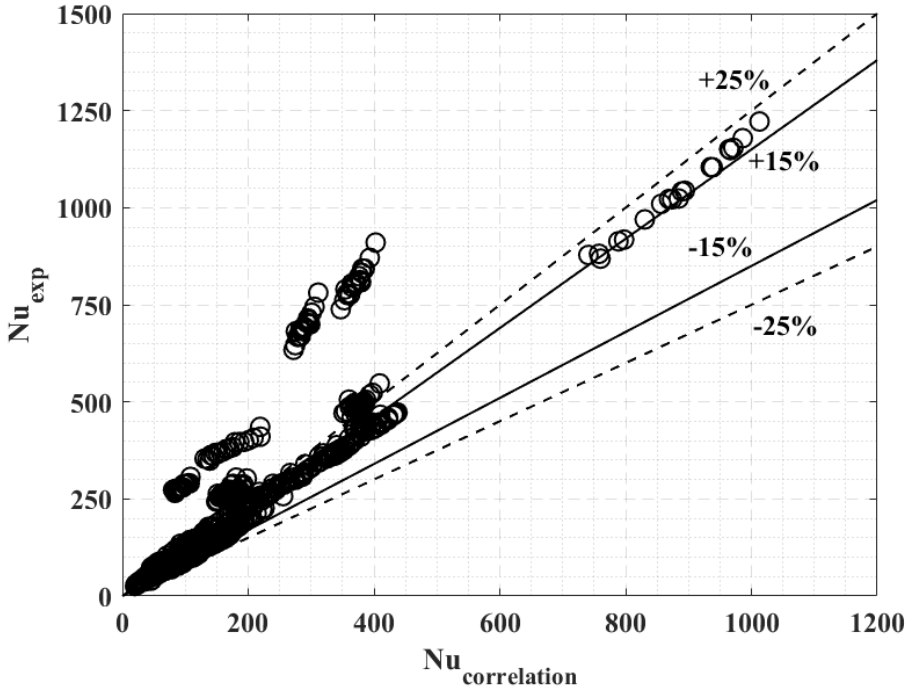

Figure 4-20: Comparison of the experimental data with Kim and Kim (2011) correlation for the upward flow in the smaller circular tube test section (ID = 7.9 mm); Total number of experimental data points are 836

Table 4-9 presents the statistics from comparison of the existing correlations with the experimental data for the downward flow in the larger circular tube test section (ID = 10.9 mm). Out of the evaluated correlations, Kim and Kim (2011) correlation from Equation (2.35) performed the best followed by the correlations of Bishop (1964) and Yamagata *et al.* (1972). Kim and Kim (2011) correlation predicted the experimental data with MAE of ±15.6% and RMSE of ±17.8%. Out of the 770 experimental data points, 57.9% and 88.4% of the data points were predicted with error less than ±15% and ±25% respectively. The predictions using the Kim and Kim (2011) correlation are plotted against the experimental Nusselt numbers for the downward flow in the larger circular test section in Figure 4-21.

Table 4-9: Statistics from comparison of the existing correlations with the experimental data for the downward flow in the larger circular tube test section (*ID* = 10.9 mm); Total number of experimental data points are 770

Correlation	Equation	MAE (%)	RMSE (%)	Percentage of data points with Error < ±15%	Percentage of data points with Error < ±25%
Dittus-Boelter (1930)	(2.15)	87.5%	182.6%	23.1%	34.4%
Gnielinski (1976)	(2.16)	82.8%	104.7%	2.2%	5.7%
Shitsman (1959)	(2.18)	22.9%	38.9%	54.3%	70.8%
Bishop (1964)	(2.19)	16.2%	21.2%	54.0%	77.7%
Swenson (1965)	(2.20)	26.6%	29.1%	14.2%	45.9%
Yamagata *et al.* (1972)	(2.21)	18.1%	26.6%	57.7%	79.0%
Krasnoshchekov and Protopopov (1959)	(2.22)	32.0%	36.8%	16.6%	41.3%
Krasnoshchekov *et al.* (1966)	(2.23)	35.4%	39.9%	10.8%	28.9%
Jackson and Fewester (1975)	(2.24)	20.1%	24.9%	42.7%	69.5%
Jackson (2002)	(2.25)	24.5%	36.4%	38.9%	62.1%
Liao and Zhao (2002)	(2.28)	41.8%	52.5%	21.7%	33.4%
Bae *et al.* (2010)	(2.29)	29.9%	44.1%	31.2%	53.5%
Kim and Kim (2011)	(2.31)	15.6%	17.8%	57.9%	88.4%

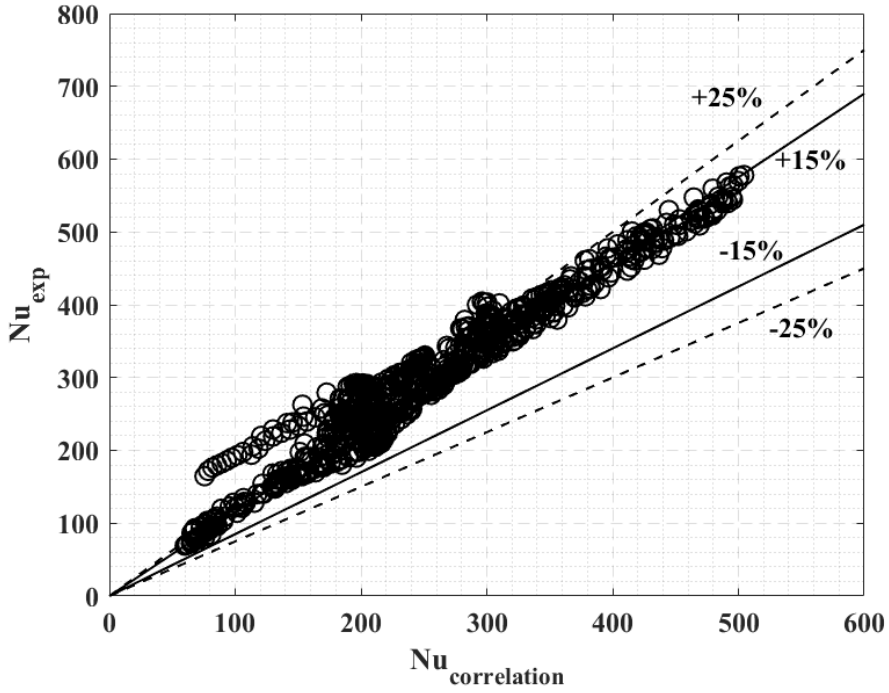

Figure 4-21: Comparison of the experimental data with Kim and Kim (2011) correlation for downward flow in the larger circular tube test section (ID = 10.9 mm); Total number of experimental data points are 770

Table 4-10 presents the statistics from comparison of the existing correlations with the experimental data for the downward flow in the smaller circular tube test section (ID = 7.9 mm). Out of the evaluated correlations, Jackson and Fewester (1975) correlation from Equation (2.24) performed the best followed by the correlations of Kim and Kim (2011) and Jackson (2002). Kim and Kim (2011) correlation predicted the experimental data with MAE of ±20.7% and RMSE of ±27%. Out of the 798 experimental data points, 47% and 72.4% of the data points were predicted with error less than ±15% and ±25% respectively. The predictions using the Kim and Kim (2011) correlation are plotted against the experimental Nusselt numbers for the downward flow in the smaller circular test section in Figure 4-22. The outliner data points in Figure 4-22 (largest deviation between the correlation and experimental data) are the data points with temperatures close to the

pseudocritical temperature at high mass flux and low heat flux conditions. Consequently, these data points have the highest uncertainties out of all the data points (up to ±50% in some cases).

Table 4-10: Statistics from comparison of the existing correlations with the experimental data for the downward flow in the smaller circular tube test section (ID = 7.9 mm); Total number of experimental data points are 798

Correlation	Equation	MAE (%)	RMSE (%)	Number of data points with Error < ±15%	Number of data points with Error < ±25%
Dittus-Boelter (1930)	(2.15)	116.0%	249.6%	18.8%	31.2%
Gnielinski (1976)	(2.16)	91.6%	135.5%	3.1%	5.9%
Shitsman (1959)	(2.18)	29.1%	44.8%	35.3%	70.1%
Bishop (1964)	(2.19)	21.8%	29.2%	46.2%	65.7%
Swenson (1965)	(2.20)	22.0%	27.9%	39.8%	67.8%
Yamagata *et al.* (1972)	(2.21)	34.6%	41.2%	17.4%	39.6%
Krasnoshchekov and Protopopov (1959)	(2.22)	39.7%	51.6%	27.7%	41.0%
Krasnoshchekov *et al.* (1966)	(2.23)	37.9%	45.1%	21.7%	38.7%
Jackson and Fewester (1975)	(2.24)	14.0%	19.3%	70.1%	82.7%
Jackson (2002)	(2.25)	21.5%	35.5%	63.7%	78.5%
Liao and Zhao (2002)	(2.28)	48.7%	57.8%	17.1%	26.4%
Bae *et al.* (2010)	(2.29)	46.6%	60.0%	13.4%	24.3%
Kim and Kim (2011)	(2.31)	20.7%	27.0%	47.0%	72.4%

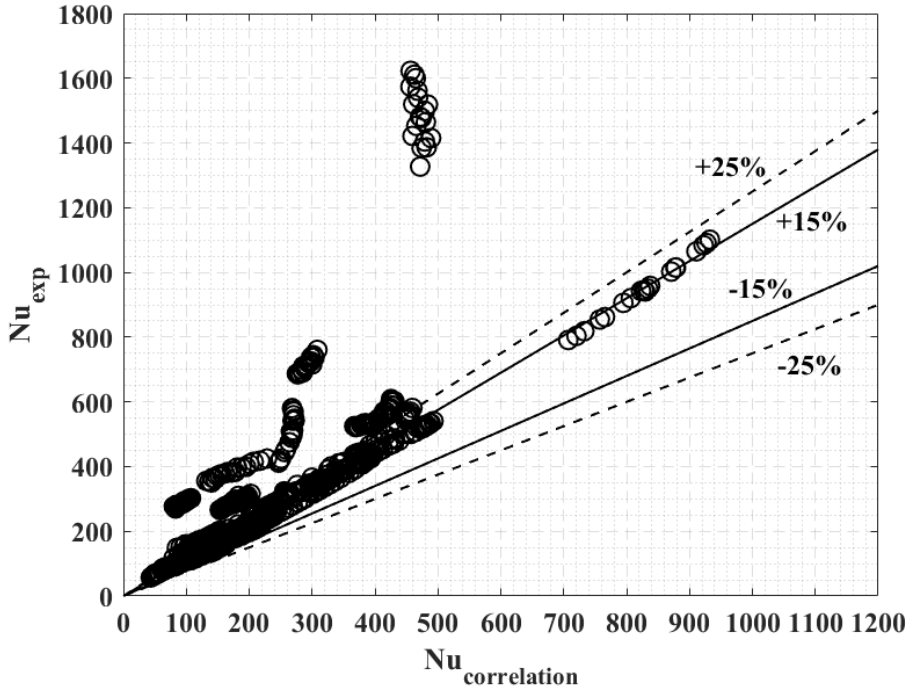

Figure 4-22: Comparison of the experimental data with Kim and Kim (2011) correlation for the downward flow in the smaller circular tube test section (ID = 7.9 mm); Total number of experimental data points are 798

Table 4-11 presents the statistics from comparison of the existing correlations with the experimental data for the horizontal flow in the larger circular tube test section (ID = 10.9 mm). Out of the evaluated correlations, Kim and Kim (2011) correlation from Equation (2.35) performed the best followed by the correlations of Swenson (1965) and Jackson and Fewester (1975). Kim and Kim (2011) correlation predicted the experimental data with MAE of ±9.9% and RMSE of ±12.6%. Out of the 640 experimental data points, 77.5% and 94.1% of the data points were predicted with error less than ±15% and ±25% respectively. The predictions using the Kim and Kim (2011) correlation are plotted against the experimental circumferential average Nusselt numbers for the horizontal flow in the larger circular test section in Figure 4-23.

Table 4-11: Statistics from comparison of the existing correlations with the experimental data for the horizontal flow in the larger circular tube test section (*ID* = 10.9 mm); Total number of experimental data points are 640

Correlation	Equation	MAE (%)	RMSE (%)	Percentage of data points with Error < ±15%	Percentage of data points with Error < ±25%
Dittus-Boelter (1930)	(2.15)	120.9%	236.5%	32.0%	47.2%
Gnielinski (1976)	(2.16)	81.3%	114.3%	7.2%	11.4%
Shitsman (1959)	(2.18)	31.9%	50.2%	46.4%	61.1%
Bishop (1964)	(2.19)	17.6%	22.6%	53.9%	69.7%
Swenson (1965)	(2.20)	14.4%	17.0%	51.6%	86.9%
Yamagata *et al.* (1972)	(2.21)	35.7%	45.0%	29.4%	43.9%
Krasnoshchekov and Protopopov (1959)	(2.22)	31.7%	38.3%	18.3%	49.7%
Krasnoshchekov *et al.* (1966)	(2.23)	31.2%	36.2%	17.7%	42.8%
Jackson and Fewester (1975)	(2.24)	16.6%	23.6%	64.4%	77.2%
Jackson (2002)	(2.25)	26.1%	43.4%	59.2%	71.1%
Liao and Zhao (2002)	(2.26)	45.8%	47.9%	3.4%	8.0%
Bae *et al.* (2010)	(2.29)	39.0%	55.6%	26.25%	51.71%
Kim and Kim (2011)	(2.31)	9.9%	12.6%	77.5%	94.1%

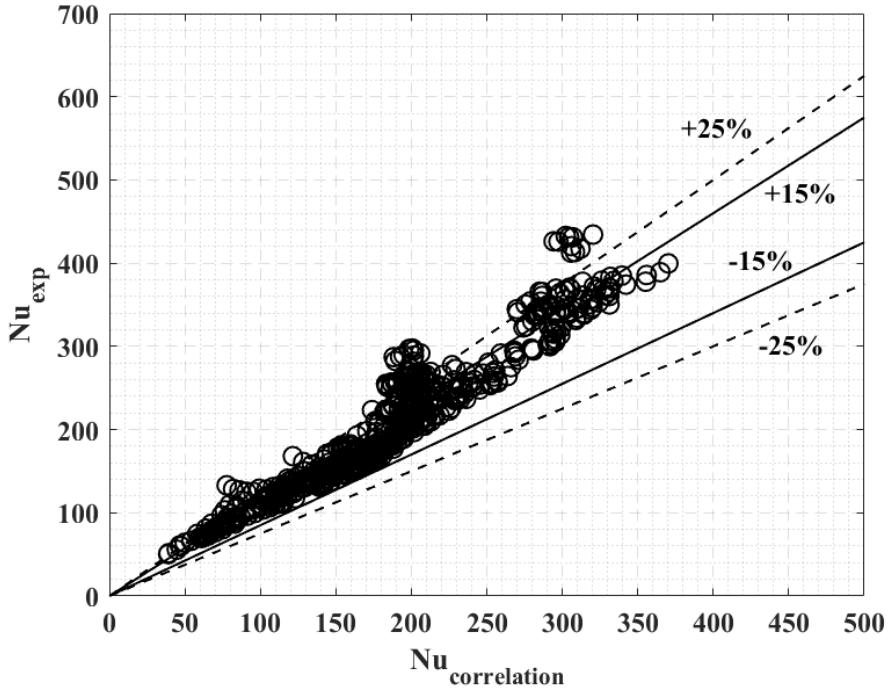

Figure 4-23: Comparison of the experimental data with Kim and Kim (2011) correlation for the horizontal flow in the larger circular tube test section (ID = 10.9 mm); Total number of experimental data points are 640

Table 4-12 presents the statistics from comparison of the existing correlations with the experimental data for the horizontal flow in the smaller circular tube test section (ID = 7.9 mm). Out of the evaluated correlations, Jackson and Fewester (1975) correlation from Equation (2.24) performed the best followed by the correlations of Kim and Kim (2011) and Swenson (1965). Kim and Kim (2011) correlation predicted the experimental data with MAE of ±22.1% and RMSE of ±30.4%. Out of the 1178 experimental data points, 49.5% and 71.5% of the data points were predicted with error less than ±15% and ±25% respectively. The predictions using the Kim and Kim (2011) correlation are plotted against the experimental circumferential average Nusselt numbers for the horizontal flow in the smaller circular test section in Figure 4-24.

Table 4-12: Statistics from comparison of existing correlations with the experimental data for the horizontal flow in smaller circular tube test section (ID = 7.9 mm); Total number of experimental data points are 1178

Correlation	Equation	MAE (%)	RMSE (%)	Percentage of data points with Error < ±15%	Percentage of data points with Error < ±25%
Dittus-Boelter (1930)	(2.15)	120.9%	243.9%	19.7%	33.4%
Gnielinski (1976)	(2.16)	88.0%	124.7%	3.65%	6.6%
Shitsman (1959)	(2.18)	33.4%	48.9%	31.3%	54.8%
Bishop (1964)	(2.19)	26.2%	35.4%	37.8%	63.5%
Swenson (1965)	(2.20)	25.7%	32.3%	36.2%	56.3%
Yamagata *et al.* (1972)	(2.21)	39.4%	52.3%	23.3%	43.6%
Krasnoshchekov and Protopopov (1959)	(2.22)	39.4%	53.1%	30.5%	43.5%
Krasnoshchekov *et al.* (1966)	(2.23)	38.1%	47.2%	24.3%	39.1%
Jackson and Fewester (1975)	(2.24)	19.7%	28.4%	54.6%	73.5%
Jackson (2002)	(2.25)	26.3%	42.8%	50.7%	68.5%
Liao and Zhao (2002)	(2.26)	62.1%	63.8%	1.1%	2.1%
Bae *et al.* (2010)	(2.29)	50.5%	65.1%	6.6%	19.9%
Kim and Kim (2011)	(2.31)	22.1%	30.4%	49.5%	71.5%

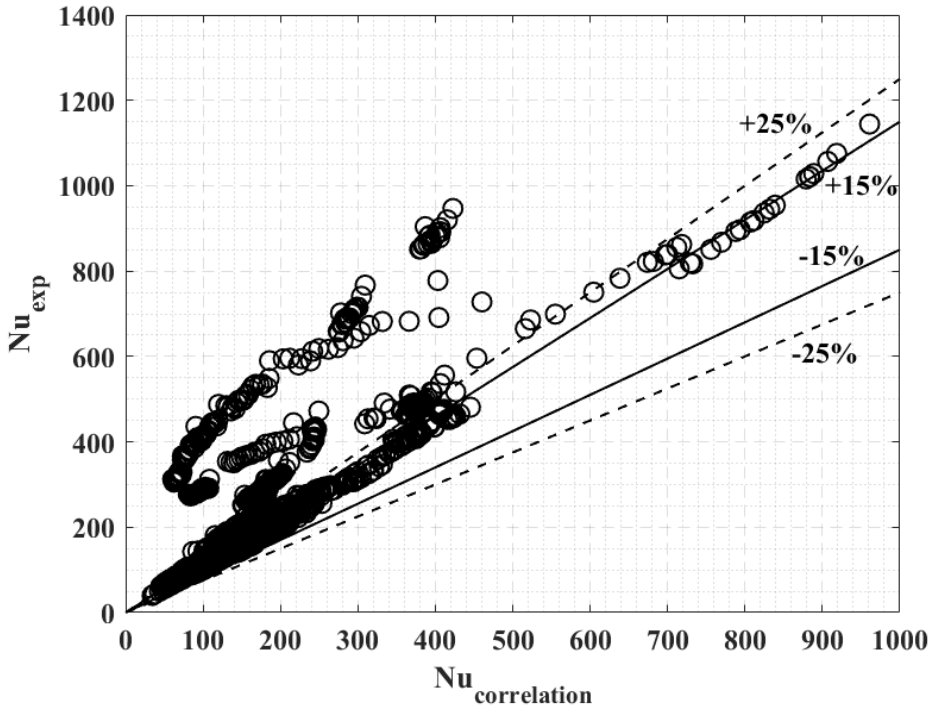

Figure 4-24: Comparison of the experimental data with Kim and Kim (2011) correlation for the horizontal flow in the smaller circular tube test section (ID = 7.9 mm); Total number of experimental data points are 1178

4.5 Model Development

Based on the comparison of the experimental data with the existing correlations from the literature, the calculated Nusselt number for the upward, downward and horizontal flows is assumed to be of form,

$$Nu_{calc} = aRe_b^b Pr_b^c \left(\frac{\rho_w}{\rho_b}\right)^d \left(\frac{\mu_w}{\mu_b}\right)^e \left(\frac{\overline{C_{pb}}}{C_{pb}}\right)^f q^{+g} \tag{4.31}$$

where $\overline{C_{pb}} = \frac{i_w - i_b}{T_w - T_b}$ and $q^+ = \beta Q"/GC_{pb}$. Equation (4.31) is similar in form to the correlation of Kim and Kim (2011) from Equation (2.31) since it performed well during evaluation of the correlations in the previous section. The coefficients a through g are

calculated based on the least-squares curve fitting procedure to the upward, downward and horizontal flow experimental data for both the circular tube test sections:

$$\sum_{i=1}^{N_{expt}} \left(Nu_{calc} - Nu_{exp}\right)^2 \rightarrow minimum \tag{4.32}$$

Table 4-13 summarizes the coefficients a through g determined for the upward, downward and horizontal flows.

Table 4-13: Coefficients a through g determined from fitting the Nusselt number of the form Equation (4.31) to the experimental data for both the circular tube test sections

	a	b	c	d	e	f	g
Upward flow	0.0324	0.9241	0.5449	1.1735	-0.5825	0.5773	0.2126
Downward flow	0.1953	0.9024	0.6790	1.8231	-0.8254	0.6300	0.3805
Horizontal flow	0.0976	0.8093	0.5395	1.0211	-0.3790	0.5313	0.1754

Figure 4-25 through Figure 4-27 present predictions using the upward, downward and horizontal flow Nusselt number correlations (from Equation (4.31) and Table 4-13) to the experimentally measured values for both the circular tube test sections.

The proposed Nusselt number correlation for the upward flow was able to predict the experimental Nusselt numbers with MAE of ±12.4% and RMSE of ±17.6%. Out of the 1486 data points, 74.9% of the experimental data is predicted within ±15% and 85.1% of the experimental data is predicted within ±25%.

The proposed Nusselt number correlation for the downward flow was able to predict the experimental Nusselt numbers with MAE of ±16.3% and RMSE of ±20.1%. Out of the 1568 data points, 61.2% of the experimental data is predicted within ±15% and 79.1% of the experimental data is predicted within ±25%.

The proposed Nusselt number correlation for the horizontal flow was able to predict the experimental Nusselt numbers with MAE of ±14.2% and RMSE of ±19.8%. Out of the 1818 data points, 69.7% of the experimental data is predicted within ±15% and 84.6% of the experimental data is predicted within ±25%.

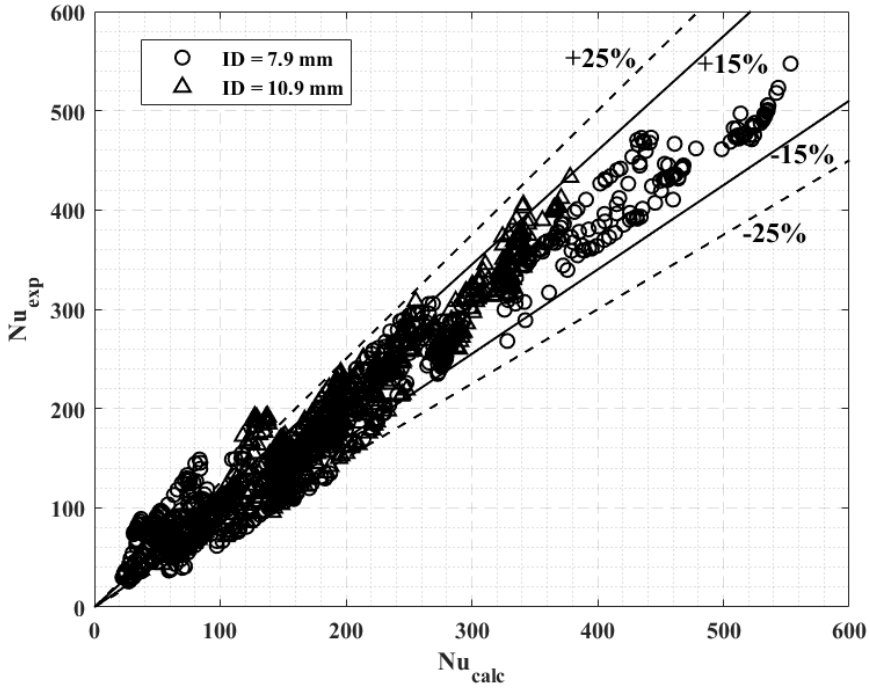

Figure 4-25: Comparison of the experimental data with model developed for upward flow; Total number of experimental data points are 1486

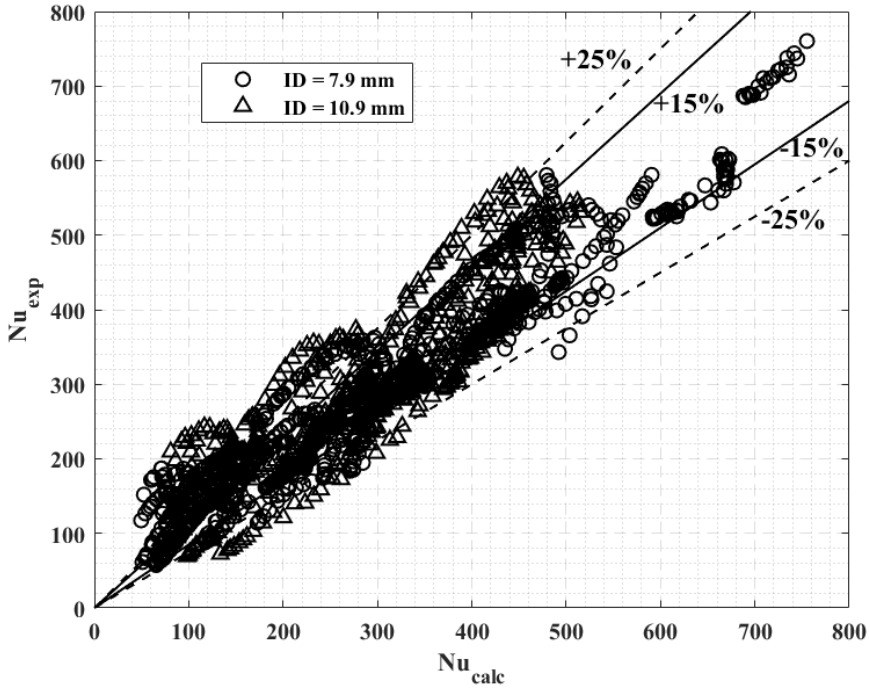

Figure 4-26: Comparison of the experimental data with model developed for downward flow; Total number of experimental data points are 1568

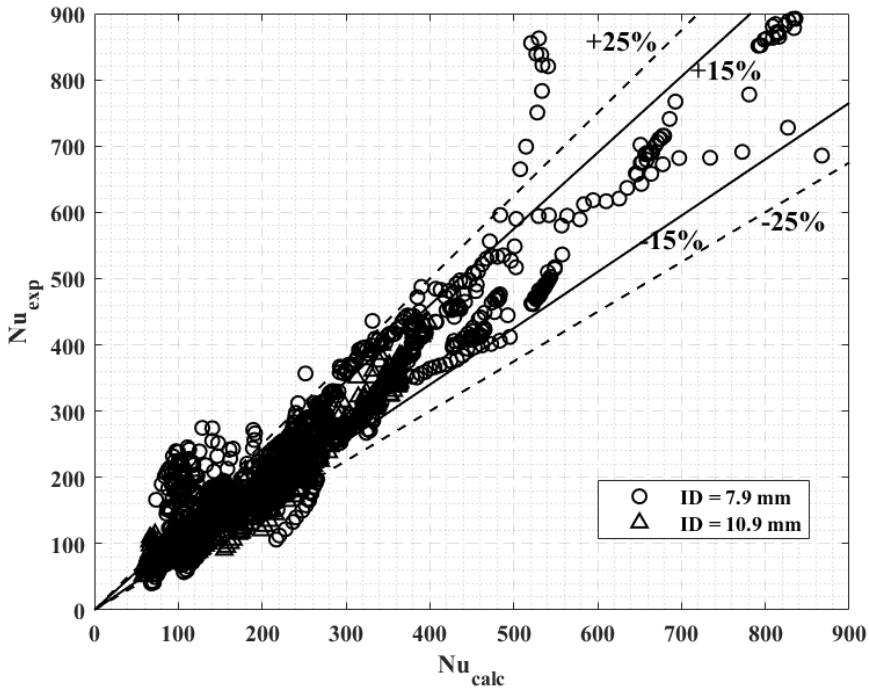

Figure 4-27: Comparison of the experimental data with model developed for horizontal flow; Total number of experimental data points are 1818

CHAPTER 5. PCHE TEST SECTIONS DATA ANALYSIS AND RESULTS

The previous chapter discussed fundamental heat transfer characteristics of supercritical CO_2 flow for flow inside heated circular tubes. This chapter is dedicated for data analysis, discussion of the results for flow through both the discontinuous (offset rectangular fin and NACA0020 fin) PCHE test sections. A series of experiments were conducted by varying the fluid inlet temperature, mass flow rate, system pressure; refer to Table 5-1 for the range of experimental conditions. A total of 453 and 306 experiments were conducted for the rectangular and NACA0020 airfoil fin PCHE test sections respectively. These operating conditions covered a wide range of Reynolds number, $2700 < Re < 38{,}000$ and Prandtl number, $0.8 < Pr < 25$.

Table 5-1: Experimental conditions for the PCHE test sections

Experimental parameters	Range of values
Normalized pressure, P/P_c	1.015, 1.096, 1.38
CO_2 Inlet temperature (°C)	50 – 200 °C (In increments of 10 °C) 20 – 50 °C (In increments of 5 °C)
CO_2 mass flow rate (kg/h)	8.8 – 28.8 kg/h (In increments of 2.9 kg/h)
Water Inlet temperature (°C)	10 – 20 °C
Water volumetric flow rate (GPM)	0.05 – 0.1 GPM

During the experiments, all independent parameters such as the test section inlet temperature, mass flow rate, pressure etc. were controlled and monitored. For each experiment, the system was assumed to have achieved steady state once the experimental parameters were constant (within the accuracy of the associated instrumentation) for at least ten minutes. Once the system achieved steady state, the data was recorded for 500

seconds at the rate of 1 Hz and the average of data points was used for the data processing. The following sections describe the data reduction procedure for calculating the local and average heat transfer coefficients, frictional pressure drop and the associated uncertainty.

5.1 Heat transfer data reduction and associated uncertainty

5.1.1 Heat removal

The local heat removal for each cooling block is calculated using the measured inlet and outlet temperatures and the volumetric flow rate of water as in Equation (5.1). Approximately 3" thick insulation layer is wrapped around the PCHE test sections, therefore, the heat loss to the ambient is assumed to be negligible. Water properties are calculated based on the average of the inlet and outlet temperatures as the water properties don't vary considerably in the temperature range of interest and the temperatures are far away from the boiling point. The total water side heat duty is determined by summing the heat removal for all twenty cooling blocks.

$$Q_{H_2O} = \sum_1^{20} \dot{V} \rho C_p (T_{water,out} - T_{water,in}) \tag{5.1}$$

The CO_2 side heat duty is determined from the energy balance as,

$$Q_{CO_2} = \dot{m}_{CO_2} (i_{in} - i_{out}) \tag{5.2}$$

where i is the enthalpy (J/kg) and is determined from the measured inlet/outlet temperatures and pressures.

Uncertainty in the measurement of local heat removal rate is determined using the Kline and McClintock method [105] as shown in Equation (5.3).

$$\frac{\sigma_{Q_{H_2O}}}{Q_{H_2O}} = \left[\left(\frac{\sigma_{\dot{V}}}{\dot{V}}\right)^2 + \left(\frac{\sigma_{\Delta T}}{\Delta T}\right)^2\right]^{0.5} \tag{5.3}$$

where $\Delta T = T_{water,out} - T_{water,in}$

Uncertainty in the CO_2 side heat duty is calculated as,

$$\frac{\sigma_{Q_{CO_2}}}{Q_{CO_2}} = \left[\left(\frac{\sigma_{\dot{m}_{CO_2}}}{\dot{m}_{CO_2}}\right)^2 + \left(\frac{\sigma_{i_{in}}}{i_{in}-i_{out}}\right)^2 + \left(\frac{\sigma_{i_{out}}}{i_{in}-i_{out}}\right)^2\right]^{0.5} \tag{5.4}$$

Figure 5-1 compares the CO_2 and water side heat duties for the offset rectangular fin PCHE test section. The CO_2 and water side heat duties agreed within ±10% for all the experiments. The maximum difference was observed when the measured CO_2 inlet/outlet temperature is close to the pseudocritical temperature. Although not shown here, similar agreement was observed for the offset NACA0020 airfoil fin PCHE test section as well.

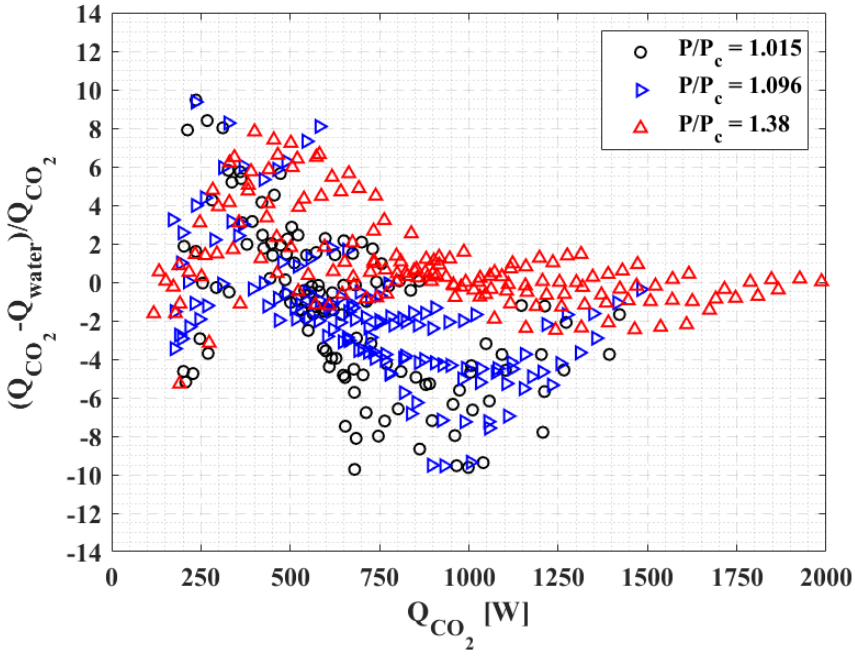

Figure 5-1: Comparison of the measured heat duties from the CO_2 and the water sides. Data is plotted for the offset rectangular fin PCHE test section at three different system pressures

5.1.2 Bulk fluid temperature

Bulk fluid temperature is calculated at the ten axial locations corresponding to the cooling blocks locations. This was accomplished by performing an energy balance at each subsection (see Figure 5-2), which consists of the cooling block pairs, the section of the mating plate and the PCHE test plates.

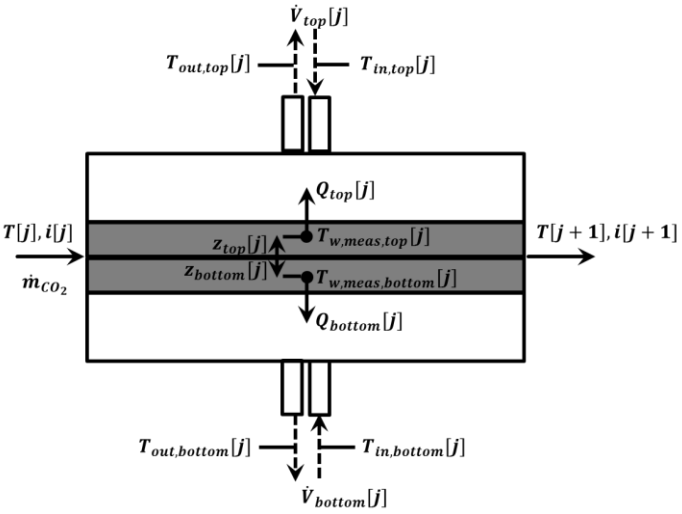

Figure 5-2: One of the 10 subsection of the PCHE test section showing relevant variables used during for data reduction

The measured CO_2 inlet pressure and temperature to the test section are used to calculate the specific enthalpy at the inlet (i_{in} or $i[1]$). Assuming a linear pressure drop across the test section, the bulk enthalpy at the exit of each subsection is determined as follows:

$$i[j+1] = i[j] - \frac{Q_{top}[j]+Q_{bottom}[j]}{\dot{m}_{CO_2}} \tag{5.5}$$

$$i_b[j] = 0.5(i[j] + i[j+1])$$

Uncertainty in the local bulk enthalpy is calculated as follows,

$$\sigma_{i[j+1]} = \left(\sigma_{i[j]}^2 + \left(\Delta i.\frac{\sigma_{Q[j]}}{Q[j]}\right)^2 + \left(\Delta i.\frac{\sigma_{\dot{m}_{CO_2}}}{\dot{m}_{CO_2}}\right)^2\right)^{0.5} \quad (5.6)$$

$$\sigma_Q[j] = \left(\sigma_{Q_{top}[j]}^2 + \sigma_{Q_{bottom}[j]}^2\right)^{0.5}$$

$$\sigma_{i_b[j]} = 0.5\left(\sigma_{i[j]}^2 + \sigma_{i[j+1]}^2\right)^{0.5}$$

where $\Delta i = i[j] - i[j+1]$

The local bulk temperature and other state-dependent thermophysical properties are determined based on the local bulk enthalpy and the pressure for each subsection. All the fluid properties are calculated using the NIST REFPROP V9.1 [104].

5.1.3 Wall temperature

The local wall temperatures for the mating plate and the PCHE test plate are determined according to the plane-wall conduction equation, as shown in Equations (5.7) and (5.8) respectively. The average of the two wall temperatures is used to determine the local heat transfer coefficient for each subsection.

$$T_{w,calc,top}[j] = T_{w,meas,top}[j] + \frac{Q_{top}[j].z_{top}[j]}{k_{ss316}A_{cb}} \quad (5.7)$$

$$T_{w,calc,bottom}[j] = T_{w,meas,bottom}[j] + \frac{Q_{bottom}[j].z_{bottom}[j]}{k_{ss316}A_{cb}} \quad (5.8)$$

$$T_w[j] = 0.5\ (T_{w,calc,top}[j] + T_{w,calc,bottom}[j]) \quad (5.9)$$

where A_{cb} is the effective heat transfer of the cooling block and is equal to 35.3 mm x 50.8 mm. An uncertainty of 5% is assumed in the usage of the cooling block heat transfer area.

Uncertainty in the calculated local wall temperature is estimated as follows,

$$\sigma_{T_{w,calc}[j]} = \left(\sigma^2_{T_{w,meas}[j]} + \left(\Delta T.\frac{\sigma_{Q[j]}}{Q[j]}\right)^2 + \left(\Delta T.\frac{\sigma_{z[j]}}{z[j]}\right)^2 + \left(\Delta T.\frac{\sigma_{A_{cb}}}{A_{cb}}\right)^2\right)^{0.5} \quad (5.10)$$

$$\sigma_{T_w[j]} = 0.5\left(\sigma^2_{T_{w,calc,top}[j]} + \sigma^2_{T_{w,calc,bottom}[j]}\right)^{0.5} \quad (5.11)$$

where $\Delta T = T_{w,calc}[j] - T_{w,meas}[j]$

5.1.4 Local and average heat transfer coefficient and Nusselt number

The local heat removal, wall temperature and bulk fluid temperature are used to calculate the local heat transfer coefficients and Nusselt numbers as shown in Equation (5.12) and (5.13) respectively.

$$htc[j] = \frac{Q_{top}[j]+Q_{bottom}[j]}{A_s.(T_b[j]-T_w[j])} \quad (5.12)$$

$$Nu[j] = htc[j].\frac{D_h}{k_b[j]} \quad (5.13)$$

where A_s and D_h are the heat transfer area of one subsection and hydraulic diameter determined from the laser scanning of the PCHE test plates; Refer to Table 3-1 and Table 3-2 for these parameters.

Finally, uncertainty in the local heat transfer coefficient and the local Nusselt number is calculated as shown in Equation (5.14) and Equation (5.15) respectively.

$$\frac{\sigma_{htc[j]}}{htc[j]} = \left[\left(\frac{\sigma_{Q[j]}}{Q[j]}\right)^2 + \left(\frac{\sigma_{A_s}}{A_s}\right)^2 + \left(\frac{\sigma_{T_w[j]}}{T_w[j]-T_b[j]}\right)^2 + \left(\frac{\sigma_{T_b[j]}}{T_w[j]-T_b[j]}\right)^2\right]^{0.5} \quad (5.14)$$

$$\frac{\sigma_{Nu[j]}}{Nu[j]} = \left[\left(\frac{\sigma_{htc[j]}}{htc[j]}\right)^2 + \left(\frac{\sigma_{D_h}}{D_h}\right)^2 + \left(\frac{\sigma_{k_b[j]}}{k_b[j]}\right)^2\right]^{0.5} \quad (5.15)$$

Average heat transfer coefficients and Nusselt numbers are calculated according to Equation (5.16) and Equation (5.17) respectively.

$$\overline{htc} = \frac{0.5\,(Q_{CO_2}+Q_{H_2O})}{N.A_s.(\overline{T_b}-\overline{T_w})} \tag{5.16}$$

$$\overline{Nu} = \overline{htc}.\frac{D_h}{\overline{k_b}} \tag{5.17}$$

The average bulk fluid temperature ($\overline{T_b}$) and the average wall temperature ($\overline{T_w}$) are calculated by considering the non-linear variation along the length of the test section. Figure 5-3 presents an example of the bulk and the wall temperature profiles for one of the experimental cases for offset rectangular fin PCHE test section.

$$\overline{T_b} = \frac{1}{L}\int_0^L T_b(x).dx \tag{5.18}$$

$$\overline{T_w} = \frac{1}{L}\int_0^L T_w(x).dx \tag{5.19}$$

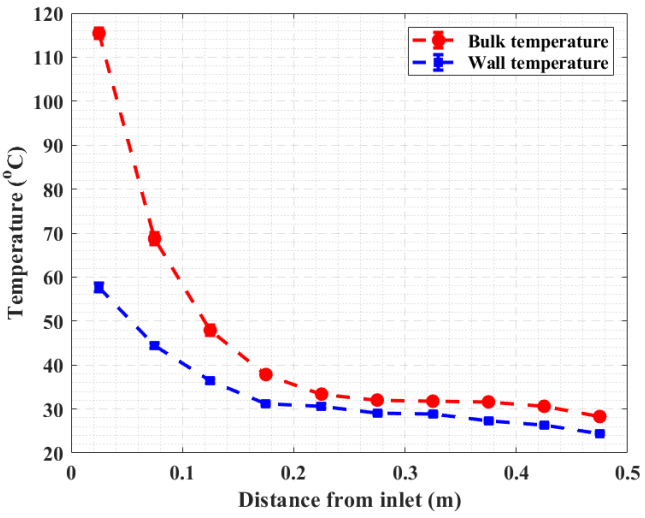

Figure 5-3: The measured wall temperature profile and the calculated bulk fluid temperature profile (from measured local heat removal rate) for the offset rectangular fin PCHE test section; P_{in}=7.51 MPa, T_{in}=150 °C, $\dot{m}_{CO_2}$=0.0245 kg/s

Since the thermophysical properties exhibit a non-linear behavior with respect to temperature at constant pressure, the average properties for each experiment are calculated according to the following set of equations:

$$\bar{\rho} = \frac{1}{L}\int_0^L \rho(T_b).dx;\ \bar{\mu} = \frac{1}{L}\int_0^L \mu(T_b).dx;\ \overline{Pr} = \frac{1}{L}\int_0^L Pr(T_b).dx \tag{5.20}$$

$$\overline{Re} = {G.D_h}/{\bar{\mu}} \tag{5.21}$$

5.2 Pressure drop data reduction and associated uncertainty

The total pressure drop across the PCHE test section is broken down into four components as in Equation (5.22) to calculate the frictional pressure drop component ($\Delta P_{friction}$).

$$\Delta P_{measured} = \Delta P_{friction} + \Delta P_{acceleration} + \Delta P_{gravity} + \Delta P_{local} \tag{5.22}$$

where $\Delta P_{acceleration}$ is pressure loss due to acceleration/deceleration, $\Delta P_{gravity}$ is pressure loss due to gravity and ΔP_{local} is entrance/exit pressure losses.

$$\Delta P_{acceleration} = G^2\left(\frac{1}{\rho_{out}} - \frac{1}{\rho_{in}}\right) \tag{5.23}$$

$$\Delta P_{gravity} = \pm g\left(\frac{i_{out}\rho_{out} + i_{in}\rho_{in}}{i_{out} + i_{in}}\right) \tag{5.24}$$

All the experiments were conducted in the horizontal flow configuration which eliminates the pressure drop component due to the gravity. The acceleration pressure losses due to the density changes along the test section are computed from the measured mass flow rate and the inlet and outlet conditions. The local pressure drop arises from the fluid

contraction at the inlet, due to the mixing manifold splitting the flow to each channel and expansion from the channels to the manifold at the outlet. Expansion and contraction pressure losses are calculated from published correlations [107].

$$\Delta P_{local} = \Delta P_{expansion} + \Delta P_{contraction} \tag{5.25}$$

$$\Delta P_{expansion} = \left[1 - \frac{A_c}{A_{manifold}}\right]^2 \rho_{out} \frac{V_{out}^2}{2} \tag{5.26}$$

$$\Delta P_{contraction} = 0.5 \left[1 - \frac{A_c}{A_{manifold}}\right]^{0.75} \rho_{out} \frac{V_{in}^2}{2} \tag{5.27}$$

where A_c is the flow cross-sectional area and $A_{manifold}$ is the cross-sectional area of the manifolds. Using this procedure, the frictional pressure drop can be extracted from the measured pressure drop from the experiments.

5.3 Results and Discussion

This section presents and discusses the heat transfer coefficient and pressure drop results for both the PCHE test sections. An example of the data reduction and the uncertainty calculations for the offset rectangular fin PCHE test section is presented in APPENDIX E.

5.3.1 Average Heat Transfer Coefficients

The measured average heat transfer coefficients are plotted as a function of average fluid bulk temperature for different mass fluxes, G and pressures in Figure 5-4 (for the offset rectangular fin PCHE test section) and Figure 5-5 (for the offset NACA0020 airfoil fin PCHE test section). For the offset rectangular fin PCHE, the average uncertainty in the measurement of average heat transfer coefficient is ±6.2%; whereas for the offset

NACA0020 airfoil PCHE test section the average uncertainty is ±5.7%. The maximum uncertainty in the average heat transfer coefficient occurred in the vicinity of the pseudocritical temperature for P/P_c=1.014 and highest value of mass flux. The heat transfer coefficient attains a peak value in the vicinity of pseudocritical temperature (marked as dashed vertical lines in Figure 5-4 and Figure 5-5) due to increased specific heat. The trends are similar to the results of the circular tube test sections described in CHAPTER 4. The peak value of the heat transfer coefficient decreases with mass flux and pressure. For example, the measured peak value of heat transfer coefficient for the NACA0020 airfoil fin PCHE at P/P_c = 1.014 is 11,924.2±803.1 W/m^2-K for G = 660 kg/m^{2}s whereas the value decreases to 4176.9±169.5 W/m^2-K for G = 220 kg/m^{2}s. As the pressure is increased to P/P_c = 1.38, the peak value of heat transfer coefficient decreased to 6948.3±279.7 W/m^2-K for G = 660 kg/m^{2}s.

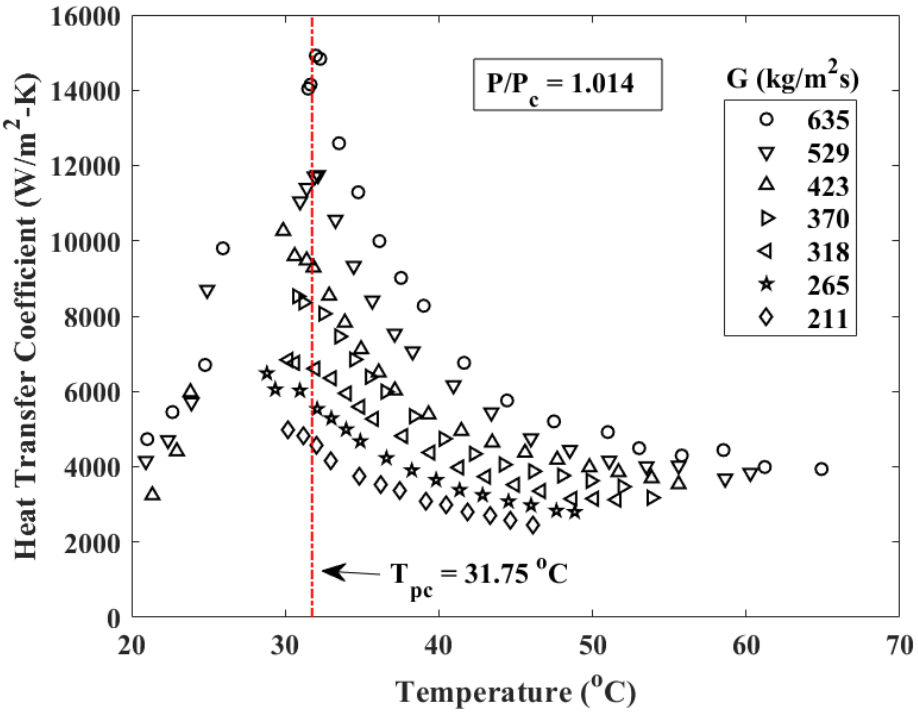

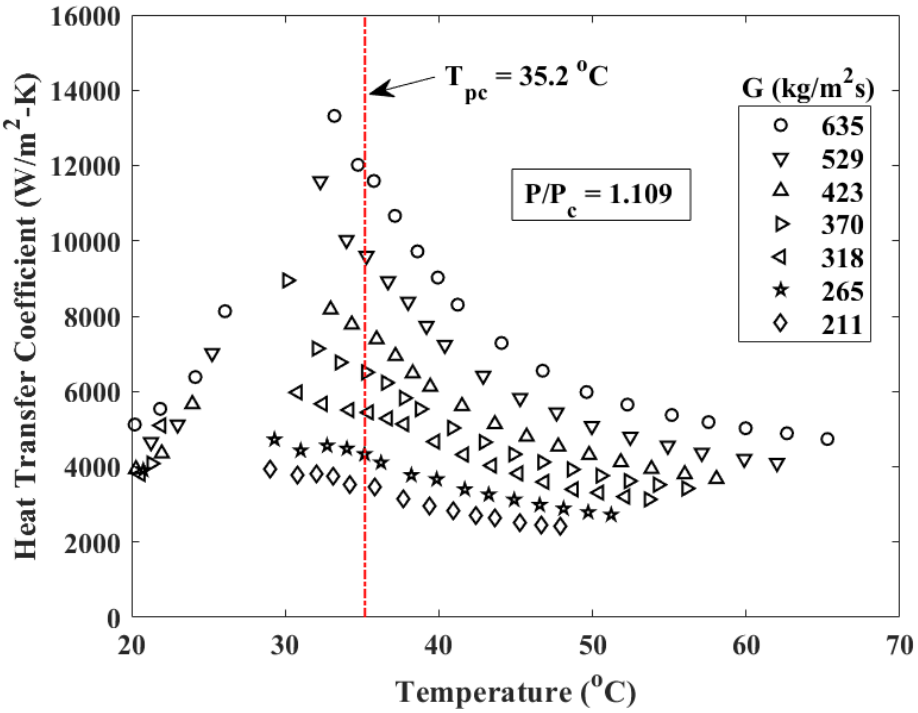

Figure 5-4: Average heat transfer coefficients plotted as a function of the average bulk fluid temperature for the offset rectangular fin PCHE test section

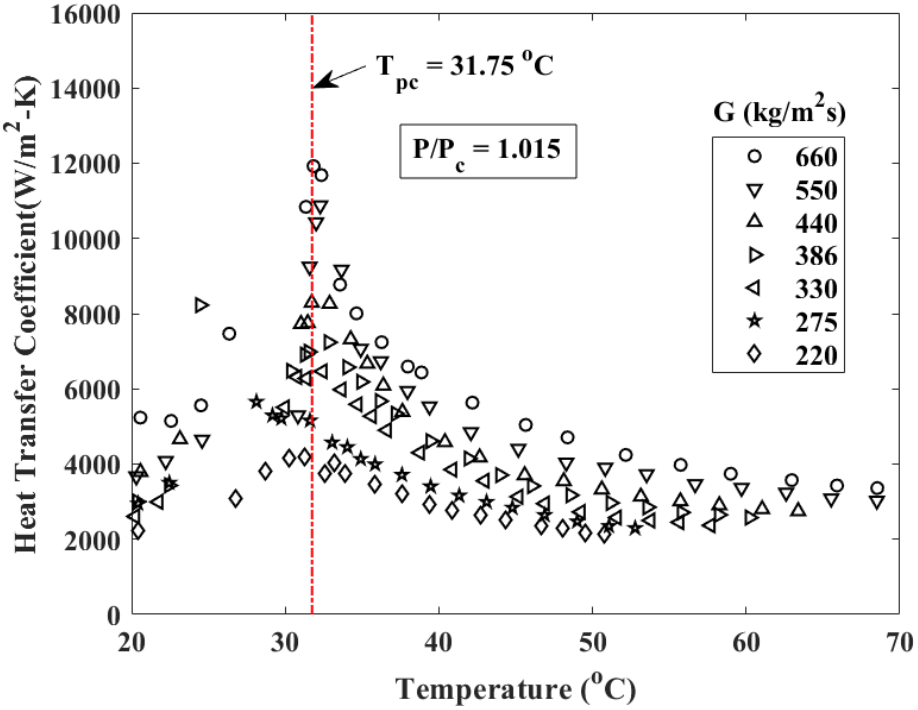

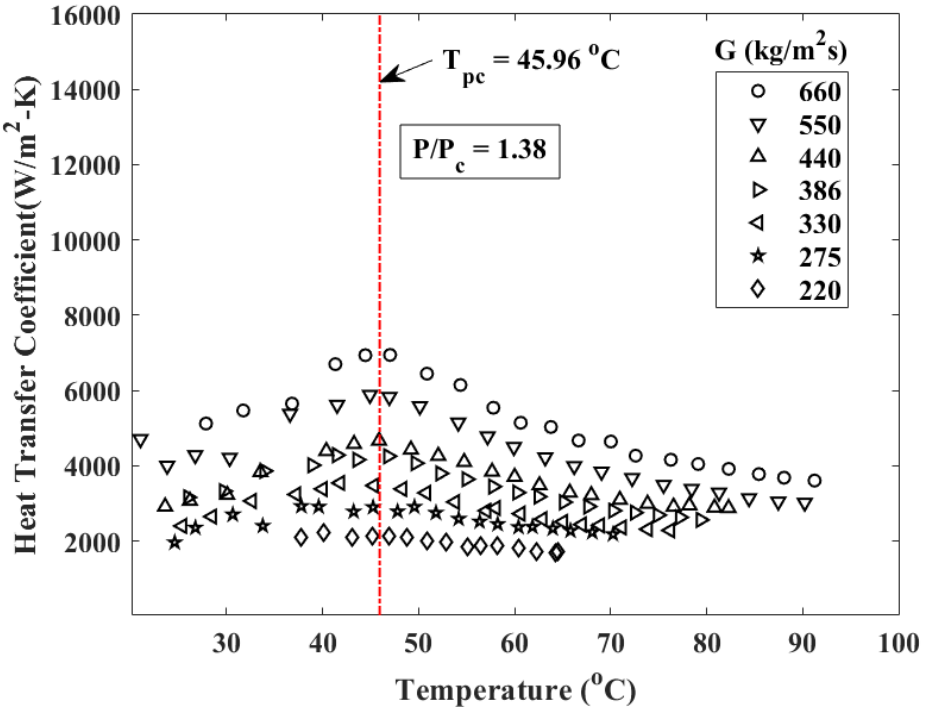

Figure 5-5: Average heat transfer coefficients plotted as a function of the average bulk fluid temperature for the offset NACA0020 Airfoil fin PCHE test section

This dependence of the average heat transfer coefficient on the pressure and the temperature can be attributed to the variation in isobaric specific heat and Prandtl number; see Figure 1-2 for example. The heat transfer coefficients of the offset rectangular fin PCHE test section are higher than the offset NACA0020 airfoil fin PCHE test section under identical Reynolds number, $\overline{Re}$ and Prandtl number, $\overline{Pr}$. For example, at P/P_c = 1.38, $\overline{T_b}$ = 84.4 °C and G = 550 kg/m^{2}s, the measured average heat transfer coefficient for the offset NACA0020 airfoil fin PCHE is 3140.7±70.9 W/m^2-K (at $\overline{Re}$ = 25,192 and $\overline{Pr}$ = 1.73) whereas for the offset rectangular fin PCHE, at P/P_c = 1.38, $\overline{T_b}$ = 84.9 °C and G = 635 kg/m^{2}s, the measured average heat transfer coefficient is 4709.3±131.6 W/m^2-K (at $\overline{Re}$ = 25,472 and $\overline{Pr}$ = 1.86).

5.3.2 Pressure Drops

The measured pressure drops are plotted as a function of the average fluid bulk temperature, $\overline{T_b}$ for different mass fluxes, G and pressures in Figure 5-6 (for the offset rectangular fin PCHE test section) and Figure 5-7 (for the offset NACA0020 airfoil fin PCHE test section). For the offset rectangular fin PCHE, the average uncertainty in the measurement of pressure drop is ±10.4%; whereas for the offset NACA0020 airfoil PCHE test section the average uncertainty is ±11.9%. The maximum uncertainty in the measured pressure drop occurred for low values of mass flux and temperatures below the pseudocritical temperature at P/P_c = 1.014.

The pressure drops decreases with mass flux due to lower flow velocities and Reynolds numbers. For fluid temperatures greater than the pseudocritical temperature (marked as dashed vertical lines in Figure 5-6 and Figure 5-7), density and other properties of the fluid resembles that of a gas and the pressure drop is high in this region due to higher fluid velocities. As the fluid temperature falls below the pseudocritical temperature, a steep decrease in the pressure drop is noted for all the mass fluxes due to a rapid increase in the density and reduction of fluid velocity. For example, at P/P_c = 1.014, $\overline{T_b}$ = 68.5 °C and G = 660 kg/m^{2}s, the measured pressure drop for the offset NACA0020 airfoil fin PCHE is 61.97±0.76 kPa (at $\overline{Re}$ = 36,590); whereas the measured pressure drop falls to 22.43±0.73 kPa at $\overline{T_b}$ = 31.35 °C (at $\overline{Re}$ = 19,226). The decrease in pressure drop across the pseudocritical temperature is less drastic as the pressure increases, which can again be attributed to the density variation at these pressures; see Figure 1-4 for an example of variation of the density with pressure and temperature. The measured pressure drops of the

offset rectangular fin PCHE test section are higher than the offset NACA0020 airfoil fin PCHE test section under identical Reynolds number. For example, at P/P_c = 1.38, $\overline{T_b}$ = 91.2 °C and G = 660 kg/m^{2}s, the measured pressure drop for NACA0020 airfoil fin PCHE is 44.8±0.28 kPa (at $\overline{Re}$ = 31,018); For the offset rectangular fin PCHE, at P/P_c = 1.38, $\overline{T_b}$ = 84.9 °C and G = 635 kg/m^{2}s, the measured pressure drop is 52.0±0.62 kPa (at $\overline{Re}$ = 25,472).

The measured pressure drop is broken down into the local (expansion/contraction) loss at the inlet/outlet, acceleration pressure loss components as described in the data reduction procedure. The local and acceleration losses as a percentage of the total pressure drop are plotted against the average fluid temperature in Figure 5-8 for the offset rectangular fin PCHE.

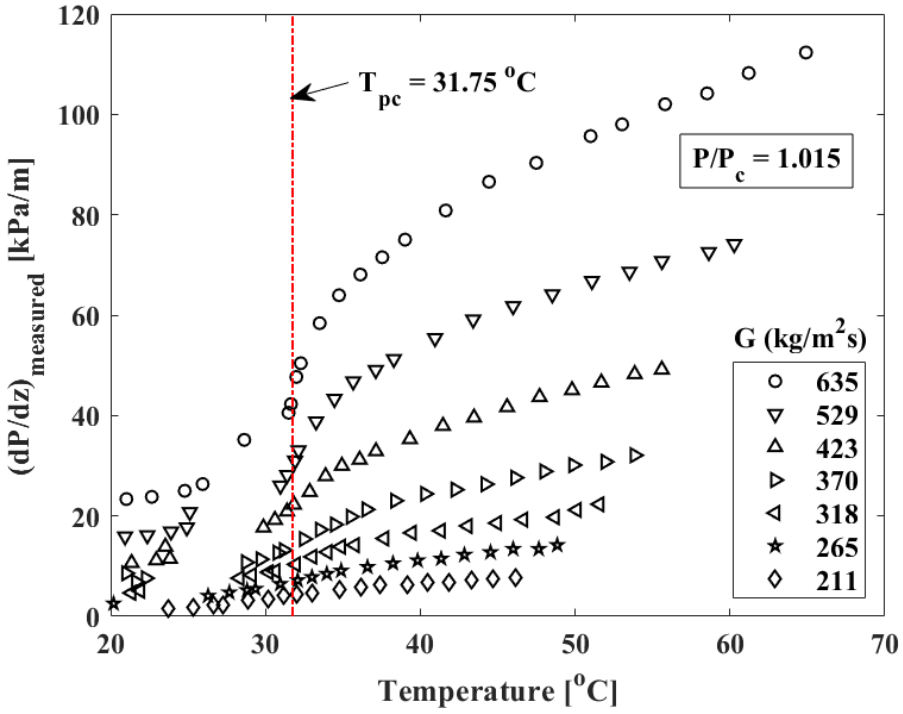

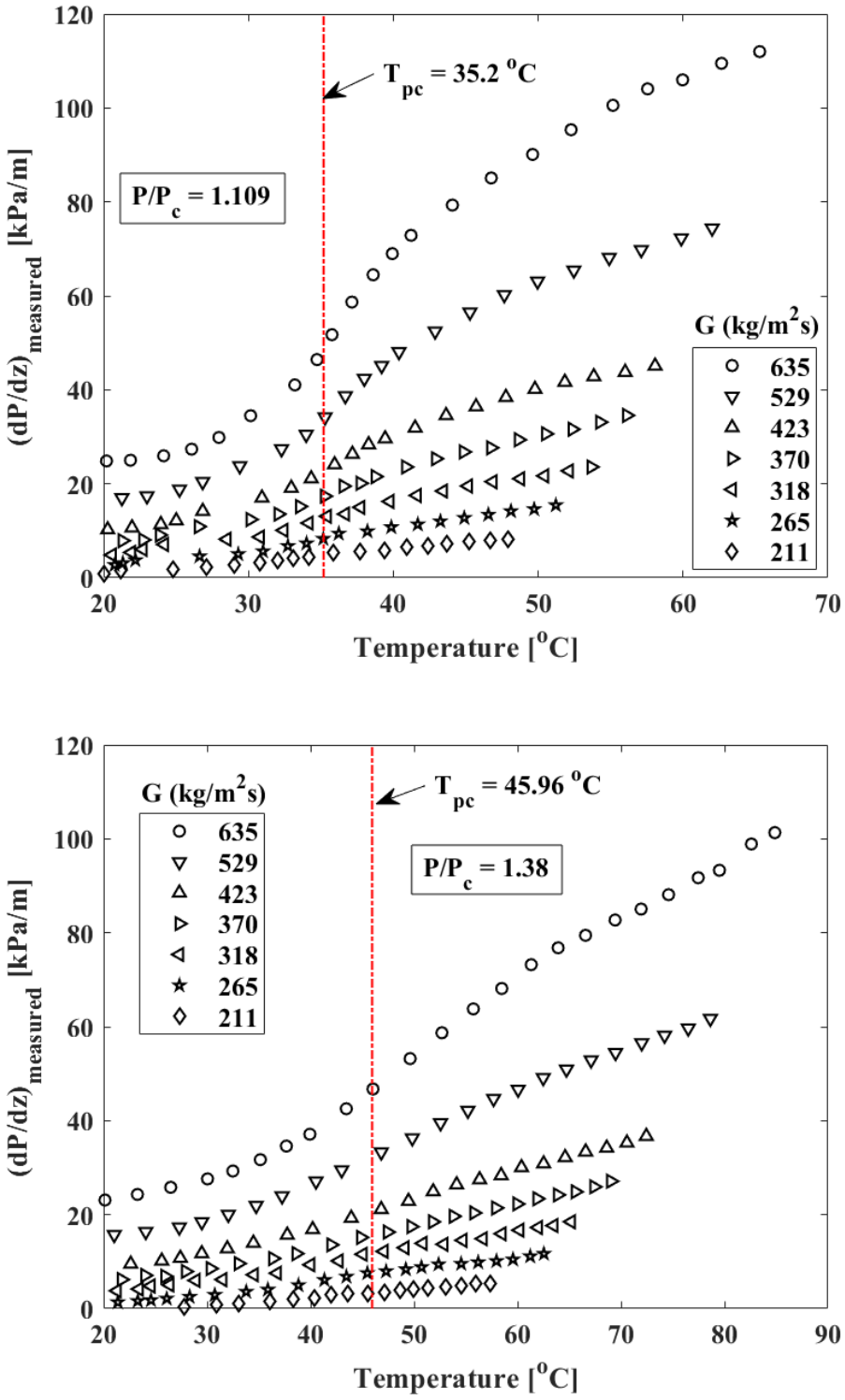

Figure 5-6: Measured pressure drops plotted as a function of the average bulk fluid temperature for the offset rectangular fin PCHE test section

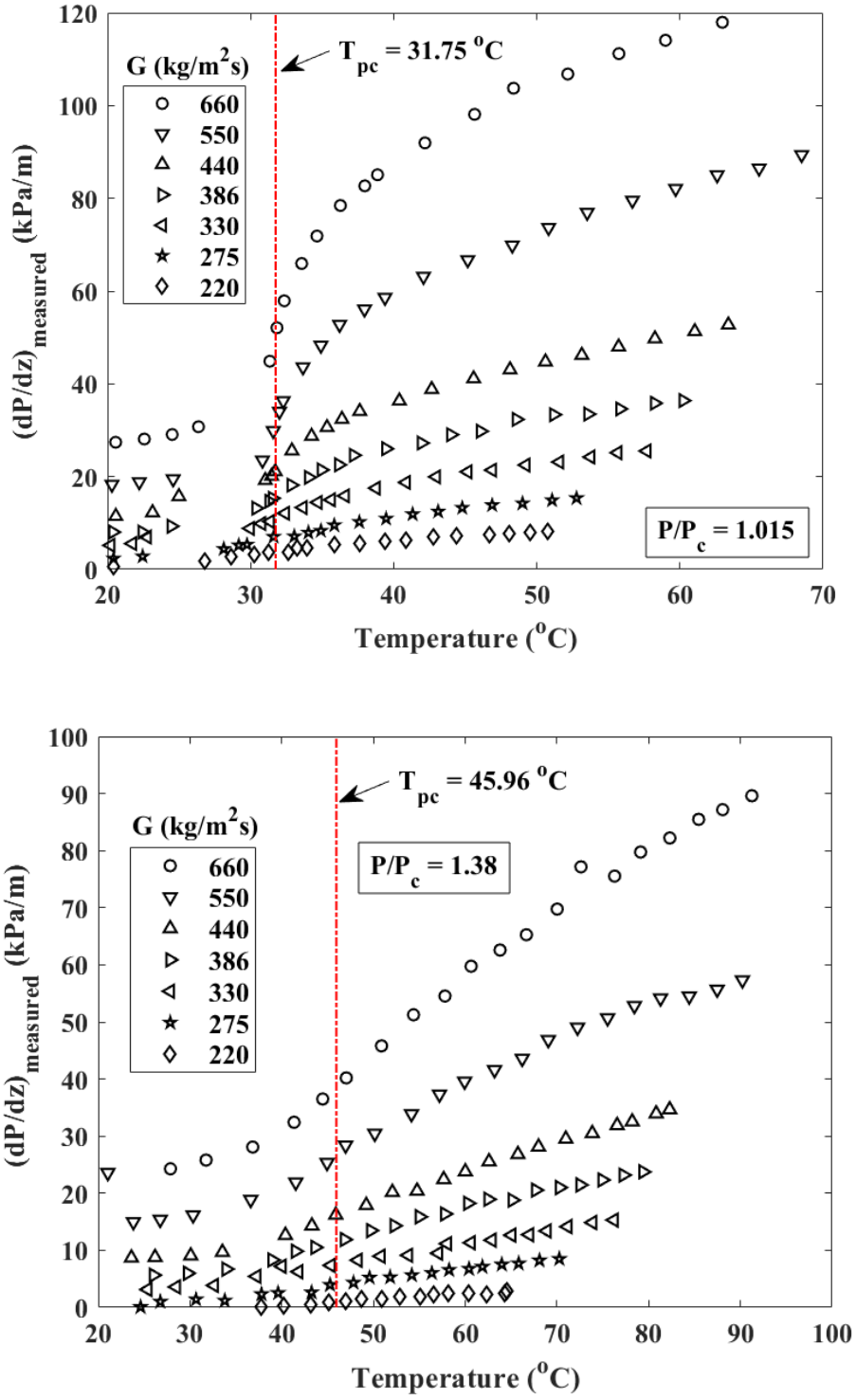

Figure 5-7: Measured pressure drop plotted as a function of the average bulk fluid temperature for the offset NACA0020 Airfoil fin PCHE test section

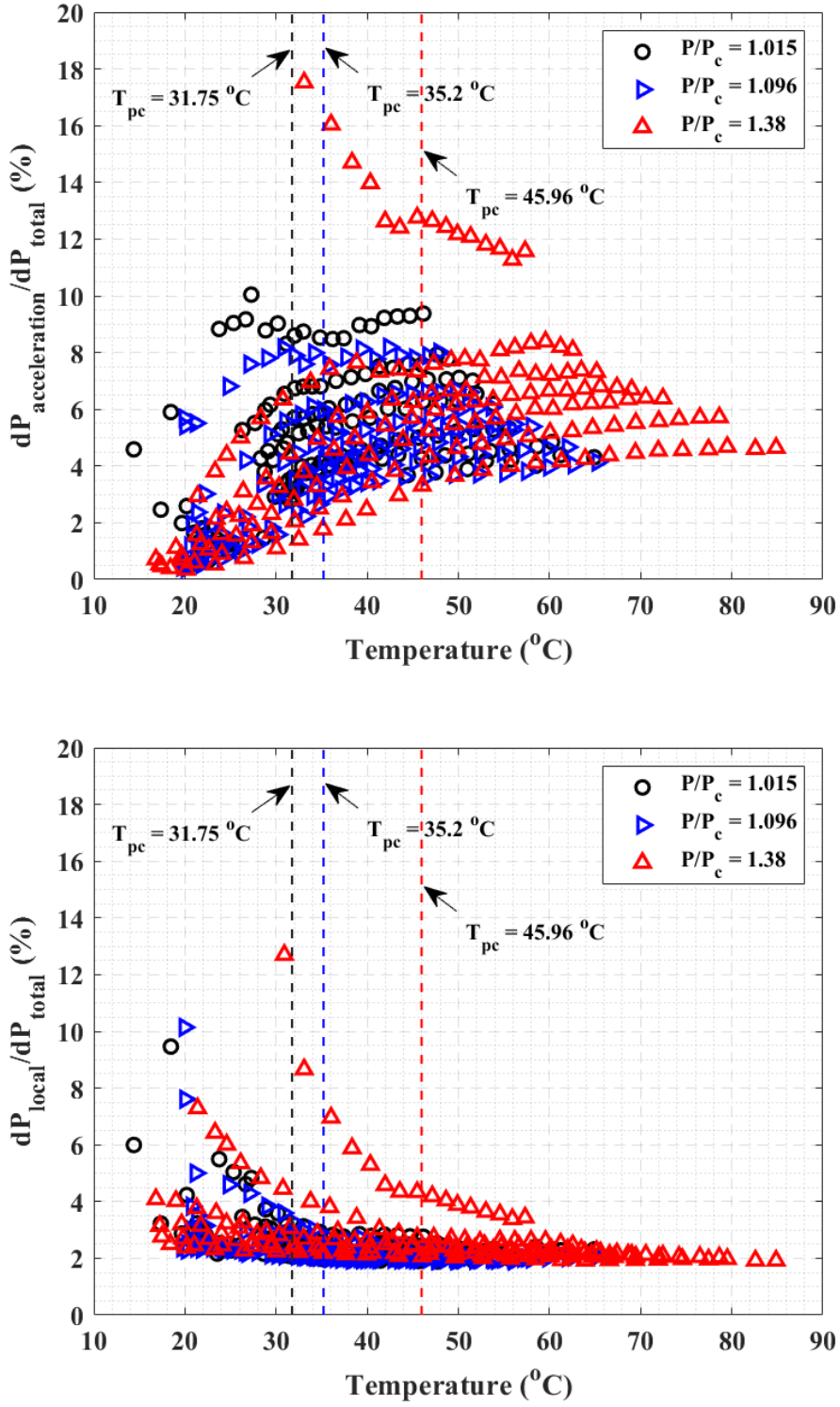

Figure 5-8: Fraction of the acceleration (top) and the local (bottom) pressures losses plotted as a function of the average fluid temperature for the offset rectangular fin PCHE test section

The local (entrance/exit) losses are only a small fraction of the total pressure drop, typically in the range of 2-6%. The acceleration pressure losses are highest in the vicinity of pseudocritical temperature where the fluid transition from gas-like to liquid-like densities. The acceleration pressure losses are typically less than 10% of the total pressure drop and are highest for low mass fluxes. Therefore, the frictional pressure loss is the major fraction of the total pressure drop (typically > 80%).

A computational fluid dynamics (CFD) study was conducted using ANSYS FLUENT to understand the capabilities of existing models to predict the experimental data for PCHEs. When compared to the experimental data, the CFD models under-predicted the pressure drop by ~30-40% and for both the PCHEs. Overall good agreement between the CFD models and the experimental data was observed for the total calculated heat duty. Four different turbulence models from FLUENT database (SST k-ω, Standard k-ε, RNG k-ε, Realizable k-ε) [108] were selected to investigate the choice of turbulence models on the numerical solution. All the turbulence models predicted the trends in heat transfer coefficients. For the temperatures far away the pseudocritical temperature, the differences between the four turbulence models is quite small and all the models agreed well with the experimental data. However, for bulk temperatures close to the pseudocritical temperature, differences between the turbulence models and the experimental data were found to be greater than >30% in some cases. Out of the four turbulence models, RNG k-ε and SST k-ω models offered best agreement with the experimental data. More details about the CFD study can be found in APPENDIX F.COmputational Fluid Dynamics study

5.4 Friction Factor Model Development

Frictional pressure drop for each of the experimental runs is calculated as shown in Equation (5.28) to account for the density variation along the test section.

$$\Delta P_{calc} = \sum_{i=1}^{10} 2 \left(\frac{L}{N.D_h}\right) \frac{G^2}{\rho_i} f_i \tag{5.28}$$

where ρ_i and f_i represent the calculated local bulk fluid density and friction factor.

Assuming a friction factor of the form,

$$f_i = aRe_i^b \tag{5.29}$$

The coefficients a and b are calculated from least-squares curve fitting procedure to the experimental data, as depicted in Equation (5.30).

$$\sum_{i=1}^{N_{expt}} \left(\Delta P_{calc}^i - \Delta P_{exp}^i\right)^2 \rightarrow minimum \tag{5.30}$$

Table 5-2 summarizes the coefficients a and b determined for both the PCHE test sections. For the range of Reynolds numbers tested, the friction factor was found to be nearly independent of the Reynolds number for both the test sections. This indicates that the pressure losses for both the PCHEs are dominated by form losses due to flow across the fins.

Table 5-2: Coefficients a and b determined from fitting the fanning friction factor of Equation (5.29) form to the experimental data for both the PCHE test sections

Test section	a	b
Offset rectangular fin PCHE	0.0276	0
Offset NACA0020 airfoil fin PCHE	0.0256	0

Figure 5-9 and Figure 5-10 present the predictions from the fitted friction factor correlation to the experimentally measured values for the offset rectangular fin and the offset NACA0020 airfoil fin PCHE test sections respectively.

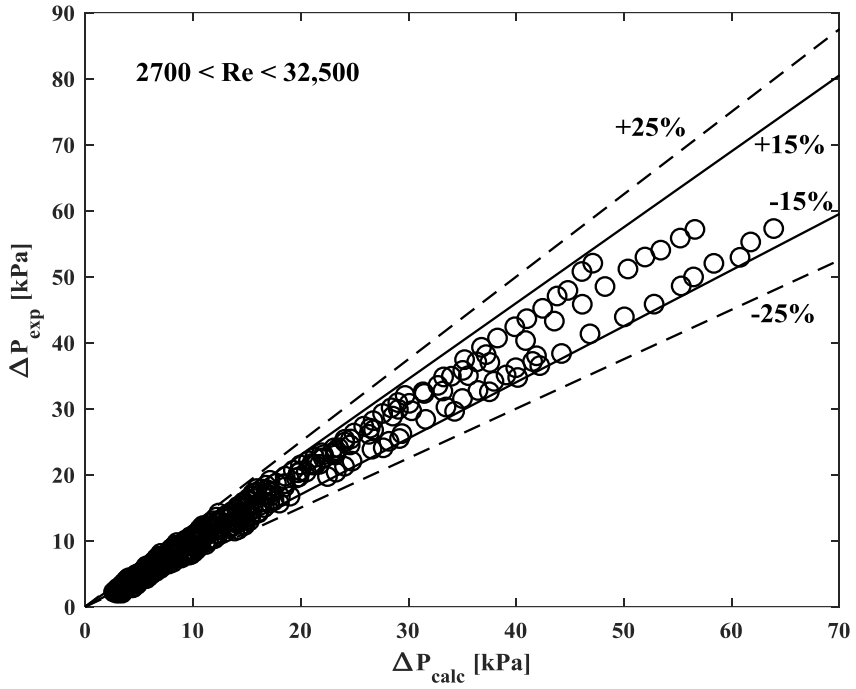

Figure 5-9: Experimental vs calculated frictional pressure drops for the offset rectangular fin PCHE test section

The proposed friction factor correlation was able to predict the frictional pressure drops with mean absolute error (MAE) of ±11% and standard deviation error of ±13.5% for the offset rectangular fin PCHE test section. 75% of the experimental data is predicted within ±15% and 92% of the experimental data is predicted within ±25%.

For the offset NACA0020 airfoil fin PCHE test section, the MAE is ±11% and the standard deviation error is ±14.7%. 79% of the experimental data is predicted within ±15% and 90% of the experimental data is predicted within ±25%.

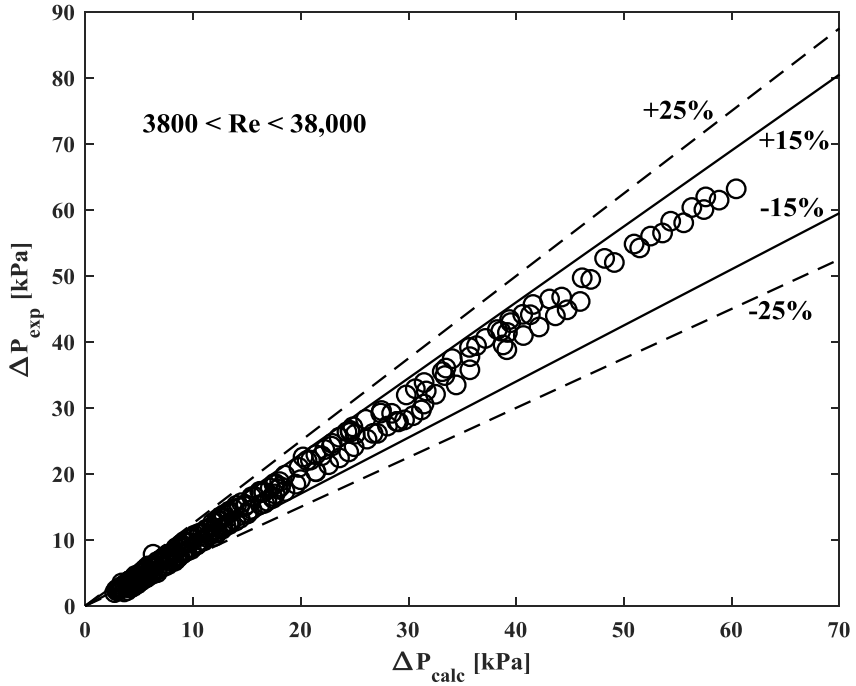

Figure 5-10: Experimental vs calculated frictional pressure drops for the offset NACA0020 airfoil fin PCHE test section

5.5 Nusselt Number Model Development

The calculated average Nusselt number for each experimental run is assumed to be of the form,

$$\overline{Nu_{calc}} = a\overline{Re}^{b}\overline{Pr}^{c}\left(\frac{\overline{\rho_b}}{\overline{\rho_w}}\right)^{d}\left(\frac{\overline{C_{pb}}}{\overline{C_p}}\right)^{e} \tag{5.31}$$

where $\overline{C_p} = \frac{\overline{i_w}-\overline{i_b}}{\overline{T_w}-\overline{T_b}}$ and other average properties are calculated as described in Equation (5.20). A close look at Equation (5.31) reveals that the equation is of Dittus-Boelter correlation form ($a\overline{Re}^{b}\overline{Pr}^{c}$) with additional wall to bulk property ratios to account for the variation in thermophysical properties, as recommended by Jackson [63] to correlate the

heat transfer data in the supercritical region. The coefficients a through e are calculated from least-squares curve fitting to the experimental data as depicted in Equation (5.32).

$$\sum_{i=1}^{N_{expt}} \left(\overline{Nu_{calc}^{i}} - \overline{Nu_{exp}^{i}}\right)^2 \rightarrow minimum \tag{5.32}$$

Table 5-3 summarizes the coefficients a through e determined for both the PCHE test sections.

Table 5-3: Coefficients a through e determined from fitting the Nusselt number of Equation (5.31) form to the experimental data for both the PCHE test sections

Test section	a	b	c	d	e
Offset rectangular fin PCHE	0.1034	0.7054	0.3489	0.9302	-0.3660
Offset NACA0020 airfoil fin PCHE	0.0601	0.7326	0.3453	0.4329	-0.3556

Figure 5-11 and Figure 5-12 present predictions from the Nusselt number correlation to the experimentally measured values for the offset rectangular fin PCHE and the offset NACA0020 airfoil fin PCHE test sections respectively.

The proposed Nusselt number correlation was able to predict the experimental Nusselt numbers with MAE of ±9.1% and standard deviation error of ±15.4% for the offset rectangular fin PCHE test section. 82% of the experimental data is predicted within ±15% and 90% of the experimental data is predicted within ±25%.

For the offset NACA0020 airfoil PCHE test section, the MAE is ±5.2% and the standard deviation is ±8%. 92% of the experimental data is predicted within ±15% and 98% of the experimental data is predicted within ±25%.

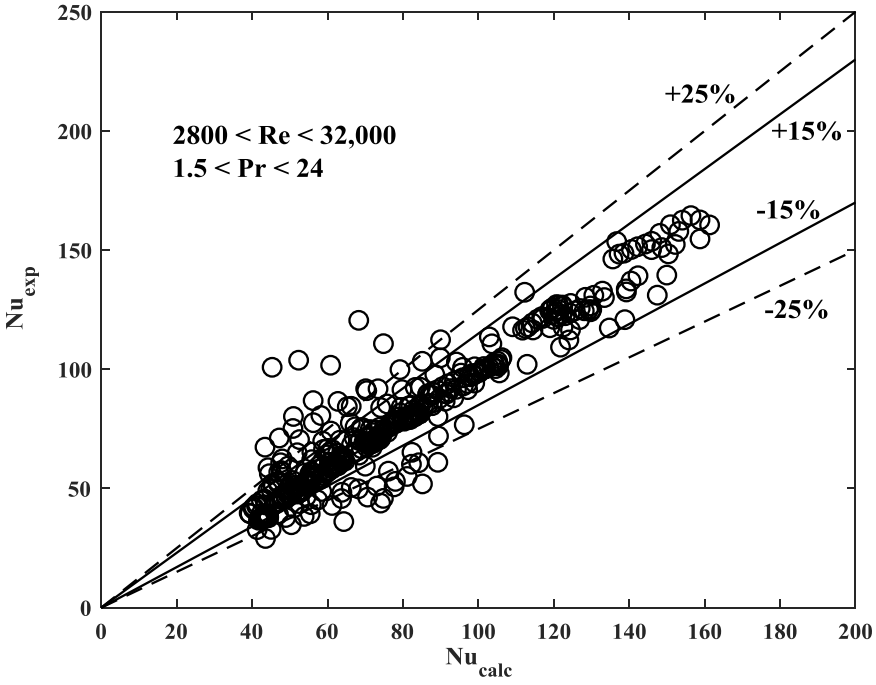

Figure 5-11: Experimental vs calculated average Nusselt numbers for the offset rectangular fin PCHE test section

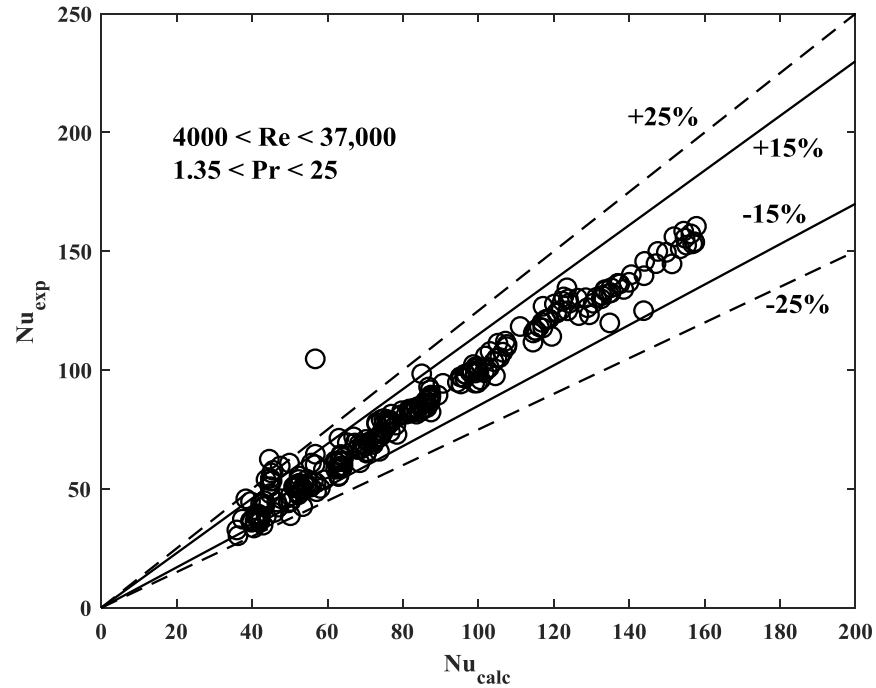

Figure 5-12: Experimental vs calculated average Nusselt numbers for the offset NACA0020 airfoil fin PCHE test section

5.6 Nusselt Number correlation for Gas-Like Regime

Equation (5.31) captures the heat transfer data quite well near the critical point but requires an iterative process to calculate the wall temperature and the Nusselt number. For fluid temperatures much higher than the critical temperature, the fluid essentially behaves like a gas and the Nusselt number correlation can be simplified for design purposes. Based on the variation in the thermophysical properties, the fluid behavior can be divided into three regimes; liquid-like, pseudo-critical, and gas-like. Transition between these flow regimes can be quantitatively defined based on the specific work of thermal expansion/contraction, $E_o = P\beta/\rho C_P$ [109, 110].

Figure 5-13 shows a plot of E_o with respect to temperature and enthalpy for carbon dioxide at three different operating pressures. The plot of E_o versus enthalpy shows a gradual increase to a point where E_o=0.05, followed by an abrupt change in the slope until E_o ~ 0.24 where the curve reaches maximum, and then decreases with further increase in enthalpy. Based on this trend, the three regimes are defined: (a) a liquid-like regime where the change in E_o with temperature/enthalpy is gradual due to small property variations; (b) a pseudo-critical transition regime where the change in E_o is rapid with temperature; and (c) the gas-like regime where the E_o starts to decrease as the temperature increases. The transition from the pseudo-critical transition regime to the gas-like regime can be found when dE_o/dT=0.

Table 5-4 shows the corresponding temperature ranges for the three different flow regimes described above and Equation (5.33) represents the temperature at which transition to gas-like phase occurs as a function of the pressure.

$$T_{GL} = 0.0034P^3 - 0.3284P^2 + 15.963P - 43.85 \quad (5.33)$$

where T_{GL} is in ºC and P is in MPa

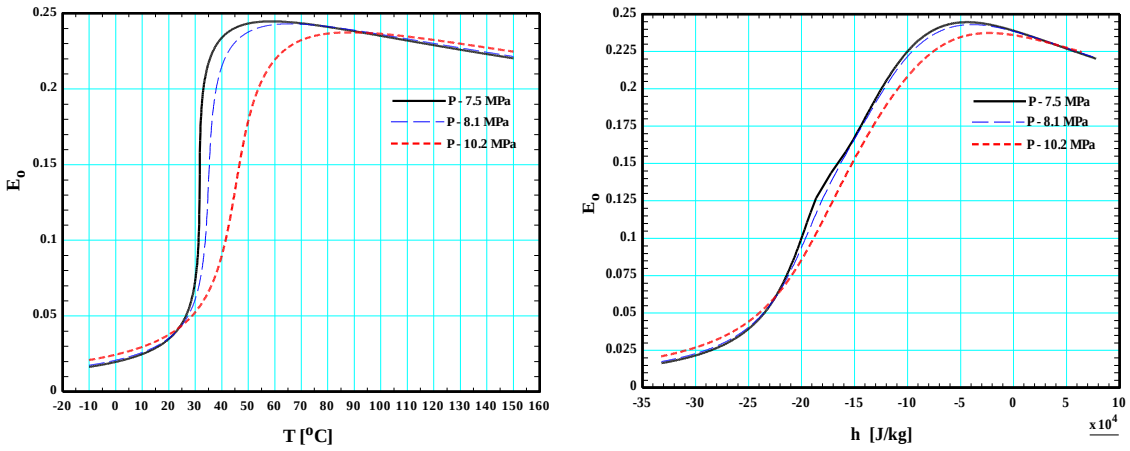

Figure 5-13: Plot of E_o versus temperature and enthalpy for carbon dioxide at three different pressures in the critical region

The Nusselt number correlation presented in (5.31) can be extended to the gas-like regime by dropping the property ratio terms, since the variation in thermophysical properties is not as drastic as in the pseudo-critical region. Equations (5.34) and (5.35) can be used to calculate the gas-like regime Nusselt numbers for the offset rectangular fin PCHE and the offset NACA 0020 airfoil fin PCHE test sections respectively.

$$Nu_{calc} = 0.1034\, Re^{0.7054} Pr^{0.3489} \quad (5.34)$$

$$Nu_{calc} = 0.0601\, Re^{0.7326} Pr^{0.3453} \quad (5.35)$$

Table 5-4: Temperature boundaries determined for three different flow regimes

Pressure [MPa]	Liquid-like regime	Pseudo-critical transition regime	Gas-like regime
7.5	T < 26.46 ºC	26.46 ºC ≤ T ≤ 58.79 ºC	T > 58.79 ºC
8.1	T < 27.25 ºC	27.25 ºC ≤ T ≤ 65.76 ºC	T > 65.76 ºC
10.2	T < 28.82 ºC	28.82 ºC ≤ T ≤ 88.44 ºC	T > 88.44 ºC

The correlations described above are screened against the measured experimental local Nusselt numbers for $T_b > T_{GL}$. Figure 5-14 and Figure 5-15 present the comparison between experimentally measured gas-like Nusselt numbers and calculated values for the offset rectangular fin PCHE and the offset NACA0020 airfoil PCHE test sections respectively. The proposed correlation was able to predict the experimental Nusselt numbers with MAE of ±5.6% and standard deviation error of ±6.9% for the offset NACA0020 airfoil PCHE test section. For the offset rectangular fin PCHE test section, the MAE is ±11.5% and the standard deviation error is ±13.2%.

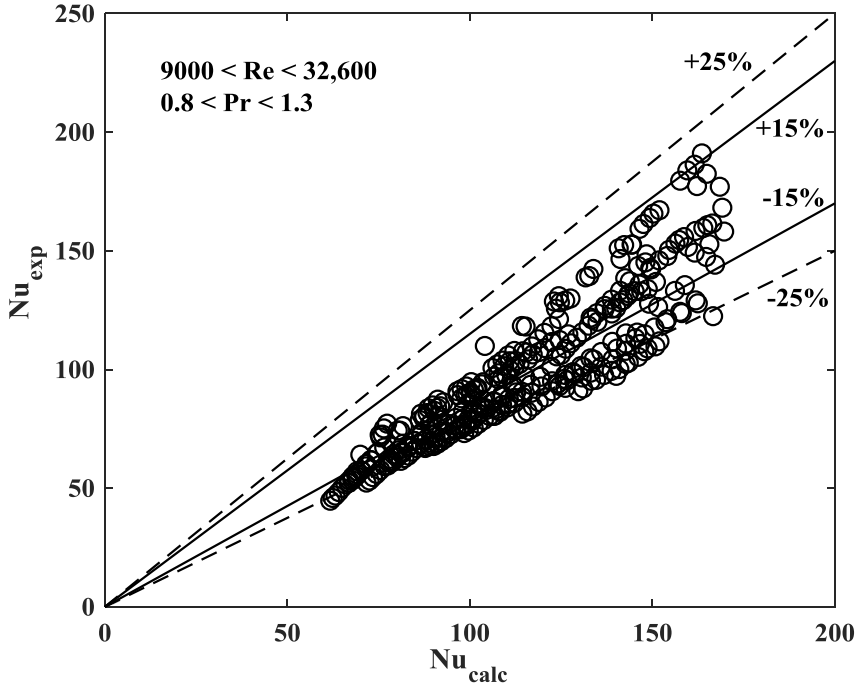

Figure 5-14: Experimental vs calculated Nusselt Numbers for the offset rectangular fin PCHE test section in the gas-like regime

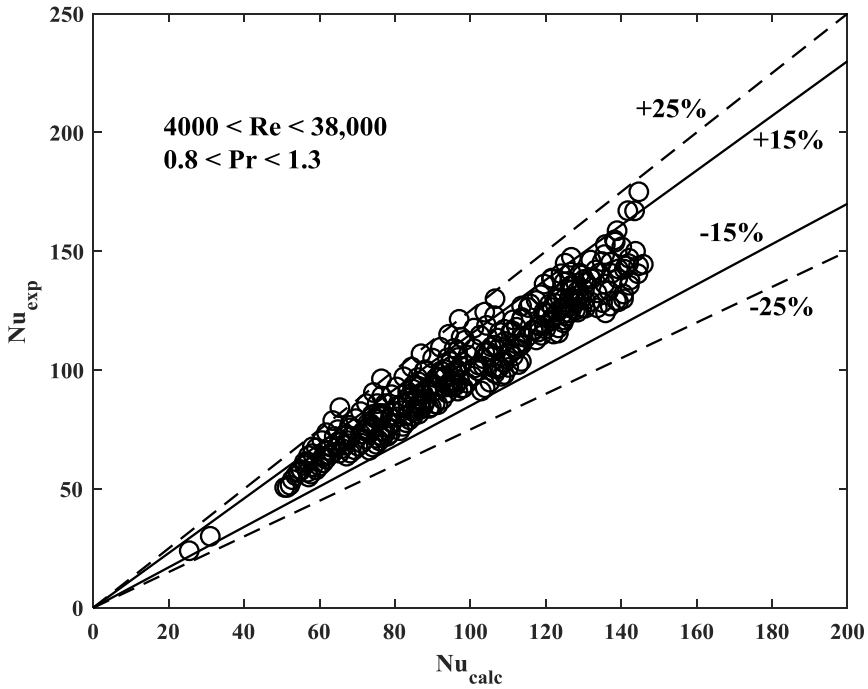

Figure 5-15: Experimental vs calculated Nusselt Numbers for the offset NACA0020 airfoil fin PCHE test section in the gas-like regime

CHAPTER 6. IMPACT OF TESTED HEAT EXCHANGERS ON PERFORMANCE AND COST OF SCO_2 BRAYTON CYCLE

A steady-state thermodynamic model for the supercritical CO_2 (sCO_2) Brayton cycle was developed to study the impact of tested PCHEs on the performance and the capital cost of the cycle. This chapter provides details of the steady-state model, capital cost estimation methodology and presents cost-based optimization simulation results for several PCHEs. Figure 6-1 shows a schematic of the recompression Brayton cycle (RCBC) coupled to a sodium-cooled fast nuclear reactor (AFR-100) [111]. Detailed explanation of the RCBC layout can be found in CHAPTER 1.

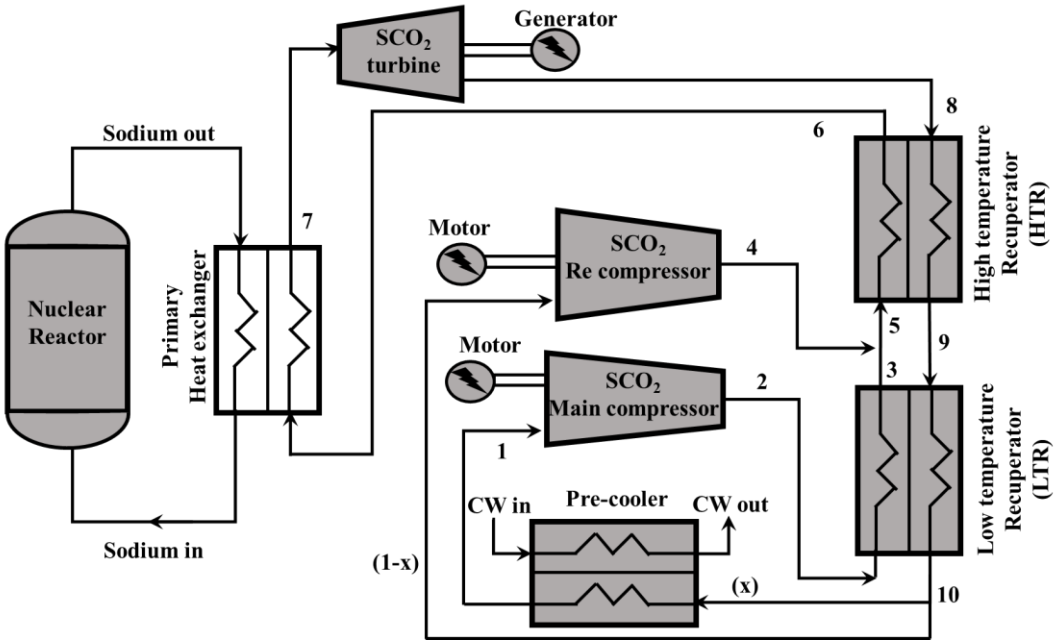

Figure 6-1: Schematic of Recompression Brayton Cycle (RCBC)

6.1 Turbomachinery Models

For the turbomachinery components, i.e. the main compressor, the re-compressor and the turbine, inlet pressure (P_{in}) and temperature (T_{in}), outlet pressure (P_{out}) and isentropic efficiency ($\varepsilon_{compressor}$ or $\varepsilon_{turbine}$) are provided as the inputs. The outputs of the turbomachinery model are the outlet temperature (T_{out}) and the power consumption/generation ($\dot{W}$). The calculation procedure for the turbomachinery components is described in the equations below:

$$s_{in} = s(T_{in}, P_{in}) \tag{6.1}$$

$$h_{in} = h(T_{in}, P_{in}) \tag{6.2}$$

$$h_{out,s} = h(s_{in}, P_{out}) \tag{6.3}$$

$$h_{out} = h_{in} + \frac{1}{\varepsilon_{compressor}}(h_{out,s} - h_{in}) \tag{6.4}$$

$$h_{out} = h_{in} - \varepsilon_{turbine}(h_{in} - h_{out,s}) \tag{6.5}$$

$$T_{out} = T(h_{out}, P_{out}) \tag{6.6}$$

$$\dot{W} = \dot{m}(h_{in} - h_{out}) \tag{6.7}$$

where h_{in} and s_{in} is the inlet enthalpy and entropy respectively. $h_{out,s}$ is the outlet enthalpy for ideal compression or expansion processes during which the entropy remains constant, i.e. s_{out}=s_{in}. The suffixes in and out denotes the inlet and outlet conditions respectively. The outlet enthalpy for the compression and the expansion process is calculated using Equation (6.4) and Equation (6.5) respectively. $\dot{m}$ is the mass flow rate of CO_2 entering the turbomachinery components. All the CO_2 properties are calculated using the REFPROP V9.1 database. A more detailed turbine and compressor design procedure can be

incorporated to calculate the isentropic efficiencies as a function of the cycle conditions [112]. However, for the purpose of the present work the isentropic efficiencies are assumed to be constant.

6.2 Heat Exchanger Models

In the sCO_2 recompression Brayton cycle (RCBC) layout, there are several types of heat exchangers, i.e. the primary heat exchanger, recuperators and the pre-cooler. In the primary heat exchanger (PHX), CO_2 is heated (via heat transferred from sodium) before entering the turbine. There are two recuperators – the high temperature recuperator (HTR) and the low temperature recuperator (LTR) where both the hot and cold streams are CO_2. The recuperators pre-heat CO_2 prior to the PHX by extracting excess heat available in the hot exhaust stream from the turbine. The pre-cooler rejects the remaining excess heat from the cycle to the cooling water (CW). The heat gained by the cooling water is rejected to the atmosphere in a cooling tower [113]. Alternatively, the excess heat from CO_2 can be rejected to the atmosphere directly using a direct dry cooler [5]. Two versions of the heat exchanger model are developed depending on the application. In one version of the heat exchanger model (referred to as PCHE performance), the model calculates the outlet temperature, outlet pressure of hot and cold streams when the inlet temperature, inlet pressure and mass flow rate of both the streams are provided as the inputs. In the second version of the heat exchanger model (referred to as PCHE sizing), the model calculates the required heat exchanger length to meet a desired heat duty when the inlet temperature, pressure and mass flow rate of the hot and cold streams are provided as the inputs. Irrespective of the heat exchanger model (PCHE performance or PCHE sizing), the underlying theory and assumptions are the same. Since the properties of CO_2 vary

drastically near the critical point, the heat exchanger is divided into several nodes as shown in Figure 6-2.

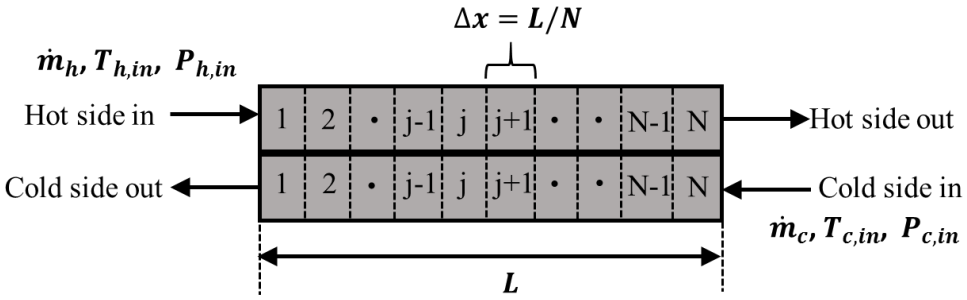

Figure 6-2: Discretization scheme of the heat exchangers

For each node, the properties of the hot and cold streams are assumed to be constant. The hot and cold stream inlet pressure, inlet temperature and mass flow rates are provided as the input. The heat exchanger model calculations proceed as follows:

1) For node j, the average temperature (T_{avg}) and pressure (P_{avg}) of the hot and cold streams are calculated. Fluid properties (μ, ρ, C_p, k etc.) are calculated at the average temperature and pressure.
2) The hot and cold side heat transfer coefficients, friction factors are calculated based on the average fluid properties, PCHE flow geometry and the mass flow rate (all of which effects the flow Reynolds number). The overall conductance, UA is calculated as follows:

$$UA = \frac{1}{\frac{1}{htc_h A_{s,h} \eta_h} + \frac{t_w}{k_w A_w} + \frac{1}{htc_c A_{s,c} \eta_c}} \tag{6.8}$$

where htc_h and htc_c are the hot and cold side heat transfer coefficients. $A_{s,h}$ and $A_{s,c}$ are the hot and cold side heat transfer areas. η_h and η_c are the hot and cold

side fin efficiencies. k_w is the thermal conductivity of the heat exchanger material and t_w is the plate thickness.

3) In case of the PCHE performance model, the heat transfer rate (Q), hot and cold streams exit enthalpies ($i_{h,out}, i_{c,out}$) and pressure ($P_{h,out}, P_{c,out}$) for the node j are calculated as follows:

$$Q = UA.(T_{h,avg} - T_{c,avg}) \tag{6.9}$$

$$i_{h,out} = i_{h,in} - \frac{Q}{\dot{m}_h} \tag{6.10}$$

$$i_{c,out} = i_{c,in} + \frac{Q}{\dot{m}_c} \tag{6.11}$$

$$P_{h,out} = P_{h,in} - 2\left(\frac{\Delta x}{D_{h,h}}\right)\frac{G_h^2}{\rho_h} f_h - \Delta P_{acc,h} \tag{6.12}$$

$$P_{c,out} = P_{c,in} - 2\left(\frac{\Delta x}{D_{h,c}}\right)\frac{G_c^2}{\rho_c} f_c - \Delta P_{acc,c} \tag{6.13}$$

where G_h and G_c are the hot and cold side mass fluxes. $D_{h,h}$ and $D_{h,c}$ are the hot and cold side hydraulic diameters. f_h and f_c are the hot and cold side friction factors. ΔP_{acc} is the pressure drop due to flow acceleration as described in Equation (5.23). Cold and hot side outlet temperatures are finally calculated based on the outlet enthalpies and pressures.

In the case of PCHE sizing model, length (Δx) of the node j is calculated as follows:

$$\Delta x = \frac{Q * Res_{total}}{N*(T_{h,avg} - T_{c,avg})} \tag{6.14}$$

where Q is the desired heat duty, N is the total number of discretization nodes and Res_{total} is the total resistance defined as,

$$Res_{total} = \frac{1}{htc_h WP_{s,h} \eta_h} + \frac{t_w}{WP_w k_w} + \frac{1}{htc_c WP_{s,c} \eta_c} \quad (6.15)$$

where $WP_{s,h}$ and $WP_{s,c}$ are the hot and cold side wetted perimeters. The total required length of the heat exchanger is calculated by summing the calculated lengths of all the individual control volumes.

4) The model iterates until the variation of the calculated enthalpies, pressures and temperatures are within the specified tolerance limits (10^{-5}).

6.3 Heat Transfer and Pressure drop Models

One of the objectives of this dissertation is to understand the effect of the continuous channel type PCHEs and the discontinuous fin type PCHEs on the cycle performance and the capital cost. The Nusselt number and friction factor for the semi-circular continuous channel type PCHEs are calculated using correlations proposed by Moisseytsev *et al.* (2010) [88]; Refer to Equations (2.57)-(2.61). Three different discontinuous fin type PCHEs (S-shaped, the offset rectangular fins and the offset NACA0020 airfoil fins) were selected for investigation. The Nusselt number and the friction factor for the discontinuous S-shaped fin PCHE are calculated according to the correlations proposed by Ngo *et al.* (2007) [86]; Refer to Equations (2.66) and (2.67). For the offset rectangular fin and the offset NACA0020 airfoil fin PCHEs, the Nusselt number and the friction factor are calculated using the correlations developed in CHAPTER 5. Figure 6-3 compares the friction factor and the Nusselt number of the PCHEs under consideration here.

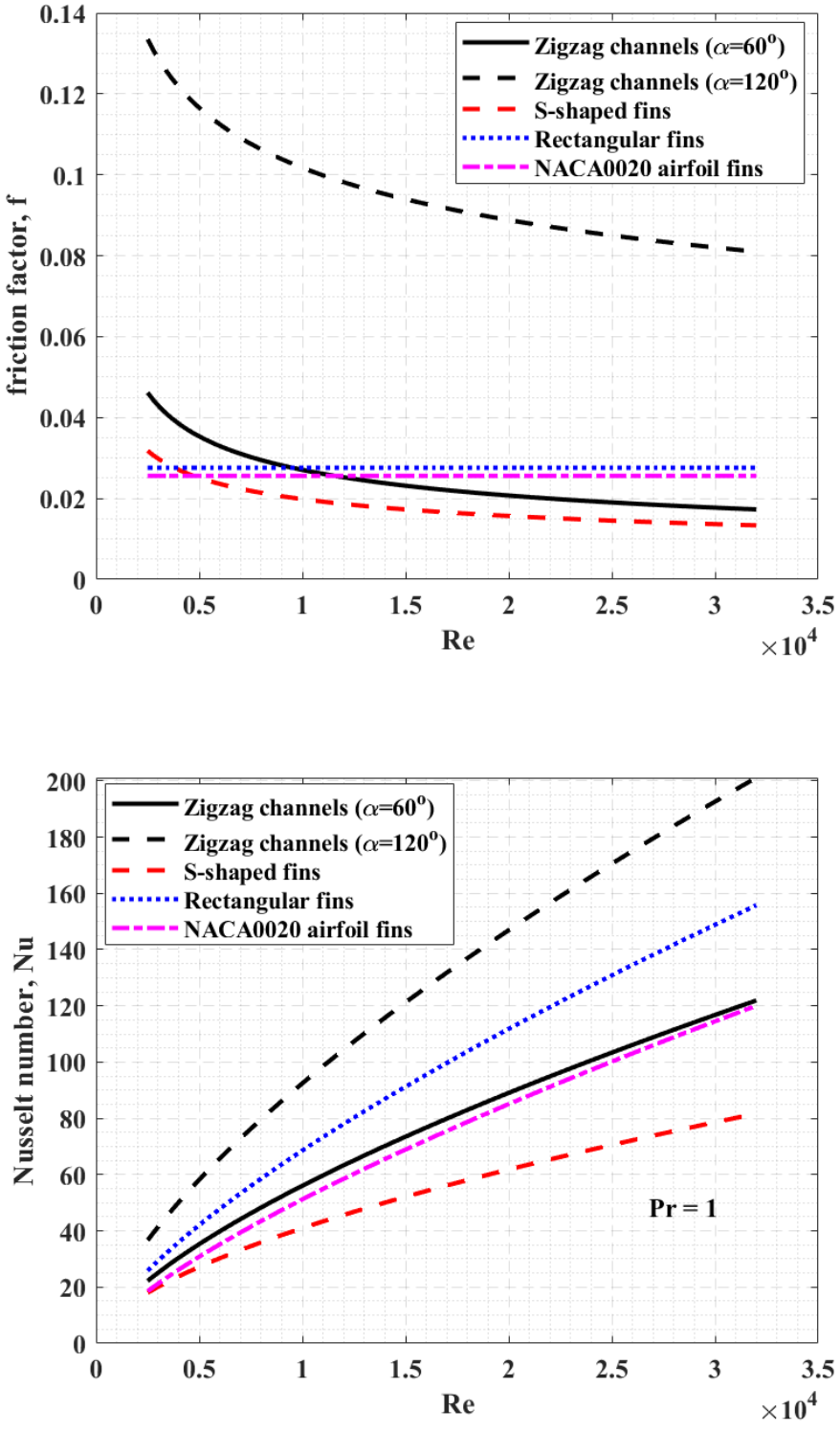

Figure 6-3: Fanning friction factor and Nusselt number of different PCHEs plotted as a function of Reynolds number

From Figure 6-3, both the offset rectangular fin and the offset NACA0020 airfoil fin PCHEs offer significantly lower friction factor compared to the zigzag channel ($\alpha = 2\theta_b$=120°) but higher than the S-shaped fins and zigzag channel ($\alpha = 2\theta_b$=60°) for majority of the turbulent flow regime (Re>10,000). However, the Nusselt number of both the offset rectangular fin and the offset NACA0020 airfoil fin PCHEs is higher than that of S-shaped fin. Increasing the channel bending angle (α) from 60° to 120° increases the Nusselt number (and the heat transfer coefficient) nearly two-fold.

6.4 Recompression Brayton Cycle Model Flowsheet

The flowsheet of the recompression Brayton cycle (RCBC) model is shown in Figure 6-4. The model reads the cycle inputs shown in Table 6-1 and are kept constant throughout this study. In the first step, the turbomachinery equations (6.1)–(6.7) are solved for the main compressor, the re-compressor and the turbine. For the first iteration, the re-compressor inlet pressure is set equal to the main compressor inlet pressure and the re-compressor inlet temperature is set equal to the main compressor outlet temperature plus 10 °C (a reasonable assumption for the cold end approach temperature of the LTR). The turbine inlet and outlet pressures are calculated as follows:

$$P_{turbine,in} = P_{MC,out} - \Delta P_{LTR,c} - \Delta P_{HTR,c} - \Delta P_{PHX,c} \quad (6.16)$$

$$P_{turbine,out} = P_{MC,in} + \Delta P_{LTR,h} + \Delta P_{HTR,h} + \Delta P_{pre-cooler,h} \quad (6.17)$$

where ΔP is the pressure drop of streams in heat exchangers and subscripts h and c represent the hot and the cold streams respectively. For the first iteration, all the pressure drops are assumed to be zero and the pressure drops are calculated and updated during the subsequent iterations. Also, the turbine inlet temperature is assumed to be equal to the

sodium inlet temperature minus 10 °C for the first iteration and updated to the calculated value (from PCHE performance model for the PHX) for the subsequent iterations.

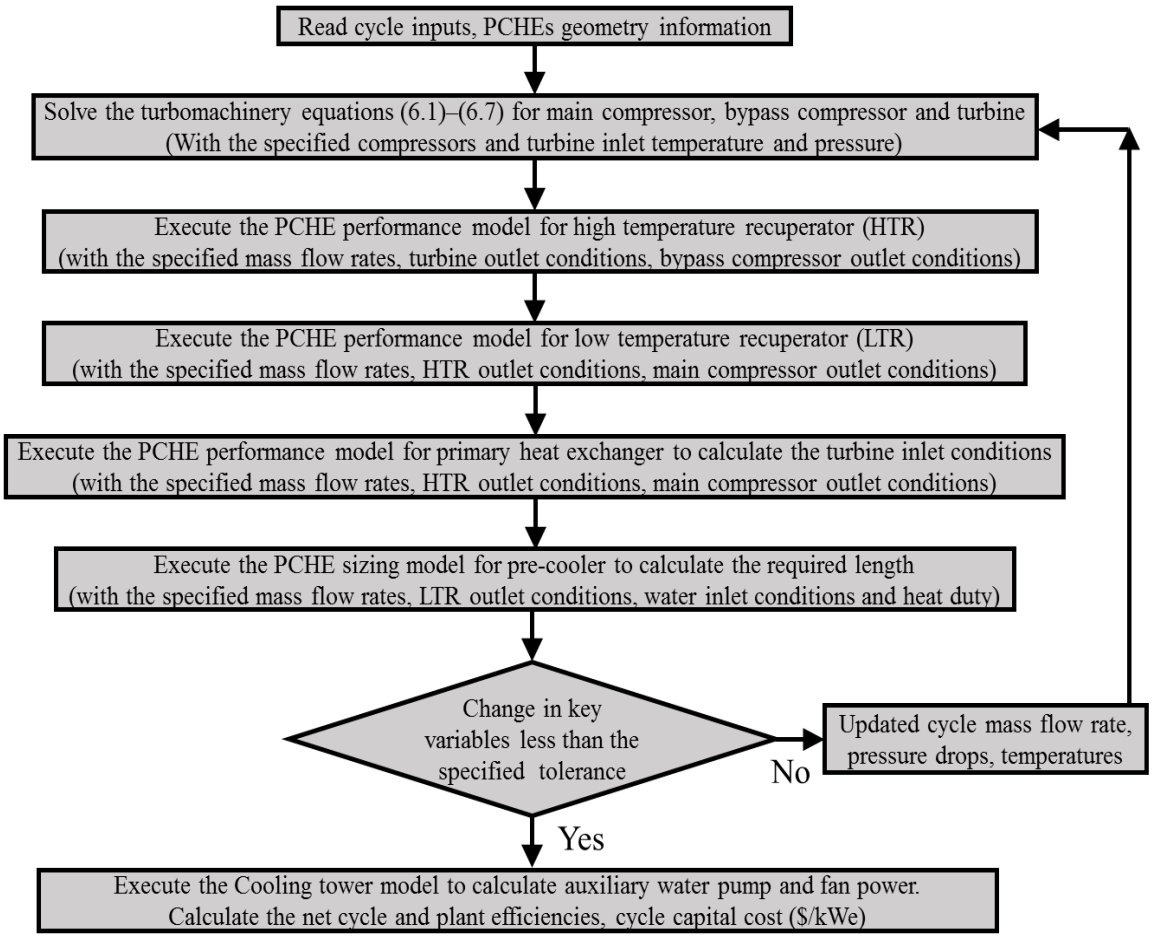

Figure 6-4: Flowsheet of the recompression Brayton cycle (RCBC) model

After the code obtains the solution to the turbomachinery models, the PCHE performance model is executed for the HTR. The hot side inlet conditions are set equal to the turbine exhaust conditions and the cold side inlet conditions are set equal to the re-compressor outlet conditions. The hot side outlet conditions calculated from the PCHE performance model for the HTR are used as the inputs to the hot side inlet conditions for the LTR. The cold side inlet conditions for the LTR are set equal to the main compressor outlet conditions. The PCHE performance model for the PHX calculates the heat duty of

the PHX and the new turbine inlet temperature. The mass flow rate of CO_2 is adjusted until the calculated PHX heat duty is equal to the reactor thermal input (250 MW_{th}). In the next step, the PCHE sizing model is executed for the pre-cooler to calculate the required length of the pre-cooler. The hot side outlet conditions from the LTR model are set equal to the hot side inlet conditions to the pre-cooler. The cooling water parameters can be found in Table 6-1.

The model then checks for the convergence of key variables (calculated PHX heat duty, pressure drops and effectiveness of all the heat exchangers). If the change in variables is not within the specified tolerance (10^{-5}), the model is executed again with updated mass flow rate, pressure drops and temperatures until the convergence criteria is met. Finally, the cooling tower model is executed to calculate the cooling water pump power, the cooling tower fan power and the capital cost of the cooling tower. Details of the cooling tower model and the cooling tower capital cost estimation methodology can be found in Pidaparti *et al.* (2015) [113] and APPENDIX H. The cycle efficiency (η_{cycle}) and the plant efficiency (η_{plant}) are calculated according to the following formulas:

$$\eta_{cycle} = \frac{\dot{W}_{turbine} - \dot{W}_{MC} - \dot{W}_{RC}}{Q_{Reactor}} \tag{6.18}$$

$$\eta_{plant} = \frac{\dot{W}_{turbine} - \dot{W}_{MC} - \dot{W}_{RC} - \dot{W}_{pump} - \dot{W}_{fan}}{Q_{Reactor}} \tag{6.19}$$

where $\dot{W}_{turbine}$ is the power generated by the turbine, $\dot{W}_{MC}$ is the power consumption by the main compressor, $\dot{W}_{RC}$ is the power consumption by the re-compressor, $\dot{W}_{pump}$ is the power consumption by the cooling water pump, $\dot{W}_{fan}$ is the power consumption by the cooling tower fans and $Q_{reactor}$ is the reactor thermal input. The current model calculations

were compared to the ANL PDC [113] for the reference conditions listed in Table 6-1. The cycle efficiency calculated by the current model is ~0.5% higher than the ANL PDC. The differences can be attributed to the piping pressure losses between different components which are considered in the ANL PDC.

Table 6-1: Recompression Brayton cycle (RCBC) model inputs

sCO_2 cycle parameters	Values
Main compressor inlet conditions (MPa/°C)	7.621/32.8
Main compressor outlet pressure (MPa)	20
Sodium temperature entering reactor/exiting PHX (°C)	373
Sodium temperature leaving reactor/entering PHX (°C)	528
Reactor thermal input (MW_{th})	250
Main compressor isentropic efficiency (%)	89.1
Re-compressor isentropic efficiency (%)	90.1
Turbine isentropic efficiency (%)	92.8
Cooling water conditions entering pre-cooler (MPa/°C)	0.202/30
Cooling water flow rate (kg/s)	6,000
Ambient dry bulb temperature (°C)	30.27
Ambient wet bulb temperature (°C)	20.22

6.5 Plant Capital Cost Methodology and Cost-Based Optimization

As described earlier, all the heat exchangers in the power cycle are envisioned to be printed circuit heat exchangers (PCHEs). A simplified capital cost estimation methodology for the PHCEs is as follows [114]:

1) The mass of raw material required for fabrication of each PCHE block is calculated from the volume of the PCHE block and the material density.

$$M_{block} = V_{block} \cdot \rho_{316ss} \tag{6.20}$$

2) The material cost of 316 stainless steel is assumed to be 8.48 $/kg according to the market value. The total material cost of one PCHE block is calculated by multiplying the mass of block (M_{block}) and the material cost.
3) The fabrication cost to perform chemical etching and diffusion bonding depends on the PCHE construction. For example, the primary heat exchanger is anticipated to be a hybrid PCHE with large rectangular flow channels on the Sodium side and either small continuous zigzag channels or discontinuous fins on the CO_2 side. The fabrication cost for such hybrid PCHE is lower than the platelet PCHE (identical flow patterns on both the hot and the cold sides) as in the case of HTR and LTR. Based on estimates from Argonne National Laboratory, fabrication costs of $44,000, $147,500, $147,500 and $48,480 were used for PHX, HTR, LTR and pre-cooler respectively.
4) The total cost of each PCHE block is the sum of material cost and the fabrication cost. The capital cost of multiple PCHE blocks constituting a heat exchanger is calculated as follows:

$$Cost_{PCHE} = Cost_{PCHE,block}.N_{blocks} \tag{6.21}$$

The PCHE in Equation (6.21) can represent either PHX, HTR, LTR or pre-cooler. The additional costs such as costs associated with welding of PCHE blocks and headers, as well as engineering and shipping costs are neglected as they are considered to be small compared to the fabrication and the material costs. It should be noted that the market values of the material costs keep fluctuating over a period of time and the fabrication costs depend on the maturity level or scale of the fabrication technology. Therefore, the capital costs

presented in this chapter only represent qualitative trends and should not be taken to their face values.

For a power generation plant, it is important to consider the plant net electrical output (function of the plant efficiency for a fixed thermal input) as well as the capital cost of the plant. Often there is a trade-off between these two and a cost-based optimization procedure is employed to find the optimum operating conditions. This section summarizes the details of the cost-based optimization used for the plant optimization. The plant capital cost per unit electrical output ($/kWe) is calculated as:

$$\frac{\$}{kWe} = \frac{Cost_{rest}+Cost_{PHX}+Cost_{HTR}+Cost_{LTR}+Cost_{pre-cooler}+Cost_{coolingtower}}{\dot{W}_{turbine}-\dot{W}_{MC}-\dot{W}_{RC}-\dot{W}_{pump}-\dot{W}_{fan}} \quad (6.22)$$

where $Cost_{PHX}$, $Cost_{HTR}$, $Cost_{LTR}$, $Cost_{pre-cooler}$, $Cost_{coolingtower}$ is the capital cost of the primary heat exchanger, the high temperature recuperator, the low temperature recuperator, the pre-cooler and the cooling tower respectively. $Cost_{rest}$ is the capital cost of the rest of the plant, i.e. excluding the components PHX, HTR, LTR, pre-cooler and the cooling tower. Rest of the plant capital cost ($Cost_{rest}$) is assumed to be constant while varying the heat exchangers (PHX, HTR, LTR and pre-cooler) parameters. This value is taken as 4,480 $/kWe for a reference plant with net electrical output of 104.8 MWe [5].

Ideally the optimization process for all the components should be performed simultaneously but such a process would require enormous amount of computational time. In order to reduce the computational effort and simplify the optimization process, a sequential optimization method was employed. This also allows one to study the impact of different variables in an isolated manner. The flow chart of the optimization procedure is

shown in Figure 6-5. Prior to beginning of the optimization, the cycle inputs and PCHEs geometry information are read and the number of PCHE units for each heat exchanger are set to their reference values (96 PCHE units for PHX, 48 PCHE units for HTR, 48 PCHE units for LTR, 72 PCHE units for pre-cooler) to begin the optimization process with the same initial condition for all the cases. The sub-sequent subsections explain each step of the flow chart in more detail along with sample calculations. All the sample calculations are obtained using the inputs and assumptions from Table 6-1.

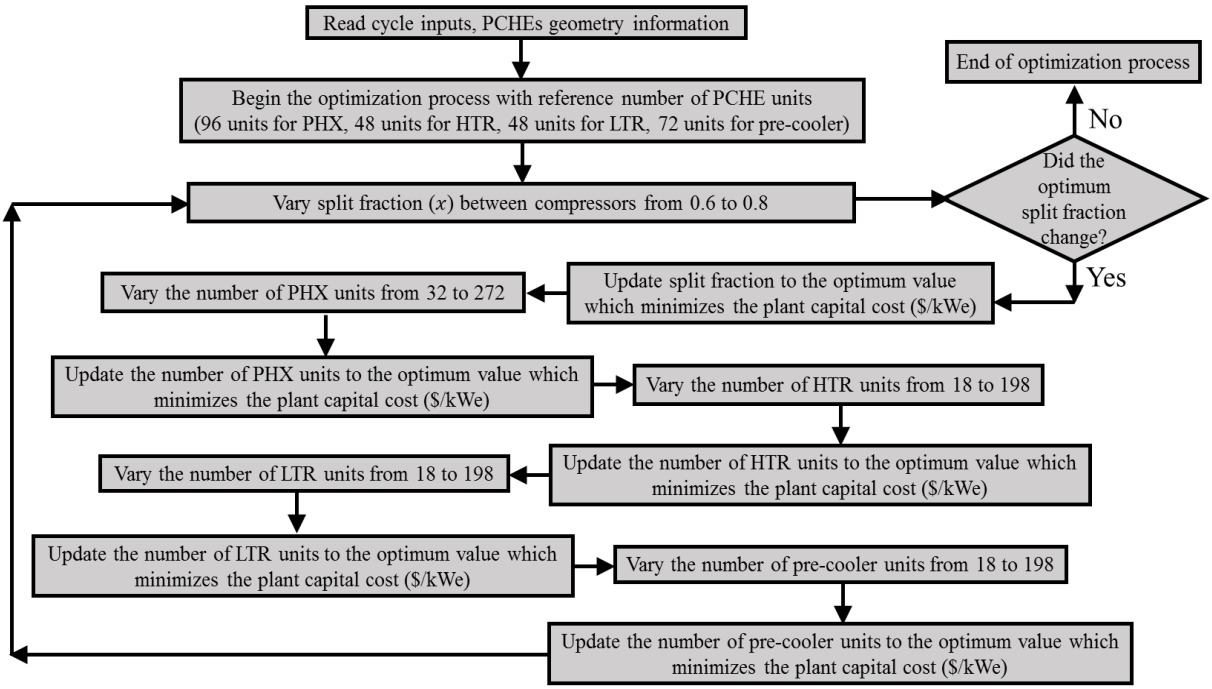

Figure 6-5: Flowsheet of the recompression Brayton cycle (RCBC) optimization procedure

6.5.1 Optimization of split fraction between the compressors

As described in CHAPTER 1, the specific heats of cold and hot streams in the LTR are significantly different which affects the recuperation effectiveness. Therefore, the split flow needs to be adjusted to find a balance between the increase in LTR effectiveness and increase in re-compressor work due to compression of fluid at lower density. Consequently,

the first step of the optimization process is to find the optimum split fraction between the main and the bypass compressors for different types of PCHEs.

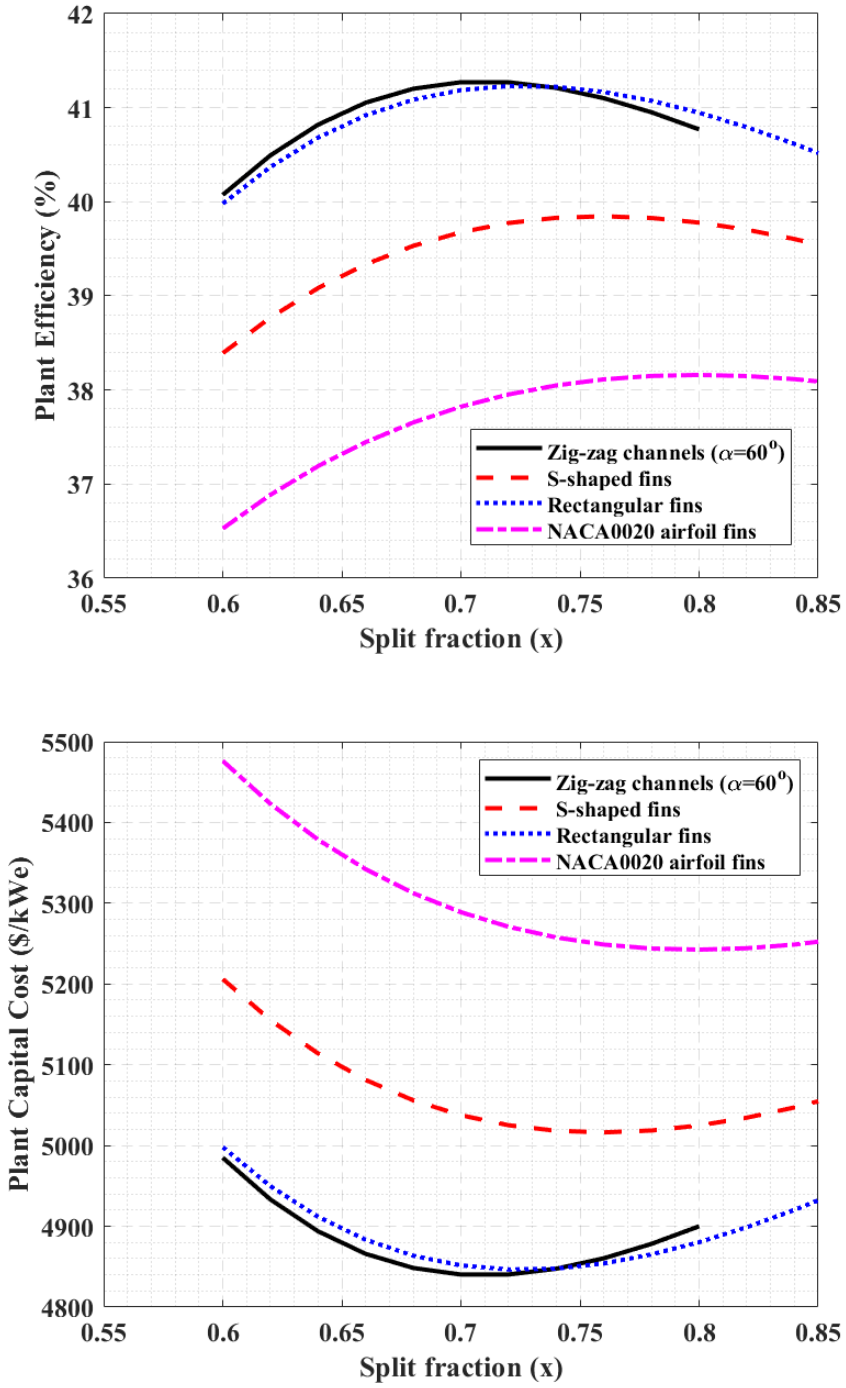

Figure 6-6: Variation of the plant efficiency (top) and the plant capital cost (bottom) with the flow split fraction between the main compressor and the re-compressor

With the number of PCHE units set to the reference values for all the heat exchangers (96 units for PHX, 48 units for HTR, 48 units for LTR and 72 units for pre-cooler), the split fraction is varied from 0.6 to 0.85. The plant efficiency and plant capital cost ($/kWe) are plotted as a function of the split fraction in Figure 6-6. There is clearly an optimum split fraction that maximizes the plant efficiency (hence, minimizes the plant capital cost) for all the PCHE types. Also, the optimum split fraction is dependent on the PCHE type. For this example, the optimum split fraction is 0.72 for the offset rectangular fin PCHEs whereas it changes to 0.8 for the NACA0020 airfoil fin PCHEs. The lower split flow fraction needed for the offset rectangular fin PCHEs is due to the higher Nusselt number (and heat transfer coefficients) compared to the offset NACA0020 airfoil PCHEs; Refer to Figure 6-3 for the Nusselt number comparison.

The dimensions of the PCHE units used for the presented sample calculations can be found in Table 6-2. In the later subsections, the effect of varying the PCHE unit length on the optimization is also discussed. It should be noted that for the pre-cooler, the unit length is calculated to meet the pre-cooler heat duty using the PCHE sizing model described earlier. In case of the continuous channel PCHEs (like zigzag channel), the plate thickness and the channel spacing to handle the desired pressure and temperature can be calculated using the ASME 13-9 code [115]. These equations are listed in APPENDIX I. Unfortunately, there is no appropriate way of calculating the plate thickness values for the discontinuous fin PCHEs. However, the same design procedure (ASME 13-9 code) is used to calculate the plate thicknesses for the discontinuous fin PCHEs (S-shaped fin, offset rectangular fin and offset NACA0020 airfoil fin).

Table 6-2: Dimensions of the PCHE units used for the sample calculations to explain the optimization procedure

Heat Exchanger location	PCHE unit dimensions		
	Width	Height	Length
Primary heat exchanger (PHX)	0.6	0.6	1.5
High temperature recuperator (HTR)	1.5	0.6	0.6
Low temperature recuperator (LTR)	1.5	0.6	0.6
Pre-cooler	0.6	0.6	Calculated

6.5.2 Optimization of Primary Heat Exchanger

In the second step of the optimization, the split fraction is set to the optimum value determined from the previous step (Section 6.5.1) and the number of PHX PCHE units is varied from 32 to 272. The plant efficiency and the plant capital cost ($/kWe) are plotted as a function of the number of PHX PCHE units in Figure 6-7. Increasing the number of PHX PCHE units (hence, increasing the PHX effectiveness) lead to higher turbine inlet temperature and reduces the CO_2 pressure drop in the PHX which in turn increases the cycle and the plant efficiency. However, the capital cost of the PHX increases with increase in number of PHX PCHE units. Due to these trade-offs there is clearly an optimum number of PHX units that minimizes the plant capital cost. For this example, the optimum number of PHX units is 100 for the offset rectangular fin PCHEs (compared to the reference value of 96). Owing to their different heat transfer and pressure drop characteristics, the optimum number of PHX units are dependent on the type of PCHE. For example, the optimum number of PHX units for the zigzag channel PCHEs (α=60^o) is 128 compared to 100 units for the offset rectangular fin PCHE. It should be noted these sample calculations are performed with the number of HTR, LTR and pre-cooler PCHE units set to the reference values of 48, 48 and 72 respectively.

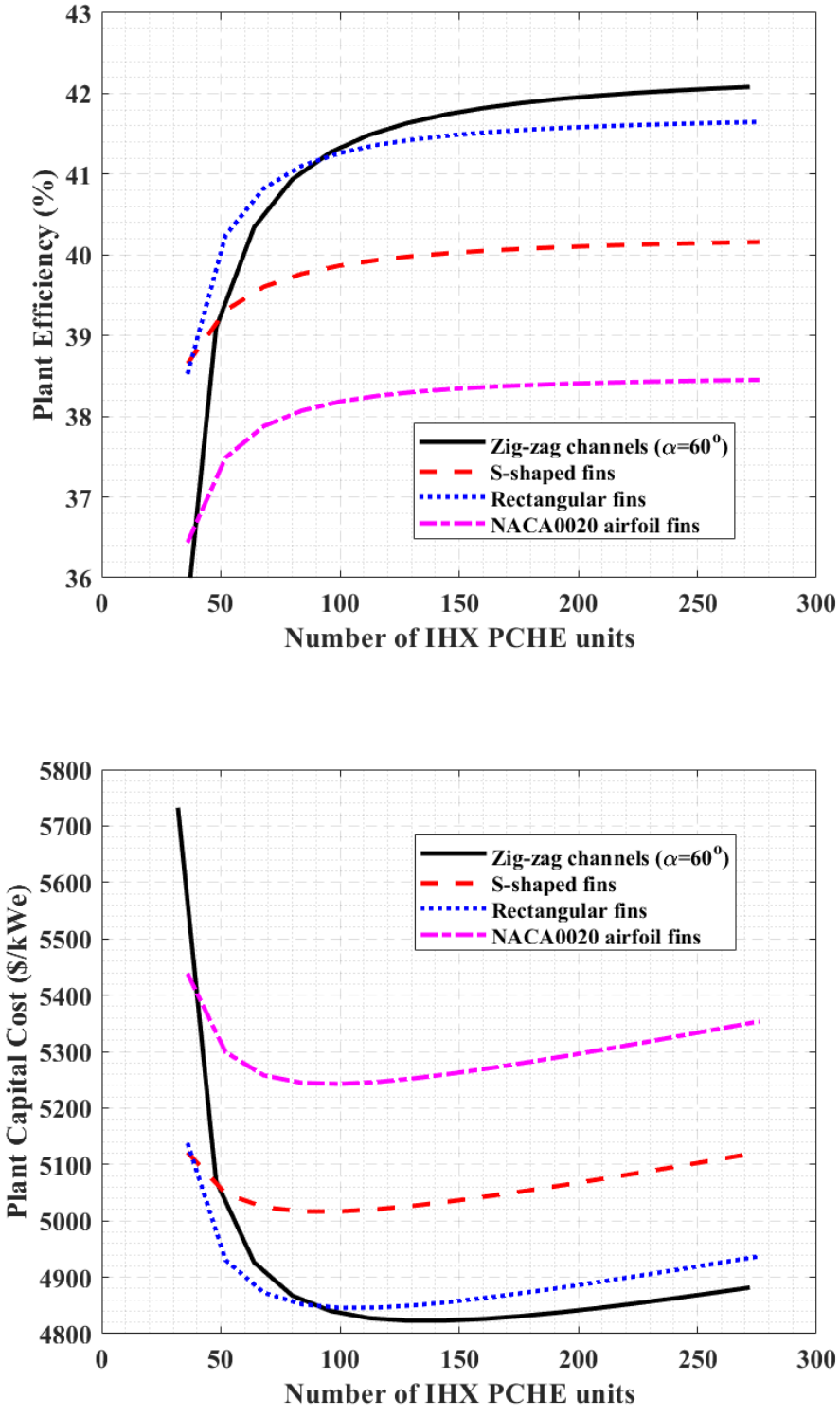

Figure 6-7: Variation of the plant efficiency (top) and the plant capital cost (bottom) with the number of PHX PCHE units

6.5.3 Optimization of recuperators

Similar to the variation of number of PHX PCHE units, increasing the number of HTR and LTR PCHE units increase the cycle and the plant efficiency (due to increased recuperation effectiveness and reduced pressure drops) but at the same time capital cost of the recuperators increase as well. In the third step of the optimization, the number of HTR PCHE units is varied from 24 to 114. The plant efficiency and the plant capital cost ($/kWe) are plotted as a function of the number of HTR PCHE units in Figure 6-8. It should be noted for the HTR optimization, the number of PHX PCHE units is set to the optimum value determined from the previous step (section 6.5.2) and the number of LTR and pre-cooler PCHE units are set to the reference values of 48 and 72 respectively. For this sample calculation, the optimum number of HTR units is 54 for the offset rectangular fin PCHE (compared to the reference value of 48). Again, the optimum number of HTR PCHE units varies for different types of PCHEs due to their different thermal-hydraulic characteristics.

Once the optimum number of HTR PCHE units is calculated, the number of HTR PCHE units is updated to the optimum value. In the next step of optimization, the number of LTR PCHE units is varied from 18 to 108 to find the optimum number of LTR PCHE units that minimize the plant capital cost ($/kWe). For the LTR optimization, the number of PHX and HTR PCHE units are set to their optimum values and the number of pre-cooler PCHE units is set to the reference value of 72. The plant efficiency and the plant capital cost ($/kWe) are plotted as a function of the number of LTR PCHE units in Figure 6-9. For this sample calculation, the optimum number of LTR PCHE units is 54 for the offset rectangular fin PCHE (compared to the reference value of 48).

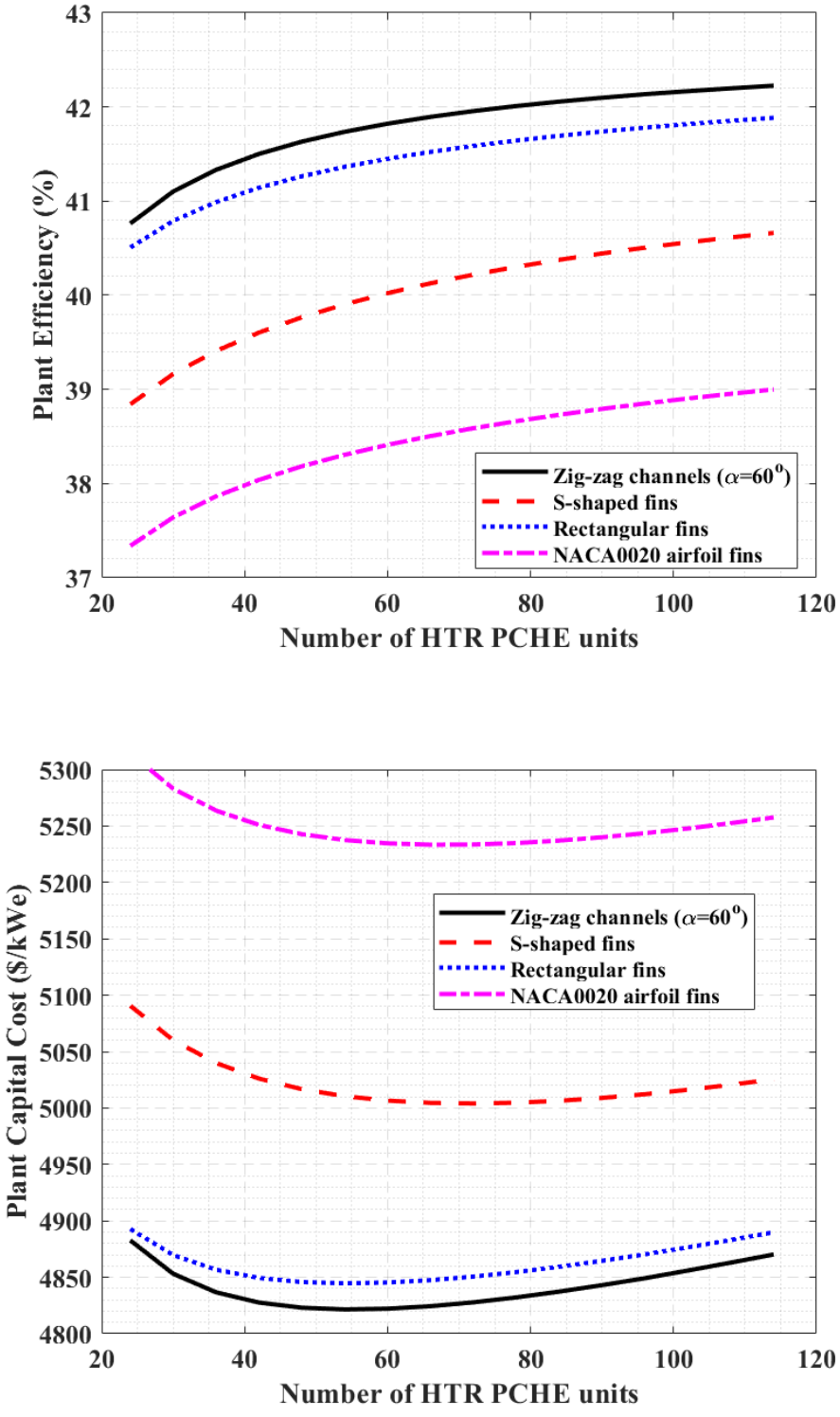

Figure 6-8: Variation of the plant efficiency (top) and the plant capital cost (bottom) with the number of HTR PCHE units

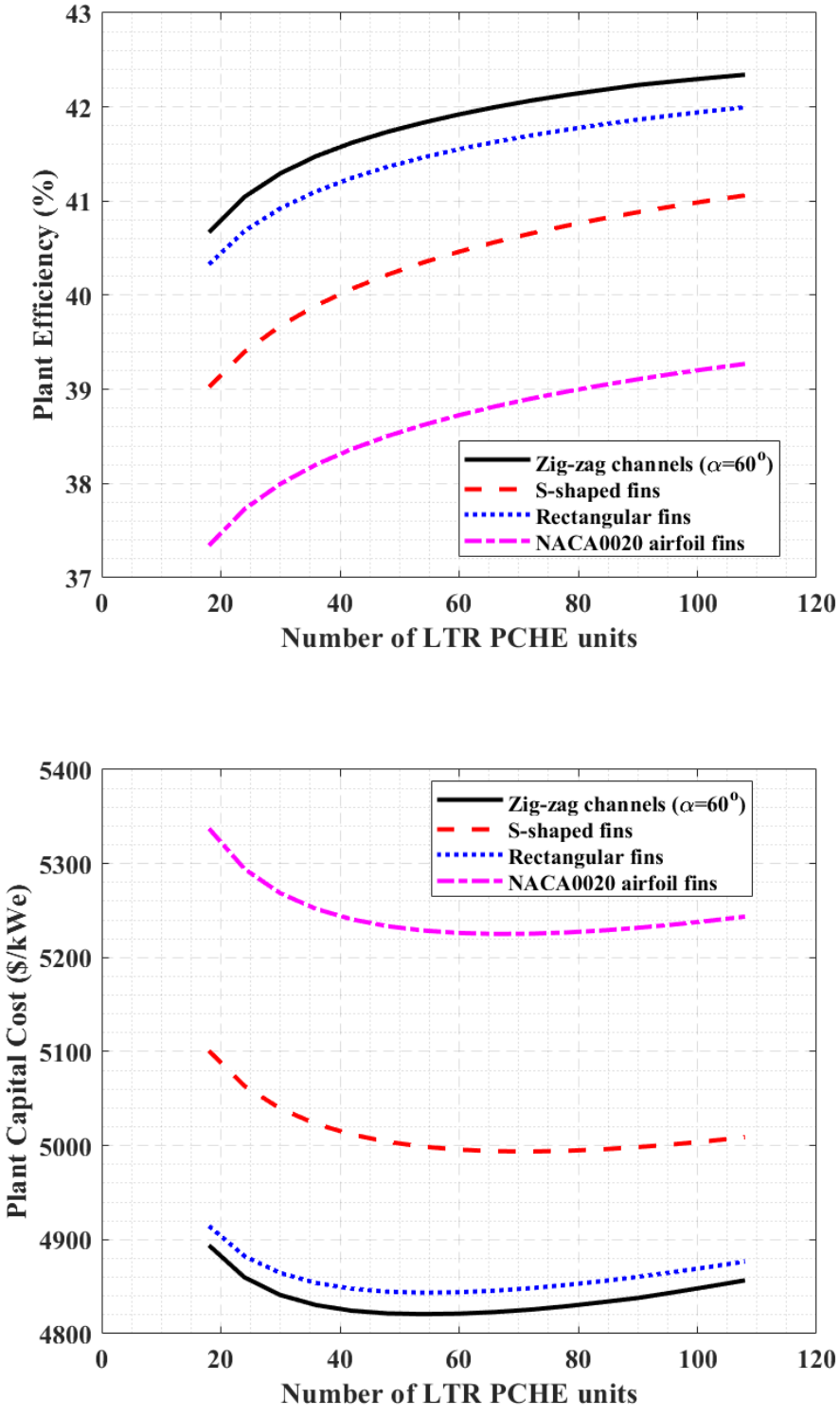

Figure 6-9: Variation of the plant efficiency (top) and the plant capital cost (bottom) with the number of LTR PCHE units

6.5.4 Optimization of pre-cooler

In the final step of the plant optimization, the number of pre-cooler PCHE units is varied from 36 to 126 to find the optimum number of pre-cooler PCHE units that minimize the plant capital cost ($/kWe). For the pre-cooler optimization, the number PCHE units for rest of the heat exchangers (PHX, HTR and LTR) are set to their respective optimum values determined from the previous steps. The plant efficiency and the plant capital cost ($/kWe) are plotted as a function of the number of pre-cooler PCHE units in Figure 6-10. For this sample calculation, the optimum number of pre-cooler PCHE units is 72 for the offset rectangular fin PCHE (compared to the reference value of 72). It should be noted that varying the number of pre-cooler PCHE units doesn't have a significant effect on the cycle efficiency since it only effects the CO_2 and water side pressure drops in the pre-cooler.

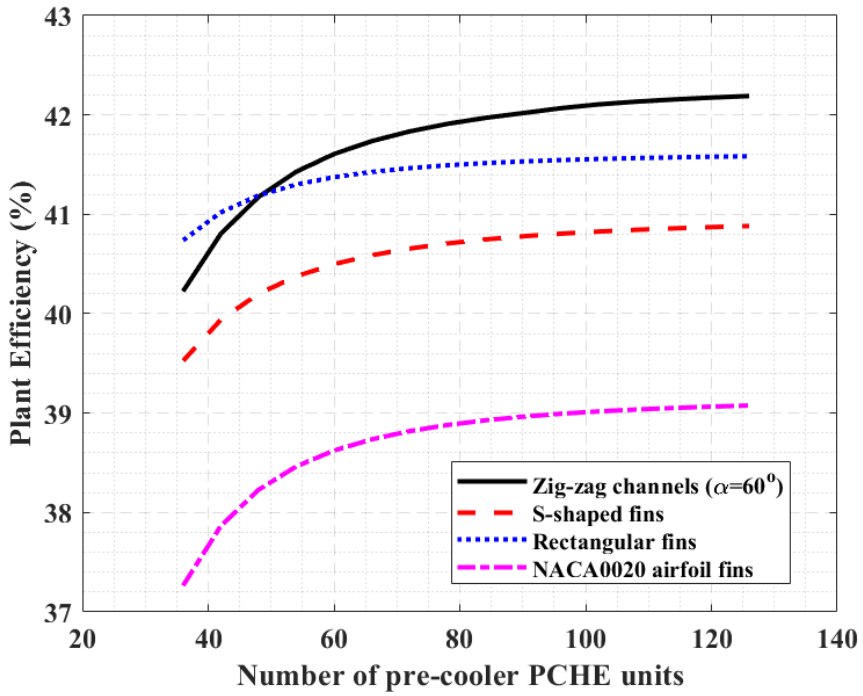

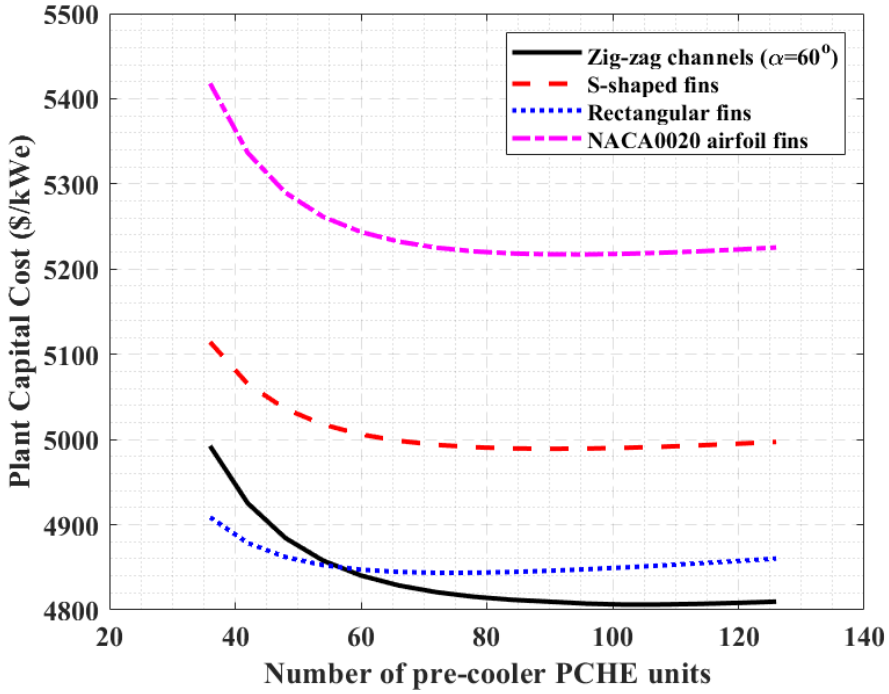

Figure 6-10: Variation of the plant efficiency (top) and the plant capital cost (bottom) with the number of pre-cooler PCHE units

However, depending on the number of PCHE units the pressure drop of the cooling water (hence, power consumption of the cooling water pump) varies which has an effect on the plant auxiliary power and the plant efficiency as evident from Figure 6-10.

6.5.5 Effect of recuperator PCHE unit length

The sample calculations presented in the previous sections are for performed for fixed recuperator PCHE unit lengths of 0.6 m (See Table 6-2). However, this might not be an optimal PCHE configuration for the discontinuous fin PCHEs. Figure 6-11 shows the effect of the number of HTR PCHE units on the plant efficiency and the capital cost for different offset rectangular fin PCHE unit lengths.

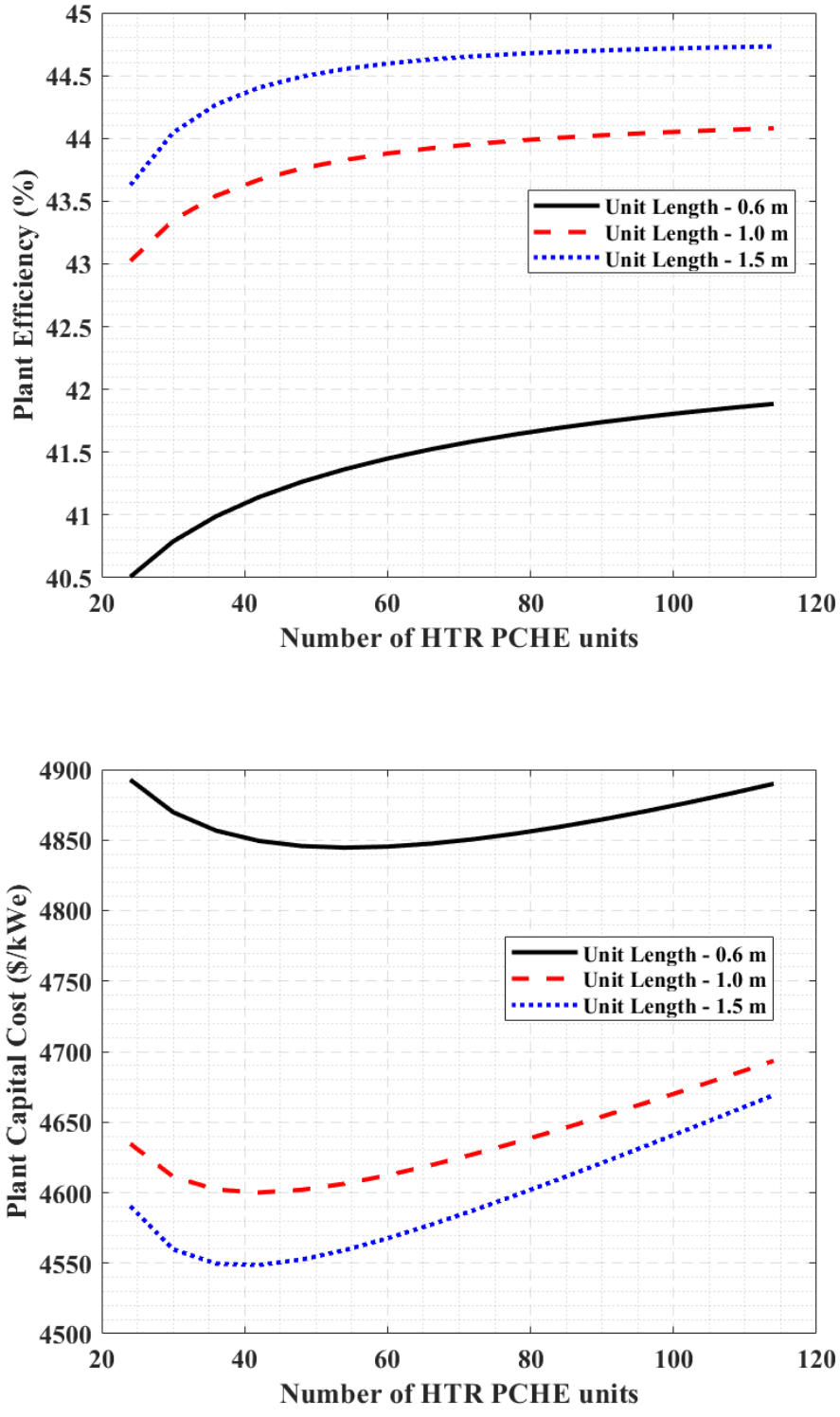

Figure 6-11: Variation of the plant efficiency (top) and the plant capital cost (bottom) with the number of HTR PCHE units for different unit lengths (for the offset rectangular fin PCHE)

From Figure 6-11, there is clearly a significant efficiency and cost benefit from increasing the length of recuperator PCHE units. For example, increasing the PCHE unit length from 0.6 m to 1.5 m decreases the optimum plant capital cost from 4,844.7 $/kWe to 4,548.7 $/kWe. At these optimum values, the plant efficiency increases from 41.36% to 44.4%. Following similar set of analyses for the other PCHE types (S-shaped fins, offset NACA0020 airfoil fins and zigzag channel), optimum heat exchanger designs were identified for the cycle. The optimum designs and operating conditions for the PHX, the HTR, the LTR and the pre-cooler are listed in Table 6-4 through Table 6-7. From these tables it can be seen that the optimum operating Reynolds number for the offset rectangular fin and offset NACA0020 airfoil fin PCHE are within the range of Reynolds numbers from experiments. The only exception is the pre-cooler water side where the optimum Re < 2,300 and the developed correlations were extrapolated outside their validity range.

For the optimum PCHE designs, the calculated plant efficiency and the plant capital cost for all PCHE types are listed in Table 6-3. The offset rectangular fin PCHEs offered the highest plant efficiency followed by the zigzag channel PCHEs (α=60°), the S-shaped fin PCHEs and the offset NACA0020 airfoil fin PCHEs. **The offset rectangular fin PCHEs offered the lowest plant capital cost followed by the S-shaped fin PCHEs, the zigzag channel PCHEs (α=60°) and the offset NACA0020 airfoil fin PCHEs.**

Table 6-3: Calculated plant efficiency and plant capital cost for optimized heat exchanger designs for all four PCHE types

PCHE type	Plant Efficiency (%)	Plant Capital Cost ($/kWe)
Zigzag channel (α=60^o)	43.98%	4630.4
S-shaped fins	43.64%	4600.8
Offset rectangular fins	43.26%	4684.6
Offset NACA0020 airfoil fins	44.22%	4541.9

As mentioned earlier, for the current analysis the plate thicknesses for all three discontinuous fin PCHEs are calculated according to the ASME 13-9 design procedure. However, the validity of this procedure for the discontinuous fin PCHEs is questionable. Therefore, in order to evaluate the true performance and cost advantages of the discontinuous fin PCHEs it is important to properly account for the mechanical design in the future. One potential way of evaluating the required plate thickness is by using finite element analysis (FEA) tools.

Table 6-4: Optimum PHX PCHE designs for different PCHE types

	Zigzag channel (α=60°)	S-shaped fins	Offset NACA0020 airfoil fins	Offset rectangular fins
Unit heat duty	1.69 MW_{th}	2.50 MW_{th}	2.16 MW_{th}	2.16 MW_{th}
Unit width	0.6	0.6	0.6	0.6
Unit height	0.6	0.6	0.6	0.6
Unit length	1.5	1.5	1.5	1.5
Number of PCHE units	148	100	116	116
Parameters below are per unit				
Hot side fluid	Sodium	Sodium	Sodium	Sodium
Hot side flow rate	8.6 kg/s	12.7 kg/s	10.9 kg/s	10.9 kg/s
Hot side inlet temperature	528 °C	528 °C	528 °C	528 °C
Hot side outlet temperature	373 °C	373 °C	373 °C	373 °C
Hot side inlet pressure	0.1 MPa	0.1 MPa	0.1 MPa	0.1 MPa
Hot side outlet pressure	0.1 MPa	0.1 MPa	0.1 MPa	0.1 MPa
Hot side pressure drop	0.03 kPa	0.16 kPa	0.08 kPa	0.08 kPa
Cols side fluid	CO_2	CO_2	CO_2	CO_2
Cold side flow rate	10.1 kg/s	14.2 kg/s	12.2 kg/s	12.6 kg/s
Cold side inlet temperature	371.9 °C	367.7 °C	367.0 °C	370.7 °C
Cold side outlet temperature	509.1 °C	510.7 °C	511.2 °C	510.7 °C
Cold side inlet pressure	19.96 MPa	19.98 MPa	19.98 MPa	19.98 MPa
Cold side outlet pressure	19.71 MPa	19.85 MPa	19.85 MPa	19.82 MPa
Cold side pressure drop	240.5 kPa	133.3 kPa	126.5 kPa	155.2 kPa
Effectiveness	99.3%	96.7%	96.3%	98.5%
Number of plates	91	85	84	89
Hot side channel width	6 mm	6 mm	6 mm	6 mm
Hot side channel depth	4 mm	4 mm	4 mm	4 mm
Hot side channel pitch	6.5 mm	6.5 mm	6.5 mm	6.5 mm
Hot side plate thickness	5.1 mm	5.1 mm	5.1 mm	5.1 mm
Hot side number of channels (per plate)	87	87	87	87
Hot side heat transfer area	203.6 m^2	189.5 m^2	186.9 m^2	197.5 m^2
Cold side channel diameter	1.3 mm	1.19 mm	1.11 mm	0.99 mm
Cold side channel pitch	1.69 mm	-	-	-
Cold side plate thickness	1.1 mm	1.56 mm	1.65 mm	1.29 mm
Cold side number of channels (per plate)	335	-	-	-
Cold side heat transfer area	130.8 m^2	153.5 m^2	111.1 m^2	125.3 m^2
Hot side Re range	740 – 940	1,180 – 1,500	1,025 – 1,300	970 – 1,230
Cold side Re range	12,700 – 14,100	23,300 – 26,150	15,600 – 17,500	14,300 – 16,000

Table 6-5: Optimum HTR PCHE designs for different PCHE types

	Zigzag channel (α=60°)	S-shaped fins	Offset NACA0020 airfoil fins	Offset rectangular fins
Unit heat duty	7.78 MW_{th}	8.45 MW_{th}	7.16 MW_{th}	8.58 MW_{th}
Unit width	1.5	1.5	1.5	1.5
Unit height	0.6	0.6	0.6	0.6
Unit length	1.5	1.5	1.5	1.5
Number of PCHE units	48	42	48	42
Parameters below are per unit				
Hot side fluid	CO_2	CO_2	CO_2	CO_2
Hot side flow rate	31.0 kg/s	33.9 kg/s	29.4 kg/s	34.7 kg/s
Hot side inlet temperature	398.8 °C	398.3 °C	398.8 °C	398.3 °C
Hot side outlet temperature	177.5 °C	178.9 °C	184.0 °C	180.2 °C
Hot side inlet pressure	7.79 MPa	7.71 MPa	7.71 MPa	7.71 MPa
Hot side outlet pressure	7.69 MPa	7.65 MPa	7.66 MPa	7.66 MPa
Hot side pressure drop	96.2 kPa	56.3 kPa	49.9 kPa	53.3 kPa
Cols side fluid	CO_2	CO_2	CO_2	CO_2
Cold side flow rate	31.0 kg/s	33.9 kg/s	29.4 kg/s	34.7 kg/s
Cold side inlet temperature	176.9 °C	175 °C	177.8 °C	178.4 °C
Cold side outlet temperature	371.9 °C	367.8 °C	366.9 °C	370.7 °C
Cold side inlet pressure	19.99 MPa	19.99 MPa	19.99 MPa	19.99 MPa
Cold side outlet pressure	19.95 MPa	19.97 MPa	19.97 MPa	19.97 MPa
Cold side pressure drop	36.4 kPa	20.7 kPa	17.6 kPa	18.9 kPa
Effectiveness	99.7%	98.2%	97.2%	99.2%
Number of plates	666	470	444	568
Hot side channel diameter	1.3 mm	1.19 mm	1.11 mm	0.99 mm
Hot side channel pitch	1.69 mm	-	-	-
Hot side plate thickness	1.1 mm	1.56 mm	1.65 mm	1.29 mm
Hot side number of channels (per plate)	290	-	-	-
Hot side heat transfer area	790.6 m^2	702.8 m^2	487.2 m^2	665.9 m^2
Cold side channel diameter	1.3 mm	1.19 mm	1.11 mm	0.99 mm
Cold side channel pitch	1.69 mm	-	-	-
Cold side plate thickness	1.1 mm	1.56 mm	1.65 mm	1.29 mm
Cold side number of channels (per plate)	290	-	-	-
Cold side heat transfer area	790.6 m^2	702.8 m^2	487.2 m^2	665.9 m^2
Hot side Re range	6,300 – 8,300	11,800 – 15,800	8,300 – 11,000	7,200 – 9,500
Cold side Re range	6,000 – 6,650	11,400 – 12,600	8,000 – 8,900	7,000 – 7,650

Table 6-6: Optimum LTR PCHE designs for different PCHE types

	Zigzag channel (α=60°)	S-shaped fins	Offset NACA0020 airfoil fins	Offset rectangular fins
Unit heat duty	3.89 MW_{th}	3.72 MW_{th}	3.78 MW_{th}	3.86 MW_{th}
Unit width	1.5	1.5	1.5	1.5
Unit height	0.6	0.6	0.6	0.6
Unit length	1.5	1.5	1.5	1.5
Number of PCHE units	42	42	42	42
Parameters below are per unit				
Hot side fluid	CO_2	CO_2	CO_2	CO_2
Hot side flow rate	35.4 kg/s	33.9 kg/s	33.6 kg/s	34.7 kg/s
Hot side inlet temperature	177.2 °C	178.3 °C	183.4 °C	179.8 °C
Hot side outlet temperature	87.1 °C	88.1 °C	90.2 °C	88.0 °C
Hot side inlet pressure	7.71 MPa	7.66 MPa	7.67 MPa	7.66 MPa
Hot side outlet pressure	7.63 MPa	7.63 MPa	7.63 MPa	7.62 MPa
Hot side pressure drop	81.1 kPa	35.5 kPa	44.2 kPa	37.6 kPa
Cols side fluid	CO_2	CO_2	CO_2	CO_2
Cold side flow rate	22.7 kg/s	22.4 kg/s	22.2 kg/s	22.2 kg/s
Cold side inlet temperature	85.1 °C	85.1 °C	85.1 °C	85.1 °C
Cold side outlet temperature	174.5 °C	170.7 °C	173.7 °C	176.1 °C
Cold side inlet pressure	20 MPa	20 MPa	20 MPa	20 MPa
Cold side outlet pressure	19.99 MPa	19.99 MPa	19.99 MPa	19.99 MPa
Cold side pressure drop	14.0 kPa	6.1 kPa	5.6 kPa	4.6 kPa
Effectiveness	97.8%	96.7%	94.8%	96.9%
Number of plates	666	470	444	568
Hot side channel diameter	1.3 mm	1.19 mm	1.11 mm	0.99 mm
Hot side channel pitch	1.69 mm	-	-	-
Hot side plate thickness	1.1 mm	1.56 mm	1.65 mm	1.29 mm
Hot side number of channels (per plate)	290	-	-	-
Hot side heat transfer area	790.6 m^2	702.8 m^2	487.2 m^2	665.9 m^2
Cold side channel diameter	1.3 mm	1.189 mm	1.112 mm	0.9973
Cold side channel pitch	1.69 mm	-	-	-
Cold side plate thickness	1.1 mm	1.56 mm	1.65 mm	1.29 mm
Cold side number of channels (per plate)	290	-	-	-
Cold side heat transfer area	790.6 m^2	702.8 m^2	487.2 m^2	665.9 m^2
Hot side Re range	9,500 – 11,000	15,800 – 18,200	12,600 – 14,600	9,600 – 11,000
Cold side Re range	3,300 – 4,900	5,600 – 8,300	4,500 – 6,600	3,300 – 4,900

Table 6-7: Optimum pre-cooler PCHE designs for different PCHE types

	Zigzag channel (α=60°)	S-shaped fins	Offset NACA0020 airfoil fins	Offset rectangular fins
Unit heat duty	1.35 MW_{th}	1.53 MW_{th}	1.54 MW_{th}	1.89 MW_{th}
Unit width	0.6	0.6	0.6	0.6
Unit height	0.6	0.6	0.6	0.6
Unit length	0.5	0.64	0.86	0.63
Number of PCHE units	102	90	90	72
Parameters below are per unit				
Hot side fluid	CO_2	CO_2	CO_2	CO_2
Hot side flow rate	9.3 kg/s	10.4 kg/s	10.4 kg/s	13.0 kg/s
Hot side inlet temperature	87.1 °C	88.5 °C	90.2 °C	88.3 °C
Hot side outlet temperature	32.8 °C	32.8 °C	32.8 °C	32.8 °C
Hot side inlet pressure	7.63 MPa	7.63 MPa	7.63 MPa	7.63 MPa
Hot side outlet pressure	7.63 MPa	7.63 MPa	7.63 MPa	7.63 MPa
Hot side pressure drop	4.75 kPa	4.21 kPa	6.70 kPa	5.46 kPa
Cols side fluid	Water	Water	Water	Water
Cold side flow rate	58.8 kg/s	66.7 kg/s	66.7 kg/s	83.3 kg/s
Cold side inlet temperature	30.0 °C	30.0 °C	30.0 °C	30.0 °C
Cold side outlet temperature	35.5 °C	35.5 °C	35.55 °C	35.45 °C
Cold side inlet pressure	0.183 MPa	0.171 kPa	0.168 MPa	0.155 MPa
Cold side outlet pressure	0.101 MPa	0.101 MPa	0.101 MPa	0.101 MPa
Cold side pressure drop	81.9 kPa	69.7 kPa	67.2 kPa	54.2 kPa
Effectiveness	95.1%	95.2%	95.3%	95.2%
Number of plates	257	181	171	219
Hot side channel diameter	1.3 mm	1.19 mm	1.11 mm	0.99 mm
Hot side channel pitch	1.69 mm	-	-	-
Hot side plate thickness	1.1 mm	1.56 mm	1.65 mm	1.29 mm
Hot side number of channels (per plate)	290	-	-	-
Hot side heat transfer area	81.3 m^2	108.3 m^2	112.5 m^2	98.3 m^2
Cold side channel diameter	1.3 mm	1.189 mm	1.112 mm	0.9973 mm
Cold side channel pitch	1.69 mm	-	-	-
Cold side plate thickness	1.3 mm	1.19 mm	1.11 mm	0.99 mm
Cold side number of channels (per plate)	290	-	-	-
Cold side heat transfer area	81.3 m^2	108.3 m^2	112.5 m^2	98.3 m^2
Hot side Re range	5,600 – 7,500	10,900 – 14,600	8,900 – 11,800	8,200 – 10,700
Cold side Re range	1,190 – 1,320	2,300 – 2,600	1,890 – 2,100	1,730 – 1,930

CHAPTER 7. SUMMARY AND CONCLUDING REMARKS

The fluid flow and heat transfer characteristics of supercritical carbon dioxide (sCO_2) flow inside circular tubes and discontinuous fin printed circuit heat exchangers were investigated.

An in-depth review of the literature was conducted to understand the heat transfer mechanisms in supercritical fluids. The heat transfer to supercritical fluids are significantly different compared to the ideal fluids due to the rapidly varying thermodynamic and transport properties near the critical point. To study the fundamental heat transfer phenomenon of sCO_2 flow near the critical point two heated circular test tubes sections with inner diameters of 7.9 mm and 10.9 mm were selected for investigation during the first phase of this dissertation. Wall temperatures and heat transfer coefficients were measured for a wide range of operating conditions by varying the fluid inlet temperature, mass flux, heat flux and system pressure. Three different test section orientations – horizontal, upward and downward flows were tested to investigate the effect of buoyancy on the heat transfer. The effect of these experimental parameters on the heat transfer was discussed in detail by presenting the measured wall temperatures and the heat transfer coefficients for select experimental cases. For conditions where the buoyancy effects are negligible (typically at high mass flux relative to the heat flux), the heat transfer coefficients were significantly enhanced near the pseudocritical temperature due to the increased specific heat and Prandtl number in this region. The magnitude of the enhancement however decreased with the increase of system pressure which is consistent with other studies from the literature.

Buoyancy and thermal-bulk flow acceleration parameters from the literature were selected to understand their influence on the heat transfer. The buoyancy parameter, Bo was greater than the threshold value of 10^{-5} for most of the experimental cases indicating strong influence of buoyancy on the heat transfer. This was also evident from the strong dependence of wall temperatures and heat transfer coefficients on the flow orientation. Under strong influence of buoyancy, the heat transfer coefficients for the downward flow were consistently higher than the upward flow; whereas a strong circumferential variation in the wall temperatures and the heat transfer coefficients was noted for the horizontal flow. The thermal-bulk flow acceleration, A_{c_b} was found to be lower than the threshold value of $4x10^{-6}$ for most of the cases indicating that the thermal-bulk flow acceleration doesn't have a significant influence on the heat transfer for the tested conditions. It was noted that higher buoyancy parameter, Bo values don't necessarily lead to lower heat transfer coefficients. In fact, at sufficiently high Bo values the flow is dominated by natural convection and the heat transfer coefficient values were found to be greater than the corresponding forced convective heat transfer coefficients.

Several existing heat transfer correlations from the literature were evaluated against the experimental data. The correlation of Kim and Kim (2011) offered best agreement with the experimental data for both the circular tube test sections. The correlation was able to predict the upward flow experimental data with mean absolute error (MAE) of ±8.6% and ±17.9% for the larger (ID=10.9 mm) and the smaller (ID=7.9 mm) circular tube test sections respectively. Relatively poorer agreement for the smaller tube was attributed to the experimental conditions being closer to the critical point. The Kim and Kim (2011) correlation was able to predict the downward flow experimental data with mean absolute

error (MAE) of ±15.6% and ±20.7% for the larger (ID=10.9 mm) and the smaller (ID=7.9 mm) circular tube test sections respectively. The Kim and Kim (2011) correlation was able to predict the horizontal flow experimental data with mean absolute error (MAE) of ±9.9% and ±22.1% for the larger (ID=10.9 mm) and the smaller (ID=7.9 mm) circular tube test sections respectively. The Kim and Kim (2011) correlation was originally developed based on upward flow heat transfer test data which possibly explains the reason for poorer agreement for the downward and the horizontal flows.

In order to better tune the correlation of Kim and Kim (2011), the model coefficients were adjusted to match the experimental data for the upward, the downward and the horizontal flows separately. With the updated coefficients, the new Nusselt number correlation for the upward flow was able to predict the experimental data with MAE of ±12.4%. Out of the 1486 data points, 74.9% of the experimental data is predicted within ±15% and 85.1% of the experimental data is predicted within ±25%. The proposed Nusselt number correlation for the downward flow was able to predict the experimental data with MAE of ±16.3%. Out of the 1568 data points, 61.2% of the experimental data is predicted within ±15% and 79.1% of the experimental data is predicted within ±25%. The proposed Nusselt number correlation for the horizontal flow was able to predict the experimental data with MAE of ±14.2%. Out of the 1818 data points, 69.7% of the experimental data is predicted within ±15% and 84.6% of the experimental data is predicted within ±25%.

In the future, any additional tests should focus on investigating the effect of thermal-bulk flow acceleration on the heat transfer. In order to investigate the thermal-bulk flow acceleration effects it is necessary to test flows in smaller diameter tubes and/or significantly higher heat fluxes, mass fluxes.

In the second part of this dissertation, the thermal-hydraulic performance of two discontinuous fin PCHEs with offset rectangular fin and offset NACA0020 airfoil fin patterns were evaluated experimentally. These PCHE test sections were fabricated using the chemical etching process. Due to the manufacturing uncertainties associated with the chemical etching process, the surface features of both the test sections were measured using a laser scanning technique to accurately determine important geometrical parameters such as the heat transfer surface area, flow cross-sectional area, hydraulic diameter etc. which are necessary to calculate the heat transfer coefficients and the friction factors. The pressure drops and the heat transfer coefficients for both the PCHEs were measured over a wide range of conditions by varying the CO_2 inlet temperature, mass flow rate, operating pressure as well as the cooling water temperature and flow rates. These operating conditions covered a wide range of Reynolds number, $2{,}700 < Re < 38{,}000$ and Prandtl number, $0.8 < Pr < 25$.

Based on the experimental data, friction factor and Nusselt number models were developed for both the PCHE test sections. The proposed friction factor models were able to predict the frictional pressure drops for the offset rectangular fin and the offset NACA0020 airfoil fin PCHEs with mean absolute error (MAE) of ±11%. The proposed Nusselt number models were able to predict the experimental Nusselt numbers for the offset rectangular fin and the offset NACA0020 airfoil fin PCHEs with mean absolute error (MAE) of ±9.1% and ±5.2% respectively. A computational fluid dynamics (CFD) study was conducted and the calculated pressure drop, and the local heat transfer coefficients were compared to the experimental data. For both the offset NACA00020 airfoil fin and the offset rectangular fin PCHEs, the CFD models underpredicted the pressure drop by

~30-40%. Although the CFD models use geometry inputs from the laser scanning data, the pressure drop can be quite sensitive to the presence of sharp edges. The roughness and the curvature of the fin's edges might have to be measured more accurately in the future to obtain a better agreement with the experimental data. For conditions far away from the critical point, the CFD models were able to capture the heat transfer data quite accurately. However, in the vicinity of the pseudocritical temperatures, up to ~30% deviation was observed between the experimental data and the CFD models. Out of the four different turbulence models considered for the CFD study, the RNG k-ε and the SST k-ω models offered the best agreement with the experimental data. These CFD models can be used to optimize the offset NACA0020 airfoil fin and the offset rectangular fin arrangements to improve the thermal-hydraulic performance of these PCHEs in the future. Also, the experimental work in the future should focus on extending the range of operating conditions for the tested PCHEs to include data at lower Re (Re < 3,200).

In the final part of this dissertation, a sCO_2 Brayton cycle model was developed to study the impact of several printed circuit heat exchanger (PCHE) types on the cycle performance and the capital cost. The developed model was validated to the existing models from the literature and four different PCHEs were selected for investigation – zigzag channel PCHE with channel bend angle (α) of 60^o, S-shaped fin PCHE, offset NACA0020 airfoil fin PCHE and offset rectangular fin PCHE. Heat transfer and pressure drop correlations for the zigzag channels and the S-shaped fins were taken from the literature whereas the correlations developed in this study were used for the offset NACA0020 airfoil and the offset rectangular fin PCHEs. A cost-based optimization procedure was employed to determine the optimum cycle conditions and the optimum heat

exchanger designs for the four selected PCHE types. The offset rectangular fin PCHE offered highest cycle efficiency and lowest capital cost ($/kWe) followed by the S-shaped fin PCHE, the zigzag channel PCHE and the offset NACA0020 airfoil fin PCHE. However, this analysis was conducted by calculating the PCHE plate thicknesses for all three discontinuous fin PCHEs using the ASME 13-9 mechanical design procedure. This design procedure is valid for the mechanical design of the continuous channel type PCHEs. However, the validity of the design procedure for discontinuous fin PCHEs is questionable. Alternative mechanical design procedures (for example, using FEA tools) should be employed in future studies to evaluate the true performance and cost benefits of the discontinuous fin PCHEs.

APPENDIX A. IN SITU CALIBRATION OF THE WALL THERMOCOUPLES

The thermocouple drift in the wall temperature measurements is corrected using an *in-situ* calibration procedure. The wall thermocouples are calibrated against the test section inlet RTD under zero heat flux (isothermal) conditions. First, the fluid inlet temperature is set to 20 °C and the system is allowed to attain a steady state with the DC power supply turned off (in the case of heated circular tube test sections) or with the cooling water flow turned off (in the case of PCHE test sections). Once the system reaches steady state, data was recorded for a period of 500 seconds with frequency of 1 Hz. This procedure is repeated for fluid inlet temperatures in the range of 20–55 °C at intervals of 5 °C. The time averaged data is used for the curve fitting procedure between the wall thermocouple and the inlet RTD measurements. An example of the linear curve fit between one the wall thermocouple and the inlet RTD for the larger circular tube test section (ID=10.9 mm) and the offset rectangular fin PCHE test section is presented in Figure A-1. Similar linear curve fits are generated for all the wall thermocouples and the equations are read into the LabVIEW program for correction of the drift in the wall temperature measurements. The wall temperature measurements were recorded under isothermal conditions prior to beginning the experiments each day. If the wall temperature measurements under isothermal conditions deviate significantly from the inlet RTD readings (error greater than 0.25 °C), the calibration procedure is conducted to correct for the drift. Typically, it was necessary to repeat the calibration procedure every 2-3 weeks.

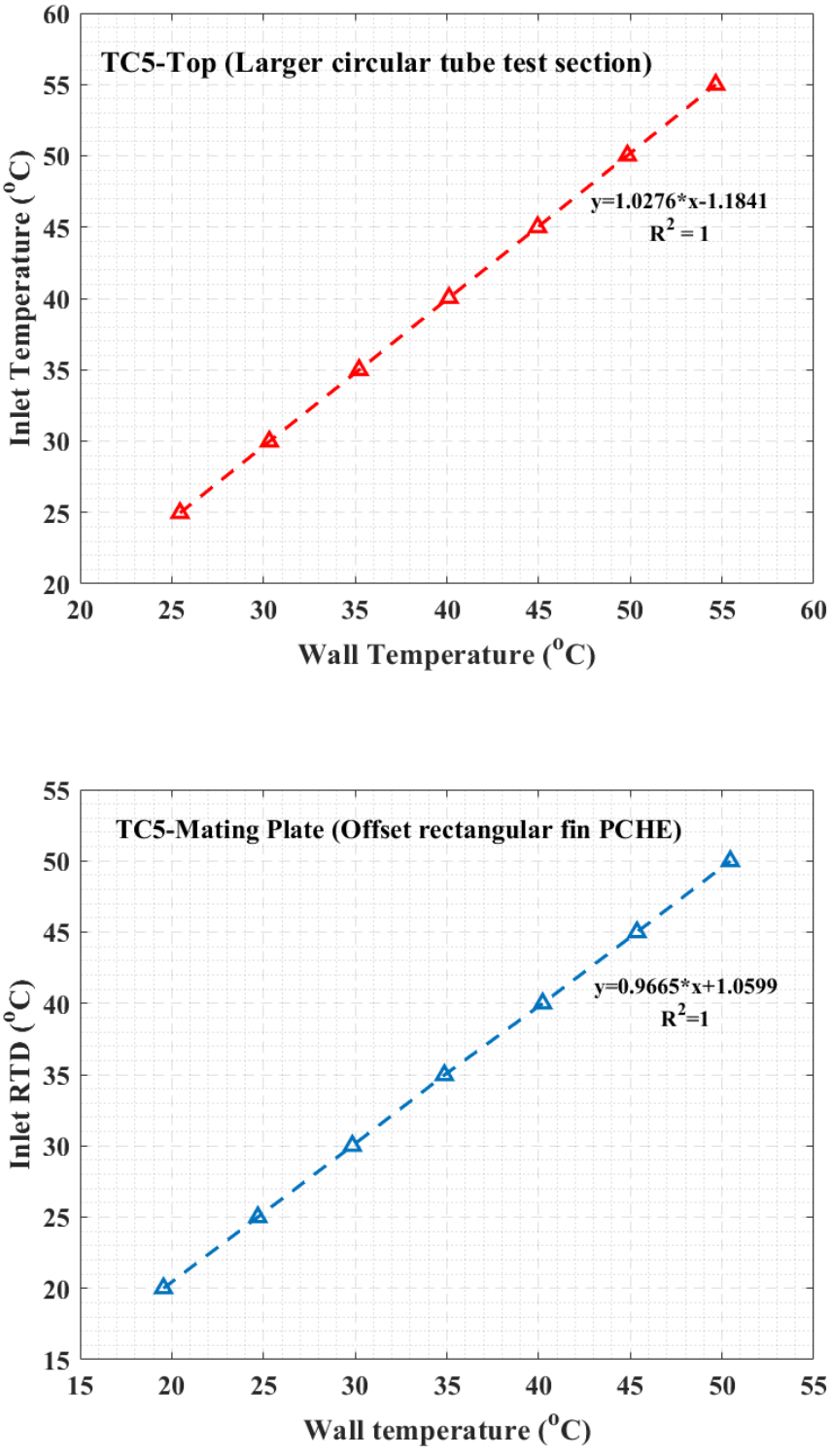

Figure A-1: An Example of calibration curves generated from *in-situ* calibration of the wall thermocouples for circular tube and PCHE test sections

APPENDIX B. VALIDATION OF THE TEST FACILITY WITH WATER

Prior to conducting test with supercritical CO_2, the test facility was tested under constant heat flux boundary condition (for the smaller circular tube test section with ID=7.9 mm) using distilled water as the working fluid. Experiments were conducted with water inlet temperature of 25 °C and several mass flow rates, heat fluxes. Wall temperatures were recorded and the bulk temperature at the locations of the thermocouples are calculated by performing energy balance between inlet to outlet assuming that the heat flux is constant (reasonable assumption when the variation of the wall temperature is small).

$$Nu_{exp} = \frac{Q"}{(T_w - T_b)}\left(\frac{ID}{k_b}\right)$$

where $Q" = \frac{VI}{\pi.ID.L}$

The experimentally determined Nusselt numbers from above were compared to the well-established empirical correlation of Dittus-Boelter to validate the test facility.

$$Nu_{DB} = 0.023 Re_b^{0.8} Pr_b^{0.4}$$

Theoretical wall temperature based on the Dittus-Boelter correlation was calculated using an energy balance and assuming constant heat flux.

$$T_{w,DB} = T_b + \frac{Q".ID}{k_b.Nu_{DB}}$$

Figure B-1 compares the measured and theoretical Nusselt numbers for mass flow rate of 0.035 kg/s and power supply heat input of 650 W. Measured Nusselt numbers agree well with the Dittus-Boelter correlation. Thermal entrance length effects were noted for the first three thermocouple readings and is evident from the variation of the Nusselt number. After the thermal entrance length, the Nusselt number stays nearly constant as expected for the constant property flows.

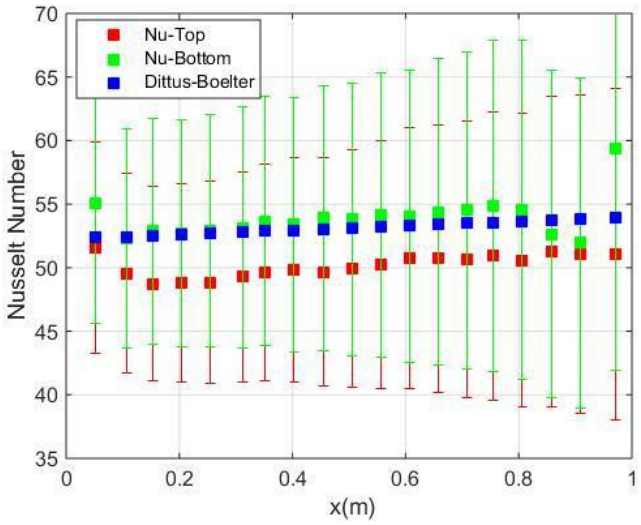

Figure B-1: Experimental Nusselt numbers determined from water calibration tests compared to the Dittus-Boelter correlation

APPENDIX C. DATA REDUCTION AND UNCERTAINTY CALCULATIONS FOR THE CIRCULAR TUBE TEST SECTION

This Appendix presents detailed calculations of the data reduction procedure and the associated uncertainty quantification for the smaller circular tube test section (ID=7.9 mm) representative example case.

Test section details and measured experimental parameters:

Test section details	
Inner diameter (D_i)	7.899 mm
Outer diameter (D_o)	9.525 mm
Wall thickness (t_{wall})	0.813 mm
Length (L)	1.0 m
Insulation thickness ($t_{insulation}$)	50.8 mm
Insulation diameter ($D_{insulation}$)	111.125 mm
Insulation thermal conductivity ($k_{insulation}$)	0.04 W/m-K
Ambient air temperature (T_{air}/T_∞)	20 °C
Measured experimental parameters	
Inlet temperature (T_{in})	25.06 °C
Inlet pressure (P_{in})	7486.7 kPa
Outlet temperature (T_{out})	35.63 °C
Outlet pressure (P_{out})	7409.8 kPa
Mass flow rate ($\dot{m}$)	0.0095 kg/s
Power supply heat input ($V_{PS}I_{PS}$)	1196.9 W

Measured outer wall temperatures:

Thermocouple location	Distance from the inlet (m)	Top side outer wall temperature, $T_{wo,top}$ (°C)	Bottom side outer wall temperature, $T_{wo,bottom}$ (°C)
x_1	0.0508	52.21±1.0	48.02±1.0
x_2	0.1079	52.66±1.0	48.50±1.0
x_3	0.1524	54.36±1.0	49.32±1.0
x_4	0.2032	56.05±1.0	50.28±1.0

x_5	0.2540	58.75±1.0	51.26±1.0
x_6	0.3111	60.72±1.0	52.29±1.0
x_7	0.3524	62.63±1.0	53.10±1.0
x_8	0.4032	64.86±1.0	54.53±1.0
x_9	0.4540	67.77±1.0	55.98±1.0
x_{10}	0.5048	70.98±1.0	57.88±1.0
x_{11}	0.5556	74.64±1.0	59.85±1.0
x_{12}	0.6064	78.38±1.0	62.01±1.0
x_{13}	0.6572	83.33±1.0	64.25±1.0
x_{14}	0.7080	88.20±1.0	67.58±1.0
x_{15}	0.7556	93.73±1.0	70.37±1.0
x_{16}	0.8065	99.68±1.0	74.57±1.0
x_{17}	0.8572	105.89±1.0	82.77±1.0
x_{18}	0.9080	110.63±1.0	89.50±1.0
x_{19}	0.9715	116.36±1.0	78.55±1.0

Local resistive heat input and volumetric heat generation calculation:

Local resistive heat input and the associated uncertainty are calculated from Equation (4.4) and Equation (4.19) respectively. Resistivity is a function of the test section temperature and is evaluated using Equation (4.2).

Local volumetric heat generation and the associated uncertainty are calculated according to Equation (4.13) and Equation (4.21) respectively.

	Local resistivity, ρ (10^{-8} Ω-m)	Local resistive heat input, Q_{PS} (W)	Local volumetric heat generation, $\dot{q}$ (W/m^3)/10^7
x_1	79.51	93.51±0.0386	5.295±0.00218
x_2	79.54	59.87±0.0247	5.297±0.00218
x_3	79.63	56.19±0.0232	5.303±0.00218
x_4	79.72	60.00±0.0247	5.309±0.00218
x_5	79.84	63.85±0.0263	5.317±0.00219
x_6	79.94	58.29±0.0240	5.324±0.00219
x_7	80.03	54.59±0.0225	5.330±0.00219
x_8	80.16	60.33±0.0249	5.338±0.00220
x_9	80.30	60.44±0.0249	5.348±0.00220
x_{10}	80.47	60.57±0.0250	5.360±0.00221
x_{11}	80.66	60.71±0.0250	5.372±0.00221

x_{12}	80.86	60.86±0.0251	5.385±0.00222
x_{13}	81.10	61.04±0.0252	5.401±0.00222
x_{14}	81.38	59.34±0.0245	5.420±0.00223
x_{15}	81.66	59.54±0.0246	5.439±0.00224
x_{16}	82.00	61.72±0.0254	5.461±0.00225
x_{17}	82.49	62.08±0.0256	5.494±0.00226
x_{18}	82.87	70.17±0.0289	5.519±0.00227
x_{19}	82.70	73.76±0.0304	5.508±0.00227

Local test section heat loss calculation:

Local heat loss is calculated from Equation (4.5) and an uncertainty of ±50% is assumed for the calculated heat loss.

	Conductive resistance, R_1 (K/W)	Convective HTC, h_{air} (W/m^2-K)	Radiative HTC, h_{rad} (W/m^2-K)	Convective and radiative resistance, $R_2 + R_3$ (K/W)	Insulation surface temperature, T_s (°C)	Local heat loss, Q_{loss} (W)
x_1	123.15	2.09	4.88	5.17	21.21	0.234±0.117
x_2	192.42	2.10	4.88	8.07	21.23	0.152±0.076
x_3	205.25	2.12	4.88	8.58	21.27	0.148±0.074
x_4	192.42	2.14	4.89	8.01	21.32	0.165±0.082
x_5	181.10	2.17	4.89	7.51	21.39	0.185±0.092
x_6	198.62	2.19	4.89	8.21	21.45	0.176±0.088
x_7	212.32	2.21	4.89	8.75	21.49	0.171±0.085
x_8	192.42	2.24	4.89	7.90	21.56	0.198±0.099
x_9	192.42	2.27	4.89	7.86	21.64	0.209±0.104
x_{10}	192.42	2.30	4.90	7.83	21.73	0.221±0.110
x_{11}	192.42	2.34	4.90	7.78	21.83	0.236±0.118
x_{12}	192.42	2.37	4.90	7.74	21.94	0.250±0.125
x_{13}	192.42	2.41	4.90	7.70	22.07	0.268±0.134
x_{14}	198.62	2.46	4.91	7.89	22.21	0.280±0.140
x_{15}	198.62	2.50	4.91	7.85	22.35	0.300±0.150
x_{16}	192.42	2.54	4.92	7.55	22.53	0.335±0.167
x_{17}	192.42	2.61	4.92	7.47	22.78	0.371±0.185
x_{18}	171.04	2.66	4.93	6.60	22.97	0.450±0.225
x_{19}	162.37	2.64	4.93	6.28	22.88	0.459±0.229

Local inner wall temperature and bulk fluid temperature calculations:

Local inner wall temperatures and the associated uncertainty are calculated from Equation (4.12) and Equation (4.21) respectively.

Local bulk fluid enthalpy, temperatures and the associated uncertainty are calculated from Equation (4.14) and Equation (4.23) respectively.

	Top inner wall temperature, $T_{wi,top}$ (°C)	Bottom inner wall temperature, $T_{wi,bottom}$ (°C)	Bulk enthalpy, i_b (kJ/kg)	Bulk pressure, P_b (kPa)	Bulk temperature, $T_b = f(i_b, P_b)$ (°C)
x_1	50.88±1.0	46.69±1.0	270.81±0.702	7486.7±0.02	26.24±0.16
x_2	51.33±1.0	47.16±1.0	278.86±0.702	7486.6±0.02	27.95±0.14
x_3	53.03±1.0	47.98±1.0	284.95±0.702	7486.6±0.02	29.02±0.12
x_4	54.72±1.0	48.94±1.0	291.05±0.702	7486.6±0.02	29.88±0.10
x_5	57.43±1.0	49.92±1.0	297.55±0.702	7486.6±0.02	30.58±0.08
x_6	59.39±1.0	50.95±1.0	303.95±0.702	7486.6±0.02	31.06±0.08
x_7	61.30±1.0	51.76±1.0	309.88±0.702	7486.6±0.02	31.33±0.08
x_8	63.53±1.0	53.19±1.0	315.90±0.702	7486.6±0.02	31.49±0.09
x_9	66.44±1.0	54.64±1.0	322.24±0.702	7486.6±0.02	31.56±0.09
x_{10}	69.66±1.0	56.54±1.0	328.58±0.702	7486.6±0.02	31.59±0.10
x_{11}	73.32±1.0	58.51±1.0	334.94±0.702	7486.6±0.02	31.62±0.10
x_{12}	77.06±1.0	60.67±1.0	341.31±0.702	7486.6±0.02	31.64±0.11
x_{13}	82.01±1.0	62.91±1.0	347.70±0.702	7486.6±0.02	31.68±0.12
x_{14}	86.88±1.0	66.24±1.0	354.01±0.703	7486.6±0.02	31.74±0.12
x_{15}	92.42±1.0	69.03±1.0	360.23±0.703	7486.6±0.02	31.85±0.13
x_{16}	98.37±1.0	73.23±1.0	366.58±0.703	7486.6±0.02	32.03±0.14
x_{17}	104.58±1.0	81.44±1.0	373.05±0.703	7486.5±0.02	32.32±0.15
x_{18}	109.32±1.0	88.16±1.0	379.97±0.703	7486.5±0.02	32.78±0.16
x_{19}	115.06±1.0	77.21±1.0	387.50±0.703	7486.5±0.02	33.49±0.17

Local heat transfer coefficient and Nusselt number calculations:

Local heat transfer coefficients and the associated uncertainty are calculated from Equation (4.15) and Equation (4.27) respectively.

Local Nusselt numbers and the associated uncertainty are calculated from Equation (4.16) and Equation (4.28) respectively.

	Top side heat transfer coefficient, htc_{top} (W/m^2-K)	Bottom side heat transfer coefficient, htc_{bottom} (W/m^2-K)	Top side Nusselt number, Nu_{top}	Bottom side Nusselt number, Nu_{bottom}
x_1	1922.0±81.4	2316.4±117.2	185.4±7.87	223.5±11.33
x_2	2026.3±89.8	2466.0±131.9	201.6±8.95	245.4±13.14
x_3	1974.9±85.2	2500.9±135.2	199.4±8.60	252.5±13.66
x_4	1911.1±79.7	2491.0±133.8	193.3±8.06	251.9±13.53
x_5	1770.8±68.6	2457.5±129.9	175.7±6.84	243.9±12.94
x_6	1679.3±61.8	2392.5±123.1	158.9±6.01	226.5±11.81
x_7	1589.4±55.6	2331.4±116.9	138.7±5.32	203.5±10.69
x_8	1488.5±49.0	2197.9±104.1	112.9±5.02	166.8±9.34
x_9	1369.7±41.8	2070.2±92.5	82.4±5.23	124.6±8.89
x_{10}	1257.6±35.5	1919.4±79.8	61.7±4.76	94.2±7.82
x_{11}	1150.5±30.1	1783.8±69.1	54.5±4.20	84.6±6.95
x_{12}	1058.7±25.8	1656.7±59.9	52.1±3.52	81.5±5.92
x_{13}	957.9±21.5	1543.7±52.2	56.2±2.82	90.7±5.09
x_{14}	877.1±18.3	1402.1±43.4	62.9±2.39	100.6±4.46
x_{15}	800.9±15.6	1305.0±37.8	69.0±2.11	112.4±4.21
x_{16}	734.0±13.5	1182.1±31.4	74.6±1.95	120.1±3.90
x_{17}	677.5±11.8	996.8±23.0	79.7±1.85	117.3±3.25
x_{18}	642.3±10.8	887.6±18.7	86.7±1.85	119.8±2.97
x_{19}	601.5±9.7	1122.4±28.5	92.5±1.83	172.6±4.81

APPENDIX D. AXIAL AND CIRCUMFERENTIAL CONDUCTION FOR THE CIRCULAR TUBE TEST SECTION

This Appendix presents a rough order of magnitude calculations of the axial and circumferential conduction heat transfer for the circular tube test section. These calculations were performed to understand the contributions of axial and circumferential conduction compared to the total resistive heat input from the DC power supply. The sample calculations presented here are for the representative case from APPENDIX C. For each subsection (Refer to Figure 4-1), the axial and circumferential conduction components are calculated as follows (Refer to Figure D-1 for the conduction resistance networks):

$$Q_{axial} = k_{ss316} A_{tube,axial} \frac{(T_{i-1} - T_i)}{\Delta L} + k A_{tube} \frac{(T_{i+1} - T_i)}{\Delta L}$$

$$Q_{circumferential} = 2 k_{ss316} A_{tube,circumferential} \frac{(T_{w,top} - T_{w,bottom})}{\pi\left(\frac{OD+ID}{2}\right)}$$

where k_{ss316} is the thermal conductivity of 316 stainless steel, $A_{tube,axial}$ is the conductive heat transfer area in the axial direction, $A_{tube,circumferential}$ is the conductive heat transfer area in the circumferential direction.

$$A_{tube,axial} = \frac{\pi}{4}(OD^2 - ID^2)$$

$$A_{tube,circumferential} = \Delta L \left(\frac{OD - ID}{2}\right)$$

The circumferential and axial conductive heat transfer components for the representative case from APPENDIX C are listed in Table D-1. Also listed in the table is the total resistive

heat input for each sub-section. Circumferential conductive heat transfer components are significantly higher than the corresponding axial conductive heat transfer components. The total circumferential and axial conductive heat transfer is ~2.3% of the total resistive heat input for the representative case.

Table D-1: Circumferential and axial conductive heat transfer components for the representative case

	Local resistive heat input, Q_{PS} (W)	Circumferential conductive heat transfer, Q_{radial} (W)	Axial conductive heat transfer, Q_{axial} (W)
x_2	59.87±0.0247	0.41	0.011
x_3	56.19±0.0232	0.46	-0.002
x_4	60.00±0.0247	0.56	0.007
x_5	63.85±0.0263	0.78	-0.007
x_6	58.29±0.0240	0.79	0.004
x_7	54.59±0.0225	0.84	-0.001
x_8	60.33±0.0249	1.01	0.005
x_9	60.44±0.0249	1.15	0.002
x_{10}	60.57±0.0250	1.28	0.003
x_{11}	60.71±0.0250	1.45	0.001
x_{12}	60.86±0.0251	1.60	0.009
x_{13}	61.04±0.0252	1.87	-0.001
x_{14}	59.34±0.0245	1.95	0.007
x_{15}	59.54±0.0246	2.21	0.001
x_{16}	61.72±0.0254	2.46	0.002
x_{17}	62.08±0.0256	2.26	-0.011
x_{18}	70.17±0.0289	2.32	-0.001

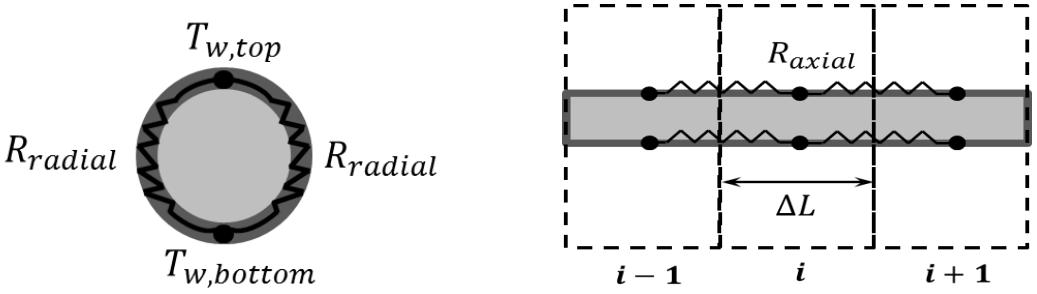

Figure D-1: Resistance network for estimation of the axial (left) and the radial (right) conductive heat transfer components

APPENDIX E. DATA REDUCTION AND UNCERTAINTY CALCULATIONS FOR THE PCHE TEST SECTION

This Appendix presents detailed calculations of the data reduction procedure and the associated uncertainty quantification for the offset rectangular fin PCHE representative example case.

Test section details and measured experimental parameters:

Test section details	
Hydraulic diameter (D_h)	0.9973±0.0141 mm
CO_2 flow cross-sectional area (A_c)	11.567±0.1156 mm^2
Length of each cooling block (L_{cb})	50 mm
Number of cooling blocks (N)	10
Total length of the test section (L)	500 mm
Water side heat transfer area of each cooling block (A_{cb})	1793.54±89.67 mm^2
CO_2 side heat transfer area per each cooling block (A_s)	2319.58±23.19 mm^2
Insulation thickness ($t_{insulation}$)	76.2 mm
Insulation thermal conductivity ($k_{insulation}$)	0.04 W/m-K
Ambient air temperature (T_{air}/T_∞)	20 °C
Measured experimental parameters	
Inlet temperature (T_{in})	150.54±0.1776 °C
Inlet pressure (P_{in})	7529.1±5.26 kPa
Outlet temperature (T_{out})	33.86±0.1532 °C
Pressure drop (ΔP)	56.26±0.5081 kPa
Outlet pressure ($P_{out} = P_{in} - \Delta P$)	7472.8±5.28 kPa
Mass flow rate ($\dot{m}$)	0.00735±0.0000735 kg/s

Calculation of the CO_2 side test section heat duty:

CO_2 side heat duty	
Inlet enthalpy, $h_{in} = f(P_{in}, T_{in})$	58,491 J/kg
Inlet enthalpy uncertainty, $\sigma_{h_{in}}$	208.2 J/kg
Outlet enthalpy, $h_{out} = f(P_{out}, T_{out})$	39,151 J/kg
Outlet enthalpy uncertainty, $\sigma_{h_{out}}$	1215.1 J/kg
CO_2 side heat duty, $Q_{CO_2} = \dot{m}(h_{in} - h_{out})$	1421.5±17.3 J/kg

Calculation of the water side test section heat duty:

The table below shows the measured water side parameters for each cooling block (10 cooling blocks referred to as "Bottom" are attached to the PCHE test plate and 10 cooling blocks referred to as "Top" are attached to the mating plate). Water pressure is assumed to be 689.4 kPa for calculation of the water properties. The heat duty for each cooling block is calculated as follows,

$$Q = \dot{V}\rho C_p(T_{out} - T_{in} - \Delta T_{isothermal})$$

where $\Delta T_{isothermal}$ is the temperature difference between the inlet and the outlet thermocouples under isothermal conditions.

Cooling block	Water inlet temperature, T_{in} (°C)	Water outlet temperature, T_{out} (°C)	$\Delta T_{isothermal}$ (°C)	Volumetric flow rate, $\dot{V}$ (GPM)	Heat duty, Q (W)
Top 1	16.42±0.15	26.55±0.15	0.19	0.0505	131.8±5.45
Top 2	13.21±0.15	23.32±0.15	0.13	0.0437	114.8±4.65
Top 3	13.15±0.15	20.80±0.15	0.02	0.0455	91.53±3.25
Top 4	13.49±0.15	20.42±0.15	-0.00	0.0372	68.08±3.64
Top 5	13.34±0.15	18.05±0.15	-0.05	0.0504	63.25±3.57
Top 6	13.15±0.15	17.38±0.15	0.04	0.0453	49.92±3.13
Top 7	13.43±0.15	17.32±0.15	-0.07	0.0412	43.08±2.84
Top 8	13.22±0.15	16.95±0.15	-0.04	0.0374	37.25±2.69
Top 9	13.20±0.15	16.95±0.15	0.03	0.0370	36.19±2.31
Top 10	13.28±0.15	17.12±0.15	-0.08	0.0304	31.51±2.46
Bottom 1	15.34±0.15	29.42±0.15	0.25	0.0467	169.9±5.12
Bottom 2	14.46±0.15	25.39±0.15	0.04	0.0431	123.5±3.61
Bottom 3	14.26±0.15	23.82±0.15	0.01	0.0353	88.60±4.43
Bottom 4	13.74±0.15	20.06±0.15	0.08	0.0460	75.64±3.84
Bottom 5	14.19±0.15	19.78±0.15	0.02	0.0415	60.85±3.41
Bottom 6	14.32±0.15	19.88±0.15	-0.01	0.0338	49.61±2.79
Bottom 7	14.31±0.15	18.43±0.15	0.06	0.0410	43.83±2.87
Bottom 8	14.39±0.15	18.14±0.15	0.00	0.0410	40.43±2.71
Bottom 9	13.94±0.15	17.02±0.15	0.04	0.0477	38.28±3.02
Bottom 10	14.40±0.15	17.40±0.15	0.02	0.0502	39.37±3.02

The water side heat duty is calculated by summing the heat duties of all individual cooling blocks (last column in the table above),

$$Q_{H_2O} = \sum_{i=1}^{20} Q_i = 1397.6 \text{ W}$$

$$\sigma_{Q_{H_2O}} = \left(\sum_{i=1}^{20} \left(\sigma_{Q_i}\right)^2\right)^{0.5} = 15.86 \text{ W}$$

The CO_2 side heat duty (Q_{CO_2}=1421.5 W) and the water side heat duty (Q_{H_2O}=1397.6 W) agree within ±1.7% for this representative case. In general, both the heat duties agreed within ±10% for all the cases with maximum deviation occurring near the pseudocritical point.

CO_2 side nodal calculations (See Figure E-1 for the location of the nodes):

$$h[1] = h_{in}$$

$$P[1] = P_{in}$$

$$h[i] = h[i-1] - \frac{Q_i}{\dot{m}}$$

$$P[i] = P[i-1] - \frac{\Delta P}{L}.L_{cb}$$

$$T[i], \rho[i], \mu[i], k[i], C_p[i], \text{Pr}[i] = f(h[i], P[i])$$

Values	h (J/kg)	P (kPa)	T (°C)	ρ (kg/m^3)	μ (kg/m-s)	k (W/m-K)	C_p (J/kg-K)	Pr
Node 1	584910	7529.1	150.54	105.35	2.2E-05	0.0307	1163.4	0.832
Node 2	543850	7523.5	116.11	120.91	2.08E-05	0.0286	1233.8	0.894
Node 3	511420	7517.9	90.83	137.60	2E-05	0.0276	1350.1	0.978
Node 4	486920	7512.3	73.56	154.12	1.96E-05	0.0274	1511.8	1.081
Node 5	467360	7506.7	61.37	170.69	1.95E-05	0.0279	1731.0	1.207
Node 6	450480	7501.0	52.30	188.23	1.96E-05	0.0291	2043.0	1.370
Node 7	436940	7495.4	46.16	205.01	1.98E-05	0.0309	2443.1	1.563
Node 8	425110	7489.8	41.71	222.03	2.02E-05	0.0334	2987.7	1.807
Node 9	414540	7484.2	38.49	239.43	2.07E-05	0.0365	3746.8	2.124

Node 10	404410	7478.6	36.06	258.29	2.13E-05	0.0406	4908.7	2.576
Node 11	394760	7473.0	34.32	278.40	2.21E-05	0.046	6748.5	3.240
Uncertainties	σ_h (J/kg)	σ_P (kPa)	σ_T (°C)	σ_ρ (kg/m^3)	σ_μ (kg/m-s)	σ_k (W/m-K)	σ_{C_p} (J/kg-K)	σ_{Pr}
Node 1	208.2	5.26	0.17	0.10	6.7E-09	0.0000121	0.28	0.000
Node 2	1122.9	5.26	0.91	0.50	3.07E-08	0.0000482	2.84	0.002
Node 3	1420.3	5.26	1.05	0.85	2.86E-08	0.0000306	7.05	0.005
Node 4	1625.3	5.26	1.07	1.25	1.82E-08	0.0000177	14.12	0.010
Node 5	1789.3	5.26	1.03	1.70	5.3E-09	0.0000886	25.75	0.018
Node 6	1919.5	5.26	0.94	2.21	2.5E-08	0.0001992	45.29	0.031
Node 7	2007.7	5.27	0.82	2.71	5.24E-08	0.0003385	74.06	0.050
Node 8	2085.4	5.27	0.69	3.25	8.42E-08	0.0005188	119.59	0.078
Node 9	2152.2	5.27	0.57	3.80	1.2E-07	0.0007486	192.93	0.118
Node 10	2216.0	5.28	0.45	4.41	1.61E-07	0.0010612	323.12	0.183
Node 11	2280.9	5.28	0.34	5.07	2.09E-07	0.0014915	564.72	0.292

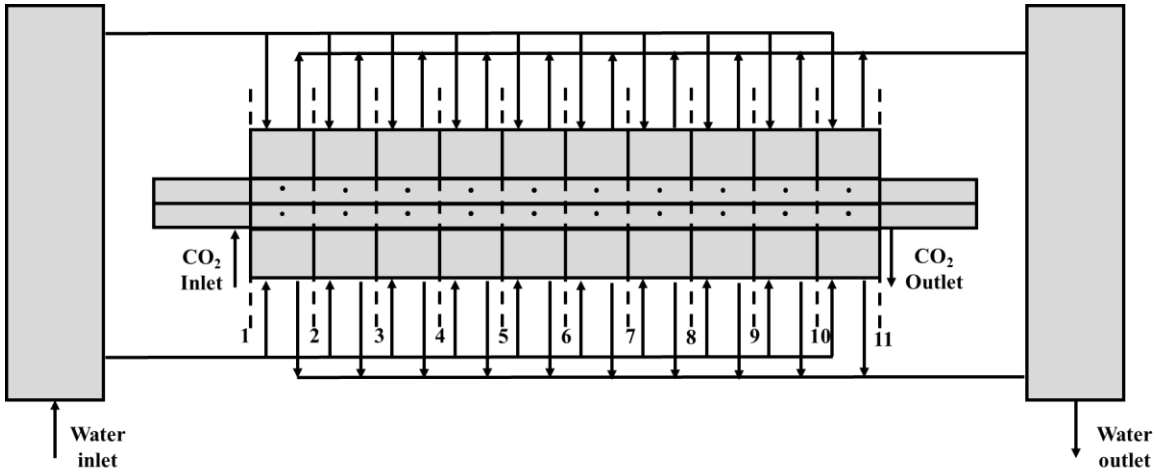

Figure E-1: Schematic showing the location of nodes used for the data processing. There are total of ten control volumes (corresponding to each cooling block) and eleven nodes.

CO_2 side local bulk calculations:

$$h_b[i] = 0.5(h[i] + h[i+1])$$

$$P_b[i] = 0.5(P[i] + P[i+1])$$

$$T_b[i], \rho_b[i], \mu_b[i], k_b[i], C_{p,b}[i], Pr_b[i] = f(h_b[i], P_b[i])$$

Values	h_b (J/kg)	P_b (kPa)	T_b (°C)	ρ_b (kg/m^3)	μ_b (kg/m-s)	k_b (W/m-K)	$C_{p,b}$ (J/kg-K)	Pr_b
CV 1	564380	7526.3	133.07	112.51	2.13E-05	0.0296	1191.4	0.859
CV 2	527640	7520.8	103.19	128.65	2.03E-05	0.028	1282.3	0.930
CV 3	499170	7515.3	81.96	145.35	1.98E-05	0.0274	1419.7	1.024
CV 4	477140	7509.7	67.26	161.96	1.95E-05	0.0275	1607.6	1.137
CV 5	458920	7503.5	56.65	179.04	1.95E-05	0.0284	1867.8	1.280
CV 6	443710	7498.0	49.09	196.28	1.97E-05	0.0299	2220.8	1.458
CV 7	431020	7492.5	43.83	213.22	2E-05	0.032	2685.5	1.674
CV 8	419830	7487.0	40.01	230.45	2.04E-05	0.0348	3325.0	1.950
CV 9	409470	7481.5	37.19	248.58	2.1E-05	0.0384	4257.3	2.327
CV10	399590	7475.9	35.12	268.07	2.17E-05	0.0431	5707.4	2.871
Uncertainties	σ_{h_b} (J/kg)	σ_{P_b} (kPa)	σ_{T_b} (°C)	σ_{ρ_b} (kg/m^3)	σ_{μ_b} (kg/m-s)	σ_{k_b} (W/m-K)	$\sigma_{C_{p,b}}$ (J/kg-K)	σ_{Pr_b}
CV 1	571	5.26	0.47	0.23	1.73E-08	2.94E-05	0.97	0.001
CV 2	905.3	5.26	0.70	0.47	2.21E-08	3.11E-05	3.19	0.002
CV 3	1079.2	5.26	0.76	0.73	1.77E-08	0.000012	7.03	0.005
CV 4	1208.6	5.26	0.75	1.03	8.7E-09	3.39E-05	13.40	0.009
CV 5	1312.1	5.26	0.70	1.37	9.5E-09	0.000097	23.99	0.017
CV 6	1388.8	5.26	0.62	1.73	2.7E-08	0.000185	40.68	0.028
CV 7	1447.4	5.27	0.54	2.10	4.79E-08	0.000297	66.07	0.044
CV 8	1498.4	5.27	0.45	2.49	7.16E-08	0.000441	106.60	0.067
CV 9	1544.6	5.28	0.36	2.90	9.88E-08	0.00063	174.99	0.103
CV10	1590.1	5.28	0.28	3.35	1.3E-07	0.000888	298.89	0.162

Measured wall temperatures:

	Thermocouple location from the surface, z (m)	Measured wall temperature, $T_{w,meas}$ (°C)
Top 1	0.0041	62.9±0.17
Top 2	0.0040	51.5±0.16
Top 3	0.0042	44.9±0.15
Top 4	0.0041	38.7±0.15
Top 5	0.0040	35.5±0.15
Top 6	0.0039	29.3±0.15
Top 7	0.0041	30.2±0.15
Top 8	0.0043	26.5±0.15
Top 9	0.0041	26.6±0.15
Top 10	0.0039	25.9±0.15
Bottom 1	0.0041	64.7±0.17
Bottom 2	0.0040	59.9±0.17
Bottom 3	0.0041	52.8±0.16
Bottom 4	0.0041	41.5±0.15
Bottom 5	0.0041	38.8±0.15

Bottom 6	0.0038	36.69±0.15
Bottom 7	0.0042	31.72±0.15
Bottom 8	0.0041	29.84±0.15
Bottom 9	0.0040	28.35±0.15
Bottom 10	0.0042	26.70±0.15

Calculated surface wall temperatures:

$$T_w = T_{w,meas} + \frac{Q_i z}{k_{ss316} A_{cb}}$$

$$T_w = 0.5(T_{w,top} + T_{w,bottom})$$

	Calculated top wall temperature, $T_{w,top}$ (°C)		Calculated bottom wall temperature, $T_{w,bottom}$ (°C)		Calculated average wall temperature, T_w (°C)
Top 1	84.29±1.78	Bottom 1	91.76±2.11	Average 1	88.03±1.38
Top 2	69.69±1.50	Bottom 2	79.40±1.52	Average 2	74.54±1.07
Top 3	60.15±1.23	Bottom 3	67.16±1.26	Average 3	63.65±0.88
Top 4	50.11±1.03	Bottom 4	53.98±1.11	Average 4	52.04±0.75
Top 5	45.80±0.95	Bottom 5	48.95±0.93	Average 5	47.38±0.66
Top 6	37.30±0.77	Bottom 6	44.38±0.71	Average 6	40.84±0.52
Top 7	37.35±0.71	Bottom 7	39.14±0.73	Average 7	38.24±0.51
Top 8	33.04±0.68	Bottom 8	36.61±0.68	Average 8	34.83±0.48
Top 9	32.62±0.59	Bottom 9	34.59±0.68	Average 9	33.61±0.45
Top 10	30.97±0.56	Bottom 10	33.49±0.72	Average 10	32.23±0.46

Heat transfer coefficient and Nusselt number calculations:

$$htc = \frac{Q_{top} + Q_{bottom}}{A_s.(T_b - T_w)}$$

$$Nu = \frac{htc.D_h}{k_b}$$

Distance from inlet, x (m)	htc (W/m^2-K)	Nu	Re_b
0.025	2889±121.5	97.3±4.3	29700
0.075	3587±187.0	127.7±6.9	31173
0.125	4243±302.8	154.5±11.2	32095
0.175	4072±325.3	147.4±11.9	32512
0.225	5768±648.1	202.4±22.9	32534
0.275	5199±563.7	173.2±18.9	32242
0.325	6714±952.4	208.9±29.8	31730

0.375	6462±887.4	185.2±25.6	31049
0.425	8967±1532.0	223.0±40.1	30213
0.475	10572±2061.7	244.6±48.0	29229

Average heat transfer coefficient for the test section is evaluated as,

$$\overline{htc} = \frac{0.5\left(Q_{CO_2}+Q_{H_2O}\right)}{N.A_s.(\overline{T_b}-\overline{T_w})}$$

where $\overline{T_b} = \frac{1}{L}\int_0^L T_b(x)$ and $\overline{T_w} = \frac{1}{L}\int_0^L T_w(x)$.

For the representative case presented here, $\overline{T_b}$ = 64.9±0.26 °C and $\overline{T_w}$ = 49.47±0.23 °C. The average heat transfer coefficient is calculated as 3939±103.2 W/m^2-K. The average Reynolds number, $\overline{Re}$=31,169±630.3 and the average Prandtl number, $\overline{Pr}$=1.56±0.028.

Average Nusselt for the test section is evaluated as,

$$\overline{Nu} = \overline{htc}.\frac{D_h}{\overline{k_b}}$$

For the representative case presented here, the average thermal conductivity, $\overline{k_b}$=0.032±0.000163 W/m-K and the average Nusselt number, $\overline{Nu}$=122.62±3.70.

APPENDIX F. COMPUTATIONAL FLUID DYNAMICS STUDY

Computational fluid dynamics (CFD) software ANSYS FLUENT is used to obtain a numerical solution for comparison against the experimental data and understand the fluid flow and heat transfer characteristics of the prototype PCHEs. ANSYS FLUENT is a commercial CFD software which solves set of governing equations, which in the present case are continuity, momentum and energy equations using the finite volume discretization techniques. The computational domain modelled in the present study is shown in Figure F-1. As can be seen, only a section of the PCHE was modelled in the spanwise direction by taking advantage of the periodic boundary condition to reduce the computational effort. However, the full length (L=500 mm) of the PCHE was modelled to resolve the variation of temperature, pressure and other variables along the length. The mass flow and the temperature were specified at the inlet (mass flow inlet boundary condition) whereas the pressure was specified at the outlet (pressure outlet boundary condition). The experimentally measured top and bottom surface wall temperatures were provided as the inputs to the model using a user-defined function (UDF). The variation of the wall temperature between any two consecutive thermocouples was assumed to be linear. FLUENT v19.0 is used for all the simulations and the governing equations were discretized up to second order spatial accuracy. The pressure-based solver approach is utilized and the coupling between the pressure and velocity fields is implemented by the SIMPLE algorithm. The thermophysical properties of CO_2 were calculated by linking FLUENT to the NIST Standard Reference property database.

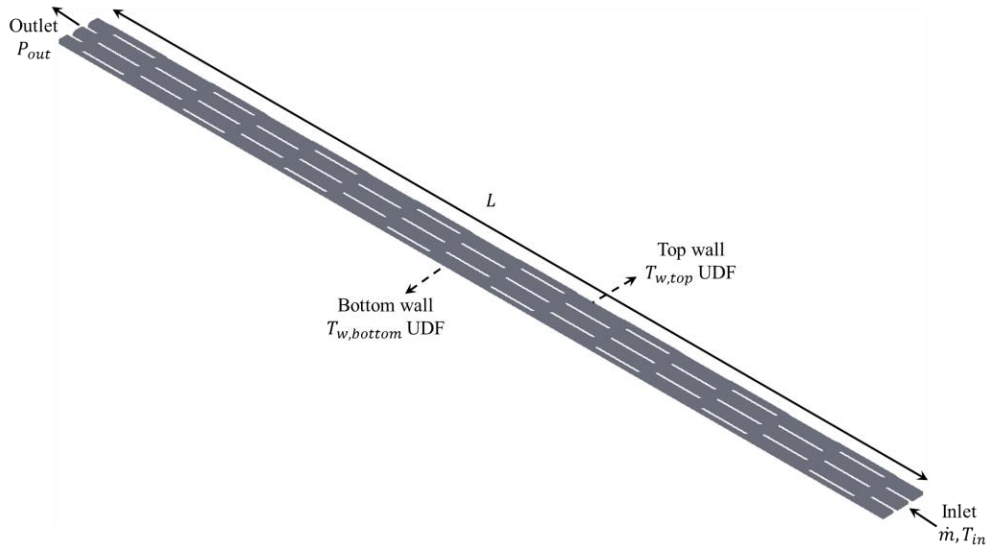

Figure F-1: Computation domain of the offset rectangular fin PCHE

Turbulence modelling

Since the flow is highly turbulent it is necessary to resolve the physics of the flow accordingly. In order to resolve all levels of turbulence, direct numerical simulations (DNS) or large eddy simulations (LES) are the most accurate approaches. However, at the same time due to large amount of computational time and resources required it is not practical to use the DNS or LES techniques at this point of time. A traditional computational approach to model the turbulence is to solve the Reynolds-Averaged Navier-Stokes (RANS) equations which require selection of an appropriate turbulence model such as k-ε or k-ω and their variants. It should however be pointed out that there is no single turbulence model that can predict all the turbulent flows with sufficient accuracy. FLUENT offers a choice of wide range of two-equation RANS based turbulence models depending on the type of problem, required level of accuracy, computational time etc. For the present study, four different turbulence models from FLUENT database were selected to

investigate the choice of turbulence model on the numerical solution. The key features of the four different turbulence models are described in Table F-1 along with some general comments on their usage.

Table F-1: Description of the four different turbulence models selected for the present study [109]

Turbulence model	General Comments
SST *k-ω*	A variant of the standard *k-ω* model. Uses a blending function to gradually transition from the standard *k-ω* model in the near-wall region to the high Reynolds number *k-ε* model outside the boundary layer. The SST k-ω model is more widely accepted and considered to be more accurate and robust for wide range of boundary layers flows with pressure gradient and flow separation.
Standard *k-ε*	The most widely used baseline two-equation turbulence model. It is robust and reasonably accurate for practical engineering purposes. The main drawback of the model is *ε* equation cannot be computed in the near-wall region and hence, require a wall function. It generally performs poorly for complex flows with strong pressure gradient and flow separation but nevertheless suitable for initial screening of designs and parametric studies.
RNG *k-ε*	A variant of the standard *k-ε* model which contain sub-models to account for low Re flows, swirl effects, strained flows etc. It is known to perform better than the standard *k-ε* model for complex shear flows and flows with strong swirl and separation.
Realizable *k-ε*	A more recently developed variant of the standard *k-ε* model. The term "realizable" indicates that the model satisfies mathematical constraints on the Reynolds stress and is consistent with the physics of turbulent flows unlike the standard or RNG *k-ε* models. The benefits and applications are similar to that of RNG *k-ε* model but might be more accurate and easier to converge than RNG *k-ε* model.

Law of the Wall and Near-Wall treatment

The near-wall region in a turbulent flow, typically known as the viscous sub-layer is characterized by large gradients of velocity, temperature and other transport variables. According to the law of the wall, the viscous sub-layer is defined based on the non-dimensional distance from the wall, $y^+ \leq 5$. For $y^+ \geq 60$, the gradient of variables become small and the region is known as fully turbulent region. The region between $5 < y^+ < 60$ acts as a buffer/blending region between the viscous sub-layer and the fully turbulent region. Therefore, for any turbulent flow, it is necessary to adequately model the viscous sublayer to obtain an accurate solution. There are traditionally two approaches to model the near-wall region; the wall function approach and the enhanced wall treatment approach. In the wall function approach, the mesh/grid in the near wall region is not fully-resolved all the way to the viscous-sub layer. Semi-empirical formulations known as "wall functions" are used to bridge the viscous sub-layer and the fully turbulent regions. The main benefit of the wall function approach is that it allows for use of a relatively coarse mesh in the near-wall region but it might not produce accurate results if the wall functions don't capture the physics of the flow adequately. In the enhanced wall treatment (EWT) approach, the mesh in the near-wall region is resolved all the way to the viscous sub-layer (such that $y^+ \leq 1$) and a blended law of the wall and two-layer models are used to bridge the regions. This approach increases the computational time due to the requirement of fine mesh in the near-wall region but is considered to be more accurate for low Reynolds number flows or flows with complex near-wall phenomenon. In the present study, the enhanced wall treatment approach is adopted wherever possible and the near-wall mesh is refined such that $y^+ < 1$. An example of the near-wall meshing adopted in the present study

for the offset rectangular fin and the offset NACA0020 airfoil PCHEs is shown in Figure F-2.

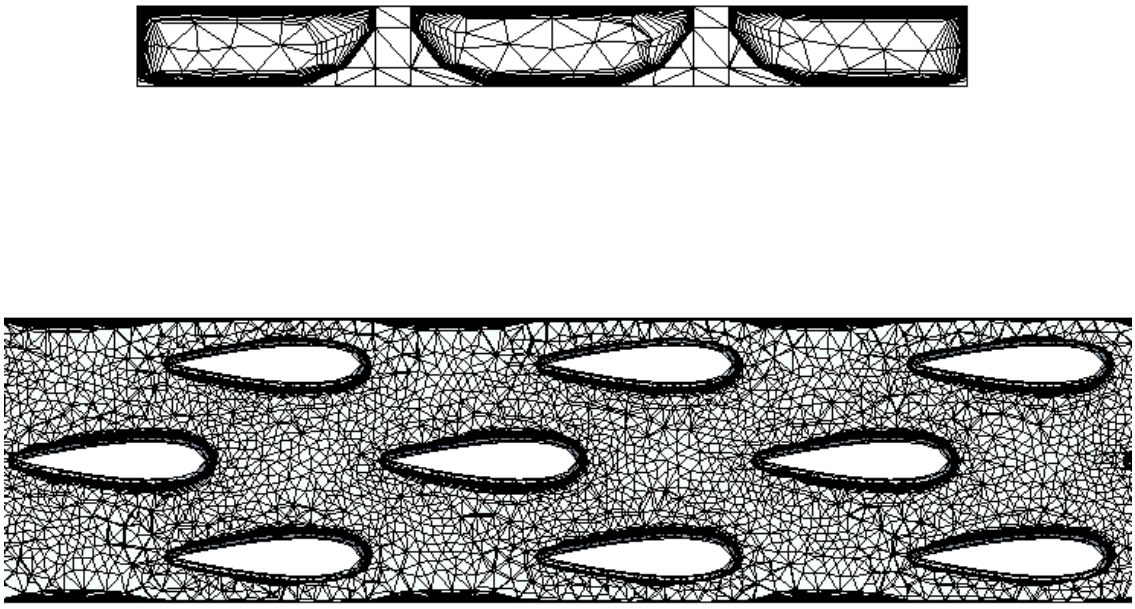

Figure F-2: An example of the near wall meshing adopted for the offset rectangular fin (top) and the offset NACA0020 airfoil fin (bottom) PCHE

Post-processing of the solution

Once a numerical solution is obtained, the heat transfer coefficient is calculated as described in this section. Firstly, the bulk enthalpy, pressure and temperature are calculated at each cross-section according to the equations below:

$$i_b = \frac{\int \rho u i dA}{\int \rho u dA} \tag{F.1}$$

$$P_b = \frac{\int P dA}{\int dA} \tag{F.2}$$

$$T_b = f(i_b, P_b) \tag{F.3}$$

where ρ is the density, u is the velocity, i is the enthalpy, P is the enthalpy of each volumetric cell at a given axial location and dA is the cross-sectional area of each cell. This information is used to calculate the local heat flux and the local heat transfer coefficient as shown in the equations below:

$$q_w"[j] = \frac{\dot{m}(i_b[j-1] - i_b[j])}{A_w} \tag{F.4}$$

$$htc[j] = \frac{q_w"[j]}{(T_b[j] - T_w[j])} \tag{F.5}$$

where A_w is the heat transfer area, T_b is the local bulk temperature and T_w is the average circumferential wall temperature (average of the top and the bottom wall temperatures).

Grid-Independent study

To ensure that the numerical solution is independent of the grid/mesh, solution is obtained using three different mesh sizes for both the PCHEs. The total heat duty and the pressure drop calculated from the CFD is compared against the experimental data for the three different meshes in Table F-2 and Table F-3 for the offset rectangular fin PCHE and the offset NACA0020 airfoil PCHE respectively. The experimental conditions and the measured wall temperatures for these cases can be found in APPENDIX G. For the offset rectangular fin PCHE, the maximum variation in the calculated heat duty for different meshes is <1% whereas the maximum variation in the pressure drop is <7.3%. For the offset NACA0020 airfoil fin PCHE, the maximum variation in the calculated heat duty for different meshes is <3% whereas the maximum variation in the pressure drop is <10.6%.

When compared to the experimental data, the CFD model underpredicted the pressure drop for the offset rectangular fin PCHE by ~40% and for the offset NACA0020 airfoil fin PCHE by ~32%.

Table F-2: Comparison of the offset rectangular fin PCHE experimental data with the numerical data for three different mesh sizes using SST *k-ω* turbulence model; The experimental conditions and the measured wall temperatures for this case can be found in Appendix F

Mesh	Number of nodes	Q_{FLUENT} (W)	Experimental data		ΔP_{FLUENT} (kPa)	ΔP_{exp} (kPa)
			Q_{CO_2} (W)	Q_{H_2O} (W)		
Coarse	348529	1915.7	1987.0±22.4	1987.6±21.5	27.5	49.7±0.62
Medium	633380	1925.2			29.2	
Fine	914135	1909.8			29.5	

Table F-3: Comparison of the offset NACA0020 airfoil fin PCHE experimental data with the numerical data for three different mesh sizes using SST *k-ω* turbulence model; The experimental conditions and measured wall temperatures for this case can be found in Appendix F

Mesh	Number of nodes	Q_{FLUENT} (W)	Experimental data		ΔP_{FLUENT} (kPa)	ΔP_{exp} (kPa)
			Q_{CO_2} (W)	Q_{H_2O} (W)		
Coarse	392472	2016.5	2006.8±22.2	1984.8±25.7	29.8	43.7±0.29
Medium	684800	2074.4			32.5	
Fine	993770	2052.3			29.4	

Figure F-3 and Figure F-4 compares the local heat transfer coefficients for the three different mesh sizes with the experimental data of the offset rectangular fin PCHE and the offset NACA0020 airfoil fin PCHE respectively. The trends in the local heat transfer coefficients agree well with the experimental data. For example, the heat transfer coefficient increase towards the outlet is predicted qualitatively by all the meshes. However, quantitatively there are some differences between the different meshes towards the outlet where the fluid temperature is close to the pseudocritical temperature.

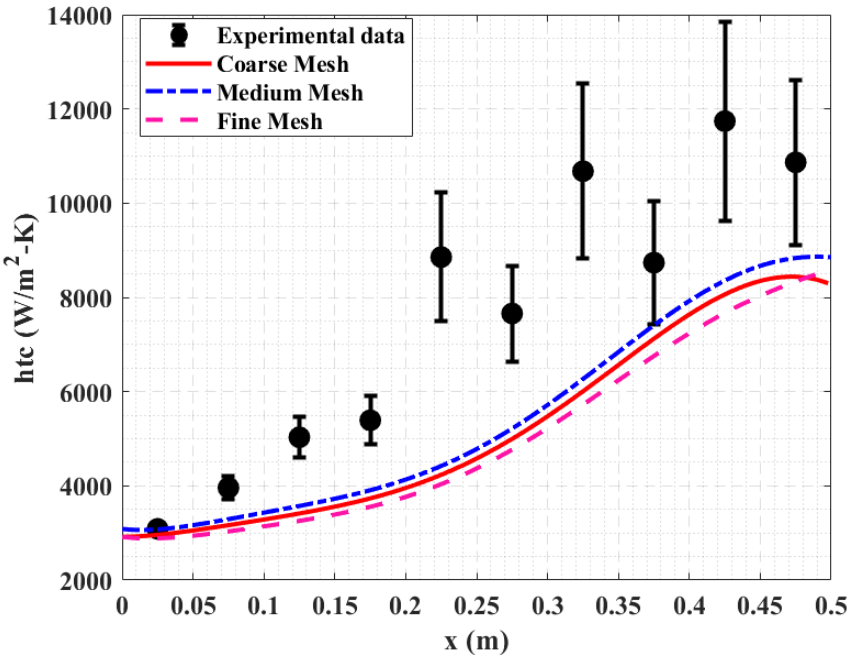

Figure F-3: Comparison of the local heat transfer coefficients obtained using three different mesh sizes and SST *k-ω* turbulence model against the experimental data for the offset rectangular fin PCHE test section

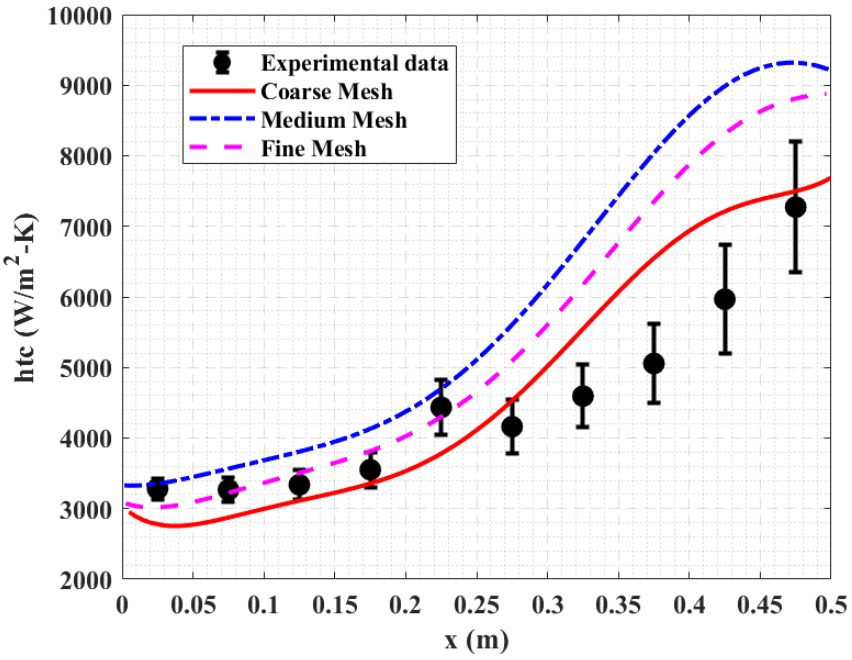

Figure F-4: Comparison of the local heat transfer coefficients obtained using three different mesh sizes and SST *k-ω* turbulence model against the experimental data for the offset NACA0020 airfoil fin PCHE test section

Comparison of different turbulence models with the experimental data

Figure F-5 and Figure F-6 compares the local heat transfer coefficients for the four different turbulence models described earlier with the experimental data of the offset rectangular fin PCHE and the offset NACA0020 airfoil fin PCHE respectively. All the turbulence models were able to predict the trends in heat transfer coefficients. For the temperatures far away the pseudocritical temperature (towards x≈0), the differences between the four turbulence models is quite small and all the models agree well with the experimental data. However, towards the outlet (T_b close to T_{pc}) the differences between the four turbulence models and the experimental data is larger. Out of the four turbulence models, RNG *k-ε* and SST *k-ω* models offered best agreement with the experimental data.

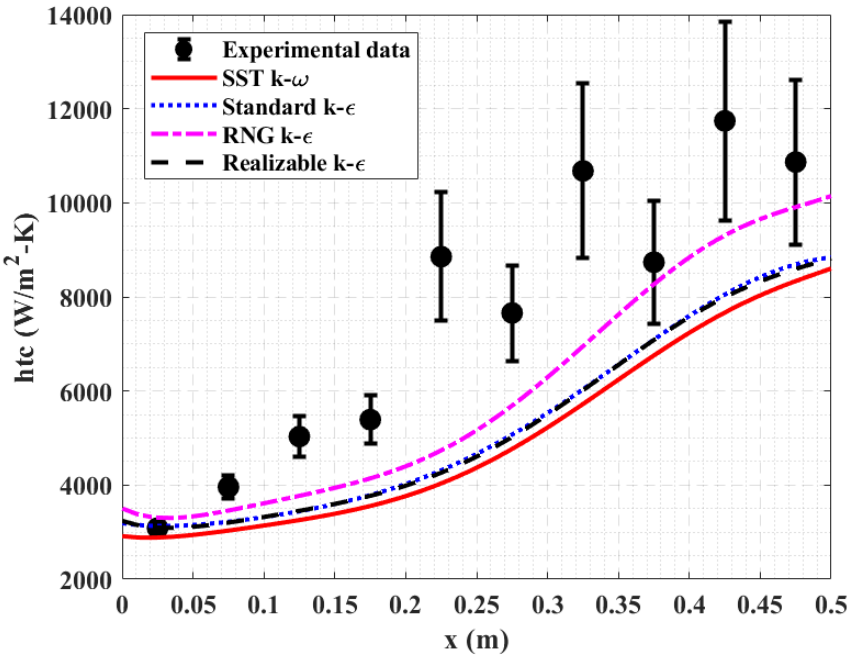

Figure F-5: Comparison of the local heat transfer coefficients obtained using four different turbulence models and fine mesh from Table F-2 against the experimental data for the offset rectangular fin PCHE test section

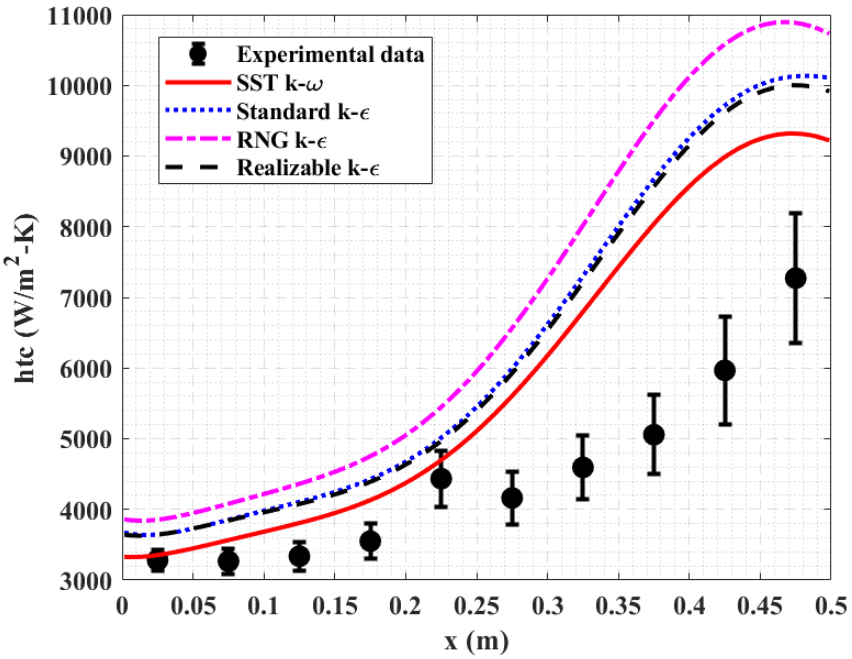

Figure F-6: Comparison of the local heat transfer coefficients obtained using four different turbulence models and medium mesh from Table F-3 against the experimental data for the offset NACA0020 airfoil fin PCHE test section

APPENDIX G. PCHE EXPERIMENTAL TEST CASES USED FOR THE CFD STUDY

The tables below present the measured experimental parameters and the wall temperatures for the test case used for CFD study of the offset rectangular fin PCHE test section.

Measured experimental parameters	
Inlet temperature (T_{in})	199.46 °C
Inlet pressure (P_{in})	10202.1 kPa
Outlet temperature (T_{out})	47.28 °C
Pressure drop (ΔP)	50.66 kPa
Outlet pressure ($P_{out} = P_{in} - \Delta P$)	10151.4 kPa
Mass flow rate ($\dot{m}$)	0.00735 kg/s

	Thermocouple location from the surface, z (m)	Measured wall temperature, $T_{w,meas}$ (°C)
Top 1	0.0041	69.66±0.17
Top 2	0.0040	68.75±0.18
Top 3	0.0042	59.86±0.16
Top 4	0.0041	51.12±0.16
Top 5	0.0040	48.13±0.16
Top 6	0.0039	39.66±0.16
Top 7	0.0041	40.06±0.15
Top 8	0.0043	34.86±0.15
Top 9	0.0041	35.67±0.16
Top 10	0.0039	32.76±0.15
Bottom 1	0.0041	74.63±0.17
Bottom 2	0.0040	83.14±0.18
Bottom 3	0.0041	71.10±0.16
Bottom 4	0.0041	58.02±0.16
Bottom 5	0.0041	53.59±0.16
Bottom 6	0.0038	50.34±0.15
Bottom 7	0.0042	43.45±0.15
Bottom 8	0.0041	41.29±0.15
Bottom 9	0.0040	39.65±0.15
Bottom 10	0.0042	37.15±0.15

The tables below present the measured experimental parameters and the wall temperatures for the test case used for CFD study of the offset NACA0020 airfoil fin PCHE test section.

Measured experimental parameters	
Inlet temperature (T_{in})	199.58 °C
Inlet pressure (P_{in})	10205.8 kPa
Outlet temperature (T_{out})	50.21 °C
Pressure drop (ΔP)	44.8 kPa
Outlet pressure ($P_{out} = P_{in} - \Delta P$)	10161 kPa
Mass flow rate ($\dot{m}$)	0.008 kg/s

	Thermocouple location from the surface, z (m)	Measured wall temperature, $T_{w,meas}$ (°C)
Top 1	0.0041	81.69±0.20
Top 2	0.0040	66.84±0.19
Top 3	0.0042	56.02±0.19
Top 4	0.0041	48.81±0.20
Top 5	0.0040	45.18±0.21
Top 6	0.0039	40.39±0.20
Top 7	0.0041	38.27±0.21
Top 8	0.0043	36.41±0.19
Top 9	0.0041	34.61±0.20
Top 10	0.0039	33.49±0.19
Bottom 1	0.0041	82.41±0.20
Bottom 2	0.0041	75.01±0.19
Bottom 3	0.0042	67.01±0.18
Bottom 4	0.0038	59.82±0.18
Bottom 5	0.0043	49.96±0.18
Bottom 6	0.0043	49.67±0.17
Bottom 7	0.0039	43.22±0.18
Bottom 8	0.0039	39.20±0.19
Bottom 9	0.0045	38.49±0.19
Bottom 10	0.0039	37.58±0.18

APPENDIX H. COOLING TOWER MODEL AND CAPITAL COST

Figure H-1 shows a simplified schematic of the cooler and the counter flow induced draft cooling tower. Also shown in the figure are key components of the cooling tower which include fill material, water-basin, drift eliminators, louvers, nozzles, fans, and circulating pump. A cooling tower model was developed to estimate the cooling tower power consumption and the capital cost. This Appendix provides details of the cooling tower model and capital cost estimation methodology.

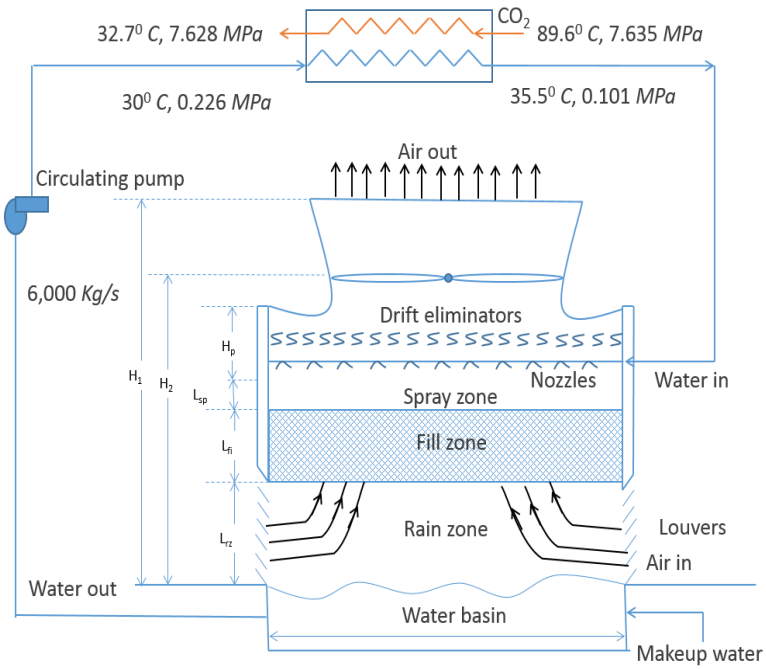

Figure H-1: Schematic of the cooling system comprising of the CO_2 cooler and the counter flow induced draft cooling tower

COOLING TOWER THEORY

The governing equations for the fill zone (main heat and mass transfer region in the cooling tower) were developed by the Merkel theory which is based on simplifying assumptions as stated below [116]:

1) Air exiting the cooling tower is saturated (100% relative humidity).
2) Lewis factor, $Le = h_c/C_{pma}h_d$ relating heat and mass transfer is assumed to be equal 1. Lewis factor is typically measured to be in the range of 0.85-0.9.
3) The evaporation losses are neglected during the energy balance.

Using these simplifying assumptions, following governing equation is obtained. This equation is well known as Merkel equation in literature:

$$Me = \frac{h_d a_{fi} L_{fill}}{G_w} = \int_{T_{wo}}^{T_{wi}} \frac{C_{pw} dT_w}{(i_{masw} - i_{ma})}$$

Merkel equation can be used to estimate the cooling tower dimensions if the mass transfer coefficient (h_d) and area density of fill (a_{fi}) are known. Due to complex nature of two-phase flow in the fill, it is extremely difficult to measure h_d and a_{fi} individually. Fortunately, these two appear as a product ($h_d a_{fi}$) in the Merkel equation and the individual values are not needed for design purposes.

DESIGN PROCEDURE

A code was developed to understand the effect of water and ambient air conditions on the size of cooling tower as well as to perform economic analysis in conjunction with

the supercritical CO_2 recompression Brayton cycle code. The code developed was validated by comparing the calculations to a quotation obtained from Delta Cooling Towers, Inc. for the conditions specified in their quotation.

Estimation of optimum $\dot{m}_w/\dot{m}_a$

For a given set of water conditions and ambient air conditions there exists an optimum value of $\dot{m}_w/\dot{m}_a$ which results in minimum construction and operating costs. Leeper [117] reported that the optimum $\dot{m}_w/\dot{m}_a$ can be estimated using following equations within 10% error by approximating the optimum air outlet temperature, T_{ao} as the average of hot and cold water temperature entering and exiting the tower,

$$T_{ao} = \frac{T_{wi}+T_{wo}}{2}$$

$$\frac{\dot{m}_w}{\dot{m}_a} = \frac{i_{mao}-i_{mai}}{C_{pw}(T_{wi}-T_{wo})}$$

Merkel number (Me)

For known water conditions, the tower Merkel number is solved numerically using the Chebyshev four-point numerical integration method as shown below,

$$Me = C_{pw}\int_{T_{wo}}^{T_{wi}} \frac{C_{pw}dT_w}{(i_{masw}-i_{ma})} = \frac{C_{pw}(T_{wi}-T_{wo})}{4}\left(\frac{1}{\Delta i_1}+\frac{1}{\Delta i_2}+\frac{1}{\Delta i_3}+\frac{1}{\Delta i_4}\right)$$

where

Δi_1 = value of $i_{masw} - i_{ma}$ at $T_{wo} + 0.1(T_{wi} - T_{wo})$

Δi_2 = value of $i_{masw} - i_{ma}$ at $T_{wo} + 0.4(T_{wi} - T_{wo})$

Δi_3 = value of $i_{masw} - i_{ma}$ at $T_{wo} + 0.6(T_{wi} - T_{wo})$

Δi_4 = value of $i_{masw} - i_{ma}$ at $T_{wo} + 0.9(T_{wi} - T_{wo})$

Estimation of floor area (A_{floor})

It is a common practice to use a certain number of small cooling tower cells instead of a single large cooling tower to reduce the total power consumption and to provide better temperature control. Lilly [118] collected information regarding different cell types and their specifications commonly used by the cooling tower manufacturers. These cells are classified based on cell sizes and blower power consumption. Choosing different cells will result in different floor area and power consumption. Using the smaller cell size will increase the required floor area of the cooling tower but will reduce the power consumption and vice-versa. The dimensions of the cell chosen for this study are of length (7'9$\frac{5}{8}$" [2.38 m]), width (18'1$\frac{1}{4}$" [5.52 m]), height (10'2$\frac{3}{4}$" [3.12 m]) and the power vs flow rate specifications of the blower is specified in Table H-1. According to Table H-1, operating the tower in different flow regimes will result in different power consumption and hence, will require different floor area accordingly. To match the vendor quote specifications, the air flow rate per cell of 95,000 cfm was selected [113].

Table H-1: Power vs Flowrate of blower used in the cooling tower cells

Flowrate (cfm [m^3/s])	Blower power (HP [KW])
70,800 [33.4]	10 [7.45]
80,750 [38.1]	15 [11.18]
88,300 [41.7]	20 [14.91]
95,000 [44.8]	25 [18.64]

The number of cells required is calculated as,

$$N_{cells} = \frac{\dot{Q}_{ao}}{95000}$$

where $\dot{Q}_{ao}$ is the total volumetric flow rate of air required to achieve the desired performance and is calculated from the air mass flow rate ($\dot{m}_a$) and air density at the outlet (ρ_{ao}). Once the required number of cells is calculated for each option, the required floor area (A_{floor}) is calculated by multiplying number of cells (N_{cells}) and area of each cell, which is equal to 7'9$\frac{5}{8}$" x 18'1$\frac{1}{4}$".

Estimation of fill height (L_{fill})

For a given thermal load, required length of a heat exchanger will depend on the surface area and the material used for construction of the heat exchanger. Similarly, the required fill height for a cooling tower will depend on the type of fill used for construction. As reported in the literature, three types of fills namely splash, trickle, and film are most commonly used. Each of these fills have different mass transfer coefficients, area density characteristics and empirical correlations are needed for estimation of the fill height. Kloppers *et al.* [119] performed experiments to investigate these fill types and proposed correlations to predict the Merkel number (Me) for each type. Out of these fill types, film fill matched the vendor data quite well. The Merkel number for film fill is given as,

$$\frac{Me}{L_{fill}} = 0.996604 G_w^{-0.469512} G_a^{0.790386}$$

where G_w and G_a are the water and air mass fluxes respectively and are defined as follows:

$$G_w = \frac{\dot{m}_w}{A_{floor}}$$

$$G_a = \frac{\dot{m}_a}{A_{floor}}$$

Once the fill height is known from the Equation above, heights of the rain zone (L_{rz}) and the spray zone (L_{sp}) are calculated as reported by Leeper [117],

$$L_{rz} = L_{fill}$$

$$L_{sp} = 0.5L_{fill}$$

The cooling tower head (H_{tower}) is then calculated as the sum of the heights of these three zones.

$$H_{tower} = L_{sp} + L_{fill} + L_{rz} = 2.5L_{fill}$$

Power consumption

Power required to operate the cooling tower is comprised of two parts, water pumping power and the air blower power. The power required to operate the water pump is calculated as,

$$P_{pump} = \frac{\dot{m}_w H_p g}{\eta_{pump}}$$

where H_p is the net required pumping head and is equal to the sum of required head in the cooling tower (H_{tower}), the cooler pressure drop head (ΔP_{cooler}) and an additional 10' of head. The efficiency of water pump (η_{pump}) is assumed to be 90%.

Blower power is calculated as,

$$P_{blower} = 25[HP].N_{cells}$$

Estimation of cooling tower cost

Cost correlation proposed by Zanker *et al.* [120] is used for estimation of the cooling tower construction cost,

$$\$_{1967} = \frac{Q_{load}\left[\frac{BTU}{hr}\right]}{C*A+39.2R-586}$$

where *R* and *A* are range and approach respectively in °F. C is defined as,

$$C = \frac{279}{[1+0.0335(85-WBT)^{1.143}]}$$

where WBT is the ambient wet bulb temperature in °F. It should be noted that the above correlation was proposed in 1967 when the material and fabrication costs were different compared to the present day. Due to inflation rate, $1 in 1967 has the same buying power as $7.08 in 2014. Hence, the value estimated from the equation above is multiplied by a factor of 7.08 to estimate the cost of tower in 2014.

APPENDIX I. PCHE MECHANICAL DESIGN PROCEDURE

Commercially available printed circuit heat exchanger (PCHE) units are fabricated by chemically etching near semi-circular channels with zigzag or straight channels on a substrate plate. The plates are then diffusion bonded to form a monolithic core. In order to simplify the mechanical design of the PCHE, the channels are approximated as rectangular channels according to the ASME 13-9 code requirements (ASME Sec VIII Div. I). Figure I-1 shows the approximated rectangular channels along with the nomenclature. In the figure, t_2 represents the thickness of the plate after etching, t_3 represents the ridge/fin thickness, $W = d$ is the channel width, $H = d/2$ is the channel depth assuming that the channels are perfectly semi-circular, and t_1 is the edge thickness. d is the channel diameter of the semi-circular channels.

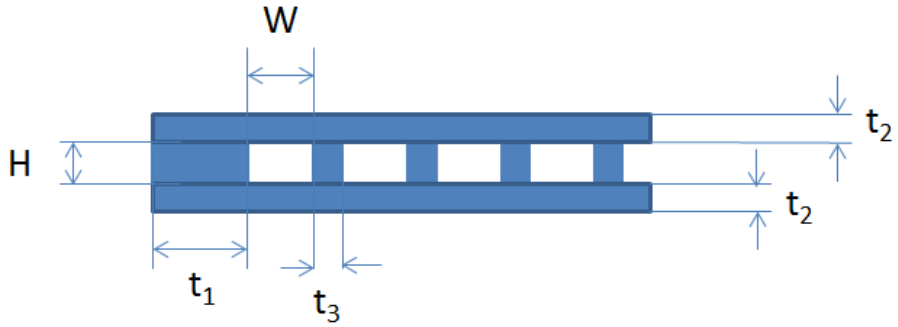

Figure I-1: Approximated PCHE channels for mechanical design and the associated nomenclature

The procedure for calculation of the edge thickness (t_1), plate thickness (t_2) and ridge thickness (t_3) involves calculation of the membrane stress (S_m) and bending stress (S_b) experienced by these members when subjected to the design pressure and temperature. These equations can be found in either ASME section 13-9 or Heatric publication [115].

Once the membrane and the bending stresses are calculated, the total stress (S_T) is calculated as,

$$S_T = S_m + S_b$$

Design pressure used to calculate the stresses is selected to be 10% greater than the cycle maximum pressure to ensure safety margin at a particular design temperature. The mechanical design is considered to be successful when the following criteria are met.

$$S_m \leq SE$$

$$S_T \leq 1.5SE$$

where E is the joint efficiency factor and is 0.7 for the diffusion bonded process based on Heatric's conservative assumption, S is the maximum allowable stress of the heat exchanger material (in the present case it is 316 stainless steel) and is a function of the design temperature.

Figure I-2 shows the maximum allowable stress as a function of the temperature for 316 stainless steel. The allowable stress data for different materials can be found in ASME B&PV Code, Section I, Part D. For operating temperatures in between the data points, maximum allowable stress is calculated using linear interpolation method. The validity of this mechanical design procedure for the discontinuous fin PCHEs is questionable. Nevertheless, for the purpose of this dissertation the plate thicknesses for the discontinuous fin PCHEs are calculated using this procedure.

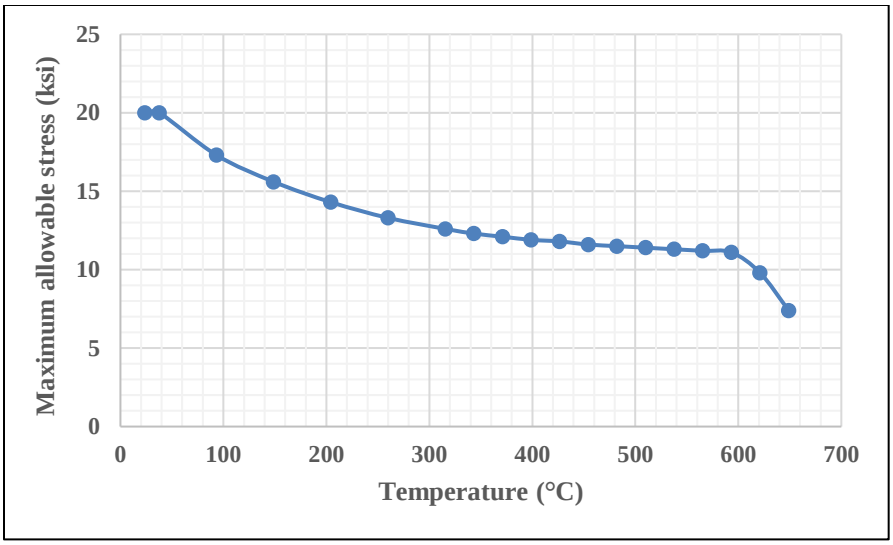

Figure I-2: Maximum allowable stress vs temperature for 316 stainless steel (Data obtained from ASME B&PV Code Section I, Part D)

REFERENCES

[1] A. E. Outlook, "US Energy Information Administration: Washington," *DC, USA*, 2016.

[2] U. S. D. O. E. N. E. R. A. Committee and others, "A technology roadmap for generation IV nuclear energy systems," *GIF-002-00*, 2002.

[3] V. Dostal, P. Hejzlar and M. J. Driscoll, "High-performance supercritical carbon dioxide cycle for next-generation nuclear reactors," *Nuclear Technology*, vol. 154, pp. 265-282, 2006.

[4] K. Sanford, "Thermodynamics/S. Klein, G. Nellis," *New York: Cambridge*, 2012.

[5] S. R. Pidaparti, P. J. Hruska, A. Moisseytsev, J. J. Sienicki and D. Ranjan, "Technical and economic feasibility of dry air cooling for the supercritical CO2 Brayton cycle using existing technology," in *The 5th International Symposium-Supercritical CO2 Power Cycles*, 2016.

[6] J. D. Jackson, "Fluid flow and convective heat transfer to fluids at supercritical pressure," *Nuclear Engineering and Design*, vol. 264, pp. 24-40, 2013.

[7] S. M. Liao and T. S. Zhao, "Measurements of heat transfer coefficients from supercritical carbon dioxide flowing in horizontal mini/micro channels," *Journal of Heat Transfer*, vol. 124, pp. 413-420, 2002.

[8] G. Angelino, "Carbon dioxide condensation cycles for power production," *Journal of Engineering for Power*, vol. 90, pp. 287-295, 1968.

[9] G. Angelino, "Real gas effects in carbon dioxide cycles," in *ASME 1969 gas turbine conference and products show*, 1969.

[10] E. G. Feher, "The supercritical thermodynamic power cycle," *Energy conversion*, vol. 8, pp. 85-90, 1968.

[11] Y. Chen, P. Lundqvist, A. Johansson and P. Platell, "A comparative study of the carbon dioxide transcritical power cycle compared with an organic Rankine cycle

with R123 as working fluid in waste heat recovery," *Applied thermal engineering*, vol. 26, pp. 2142-2147, 2006.

[12] I. L. Pioro, H. F. Khartabil and R. B. Duffey, "Heat transfer to supercritical fluids flowing in channels—empirical correlations (survey)," *Nuclear engineering and design*, vol. 230, pp. 69-91, 2004.

[13] A. A. Bishop, R. O. Sandberg and L. S. Tong, "Forced-convection heat transfer to water at near-critical temperatures and supercritical pressures," 1964.

[14] J. D. Jackson, "Forced convection heat transfer to fluids at supercritical pressure," *Turbulent forced convection in channels and bundles*, vol. 2, p. 563, 1979.

[15] B. S. Petukhov, A. F. Polyakov and B. E. Launder, "Heat transfer in turbulent mixed convection," 1988.

[16] R. C. Hendricks, R. J. Simoneau and R. V. Smith, "Survey of heat transfer to near-critical fluids," in *Advances in Cryogenic Engineering*, Springer, 1995, pp. 197-237.

[17] R. B. Duffey and I. L. Pioro, "Experimental heat transfer of supercritical carbon dioxide flowing inside channels (survey)," *Nuclear Engineering and Design*, vol. 235, pp. 913-924, 2005.

[18] R. P. Bringer and J. M. Smith, "Heat transfer in the critical region," *AIChE Journal*, vol. 3, pp. 49-55, 1957.

[19] E. A. Krasnoshchekov, V. S. Protopopov, F. Van and I. V. Kuraeva, "Experimental investigation of heat transfer for carbon dioxide in the supercritical region," in *Proceedings of the 2nd All-Soviet Union Conference on Heat and Mass Transfer, Minsk, Belarus*, 1964.

[20] P. Griffith, "ieterioratii in Heat Transfer to Fluids at Supercritical Pressure and High Heat Fluxes," 1969.

[21] B. Shiralkar and P. Griffith, "The effect of swirl, inlet conditions, flow direction, and tube diameter on the heat transfer to fluids at supercritical pressure," *Journal of heat transfer*, vol. 92, pp. 465-471, 1970.

[22] P. J. Bourke, D. J. Pulling, L. E. Gill and W. H. Denton, "Forced convective heat transfer to turbulent CO2 in the supercritical region," *International Journal of Heat and Mass Transfer,* vol. 13, pp. 1339-1348, 1970.

[23] T. Hiroaki, N. Niichi, H. Masaru and T. Ayao, "Forced convection heat transfer to fluid near critical point flowing in circular tube," *International Journal of Heat and Mass Transfer,* vol. 14, pp. 739-750, 1971.

[24] J. Fewster, "Mixed forced and free convective heat transfer to supercritical pressure fluids flowing in vertical pipes," 1976.

[25] G. A. Adebiyi and W. B. Hall, "Experimental investigation of heat transfer to supercritical pressure carbon dioxide in a horizontal pipe," *International journal of heat and mass transfer,* vol. 19, pp. 715-720, 1976.

[26] V. A. Kurganov and A. G. Kaptil'Ny, "Velocity and enthalpy fields and eddy diffusivities in a heated supercritical fluid flow," *Experimental thermal and fluid science,* vol. 5, pp. 465-478, 1992.

[27] V. A. Kurganov and A. G. Kaptilnyi, "Flow structure and turbulent transport of a supercritical pressure fluid in a vertical heated tube under the conditions of mixed convection. Experimental data," *International journal of heat and mass transfer,* vol. 36, pp. 3383-3392, 1993.

[28] S. M. Liao and T. S. Zhao, "An experimental investigation of convection heat transfer to supercritical carbon dioxide in miniature tubes," *International Journal of Heat and Mass Transfer,* vol. 45, pp. 5025-5034, 2002.

[29] P.-X. Jiang, Y.-J. Xu, J. Lv, R.-F. Shi, S. He and J. D. Jackson, "Experimental investigation of convection heat transfer of CO2 at super-critical pressures in vertical mini-tubes and in porous media," *Applied Thermal Engineering,* vol. 24, pp. 1255-1270, 2004.

[30] J. K. Kim, H. K. Jeon and J. S. Lee, "Wall temperature measurement and heat transfer correlation of turbulent supercritical carbon dioxide flow in vertical circular/non-circular tubes," *Nuclear Engineering and Design,* vol. 237, pp. 1795-1802, 2007.

[31] P.-X. Jiang, Y. Zhang, C.-R. Zhao and R.-F. Shi, "Convection heat transfer of CO2 at supercritical pressures in a vertical mini tube at relatively low Reynolds numbers," *Experimental Thermal and Fluid Science,* vol. 32, pp. 1628-1637, 2008.

[32] Y.-Y. Bae and H.-Y. Kim, "Convective heat transfer to CO2 at a supercritical pressure flowing vertically upward in tubes and an annular channel," *Experimental Thermal and Fluid Science,* vol. 33, pp. 329-339, 2009.

[33] Y.-Y. Bae, H.-Y. Kim and D.-J. Kang, "Forced and mixed convection heat transfer to supercritical CO2 vertically flowing in a uniformly-heated circular tube," *Experimental Thermal and Fluid Science,* vol. 34, pp. 1295-1308, 2010.

[34] Z.-H. Li, P.-X. Jiang, C.-R. Zhao and Y. Zhang, "Experimental investigation of convection heat transfer of CO2 at supercritical pressures in a vertical circular tube," *Experimental thermal and fluid science,* vol. 34, pp. 1162-1171, 2010.

[35] D. E. Kim and M.-H. Kim, "Experimental investigation of heat transfer in vertical upward and downward supercritical CO2 flow in a circular tube," *International Journal of Heat and Fluid Flow,* vol. 32, pp. 176-191, 2011.

[36] S. Gupta, E. Saltanov, S. J. Mokry, I. Pioro, L. Trevani and D. McGillivray, "Developing empirical heat-transfer correlations for supercritical CO2 flowing in vertical bare tubes," *Nuclear Engineering and Design,* vol. 261, pp. 116-131, 2013.

[37] H. A. M. Zahlan, "Derivation of a look-up table for trans-critical heat transfer in water-cooled tubes," 2015.

[38] K. Tanimizu and R. Sadr, "Experimental investigation of buoyancy effects on convection heat transfer of supercritical CO2 flow in a horizontal tube," *Heat and Mass Transfer,* vol. 52, pp. 713-726, 2016.

[39] S. R. Pidaparti, J. A. McFarland, M. M. Mikhaeil, M. H. Anderson and D. Ranjan, "Investigation of buoyancy effects on heat transfer characteristics of supercritical carbon dioxide in heating mode," *Journal of Nuclear Engineering and Radiation Science,* vol. 1, p. 031001, 2015.

[40] K. Goldmann, "HEAT TRANSFER TO SUPERCRITICAL WATER AND OTHER FLUIDS WITH TEMPERATURE-DEPENDENT PROPERTIES.

NUCLEAR ENGINEERING, PART I," in *Chem. Eng. Progr. Symposium Ser.*, 1954.

[41] W. B. Hall and J. D. Jackson, "Laminarization of a turbulent pipe flow by buoyancy forces," in *MECHANICAL ENGINEERING*, 1969.

[42] P. J. Bourke and D. J. Pulling, An experimental explanation of deterioration in heat transfer to supercritical carbon dioxide, Atomic Energy Research Establishment, 1971.

[43] V. A. Kurganov, V. B. Ankudinov and A. Kaptil ni, "Experimental-study of velocity and temperature-fields in an ascending flow of carbon-dioxide at supercritical pressure in a heated vertical pipe," *Teplofizika vysokikh temperatur,* vol. 24, pp. 1104-1111, 1986.

[44] J. Licht, M. Anderson and M. Corradini, "Heat transfer to water at supercritical pressures in a circular and square annular flow geometry," *International Journal of Heat and Fluid Flow,* vol. 29, pp. 156-166, 2008.

[45] M. Bazargan, D. Fraser and V. Chatoorgan, "Effect of buoyancy on heat transfer in supercritical water flow in a horizontal round tube," *Journal of heat transfer,* vol. 127, pp. 897-902, 2005.

[46] X. Cheng, Y. H. Yang and S. F. Huang, "A simplified method for heat transfer prediction of supercritical fluids in circular tubes," *Annals of Nuclear Energy*, vol. 36, pp. 1120-1128, 2009.

[47] G. A. Schatte, A. Kohlhepp, C. Wieland and H. Spliethoff, "Development of a new empirical correlation for the prediction of the onset of the deterioration of heat transfer to supercritical water in vertical tubes," *International Journal of Heat and Mass Transfer*, vol. 102, pp. 133-141, 2016.

[48] N. Kline, F. Feuerstein and S. Tavoularis, "Onset of heat transfer deterioration in vertical pipe flows of CO2 at supercritical pressures," *International Journal of Heat and Mass Transfer,* vol. 118, pp. 1056-1068, 2018.

[49] Y. V. Vikhrev, Y. D. Barulin and A. S. Kon'Kov, "A study of heat transfer in vertical tubes at supercritical pressures," *Therm. Eng*, vol. 14, pp. 116-119, 1967.

[50] K. Yamagata, K. Nishikawa, S. Hasegawa, T. Fujii and S. Yoshida, "Forced convective heat transfer to supercritical water flowing in tubes," *International journal of heat and mass transfer,* vol. 15, pp. 2575-2593, 1972.

[51] M. A. Styrikovich, T. K. Margulova and Z. L. Miropol'Skii, "Problems in the development of designs of supercritical boilers," *Teploenergetika,* vol. 14, pp. 4-7, 1967.

[52] S. Mokry, I. Pioro, A. Farah, K. King, S. Gupta, W. Peiman and P. Kirillov, "Development of supercritical water heat-transfer correlation for vertical bare tubes," *Nuclear Engineering and Design,* vol. 241, pp. 1126-1136, 2011.

[53] D. E. Kim and M. H. Kim, "Experimental study of the effects of flow acceleration and buoyancy on heat transfer in a supercritical fluid flow in a circular tube," *Nuclear Engineering and Design,* vol. 240, pp. 3336-3349, 2010.

[54] B. S. Petukhov, A. F. Polyakov, V. A. Kuleshohov and Y. L. Sheckter, "Turbulent flow and heat transfer in horizontal tubes with substantial influence of thermo-gravitational forces," in *Proc. of Fifth Int. Heat Transfer Conference,* 1974.

[55] F. W. Dittus and L. M. K. Boelter, "University of California publications on engineering," *University of California publications in Engineering,* vol. 2, p. 371, 1930.

[56] E. N. Sieder and G. E. Tate, "Heat transfer and pressure drop of liquids in tubes," *Industrial & Engineering Chemistry,* vol. 28, pp. 1429-1435, 1936.

[57] V. Gnielinski, "New equations for heat and mass transfer in turbulent pipe and channel flow," *Int. Chem. Eng.,* vol. 16, pp. 359-368, 1976.

[58] M. E. Shitsman, "Heat transfer to water, oxygen and carbon dioxide in near critical region," *Thermal Eng,* vol. 1, pp. 68-72, 1959.

[59] H. S. Swenson, J. R. Carver and C. R. d. Kakarala, "Heat transfer to supercritical water in smooth-bore tubes," *Journal of Heat Transfer,* vol. 87, pp. 477-483, 1965.

[60] E. A. Krasnoshchekov and V. S. Protopopov, "Heat transfer at supercritical region in flow of carbon dioxide and water in tubes," *Therm. Energy,* vol. 12, pp. 26-30, 1959.

[61] E. A. Krasnoshchekov, "Experimental study of heat exchagne in carbon dioxide in the supercritical range at high temperature drops," *High Temperature,* vol. 4, pp. 375-382, 1966.

[62] J. D. Jackson and J. Fewster, "Forced convection data for supercritical pressure fluids," *Report No. HTFS,* vol. 21540, 1975.

[63] J. D. Jackson, "Consideration of the heat transfer properties of supercritical pressure water in connection with the cooling of advanced nuclear reactors," in *The 13th pacific basin nuclear conference. Abstracts,* 2002.

[64] J. Pettersen, R. Rieberer and S. T. Munkejord, "Heat transfer and pressure drop for flow of supercritical and subcritical CO2 in microchannel tubes," 2000.

[65] S. S. Pitla, E. A. Groll and S. Ramadhyani, "Convective heat transfer from in-tube cooling of turbulent supercritical carbon dioxide: part 2—experimental data and numerical predictions," *HVAC&R Research,* vol. 7, pp. 367-382, 2001.

[66] S. H. Yoon, J. H. Kim, Y. W. Hwang, M. S. Kim, K. Min and Y. Kim, "Heat transfer and pressure drop characteristics during the in-tube cooling process of carbon dioxide in the supercritical region," *International Journal of Refrigeration,* vol. 26, pp. 857-864, 2003.

[67] C. Dang and E. Hihara, "In-tube cooling heat transfer of supercritical carbon dioxide. Part 1. Experimental measurement," *International journal of refrigeration,* vol. 27, pp. 736-747, 2004.

[68] G. Kuang, M. M. Ohadi and Y. Zhao, "Experimental study on gas cooling heat transfer for supercritical CO2 in microchannels," in *ASME 2004 2nd International Conference on Microchannels and Minichannels*, 2004.

[69] X. L. Huai, S. Koyama and T. S. Zhao, "An experimental study of flow and heat transfer of supercritical carbon dioxide in multi-port mini channels under cooling conditions," *Chemical Engineering Science,* vol. 60, pp. 3337-3345, 2005.

[70] C.-H. Son and S.-J. Park, "An experimental study on heat transfer and pressure drop characteristics of carbon dioxide during gas cooling process in a horizontal tube," *International Journal of Refrigeration,* vol. 29, pp. 539-546, 2006.

[71] P.-X. Jiang, C.-R. Zhao, R.-F. Shi, Y. Chen and W. Ambrosini, "Experimental and numerical study of convection heat transfer of CO2 at super-critical pressures during cooling in small vertical tube," *International Journal of Heat and Mass Transfer,* vol. 52, pp. 4748-4756, 2009.

[72] A. Bruch, A. Bontemps and S. Colasson, "Experimental investigation of heat transfer of supercritical carbon dioxide flowing in a cooled vertical tube," *International Journal of Heat and Mass Transfer,* vol. 52, pp. 2589-2598, 2009.

[73] H.-K. Oh and C.-H. Son, "New correlation to predict the heat transfer coefficient in-tube cooling of supercritical CO2 in horizontal macro-tubes," *Experimental Thermal and Fluid Science,* vol. 34, pp. 1230-1241, 2010.

[74] T. Ma, W.-x. Chu, X.-y. Xu, Y.-t. Chen and Q.-w. Wang, "An experimental study on heat transfer between supercritical carbon dioxide and water near the pseudo-critical temperature in a double pipe heat exchanger," *International Journal of Heat and Mass Transfer,* vol. 93, pp. 379-387, 2016.

[75] E. E. Wilson, "A basis for rational design of heat transfer apparatus," *The J. Am. Soc. Mech. Engrs.,* vol. 37, pp. 546-551, 1915.

[76] J. E. Hesselgreaves, R. Law and D. Reay, Compact heat exchangers: selection, design and operation, Butterworth-Heinemann, 2016.

[77] Q. Li, G. Flamant, X. Yuan, P. Neveu and L. Luo, "Compact heat exchangers: A review and future applications for a new generation of high temperature solar receivers," *Renewable and Sustainable Energy Reviews,* vol. 15, pp. 4855-4875, 2011.

[78] D. Southall, R. Le Pierres and S. J. Dewson, "Design considerations for compact heat exchangers," in *Proceedings of ICAPP*, 2008.

[79] I. Rühlich and H. Quack, "New regenerator design for cryocoolers," in *17th International Cryogenic Engineering Conference, Bournemouth, England*, 1998.

[80] A. M. Kruizenga, Heat transfer and pressure drop measurements in prototypic heat exchanges for the supercritical carbon dioxide Brayton power cycles, 2010.

[81] S. K. Mylavarapu, "Design, fabrication, performance testing, and modeling of diffusion bonded compact heat exchangers in a high-temperature helium test facility," 2011.

[82] J.-W. Seo, Y.-H. Kim, D. Kim, Y.-D. Choi and K.-J. Lee, "Heat transfer and pressure drop characteristics in straight microchannel of printed circuit heat exchangers," *Entropy,* vol. 17, pp. 3438-3457, 2015.

[83] M. Chen, X. Sun, R. N. Christensen, S. Shi, I. Skavdahl, V. Utgikar and P. Sabharwall, "Experimental and numerical study of a printed circuit heat exchanger," *Annals of Nuclear Energy,* vol. 97, pp. 221-231, 2016.

[84] W.-x. Chu, X.-h. Li, T. Ma, Y.-t. Chen and Q.-w. Wang, "Experimental investigation on SCO2-water heat transfer characteristics in a printed circuit heat exchanger with straight channels," *International Journal of Heat and Mass Transfer,* vol. 113, pp. 184-194, 2017.

[85] K. Nikitin, Y. Kato and L. Ngo, "Printed circuit heat exchanger thermal--hydraulic performance in supercritical CO2 experimental loop," *International Journal of Refrigeration,* vol. 29, pp. 807-814, 2006.

[86] T. L. Ngo, Y. Kato, K. Nikitin and T. Ishizuka, "Heat transfer and pressure drop correlations of microchannel heat exchangers with S-shaped and zigzag fins for carbon dioxide cycles," *Experimental Thermal and Fluid Science,* vol. 32, pp. 560-570, 2007.

[87] I. H. Kim, H. C. No, J. I. Lee and B. G. Jeon, "Thermal hydraulic performance analysis of the printed circuit heat exchanger using a helium test facility and CFD simulations," *Nuclear Engineering and Design,* vol. 239, pp. 2399-2408, 2009.

[88] A. Moisseytsev, J. J. Sienicki, D. H. Cho and M. R. Thomasa, "Comparison of heat exchanger modeling with data from CO 2-to-CO 2 printed circuit heat exchanger performance tests," in *Proceedings of the 2010 International Congress on Advances in Nuclear Power Plants-ICAPP'10,* 2010.

[89] M. Chen, X. Sun, R. N. Christensen, I. Skavdahl, V. Utgikar and P. Sabharwall, "Pressure drop and heat transfer characteristics of a high-temperature printed circuit heat exchanger," *Applied Thermal Engineering,* vol. 108, pp. 1409-1417, 2016.

[90] S. Baik, S. G. Kim, J. Lee and J. I. Lee, "Study on CO2--water printed circuit heat exchanger performance operating under various CO_2 phases for S-CO_2 power cycle application," *Applied Thermal Engineering,* vol. 113, pp. 1536-1546, 2017.

[91] I. H. Kim and H. C. No, "Thermal hydraulic performance analysis of a printed circuit heat exchanger using a helium--water test loop and numerical simulations," *Applied Thermal Engineering,* vol. 31, pp. 4064-4073, 2011.

[92] I. H. Kim and H. C. No, "Thermal--hydraulic physical models for a Printed Circuit Heat Exchanger covering He, He--CO2 mixture, and water fluids using experimental data and CFD," *Experimental Thermal and Fluid Science,* vol. 48, pp. 213-221, 2013.

[93] M. D. Carlson, "Measurement and Analysis of the Thermal Hydraulic Performance of Several Printed Circuit Heat Exchanger Channel Geometries," 2012.

[94] K. Nikitin, Y. Kato and T. Ishizuka, "Experimental thermal-hydraulics comparison of microchannel heat exchangers with zigzag channels and S-shaped fins for gas turbine reactors," 2007.

[95] N. Tsuzuki, Y. Kato and T. Ishiduka, "High performance printed circuit heat exchanger," *Applied Thermal Engineering,* vol. 27, pp. 1702-1707, 2007.

[96] T. L. Ngo, Y. Kato, K. Nikitin and N. Tsuzuki, "New printed circuit heat exchanger with S-shaped fins for hot water supplier," *Experimental Thermal and Fluid Science,* vol. 30, pp. 811-819, 2006.

[97] D. E. Kim, M. H. Kim, J. E. Cha and S. O. Kim, "Numerical investigation on thermal--hydraulic performance of new printed circuit heat exchanger model," *Nuclear Engineering and Design,* vol. 238, pp. 3269-3276, 2008.

[98] W.-Q. Wang, Y. Qiu, Y.-L. He and H.-Y. Shi, "Experimental study on the heat transfer performance of a molten-salt printed circuit heat exchanger with airfoil fins for concentrating solar power," *International Journal of Heat and Mass Transfer,* vol. 135, pp. 837-846, 2019.

[99] X. Y. Xu, Q. W. Wang, L. Li, S. V. Ekkad and T. Ma, "Thermal-hydraulic performance of different discontinuous fins used in a printed circuit heat exchanger for supercritical CO2," *Numerical Heat Transfer, Part A: Applications,* vol. 68, pp. 1067-1086, 2015.

[100] D. M. Allen, "Photochemical machining: from 'manufacturing's best kept secret'to a 6 billion per annum, rapid manufacturing process," *CIRP annals,* vol. 53, pp. 559-572, 2004.

[101] J. T. Black and R. A. Kohser, DeGarmo's materials and processes in manufacturing, John Wiley & Sons, 2017.

[102] C. Y. Ho and T. K. Chu, "Electrical resistivity and thermal conductivity of nine selected AISI stainless steels," 1977.

[103] S. W. Churchill and H. H. S. Chu, "Correlating equations for laminar and turbulent free convection from a vertical plate," *International journal of heat and mass transfer,* vol. 18, pp. 1323-1329, 1975.

[104] E. W. Lemmon, M. L. Huber and M. O. McLinden, "NIST Standard Reference Database 23: Reference Fluid Thermodynamic and Transport Properties-REFPROP, Version 9.1, Standard Reference Data Program," *National Institute of Standards and Technology: Gaithersburg, MD,* 2013.

[105] S. J. Kline, "„and McClintock, FA, 1953," Describing Uncertainties in Single-Sample Experiments,"," *Mechanical Engineering,* vol. 75, pp. 3-8.

[106] I. L. Pioro, R. B. Duffey and T. J. Dumouchel, "Hydraulic resistance of fluids flowing in channels at supercritical pressures (survey)," *Nuclear engineering and design,* vol. 231, pp. 187-197, 2004.

[107] I. E. Idelchik, "Handbook of hydraulic resistance hemisphere," *New York,* vol. 640, 1986.

[108] A. Fluent, "12.0 Theory Guide," *Ansys Inc,* vol. 5, 2009.

[109] S. Garimella, B. Mitra, U. C. Andresen, Y. Jiang and B. M. Fronk, "Heat transfer and pressure drop during supercritical cooling of HFC refrigerant blends," *International Journal of Heat and Mass Transfer,* vol. 91, pp. 477-493, 2015.

[110] V. A. Kurganov, "Heat transfer and pressure drop in tubes under supercritical pressure. Part 2. Heat transfer and friction at high heat fluxes. The influence of additional factors. Enhancement of deteriorated heat transfer," *Thermal engineering,* vol. 45, pp. 301-310, 1998.

[111] J. Sienicki, A. Moisseytsev and L. Krajtl, "Utilization of the supercritical CO2 Brayton cycle with sodium-cooled fast reactors," in *The 4th Internation Symposium-Supercritical CO2 Power Cycles*, 2014.

[112] A. Moisseytsev, "Passive load follow analysis of the STAR-LM and STAR-H2 systems.," 2004.

[113] S. R. Pidaparti, A. Moisseytsev, J. J. Sienicki and D. Ranjan, "Counter flow induced draft cooling tower option for supercritical carbon dioxide Brayton cycle," *Nuclear Engineering and Design,* vol. 295, pp. 549-558, 2015.

[114] A. Moisseytsev and J. J. Sicnicki, "Cost-based optimization of supercritical carbon dioxide Brayton cycle equipment," *Transactions of the American Nuclear Society,* vol. 105, pp. 675-676, 2011.

[115] R. Le Pierres, D. Southall and S. Osborne, "Impact of mechanical design issues on printed circuit heat exchangers," in *sCO2 Power Cycle Symposium, Boulder, CO, May*, 2011.

[116] J. C. Kloppers and D. G. Kröger, "Cooling tower performance evaluation: Merkel, Poppe, and e-NTU methods of analysis," *Journal of Engineering for Gas Turbines and Power*, vol. 127, pp. 1-7, 2005.

[117] S. A. Leeper, "Wet cooling towers: rule-of-thumb design and simulation," 1981.

[118] D. E. Lilly, "Analysis and performance of gas-electric hybrid chiller systems," 1998.

[119] J. C. Kloppers and D. G. Kröger, "Refinement of the transfer characteristic correlation of wet-cooling tower fills," *Heat transfer engineering*, vol. 26, pp. 35-41, 2005.

[120] A. Zanker, *Estimating cooling tower costs from operating data*, vol. 79, MCGRAW HILL INC 1221 AVENUE OF THE AMERICAS, NEW YORK, NY 10020, 1972, p. 118.

[121] S. Pidaparti, D. Jarahbashi, M. Anderson and D. Ranjan, "Unusual Heat Transfer Characteristics of Supercritical Carbon Dioxide," in *ASME 2015 International Mechanical Engineering Congress and Exposition*, 2015.